Trace Analysis Using Laser Ablation Initiated Resonant Ionisation Mass Spectrometry.

Paul Thomas McCombes

Department of Physics and Astronomy

University of Glasgow

Presented as a thesis for the degree of Doctor of Philosophy in the University of Glasgow.

ProQuest LLC.
789 East Eisenhower Parkway
P.O. Box 1346
Ann Arbor, MI 48106 – 1346

To Dad

Acknowledgements.

Many people have helped in the preparation of this thesis. I would like to thank them all but especially:-

Dr. Ken Ledingham, LIS leader, for persuading me to do this in the first place and for a constantly open door.

Dr. Ravi Singhal for help and advice with the theoretical side of the work.

Dr. Mike Towrie and Dr. Adrian Land, for the endless hours spent in room 14 trying to get the machine to work, and for taking some of the data when it did.

Ian Borthwick, for proof reading this thesis and for much valuable help in obtaining data.

Archie Marshall, Shauna Drysdale, Chris McLean, Wang Li and Ally Clark for their invaluable help and suggestions.

Bob Maxwell and Tom McCanny for their immeasurable help in the construction and operation of the instrument.

All the technical staff from the electronic and mechanical workshop who have designed numerous gizmos for the machine.

Jim Hough, who's office I wandered into and who persuaded me to stay.

SERC for the cash.

Dave Finbow and Kratos for faith in me and the CASE award.

CMS, especially Andy Bowdler and Dave Martin, for a great time during my industrial placement.

Steve Chryssoulis and Surface Science Western for the use of the gold samples.

My family, who thought it was a good idea, and friends, for endless encouragement.

PUBLICATIONS

Glasgow Resonant Ionisation Mass Spectrometer Publications.

1) The Glasgow Resonant Ionisation Mass Spectrometer.

M. Towrie, S.L.T. Drysdale, R. Jennings, A.P. Land, K.W.D. Ledingham, P.T McCombes, R.P. Singhal, M.H.C. Smyth, D.T. Stewart, C.M. Houston and C.J. McLean .

"RIS '88", Gaithersburg, Washington, (I.O.P Conference Series No. 94) p94

2) The Glasgow Resonant Ionisation Mass Spectrometer.

P.T McCombes, S.L.T. Drysdale, R. Jennings, A.P. Land, K.W.D. Ledingham, R.P. Singhal, M.H.C. Smyth, D.T. Stewart, M. Towrie and C.J. McLean.

Published in the Proceedings of the 12th International Conference on Mass Spectroscopy, Bordeaux, France, August 1988.

3) Preliminary Results from the Glasgow Resonant Ionisation Mass Spectrometer.

R. Jennings, S.L.T. Drysdale, P.T McCombes, A.P. Land, K.W.D. Ledingham, R.P. Singhal, M.H.C. Smyth, D.T. Stewart, M. Towrie, C.M. Houston and C.J. McLean.

Presented as a poster at the Adriatic Research Conference on the Applications of Lasers in Surface Science, held at the International Centre for Theoretical Physics, Trieste, Italy, August 1988.

4) Trace Analysis using Resonant Ionisation.

P.T McCombes, S.L.T. Drysdale, R. Jennings, A.P. Land, K.W.D. Ledingham, R.P Singhal, M Towrie and C.J. McLean.

Presented at the International Meeting of Kratos Equipment Users 1989

5) Trace Analysis using a Commercial Resonant Ionisation Mass Spectrometer.

M. Towrie, S.L.T. Drysdale, R. Jennings, A.P. Land, K.W.D. Ledingham, P.T McCombes, R.P. Singhal, M.H.C. Smyth and C.J. McLean.

Published in the International Journal of Mass Spectroscopy and Ion Processes.,1990

6) Resonant Ionisation Mass Spectroscopy of Calcium.

A.P. Land, R. Jennings K.W.D Ledingham, P.T McCombes, R.P. Singhal and M Towrie.

- to be published

7) Observations on Carbon Clusters During Trace Elemental Analysis of Coal Samples by Resonant Ionisation Mass Spectrometry.

R. Singhal, K.W.D. Ledingham, S.L.T. Drysdale, R. Jennings, A.P. Land, P.T McCombes, M. Towrie.

Submitted to Spectra Chim Acta

8) Characterisation of the Energy and Spatial Distribution of Neutrals Produced by Laser Ablation

P.T McCombes, I. Borthwick, R. Jennings, A.P. Land, K.W.D. Ledingham, R. Singhal, M. Towrie.

Published in the SPIE Proceedings Series Volume 1208 - Laser Photoionisation and Desorption Surface Analysis Techniques, January 1990.

9) Investigations of Atoms Liberated from Metal Surfaces by Laser Ablation.

I. Borthwick, R. Jennings, K.W.D. Ledingham, P.T McCombes, R. Singhal.

Presented at 1st National Conference on Atomic, Molecular and Optical Physics, April 1990, Belfast.

10) Resonance Ionisation Spectroscopy Applied to Trace Analysis of Gold

P.T McCombes, I. Borthwick, R. Jennings, K.W.D. Ledingham, R. Singhal.

- to be Published in the Proceedings of the International Conference on Optogalvanic Spectroscopy and Related Topics at Strathclyde University. August 1990, IOP Conference Series.

11) Observations on Carbon Clusters During Trace Elemental Analysis of Coal Samples by Resonant Ionisation Mass Spectrometry.

K.W.D. Ledingham, R. Singhal, S.L.T. Drysdale, R. Jennings, A.P. Land, P.T McCombes, M. Towrie.

To be Presented at RIS 90, Ispra, Italy. Sept 1990. To be published in "RIS '90" ,IOP publishing.

12) Studies of Laser Ablation by Resonant Ionisation Mass Spectrometry

I. Borthwick, P.T McCombes, R. Jennings, K.W.D. Ledingham, R. Singhal.

To be Presented at RIS 90, Ispra, Italy. Sept 1990. To be published in "RIS '90" ,IOP publishing.

13) Trace Analysis Using a Resonant Ionisation Mass Spectrometer.

P.T McCombes.

Talk presented to the First Annual Cambridge Mass Spectrometry Users Group Meeting, April 1990.

Other Papers

14) Resonant Laser Ablation

C.J. M^{c} Lean, J. Marsh, A.P. Land, A. Clark, R. Jennings, K.W.D. Ledingham, P.T McCombes, R. Singhal, M. Towrie.

Published in the International Journal of Mass Spectrometry and Ion Processes.

15) Detailed Characteristics of Resonant Laser Ablation

L. Wang, C.J. M^{c} Lean, I. Borthwick, R. Jennings, K.W.D. Ledingham, P.T McCombes, R. Singhal.

To be Presented at RIS 90, Ispra, Italy. Sept 1990. To be published in "RIS '90" ,IOP publishing.

16) Novel Ion Optics for Secondary Ion Suppression in Resonant Ionisation Mass Spectrometry

C.J. M^{c} Lean, P.T McCombes, R. Jennings, K.W.D. Ledingham, R. Singhal.

to be Published in Nuclear Instrumentation and Methods for Physical Research.

17) A Resonance Enhanced Multi-Photon Ionisation (REMPI) Instrument for Organic Mass Spectrometry

P.T McCombes, A.R. Bowdler, D.M. Martin.

Published by Cambridge Mass Spectrometry as a Brochure and Presented as a Poster at "Spectroscopy Across the Spectrum Conference - Techniques and Applications of Analytical Spectroscopy", Hatfield Polytechnic, July 1990.

18) Applications of Resonant Ionisation Mass Spectrometry to Depth Profiling in Type III-V Semiconductor Devices.

C.J. McLean, J.H. Marsh, J.W. Cahill, S.L.T. Drysdale, R. Jennings, A.P. Land, K.W.D. Ledingham, P.T McCombes, R.P. Singhal, M.H.C. Smyth, D.T. Stewart and M. Towrie.

"RIS '88", Gaithersburg, Washington, (I.O.P Conference Series No. 94) p73

18) Depth Profiling in III-V Semiconductor Devices Using Resonant Ionisation Mass Spectrometry.

Presented at the Triennial International Mass Spectroscopy Symposium, Salford, June 1989.

C.J. McLean, J.H. Marsh, A Clark, R. Jennings, A.P. Land, K.W.D. Ledingham, A Marshal, P.T McCombes, R.P. Singhal and M. Towrie.

SUMMARY

Title: *Trace Analysis Using Laser Ablation Initiated Resonant Ionisation Mass Spectrometry.*

This thesis deals with the practical aspects of the development and use of a resonant ionisation mass spectrometer. The first chapter gives an outline of the ideas and the applications of resonant ionisation mass spectrometry (RIMS), together with a brief historical overview of the method, showing its development in the last twenty years.

The second chapter deals with the theoretical aspects of resonant ionisation spectroscopy (RIS). Firstly time dependent perturbation theory is used to demonstrate how the selectivity and sensitivity of the method come about. Next the derivation of rate equations for a simple system, a practical way of analysing RIMS ion yields, is shown. Causes of broadening of transitions are then described. Non-linear optics and the theoretical aspects of laser ablation are then discussed.

Chapter 3 deals with the instrumentation and describes the equipment used. The mass spectrometer was designed and assembled in Glasgow and constructed by Kratos Analytical. This chapter details the improvements that have been made to the original design. Further enhancements that are possible but not implemented are given in chapter 8.

Chapter 4 describes the development of the computer software. This software is used to control the data acquisition hardware and for subsequent analysis of the data. The software was written exclusively by the author.

Chapter 5 presents some of the earlier results from the instrument. The author, together with Dr Mike Towrie and Dr Adrian Land, was responsible for the acquisition of these results

Chapter 6 examines in detail the laser ablation process. Laser ablation is used to evaporate samples to produce a flux of neutrals leaving the surface. It is the primary evaporation source used at Glasgow and it is very poorly understood, both in terms of underlying theory and some phenomenological aspects of it. For the optimal operation of the instrument the process of neutral production must be well characterised. The calcium ablation work presented was performed by the author, Dr M Towrie and

Dr A Land. The gold and lead ablation work was the exclusive work of the author. The work on aluminium and NIST steel was performed by Mr I Borthwick and the author.

Chapter 7 presents work on trace analysis of gold using RIMS. This work involves the detection of trace amounts of gold in a copper matrix. Other resonant schemes will be discussed. All work in this chapter is the sole work of the author.

Chapter 8 gives conclusions about the viability of the RIMS method in the field of trace analysis, together with a discussion of possible improvements in the instrument and the methodology.

Appendix A contains information on the physical characteristics of gold.

Appendix B gives details of field inverting optics which were designed by the author. A design of this type is expected to improve the performance of the instrument described in this thesis.

Contents

Glossary

Abbreviations, Acronyms and Portmanteaux

ADC	Analogue to Digital Convertor
BASIC	Beginners All purpose Symbolic Instruction Code
βBBO	beta Barium Borate
CAMAC	Computer Aided Measurement And Control
CCD	Charged Coupled Device
DC	Direct Current
DDG	Digital Delay Generator
DNA	DeoxyriboseNucleic Acid
DOS	Disk Operating System
EIG	Electostatic Ion Guide
EM	ElectroMagnetic
FORTRAN	FORmula TRANslation
FWHM	Full Width Half Maximum
GPIB	General Purpose Interface Bus
HPGL	Hewlett Packard Graphics Language
ICPMS	Inductively Coupled Plasma Mass Spectrometry
IEEE	Institute of Electrical and Electronic Engineers
KDP	pottasium (K) Dideutrium Phosphate
KPB	potassium (K) Penta Borate
LIMA	Laser Ionisation Mass Analyser
Nd:YAG	Neodymium Yttrium Aluminium Garnet
OGE	OptoGalvanic Effect

OPO	Optical Parametric Oscillator
PC	Personal Computer
RIMS	Resonant Ionisation Mass Spectrometry
RIS	Resonant Ionisation Spectroscopy
SFG	Sum Frequency Generation
SHG	Second Harmonic Generation
SIMS	Secondary Ion Mass Spectrometry
SIRIS	Sputter Initiated Resonant Ionisation Spectroscopy
SNMS	Secondary Neutral Mass Spectrometry
SS	Stainless Steel
SSW	Surface Science Western
TASM	Turbo ASseMbler
TDR	Transient Digital Recorder
TEM	Transverse ElectroMagnetic
THG	Third Harmonic Generation
TOF	Time Of Flight
TOF-MS	Time Of Flight Mass Spectrometry
UV	Ultra Violet
VGA	Video Graphics Array

Chapter 1 : Introduction

§1 Resonant Ionisation Spectroscopy

Resonant Ionisation Spectroscopy (RIS) is a comparatively recent analytical tool. It was not until the development of a tunable high powered light source that it was feasible. Ambartsumyan *et al* (1971) performed the first reported resonant ionisation experiment. The ultimate goal of elemental analysis was achieved in 1977 (Hurst *et al* 1977) when single atom detection was first reported by RIS.

The basic concepts behind RIS are straightforward. Every element (or molecule) has its own unique set of bound electronic energy levels. Using light of a wavelength corresponding to the energy gap between a populated and an unpopulated level an electron can be excited to the unpopulated level in a process called resonant absorption (Fig 1.1). If the electron absorbs another photon of a resonant energy while it is in this excited state it will be excited to a higher level. By repeating this process the atom will eventually become ionised. If the photons are not of resonant energy the probability of absorption is greatly reduced (Fig 1.2). Since the energy levels of an element are unique each atom can be ionised by the use of photons of different wavelengths. This gives resonant ionisation high elemental selectivity, which is one of its major advantages. By careful choice of the resonant ionisation scheme the process can also be made isotopically selective for some elements, which is the basis of recent developments in laser isotope separation (Crane *et al* 1985).

Another advantage of resonant ionisation is its ability to saturate the ionisation process ie. ionisation of every irradiated atom. The fluxes required for this (Chapter 2) are of the order of 10^{23} photons cm^{-2} s^{-1}. These fluxes are unobtainable with conventional monochromatic light sources but can easily be achieved with a pulsed tunable dye laser which can deliver up to

Fig 1.1: Resonant Absorption

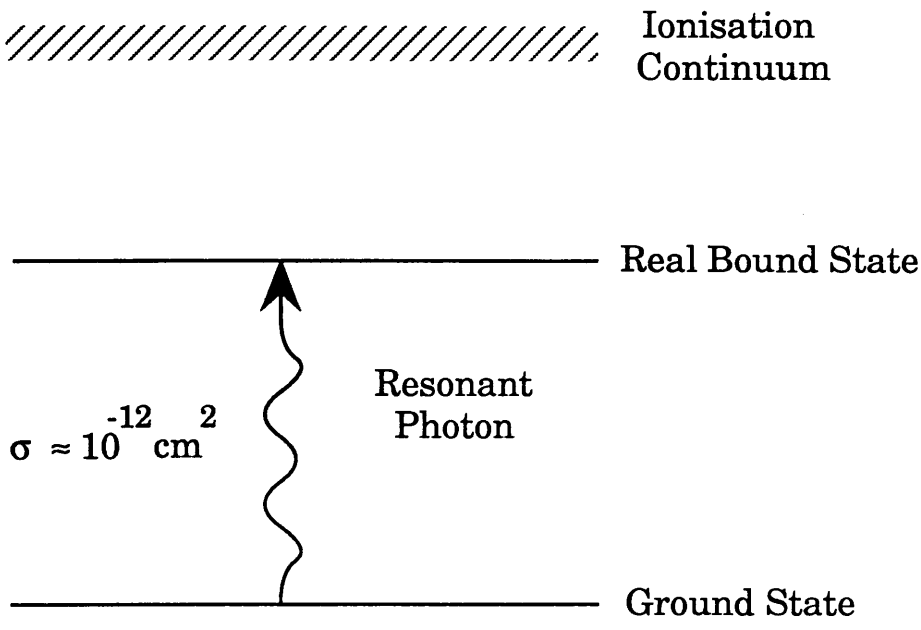

Fig 1.2: Non-resonant Absorption

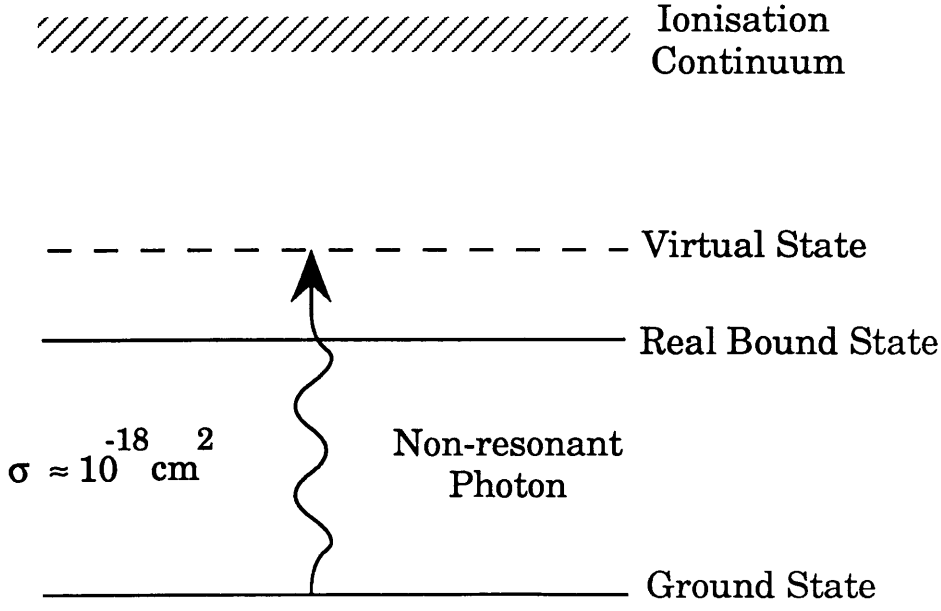

10^{28} photons cm^{-2} s^{-1} , 10 orders of magnitude greater than non-laser sources.

Hurst *et al* (1979) have listed five basic schemes using two lasers which enable all elements, bar helium and neon, to be ionised.

The schemes are shown in fig 1.3 **1-5.** The simplest scheme is **1** which involves the absorption of one photon and ionisation of the atom on absorption of the next photon of the same wavelength. The next scheme, **2,** uses a technique called frequency doubling (see chapter 2) to provide a single photon with twice the energy of the original laser (or fundamental). The absorption of a photon of the fundamental ionises the atom. Scheme **3** is the first scheme involving two colours, where absorption of photon 1 is followed by absorption of photon 2 promoting the electron to a higher bound state. Further absorption of a photon of either colour will ionise the atom. Scheme **4** is similar except that frequency 1 is doubled, as in scheme **2**. The atom is then ionised by either colour 1 or colour 2. Scheme **5** involves a transition through a "virtual" state by either or both of the photons, and the absorption of a final photon to produce an ion.

Since the difficulty involved in using any particular scheme is reflected in the scheme's number, it can be seen from the periodic table (fig 1.4) that most metals are easier to ionise than the semi-metals or non-metals. It is for this reason that resonant ionisation has been used mainly on metals by the Glasgow group .

§2 Historical Development of RIS and RIMS

The first observation of laser induced ionisation was the induction of a spark at the focal point of Q-switched ruby lasers.(Meyerand *et al* 1963, 1964; Voronov *et al* 1965). This effect was proposed to be caused by the simultaneous absorption of several photons (Keldysh 1965; Gold *et al* 1965; Bebb *et al* 1966). The simultaneous absorption of two photons was first proposed by Goppart-Mayer (1931).

The five basic Resonance Ionisation schemes

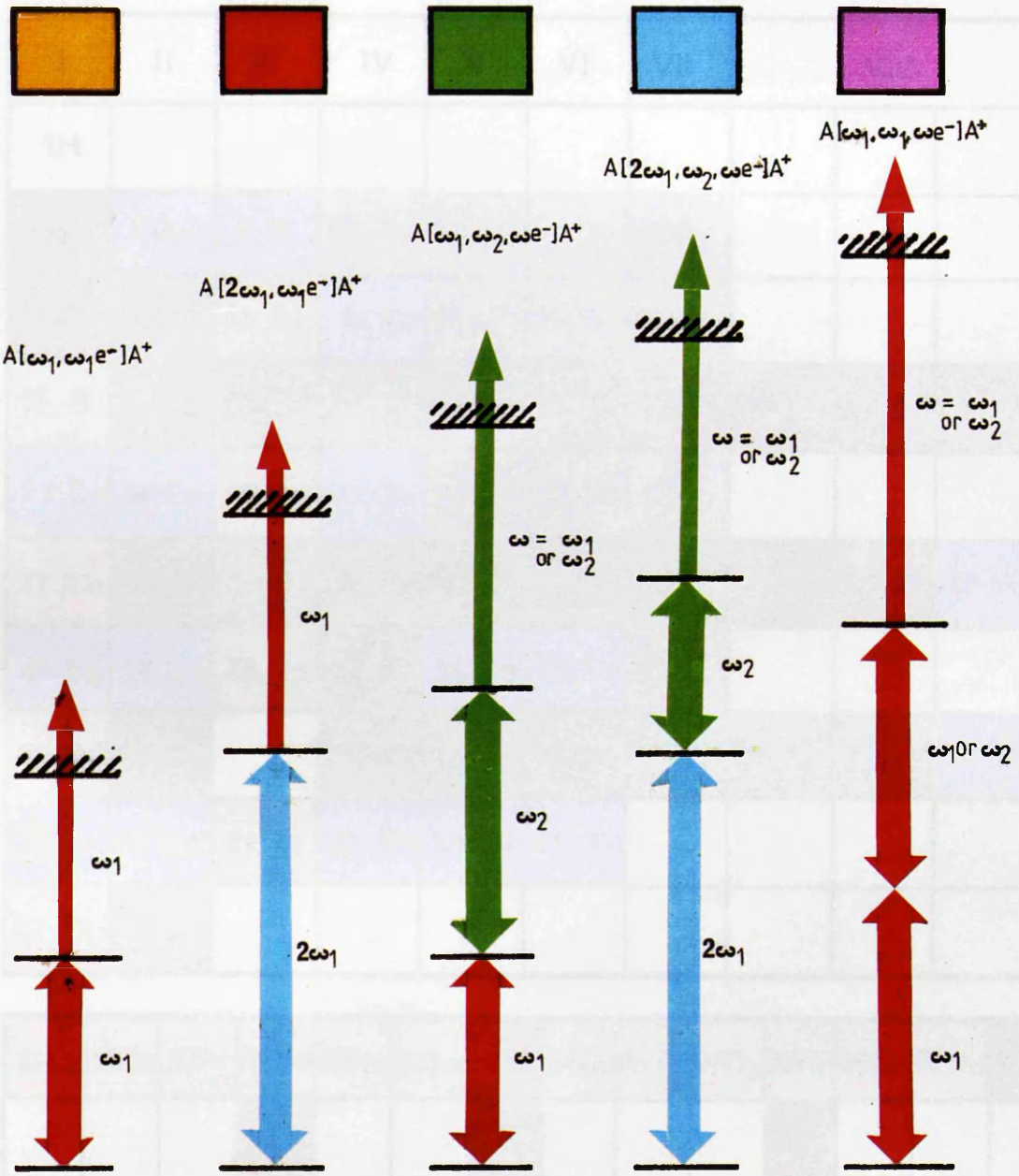

Fig 1·3

Application of the Resonance Ionisation schemes to the periodic table

I	II	III	IV	V	VI	VII	VIII			0
1H										
3Li	4 Be	5 B	6 C	7 N	8 O	9 F				
11 Na	12 Mg	13 Al	14 Si	15 P	16 S	17 Cl				
19 K	20 Ca	21 Sc	22 Ti	23 V	24 Cr	25 Mn	26 Fe	27 Co	28 Ni	
29 Cu	30 Zn	31 Ga	32 Ge	33 As	34 Se	35 Br				36 Kr
37 Rb	38 Sr	39 Y	40 Zr	41 Nb	42Mo	43 Tc	44 Ru	45 Rh	46 Pd	
47 Ag	48 Cd	49 In	50 Sn	51 Sb	52 Te	53 I				54 Xe
55 Cs	56 Ba		72 Hf	73 Ta	74 W	75 Re	76 Os	77 Ir	78 Pt	
79 Au	80 Hg	81 Tl	82 Pb	83 Bi	84 Po					
87 Fr	88 Ra									

57 La	58Ce	59Pr	60Nd	61Pm	62Sm	63Eu	64Gd	65Tb	66Dy	67Hd	68Er	69Tm	70Yb	71Lu
			92 U			95Am				90Es				

Fig 1·4

The introduction of the tunable dye laser (Sorokin *et al* 1966) marked the beginning of laser spectroscopy. As mentioned above Ambartsumyan *et al* (1971) performed the first resonant ionisation experiment when Rb atoms were ionised using a tunable dye laser. The technique was quickly extended to molecules (Ambartsumyan *et al* 1972). Saturation of the two photon resonant ionisation of helium was demonstrated by Hurst *et al* (1975).

Single atom detection was first demonstrated by Hurst *et al* (1977) who detected a single caesium atom in a proportional counter. A more complex three dye laser scheme was used in the single atom detection of ytterbium (Bekov *et al* 1978) which used field ionisation (see chapter 2) to saturate the final step. This reduced the laser power required for saturation.

The potential of resonant ionisation coupled with mass analysis was originally realised using easily ionised atoms such as sodium (Antonov *et al* 1978; Zandee *et al* 1978, ; Boesl *et al* 1980).

Time of flight mass spectrometry (TOF-MS) coupled with resonant ionisation was discussed by Beekman *et al* (1980). Boesl *et al* (1980) used this technique for the ionisation of polyatomic molecules. The mass resolution of this instrument was improved by use of an electrostatic ion mirror (Boesl *et al* 1982). Miller *et al* (1982) used resonant ionisation coupled with a magnetic sector mass spectrometer for high precision measurements of the rare earths neodymium and samarium, which are difficult to separate chemically.

Trace analysis using resonant ionisation can be realised by the use of a high transmission mass spectrometer. The single atom detection abilities of resonant ionisation allow the use of smaller samples and/or shorter analysis times. The method varies but the principle steps are the same:- the sample must be vaporised, the neutral atoms resonantly ionised and the ions mass analysed.

Winograd *et al* (1982) demonstrated the resonant ionisation of neutrals sputtered by a high energy ion beam and analysed in a TOF-MS. A detection limit of ~1 part per billion (ppb) was claimed for this arrangement using a 30Hz repetition rate (Kimock *et al* 1984). Using a similar technique but with a magnetic sector instrument instead of a TOF-MS (Parks *et al* 1983, 1985) a detection limit of 2ppb was claimed.

Trace analysis using thermal atomisation from a high temperature filament has also been extensively used (Donohue et *al* 1982; Moore *et al* 1984, 1985; Fassett *et al* 1983). Pulsed thermal sources have also been used to improve the duty cycle of this method. (Donohue *et al* 1984, Fassett *et al* 1984)

An electrothermal graphite atomiser with a TOF-MS has been used for trace analysis in the USSR (Bekov *et al* 1983, 1985, 1986).

Laser ablation has been used as a source for RIMS by several authors (Beekman *et al* 1980, Estler *et al* 1990). Alternatively, RIMS has been used as a means to investigate the laser ablation process by several groups (Apel *et al* 1987b, Beekman *et al* 1985, Estler *et al* 1987). Trace analysis using a laser ablation source has been used by Krönert *et al* (1987), who investigated short-lived gold isotopes implanted into graphite.

The duty cycle can be increased by using continuous wave lasers (Cannon *et al* 1985, Miller *et al* 1985) and by copper vapour lasers (Peuser *et al* 1985, Kronert *et al* 1985, Bekov *et al* 1986).

Ultrasensitive laser isotope analysis has been reported by Snyder *et al* (1985) who used an ion storage ring. Snyder reports isotopic sensitivity of 10^{-12} for ^{90}Sr and ^{88}Sr and estimates that instruments with isotopic sensitivities of 10^{-15} are possible using similar equipment. Bekov *et al* (1985) report trace detection of Ruthenium at sensitivities of 1 part in 10^{12} in a variety of samples (original mass of samples ~25g or 1L in the case of seawater). This represents the most sensitive bulk RIS analysis to date.

§3 Applications of Resonant Ionisation Spectroscopy.

With the possibilities of single atom detection, the most obvious applications of RIS and RIMS are in fields involving trace analysis. Below are a selection of the more interesting applications recently reported which utilise RIMS.

The field of environmental analysis is the most obvious candidate for the application of trace analysis. By the use of RIMS the detection of low level radioactive decay products in the environment below that currently feasible with decay based techniques is feasible (Houston *et al* 1988).

Two closely allied fields, geology and archeology, can also benefit from the selectivity and sensitivity of RIMS. Both of these rely on radioisotope dating. Kudryavtsev and Letokhov (1990) have detailed most of the important elements whose isotope ratios can be used for this purpose. These are shown in table 1.1, together with applications for each one. The very low levels of some of these isotopes require the most sensitive analytical methods available (see Letokhov 1987 chapter 9 for a comprehensive review of detection of rare isotopes)

Table 1.1 Useful Radioisotopes for Monitoring and Dating

Isotope	$T_{1/2}$	Rel. Conc.	Application
^{10}Be	1.5 Myr	10^{-10}	dating
^{14}C	5.7 kyr	10^{-12}	dating
^{26}Al	0.14 Myr	10^{-14}	dating
^{32}Si	172 yr	10^{-14}	ground water dating
^{36}Cl	0.3 Myr	10^{-17}	dating
^{41}Ca	80 kyr	10^{-14}	dating
^{81}Kr	0.21 Myr	10^{-13}	neutrino dating
^{85}Kr	10.8 yr	10^{-11}	monitoring
^{90}Sr	28.5 yr	10^{-10}	monitoring
^{129}I	15.7 Myr	10^{-12}	geological marker
^{137}Cs	33 yr	N/A	monitoring
^{205}Pb	15 Myr	N/A	neutrino detection

Adapted from Kudryavtsev Y.A. (1990)

Another application which requires trace analysis is the manufacture and testing of semi-conductor devices. Modern semi-conductors require exceptionally high purity levels and RIMS can provide a very sensitive indication of the levels of elemental contaminants in the base material. RIMS is also useful in the profiling of semiconductors, in which dopants may be present at trace levels (Downey *et al* 1990)

Biological applications are another important field for RIMS. Living tissue contains very poorly defined levels of trace elements at very low levels. RIMS has important applications in both defining norms for tissue types and detecting abnormal concentrations of elements (Quinn *et al* 1990).

More esoteric applications of RIMS include magnetic monopole detection (Kroll *et al* 1985), double beta decay (Ullman 1985) and the solar neutrino problem (Ames *et al* 1990).

Molecular 'RIMS' is another offshoot that is being currently investigated. Like atoms, molecules also have a resonant structure. In the case of molecules the resonant structure is much wider than for an atomic system, and because of this width the resonant structure is not unique for any specific molecule. Methods to narrow the molecular resonances, such as supersonic jet cooling, and other methods to increase sensitivity and selectivity, such as laser induced fragmentation, are objects of active research (Marshall *et al* 1990, Boesl *et al* 1990). Success with this promising branch of analysis will extend the field of environmental analysis to include low level toxic molecular contaminants eg. Dioxans. Explosive and drug detection in security applications is another possible application for mature molecular RIMS. Hahn *et al* (1987) have already reported detection of subfemtomole amounts of organic molecules (protoporphyrin IX dimethyl ester) using 266nm laser light to post-ionise. Hahn estimates that sensitivity can be increased by at least 3 orders of magnitude for this application.

A very recent, and intriguing, possibility for RIMS is in the Human Genome project. By tagging the four different bases in

DNA with tin, it is possible to use RIMS to detect each different base with very high efficiency (Arlinghaus *et al* 1990).

Chapter 2 : Theory

§ 1 Introduction

This chapter will detail some of the theoretical underpinnings of RIMS. It will deal firstly with the theory of photon-atom interactions, which leads to resonant and non-resonant transitions in atoms. This approach allows the cross sections for transitions to be calculated from first principles. However this method is not convenient for the calculations of ion yields for which the rate equation method will be introduced. Linewidths and other effects which will then be considered. The theory of harmonic generation from laser light will be considered and finally the theory of laser ablation/desorption will be discussed.

§ 2 Photon-Atom Interactions

Semi-classical Approximation

A complete quantum mechanical description of photon atom interactions (Loudon 1973) is complex and, in the context of resonant ionisation, of no added practical value. A more profitable course is to consider the laser as a classical source of electromagnetic (EM) waves and to describe the interaction of these waves with a quantum mechanical atom using the semi-classical approximation (Laud 1985). Using this approach it is possible to obtain expressions for the induced absorption cross section of an atom.

The behaviour of electrons in an unperturbed atom can be described by Schrödinger's Equation:-

$$\hat{H}_0|\Psi, t\rangle = i\hbar \frac{\partial}{\partial t}|\Psi, t\rangle \qquad (2.1)$$

where

$\hat{H}_0$ is the time independent Hamiltonian
$|\Psi, t\rangle$ is a time dependent state (2.2)

The time dependence of an unperturbed state $|\psi_n, t\rangle$ has the form

$$|\psi_n, t\rangle = e^{(-i\omega_n t)}|u_n\rangle \tag{2.3}$$

where E_n = eigenvalue of $\hat{H}_0 = \hbar\omega_n$ and $|u_n\rangle$ is independent of time and satisfies the equation

$$\hat{H}_0|u_n\rangle = \hbar\omega_n|u_n\rangle \tag{2.4}$$

If the basic solutions $|\psi_1, t\rangle$, $|\psi_2, t\rangle$ ... are known then the solution to (2.1) can be written as

$$|\Psi, t\rangle = \sum_n c_n |\psi_n, t\rangle = \sum_n c_n e^{-i\omega_n t}|u_n\rangle \tag{2.5}$$

Considering a two level atom with energy eigenvalues $E_a = \hbar\omega_a$ and $E_b = \hbar\omega_b$ then this becomes

$$|\Psi, t\rangle = c_a e^{-i\omega_a t}|u_a\rangle + c_b e^{-i\omega_b t}|u_b\rangle \tag{2.6}$$

If the atom is isolated then the probability of being in state a or b is $|c_a|^2$ and $|c_b|^2$ respectively.

By applying Schrödinger's equation to the atom in a new time dependent potential distribution the time dependence of the wavefunction Ψ may be obtained. The perturbed Schrödinger equation can be written as

$$\hat{H}|\Psi, t\rangle = i\hbar \frac{\partial}{\partial t}|\Psi, t\rangle \tag{2.7}$$

with

$$\hat{H} = \hat{H}_0 + \hat{H}'(t) \tag{2.8}$$

where $H'(t)$ is a small term from external forces. Assuming that the solution is of the form

$$|\Psi\rangle = \sum_n c_n(t) e^{-i\omega_n t} |u_n\rangle \tag{2.9}$$

With the coefficients c_n time varying. Substituting into (2.7) gives

$$\begin{aligned} \hat{H}|\Psi\rangle &= \left(\hat{H}_0 + \hat{H}'(t)\right)|\Psi\rangle \\ &= \left(\hat{H}_0 + \hat{H}'(t)\right) \sum_n c_n(t) e^{-i\omega_n t} |u_n\rangle \\ &= i\hbar \sum_n \{\dot{c}_n(t) - i\omega_n c_n(t)\} e^{-i\omega_n t} |u_n\rangle \end{aligned} \tag{2.10}$$

multiplying both sides by the complex conjugate of $|u_m\rangle$ and integrating over both coordinates gives

$$\begin{aligned} &\sum_n c_n(t) e^{-i\omega_n t} \langle u_m | \hat{H}_0 | u_n \rangle + \sum_n c_n(t) e^{-i\omega_n t} \langle u_m | \hat{H}' | u_n \rangle \\ &= i\hbar \sum_n \dot{c}_n(t) e^{-i\omega_n t} \langle u_m | u_n \rangle + \sum_n \hbar\omega_n c_n(t) e^{-i\omega_n t} \langle u_m | u_n \rangle \end{aligned} \tag{2.11}$$

or

$$\begin{aligned} &\sum_n c_n(t) \hbar\omega_n e^{-i\omega_n t} \langle u_m | u_n \rangle + \sum_n c_n(t) e^{-i\omega_n t} \langle u_m | \hat{H}' | u_n \rangle \\ &= i\hbar \sum_n \dot{c}_n(t) e^{-i\omega_n t} \langle u_m | u_n \rangle + \sum_n \hbar\omega_n c_n(t) e^{-i\omega_n t} \langle u_m | u_n \rangle \end{aligned} \tag{2.12}$$

therefore

$$i\hbar\, \dot{c}_m(t) e^{-i\omega_m t} = \sum_n c_n(t) e^{-i\omega_n t} \langle u_m | \hat{H}' | u_n \rangle \tag{2.13}$$

so

$$\dot{c}_m(t) = \frac{1}{i\hbar} \sum_n c_n(t) e^{-i\omega_{nm} t} \hat{H}'_{mn} \tag{2.14}$$

where

$$\omega_{nm} = \frac{E_n - E_m}{\hbar} \text{ and } \hat{H}'_{mn} = \langle u_m | \hat{H}' | u_n \rangle = \int u_m^* \hat{H}' u_n \, d\tau$$

These are the matrix elements of $\hat{H}'$. If the system is in state n at t=0 when the perturbation is switched on then the probability of the system being in state m at $t=t'$ is given by $|c_m(t')|^2$. Integrating equation (2.14) gives

$$c_m(t') = \frac{1}{i\hbar} \sum_n \int_0^{t'} c_n(t) e^{-i\omega_{nm} t} \hat{H}'_{mn} \, dt \qquad (2.15)$$

from which the probability can be found. Assuming a two level system then by (2.14) simplifies to

$$\begin{aligned} \dot{c}_a(t) &= \frac{1}{i\hbar}\{c_a(t)\hat{H}'_{aa} + c_b(t) e^{-i\omega_{ba} t} \hat{H}'_{ab}\} \\ \dot{c}_b(t) &= \frac{1}{i\hbar}\{c_b(t)\hat{H}'_{bb} + c_a(t) e^{-i\omega_{ab} t} \hat{H}'_{ba}\} \end{aligned} \qquad (2.16)$$

To evaluate equations (2.16) the form of the interaction Hamiltonian must be known. An electromagnetic wave can be described classically as (Dermtröder 1981)

$$\mathbf{E} = \mathbf{E}_0 \cos(kz - \omega t) \qquad (2.17)$$

Since an atom is much smaller than the wavelength of an electromagnetic wave in the visible part of the spectrum the term kz can be ignored (ibid) and (2.17) can be simplified to

$$\mathbf{E} = \mathbf{E}_0 \cos \omega t \qquad (2.18)$$

The dipole moment of a point charge e at position $\mathbf{r}$ is $e\mathbf{r}$. The electric dipole moment of the atom is

$$-\sum_j e \mathbf{r}_j = -e\mathbf{D} \qquad (2.19)$$

where

$$\mathbf{D} = \sum_j \mathbf{r}_j \tag{2.20}$$

The potential energy of a dipole in the electromagnetic field described above is

$$\sum_j e\,\mathbf{r}_j.\mathbf{E}_0 \cos\,\omega t = e\,\mathbf{D}.\mathbf{E}_0 \cos\,\omega t \tag{2.21}$$

The Hamiltonian can then be written as

$$\hat{H}' = e\,\mathbf{D}.\mathbf{E}_0 \cos\,\omega t \tag{2.22}$$

so

$$\hat{H}'_{bb} = \langle u_b|\hat{H}'|u_b\rangle = \int u_b^*\left(\sum e\,\mathbf{r}_j.\mathbf{E}\cos\,\omega t\right)u_b d\tau \tag{2.23}$$

From parity considerations $\hat{H}'_{bb} = \hat{H}'_{aa} = 0$. If $|u_a\rangle$ and $|u_b\rangle$ have opposite parities then $\hat{H}'_{ab} \neq 0$ and $\hat{H}'_{ba} \neq 0$. Therefore (2.16) can be written as

$$\begin{aligned} \dot{c}_a(t) &= \frac{1}{i\hbar}c_b(t)e^{-i\omega_{ba}t}\,\hat{H}'_{ab} \\ \dot{c}_b(t) &= \frac{1}{i\hbar}c_a(t)e^{-i\omega_{ab}t}\,\hat{H}'_{ba} \end{aligned} \tag{2.24}$$

Assuming that t' is small and that the perturbation is weak then as a first approximation $c_a(t) = 1$ and $c_b(t) = 0$. Then

$$\begin{aligned} \dot{c}_a(t) &= 0 \\ \dot{c}_b(t) &= \frac{1}{i\hbar}e^{-i\omega_{ab}t}\,\hat{H}'_{ba} \end{aligned} \tag{2.25}$$

which leads to the solutions

$$\begin{aligned} c_a(t) &= 1 \\ c_b(t) &= \frac{1}{i\hbar}\int_0^{t'} e^{-i\omega_{ab}t}\,\hat{H}'_{ba}\,dt \end{aligned} \tag{2.26}$$

in the first approximation. By substituting these solutions back into (2.24) second order approximations can be found. This process may be repeated for higher orders.

The probability of a transition to state b may be found by integrating (2.26). Thus

$$\begin{aligned} c_b(t') &= \frac{1}{i\hbar}\int_0^{t'} e^{-i\omega_{ab}t}\,\hat{\mathrm{H}}'_{ba}\,dt \\ &= \frac{1}{i\hbar}\int_0^{t'} e^{-i\omega_{ab}t}\left\langle u_b\left|\sum_j \mathbf{r}_j.\mathbf{E}_0\cos\,\omega t\right|u_a\right\rangle dt \\ &= \frac{\langle u_b|e\,X\,\mathbf{E}_0|u_a\rangle}{i\hbar}\int_0^{t'} e^{-i\omega_{ab}t}\cos\,\omega t\,dt \\ &= \frac{e\,\mathbf{E}_0 X_{ba}}{2\hbar}\left[\frac{1-e^{-i(\omega_{ba}+\omega)t'}}{\omega_{ba}+\omega}+\frac{1-e^{-i(\omega_{ba}-\omega)t'}}{\omega_{ba}-\omega}\right] \end{aligned} \qquad (2.27)$$

where X is the component of $\mathbf{D}$ in the direction of $\mathbf{E}_0$, ie the x direction and $X_{ba} = \langle u_b|X\,|u_a\rangle$.

On examination, the probability of the atom being in state b can be large only if one of the denominators is near zero, which occurs when $|\omega_{ba}| \approx \omega$. This allows one of the terms in (2.27) to be neglected. This is the rotating wave approximation (Feynman 1957). For transitions from state a to state b the second term is much larger than the first which allows the first term to be ignored. The probability of a transition to state b in unit time, in the limit of long times, is

$$\begin{aligned} \frac{1}{t'}|c_b(t)|^2 &= \frac{e^2\mathbf{E}_0^2|X_{ba}|^2}{4\hbar^2}\lim_{t'\to\infty}\left|\frac{1-e^{-i(\omega_{ba}-\omega)t'}}{(\omega_{ba}-\omega)}\right|^2\frac{1}{t'} \\ &= \frac{e^2\mathbf{E}_0^2|X_{ba}|^2}{\hbar^2}\lim_{t'\to\infty}\frac{\sin^2\frac{\omega_{ba}-\omega}{2}t'}{(\omega_{ba}-\omega)^2 t'} \end{aligned} \qquad (2.28)$$

Since the Dirac delta function can be defined as

$$\delta(\omega_{ba} - \omega) = \frac{2}{\pi} \lim_{t' \to \infty} \frac{\sin^2 \frac{\omega_{ba} - \omega}{2} t'}{(\omega_{ba} - \omega)^2 t'} \qquad (2.29)$$

(2.28) can be written as

$$\frac{1}{t'} |c_b(t)|^2 = \frac{e^2 \mathbf{E}_0^2 |X_{ba}|^2 \pi}{2\hbar^2} \delta(\omega_{ba} - \omega) \qquad (2.30)$$

This contains the assumption that the transition frequency ω_{ba} is a well defined quantity. In practice there will be some width $\Delta\omega$ which corresponds to the uncertainty in ω_{ba}. Sources of this uncertainty will be dealt with in §4. The energy density in an electromagnetic wave $\rho(\omega)$ is related to $\mathbf{E}_0$ by

$$\int \rho(\omega)\, d\omega = \frac{\mathbf{E}_0^2 \varepsilon_0}{2} \qquad (2.31)$$

so (2.30) can be written as

$$\frac{1}{t} |c_b(t)|^2 = \frac{\pi e^2 |X_{ba}|^2}{\varepsilon_0 \hbar^2} \int_{\omega_{ba} - \frac{\Delta\omega}{2}}^{\omega_{ba} + \frac{\Delta\omega}{2}} \rho(\omega) \delta(\omega_{ba} - \omega) d\omega \qquad (2.32)$$

or, using the properties of the delta function

$$\begin{aligned} \frac{1}{t} |c_b(t)|^2 &= \frac{\pi e^2 |X_{ba}|^2}{\varepsilon_0 \hbar^2} \int_{-\infty}^{\infty} \rho(\omega) \delta(\omega_{ba} - \omega) d\omega \\ &= \frac{\pi e^2 |X_{ba}|^2}{\varepsilon_0 \hbar^2} \rho(\omega_{ba}) \end{aligned} \qquad (2.33)$$

This has been derived for a single atom. When dealing with a gas of many similar atoms X_{ba} can be replaced since

$$X_{ba} = \langle u_b | X | u_a \rangle = \langle u_b | \hat{\mathbf{e}}_x . \mathbf{D} | u_a \rangle$$
$$= \hat{\mathbf{e}}_x . \mathbf{D}_{ba} \tag{2.34}$$

where $\hat{\mathbf{e}}_x$ is the unit vector in the x direction. In a gas of atoms the spatial directions of $\mathbf{D}_{ba}$ will vary randomly. Averaging over the random orientations gives

$$|X_{ba}|^2 = |D_{ba}|^2 \overline{\cos^2 \theta} = \frac{1}{3}|D_{ba}|^2 \tag{2.35}$$

The incident energy flux ($Jcm^{-2}s^{-1}$)is related to the energy density by $I(\omega) = \rho(\omega_{ba})c$ where c is the velocity of light.

The transition rate from a to b is then

$$B_{ba} = \frac{\pi e^2 |D_{ba}|^2}{3c\varepsilon_0 \hbar^2} I(\omega_{ba}) \tag{2.36}$$

B_{ba} is known as the Einstein coefficient.

Electric Dipole Matrix Element

In this formulation the parameter governing the rate of single photon transitions between the two states is the dipole matrix element D_{ba}. Evaluation of this quantity requires knowledge of the electronic wavefunctions of the states of the atom concerned and for non-hydrogenic atoms can only be calculated approximately. An expression for the oscillator strength of the transition from a to b can be made. The oscillator strength is defined as

$$|f_{ab}| = |D_{ab}|^2 \frac{2\pi\omega_{ba}}{3\hbar} \tag{2.37}$$

with oscillator strength positive for absorption and negative for emission.

For degenerate states

$$f_{ba} = - f_{ab} \frac{g_b}{g_a} \tag{2.38}$$

where g_a and g_b are the degeneracies of states a and b respectively.

Defining the transition rate as a cross section ie. the rate of absorption of energy per atom per unit time divided by the incident energy flux

$$\sigma_{ba} = \frac{\hbar\omega}{I(\omega)} B_{ba} \tag{2.39}$$

The cross section for a single photon resonant absorption is $\sim 10^{-12} cm^2$ (Bekov *et al* 1983)

Strong Field Interactions

The derivation above only considers the case of the perturbation being weak. In the case of a strong laser produced field the population of the upper level may approach that of the lower level. In this case, using equation (2.24) and again using the rotating wave approximation we obtain

$$\begin{aligned} \dot{c}_a &= c_b D_{ab} \frac{e\,\mathbf{E}_0}{2\hbar} e^{-i(\omega_{ba} - \omega)} = c_b R_{ab} e^{-i(\omega_{ba} - \omega)} \\ \dot{c}_b &= c_a D_{ab} \frac{e\,\mathbf{E}_0}{2\hbar} e^{-i(\omega_{ba} - \omega)} = c_a R_{ab} e^{-i(\omega_{ba} - \omega)} \end{aligned} \tag{2.40}$$

with

$$\begin{aligned} D_{ab} &= D_{ba} \\ R_{ab} &= D_{ab} \frac{e\,\mathbf{E}_0}{2\hbar} \end{aligned} \tag{2.41}$$

Starting from the condition that all the atoms are in state a at time t=0 these equations give as the probability of being in state b after time t

$$P_b = |c_b|^2 = \frac{4R_{ab}^2}{\Omega^2} \sin^2 \frac{\Omega t}{2}$$
$$\Omega = \sqrt{(\omega_{ab} - \omega)^2 + 4R_{ab}^2} \qquad (2.42)$$

This introduces a sinusoidal time dependence on resonance and the system oscillates between levels a and b with frequency R_{ab}. This is called the Rabi flopping frequency (Rabi 1937) and is illustrated in fig 2.1. It is dependent on the matrix element D_{ab} and the electric field strength E_0. Slightly off resonance the flopping frequency is dependent on the degree of detuning from the transition frequency.

The width of the transition, $4R_{ab}$, broadens as the electric field is increased. This is power broadening. The effects of this phenomenon are dealt with in §4.

Multiphoton Transitions

The first order perturbation theory applied above only considers the absorption of one photon at a time. By use of second order perturbation theory two photon transitions can be considered. Continuing from equations (2.24) and inserting the coefficients obtained from (2.27) the following may be obtained for a transition to a higher level d

$$\dot{{}^2c}_d = \frac{1}{i\hbar} \sum_b {}^1c_b \langle u_d | \hat{H}' | u_b \rangle e^{i\omega_{ab} t}$$
$$= \frac{1}{i\hbar} \sum_b \frac{e^2 E_0^2 D_{db} D_{ba}}{4\hbar} \left\{ \frac{1 - e^{-i(\omega_{ba} + \omega)t}}{\omega_{ba} + \omega} + \frac{1 - e^{-i(\omega_{ba} - \omega)t}}{\omega_{ba} - \omega} \right\} \qquad (2.43)$$
$$\times \left(e^{-i(\omega_{db} + \omega)t} + e^{-i(\omega_{db} - \omega)t} \right)$$

where $E_a < E_b < E_d$. Retaining only terms whose denominators approach zero again we obtain

Fig 2.1: Rabi Flopping for Resonant Excitation

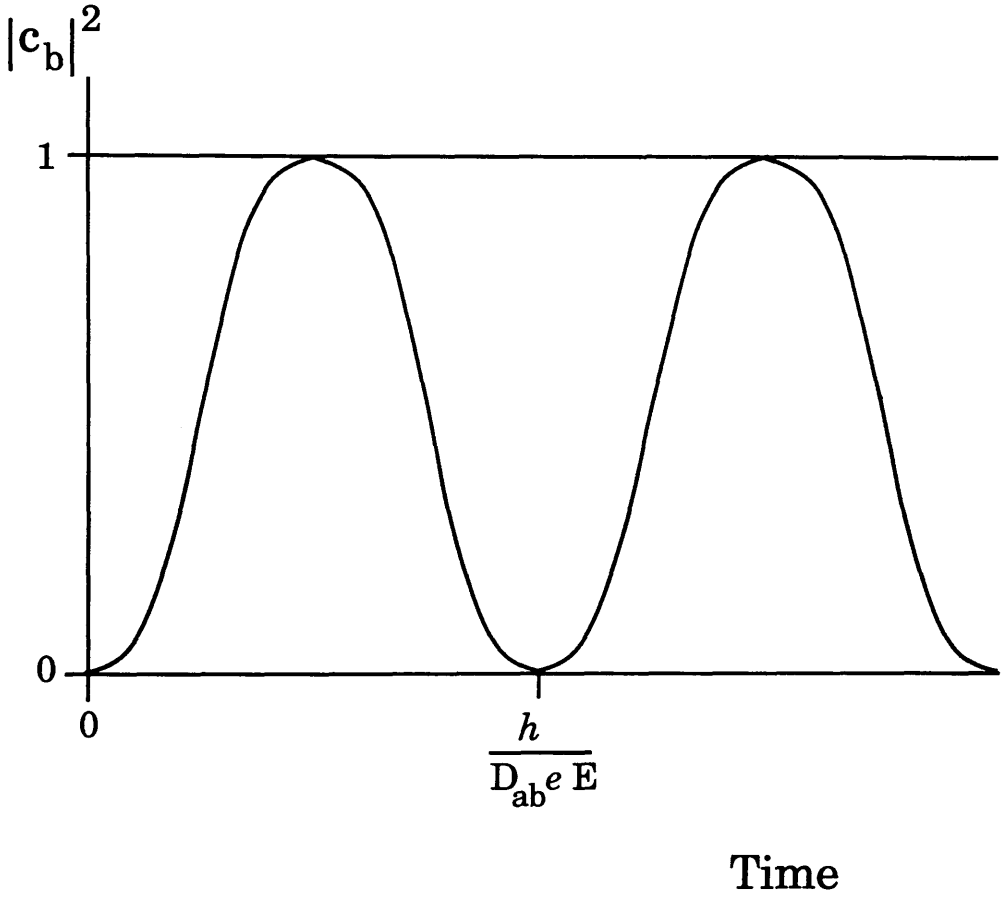

$$^2c_d = \sum_b \frac{e^2 E_0^2 D_{db} D_{ba}}{4\hbar} \times \left\{ \frac{1 - e^{-i(\omega_{ba} - \omega)t}}{(\omega_{ba} - \omega)(\omega_{db} - \omega)} + \frac{1 - e^{-i(\omega_{ba} - 2\omega)t}}{(\omega_{ba} - \omega)(\omega_{da} - 2\omega)} \right\} \quad (2.44)$$

On examination, it can be seen that a resonant process corresponding to two photon absorption occurs at $\omega_{da}=2\omega$ as the denominator of the second term tends to zero.

The rate of two photon absorption is given by

$$B_{da} = \sum_b \frac{e^4 E_0^4 |D_{db} D_{ba}|^2}{16\hbar^2} \delta(\omega_{da} - \omega) \quad (2.45)$$

Again, corrections can be made for the widths of spectral lines etc.

The states b in the above equation are known as virtual states. Transitions into virtual states obey the one photon selection rules which are given below. The rate of two photon absorption cannot be solved rigorously as it depends strongly upon the statistical properties of laser light, which are generally not reproducible shot to shot.

The above theory can be extended to N photon absorbance by extending perturbation theory to N'th order.

Selection Rules for Electric Dipole Transitions

For a one photon process with strictly L-S coupling the selection rules are (Corney 1977):-

$\Delta l = \pm 1$

$\Delta L = 0, \pm 1 \qquad (L=0 \not\leftrightarrow L=0)$

$\Delta S = 0$

$\Delta J = 0, \pm 1 \ (J=0 \not\leftrightarrow J=0)$

where Δl is the change in parity, ΔL is the change in orbital angular momentum, ΔS is the change in the electron spin and ΔJ is the change in total angular momentum.

For two photon transitions the selection rules are:-

$$\Delta l = 0, \pm 2$$

$$\Delta L = 0, \pm 1, \pm 2$$

$$\Delta S = 0$$

$$\Delta J = 0, \pm 1, \pm 2$$

These selection rules are valid where magnetic interactions are much smaller than residual electrostatic interactions. This is not always the case in heavier elements.

The case $\Delta L = 0$ for single photon transitions can be observed in atoms with many valence electrons eg. carbon. In the case of one or two optically active electrons $\Delta L = \pm 1$.

Ionisation Methods

Photoionisation

In photoionisation the final state will be an electron ejected from the atom by the absorption of a photon in an unbound continuum state moving in the field of an ion. If the electron occupies a state energetically close to the bound states then the calculations of cross sections are very difficult as the ion will exert considerable influence on the electron. Calculations of the cross section for photoionisation (Marr 1967) have values of $\sim 10^{-18}$ cm^2. These values are around 10^6 times smaller than the cross sections for resonant bound-bound transitions, which makes photoionisation very inefficient in comparison.

Autoionisation.

Autoionisation occurs when there are excited states involving two electrons which decay non-radiatively to give one electron and one ion (Fig 2.2). Due to the excitation process, which only

Fig 2.2: Autoionisation

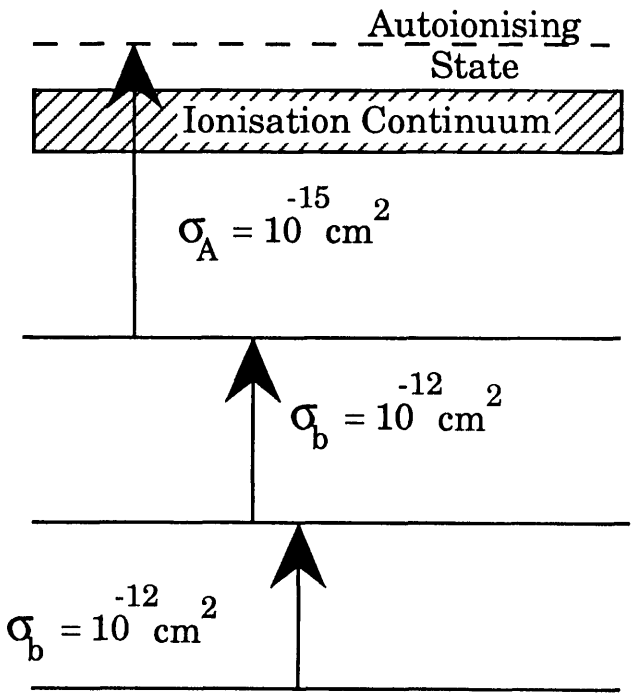

Ionisation via an Autoionisation State

Fig 2.3: Field Ionisation

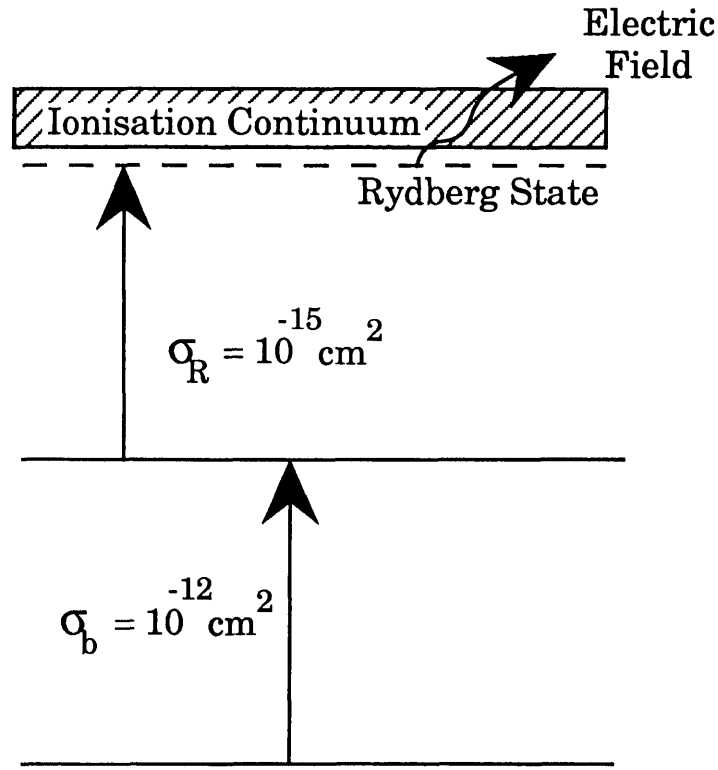

Ionisation by Electric Field
From a Rydberg State

involves bound-bound transitions, the autoionising process is more efficient than normal photoionisation and has a typical cross section of ~$10^{-15}cm^2$ (Lambdropolus 1984).

A limitation on the usefulness of autoionising states is that two (or more) valence electrons are required. This limits the range of applicability of this method.

Field Ionisation

From a high lying Rydberg state an atom can be ionised by the application of a strong electric field (fig 2.3), which is sufficient to increase the electron's energy to a value above the binding energy of the atom. This results in an ion-electron pair. It is comparatively easy to saturate an ionisation process using this method. Field values of ~10^4 Vcm^{-1} are required. (Letokhov 1987).

§ 3 Population Rate Equations.

Introduction

The semiclassical approximation, outlined above, is obviously very complex. The outline above only deals with the case of one intermediate state. When many different levels are involved (as in Hurst's scheme 4), or two levels lie close, the theory above tends to become unwieldly. In this case a far simpler and much more useful approach to the problem is to use rate equations.

Ackerhalt and Shore (1977) introduced rate equations as a simplification of the semiclassical approximation. Their approach dealt with a N-level atom, where the rate equations comprise N equations in N real variables. The Schrödinger equation for the same system comprises N equations for N complex variables, and another approach, the optical Bloch equations, have N real and $\frac{N(N-1)}{2}$ complex variables (ibid). Thus rate equations offer computation simplicity as well as a physically intuitive model.

Derivation of Rate Equations

Walcox and Lamb (1960) showed that rate equations could be derived formally from the optical Bloch equations. This technique relies on the fact that that off-diagonal density matrix elements tend rapidly to a steady state value. This is usually true in the case of RIS.

An simpler and more intuitive model was presented by Zakheim *et al* (1980) which considered a three level system (fig 2.4) with two bound states and a continuum level. Laser photons induce absorption by and emission from the atomic states which changes the relative population of the states under study. The absorption and emission rates are related to the Einstein coefficients and are assumed known. Excited states can decay by either spontaneous or stimulated emission. m-photon processes, where $m \geq 2$, are incorporated in any step by choosing the appropriate value of the laser flux for that step. The cross section would have units of $cm^{2m}s^{m-1}$.

From fig 2.4 the rate of change of the population of the ground, intermediate and continuum levels are

$$\frac{dN_0}{dt} = -N_0\sigma_A\,\Phi + \frac{N_1}{\tau} + N_1\sigma_s\,\Phi$$

$$\frac{dN_1}{dt} = N_0\sigma_A\,\Phi - \frac{N_1}{\tau} - \beta N_1 - N_1\sigma_I\,\Phi - N_1\sigma_s\,\Phi \qquad (2.46)$$

$$\frac{dN_I}{dt} = N_1\sigma_I\,\Phi$$

where N_0, N_1, N_I are the population of atoms in states 0, 1 and the ionisation continuum respectively.

Φ ..... laser flux (photons per unit area per unit time)
τ ..... mean lifetime of state 1
σ_A ..... cross section for state $0 \rightarrow 1$
σ_I ..... cross section for state $1 \rightarrow$ continuum

Fig 2.4 Population Rate Equation Scheme

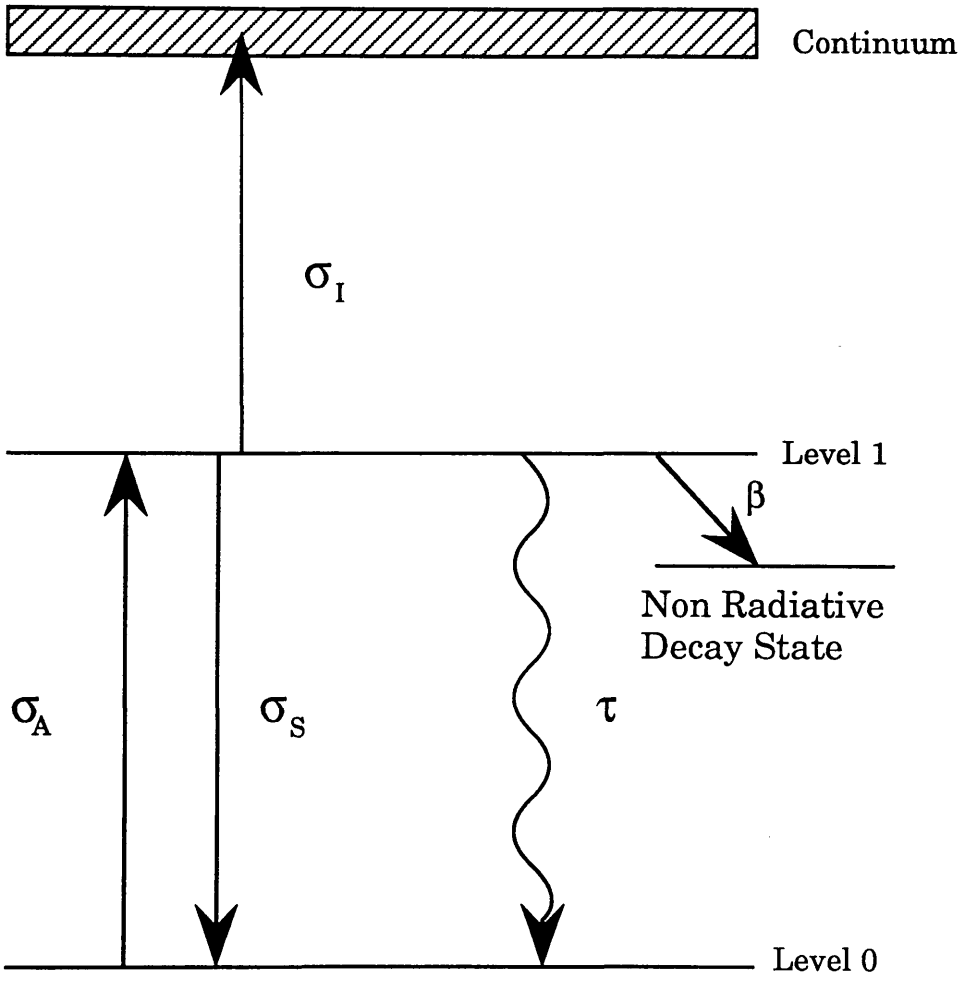

σ_s .....cross section for state $1 \rightarrow 0$
β.....rate of non radiative decay from level $1 \not\rightarrow 0$

These equations can be rearranged to give

$$\frac{d^2N_1}{dt^2} + 2b\frac{dN_1}{dt} + w^2N_1 = 0 \qquad (2.47)$$

with $(2\sigma_A + \sigma_I)\Phi + \frac{1}{\tau} + \beta = 2b$ and $\sigma_A\Phi(\beta+\sigma_I\Phi)=w^2$.

If N_1 is of the form $e^{-\lambda t}$ then 2.47 can be written as

$$\lambda^2 - 2b\lambda + w^2 = 0 \qquad (2.48)$$

hence

$$N_1 = A(e^{-\lambda_1 t} - e^{-\lambda_2 t}) \qquad (2.49)$$

with

$$\lambda_1 = b - \sqrt{b^2 - w^2}$$
$$\lambda_2 = b + \sqrt{b^2 - w^2} \qquad (2.50)$$

where λ_1 and λ_2 are the roots of equation 2.48. Solving for N_1 gives:-

$$N_1 = \frac{N_0(0)\sigma_A\Phi}{\lambda_2 - \lambda_1}[e^{-\lambda_1 t} - e^{-\lambda_2 t}] \qquad (2.51)$$

where $N_0(0)$ is the population of state 0 at t=0. If the intermediate step is real then it can be assumed that $\sigma_A=\sigma_S \gg \sigma_I$. This simplifies 2.51 to

$$N_1 = \frac{N_0(0)\sigma_A\Phi}{2\sigma_A\Phi + \frac{1}{\tau} + \beta}e^{-\lambda_1 t} \qquad (2.52)$$

Assuming that β is much less that the ionisation rate $\sigma_I\Phi$. then one condition for saturation is the flux condition. This is

$$\sigma_A \Phi \gg \frac{1}{\tau} \tag{2.53}$$

This simplifies 2.52 to

$$N_1 = \frac{N_0(0)}{2} e^{-\lambda_1 t} \tag{2.54}$$

Writing λ_1 in terms of ionisation cross section and the flux gives

$$\lambda_1 = \frac{\sigma_I \Phi}{2} \tag{2.55}$$

This allows writing of N_I in terms of N_0. This gives

$$\begin{aligned} N_I &= \sigma_I \Phi \int_0^T \frac{N_0(0)}{2} e^{-\lambda_1 t} \, dt \\ &= \frac{\sigma_I \Phi N_0(0)}{2} \left[-\frac{1}{\lambda_1} e^{-\lambda_1 T} + \frac{1}{\lambda_1} \right] \end{aligned} \tag{2.56}$$

Imposing a second condition, the fluence condition, which is

$$\sigma_I \phi \gg 1 \tag{2.57}$$

where ϕ is the laser fluence ie. number of photons per unit area = ΦT. This simplifies 2.56 to

$$N_I = N_0(0) \tag{2.58}$$

At the end of the laser pulse all the atoms in the ground state have become ionised. This is the definition of saturation. This is true for a laser pulse of length T provided

$$\begin{gathered} \sigma_I \Phi T \gg 1 \\ \sigma_A \Phi \gg \frac{1}{\tau} \\ T \ll \beta \end{gathered} \tag{2.59}$$

Typical values for the terms used are

T ..... 10^{-8} sec
τ ..... 10^{-8} sec
σ_I ..... 10^{-18} cm^2
σ_A ..... $10^{-11} \rightarrow 10^{-12}$ cm^2
β ..... 10^{-6} sec

Therefore the flux condition for saturation for a pulse length of 10^{-8}sec is

$$\phi_A \gg 10^{11} \rightarrow 10^{12} \text{ photons/cm}^2$$

or $$\phi_A \gg 0.5 \rightarrow 5.0 \text{ nJ/mm}^2$$

as $1J = 5 \times 10^{15} \times \lambda\,(\text{nm})$ photons. The fluence condition gives

$$\phi_I \gg 10^{17} \rightarrow 10^{18} \text{ photons/cm}^2$$

or $$\phi_I \gg 0.5 \rightarrow 5.0 \text{ mJ/mm}^2$$

Weak Light Intensities

From 2.51, and using the conditions that $\sigma_A=\sigma_S \gg \sigma_I$ and $\sigma_I \gg \Phi\beta$ then

$$N_I = \frac{N_0(0)\sigma_A\sigma_I\,\Phi^2}{\lambda_2^2}\left\{\frac{\lambda_2}{\lambda_1}\left(1-e^{-\lambda_1 t}\right)-\left(1-e^{-\lambda_2 t}\right)\right\} \quad (2.60)$$

If the fluence does not saturate the ionisation step and the relaxation is less than the spontaneous decay rate then this becomes

$$N_I = \frac{N_0(0)4\sigma_A^2\,\phi^2}{\sigma_A\left(2\sigma_A\,\phi+\frac{T}{\tau}\right)^2}\left\{\frac{T}{\tau}+2\sigma_A\,\phi-1+e^{-\left(2\sigma_A\,\phi+\frac{T}{\tau}\right)}\right\} \quad (2.61)$$

where $\Phi T = \phi =$ photon fluence.

Long Pulse Length

If the pulse length is long compared to the lifetime of state 1 and the rate of excitation is less then the spontaneous decay rate (ie $T \gg \tau$ and $\sigma_A\Phi \ll \frac{1}{\tau}$) then

$$N_I = N_0(0)\sigma_A\sigma_I \ \Phi^2 \ T \qquad (2.62)$$

However, if the excitation state is saturated ie $\sigma_A\Phi \gg \frac{1}{\tau}$ then

$$N_I = \tfrac{1}{2}N_0(0)\sigma_I \ \Phi \ T \qquad (2.63)$$

Hence as the light intensity is increased then the yield changes from a quadratic dependence on laser flux to a linear dependence on laser fluence.

Short Pulse Length

If the pulse length is short compared to the lifetime of state 1 and the rate of excitation is less then the spontaneous decay rate (ie $T \ll \tau$ and $\sigma_A\Phi \ll \frac{1}{\tau}$) then

$$N_I = N_0(0)\sigma_A\sigma_I \ \Phi^2 \ T^2 \qquad (2.64)$$

If the excitation state is saturated ie $\sigma_A\Phi \gg \frac{1}{\tau}$ then

$$N_I = \tfrac{1}{2}N_0(0)\sigma_I \ \Phi \ T \qquad (2.65)$$

As the light intensity is increased then the yield changes from a quadratic dependence on laser fluence to a linear dependence on laser fluence.

The rate equation approach has some disadvantages over the quantum mechanical or semiclassical approaches. Firstly it depends on a knowledge of cross sections that cannot be derived using the rate equation model, whereas in the semiclassical approximation these cross sections can be calculated from a knowledge of the atom's electronic structure. Rate equations are

not always valid and their validity depends on the atoms being resonantly excited. In the case where the width of the atomic transition is greater than the laser line width or the laser is off resonance then rate equations are not valid as given here since the atoms are not being resonantly excited (see §4 for details of atomic widths). One advantage of rate equations is that the mathematics is fairly simple and can easily be extended to more complex systems (Singhal *et al*1988, Singhal *et al*1990).

This analysis assumes that the laser has a flat top intensity distribution ie. ϕ and Φ are constant. By an extension of the analysis any laser temporal profile can be analysed, although this has a drawback as the analytical solution presented above is not valid, and the analysis must proceed via computer modelling. In practice, for laser pulses on the timescale of several nanoseconds the time profile is not significant when excitation proceeds through real states. If subnanosecond pulses are used or ionisation proceeds via a virtual state then the temporal profile of the pulse does become of importance (Ackerhalt *et al* 1977).

The model can also take into account variations in the intensity of the laser across the ionisation region by using the same method as for analysing the temporal profile of the pulse.

§ 4 Linewidths and Broadening Mechanisms.

As mentioned in §2, there are several sources of broadening of excited states that play an important part in RIMS. The relative sizes, mechanisms and importance of these effects will now be discussed.

Natural Linewidths

An excited state in an atom has a lifetime associated with it. By applying the uncertainty principle $\Delta E_i = \frac{\hbar}{\tau_i}$ and the frequency of the radiation $\omega_i = \frac{E_i}{\hbar}$ has an uncertainty

$$\Delta\omega_i = \frac{1}{\tau_i} \tag{2.66}$$

If the transition is between an excited state i and an excited state j then the width is now

$$\Delta\omega_{ij} = \frac{1}{\tau_i} + \frac{1}{\tau_j} \tag{2.67}$$

For instance the natural width of the sodium D_1 line at 589.1nm which corresponds to a transition from the $3P_{3/2}$ to the $3S_{1/2}$ ground state has a lifetime of 16ns and a width of 10MHz = 3.3×10^{-4} cm^{-1}.

The shape of the line may be obtained quantum mechanically and is given by the Lorentzian distribution

$$I_{ij}(\omega) = I_0 \frac{\Gamma_{ij}}{2\pi\left((\omega - \omega_{ij})^2 + \frac{\Gamma_{ij}^2}{4}\right)} \tag{2.68}$$

with $\Gamma_{ij} = \Delta\omega_{ij} = \frac{1}{\tau_i} + \frac{1}{\tau_j} = \mathrm{FWHM}$.

Doppler Width

If an atom is moving with speed v with respect to an observer and undergoes a transition with frequency ω_{ij} then then the observed frequency is given by

$$\omega'_{ij} = \omega_{ij}\left(1 - \frac{\mathbf{v}.\hat{\mathbf{r}}}{c}\right) \tag{2.69}$$

where $\hat{\mathbf{r}}$ is a unit vector from the observer to the atom. If we take $\hat{\mathbf{r}}$ to be in the z direction and assuming that the atoms have a Maxwellian distribution of velocities the frequency distribution of the light is

$$I(\omega'_{ij}) = I_0(\omega_{ij}) e^{\frac{mc^2}{2kT}\left(\frac{\omega - \omega_{ij}}{\omega_{ij}}\right)^2} \tag{2.70}$$

with a FWHM given by

$$\Delta\omega_{\frac{1}{2}} = \frac{2\omega_{ij}}{c}\left[\frac{2kT\ \log_e 2}{m}\right] \qquad (2.71)$$

For example, the sodium line mentioned earlier at temperature T=500K has a width of ~200MHz = 6.6×10^{-3}cm^{-1}.

Pressure Broadening

Elastic collisions occur when two atoms interact with no transfer of internal energy. Elastic collision causes shifting of the atomic energy levels which results in a broadening of the spectral lines as well as a shift in the central frequency. The shift and the broadening depend upon how the energy levels are modified by the collision.

Inelastic collisions can also occur. In this case the excitation energy E_i of one of the partners in the collision is transferred either partially or completely to the other partner. This acts as a mechanism to depopulate the excited state. If the number of collisions per second removing atoms from the excited state is W_c then the width of the line is given by

$$\Gamma = \hbar\left(W_c + \frac{1}{\tau_i}\right) \qquad (2.72)$$

For the 589.1nm line in sodium, the pressure broadening of the line in 1 atm of Argon is ~0.7 cm^{-1} = 2×10^{10} Hz. At pressures of a few millibar the pressure broadening is less than the Doppler width.

Laser Power Broadening.

As mentioned in §2, at high laser powers the width of the transition can be widened by the electric field of the laser. For a laser of 10μJmm^{-2} then the E_0 is of the order of 10^6 Vm^{-1}. If a transition has an oscillator strength of 0.01 (a typical value) then the Rabi frequency is 2.5×10^9 Hz. The power broadening is therefore ~1×10^{10} Hz.

Laser Bandwidth

The bandwidth of laser used in RIS depends on the particular laser. The lasers used at Glasgow have, at best, a bandwidth of ~30GHz. The laser bandwidth is thus the most important contribution to the observed width of resonant transitions.

From Hurst *et al* (1979) the average cross section for absorption from state a to b if the laser bandwidth is wider than the broadened width of the transition is given by

$$\sigma_{ab} = \frac{g_b}{g_a}\frac{\lambda^2}{8\pi}\frac{\Gamma_{ab}}{\Delta\nu_L} \qquad (2.73)$$

where $\Delta\nu_L$ is the laser bandwidth.

§ 5 Non-linear Optics

Most practical experiments in RIMS or RIS make use of non-linear optical effects. The most commonly used non-linear effect is frequency doubling (or second harmonic generation (SHG)) and this shall be examined in some detail. Others, such as third harmonic generation (THG) and sum frequency generation (SFG), shall also be mentioned.

In a non-linear medium under high radiation intensities the polarisation P of the atoms in a medium may be expressed as:-

$$P = \chi_1 E + \chi_2 E^2 + \chi_3 E^3 + \ldots \qquad (2.74)$$

where χ_i is the i'th order non-linear susceptibility. For radiation of frequency ω and $E = E_0 \sin \omega t$ this can be expanded to give:-

$$\begin{aligned} P = \chi_1 E_0 \sin \omega t &+ \chi_2 E_0^2(1 - \cos 2\omega t) \\ &+ \chi_3 E_0^3(3 \sin \omega t - \sin 3\omega t) + \ldots \end{aligned} \qquad (2.75)$$

A polarisation wave of wavelength $\lambda_1=\frac{2\pi c}{\omega n_1}$ is set up in the medium where n_1 is the refractive index of the crystal at the fundamental frequency ω. The polarisation wave induces the generation of light at frequency 2ω with wavelength $\lambda_2=\frac{\pi c}{\omega n_2}$, where n_2 is the refractive index of the crystal at frequency 2ω. Since in most crystals $n_1 \neq n_2$ it follows that $\lambda_1 \neq \lambda_2$ and the beams propagate out of phase. For propagation along the direction of the secondary beam the intensity of the beam is (Shen 1984):-

$$I(2\omega) \propto \frac{\sin^2\left(\frac{2\pi\Delta n l}{\lambda}\right)}{\left(\frac{2\pi\Delta n l}{\lambda}\right)^2} \qquad (2.76)$$

where $\Delta n = n_1 - n_2$, l is the distance along the beam and λ is the wavelength of the fundamental in vacuo. When the argument of the sine is equal to $\frac{\pi}{2}$ (i.e. $l=\frac{\lambda}{4\Delta n}$.) then the intensity is maximised. For normal crystals the distance for which I is significant is $l \leq 10\mu m$. For larger coherence lengths Δn must be made small and therefore $n_1 \approx n_2$. Usually in crystals $n_1 > n_2$.Another restriction in the crystal is that it must be non-centro-symmetric, as these are the only crystals where χ_2 is non-vanishing (Thomas 1990).

These restrictions can be overcome by the use of a suitable birefringent crystal. One property of a birefringent crystal is that waves of different polarisations have different velocities in the crystal. An ordinary ray has a constant velocity independent of its orientation with respect to the optical axis whereas an extraordinary ray has a velocity that is dependent on its orientation with respect to the optical axis. This is shown for KD*P in fig 2.5. Where the surfaces meet the fundamental and harmonic are phase matched and $n_1 = n_2$. For these crystals l can be large (~ a few cm) and high efficiencies (>20%) may be obtained for operation at $100MW/cm^2$. Details of the doubling systems used are given in chapter 3.

Fig 2.5: Phase Matching in KD*P

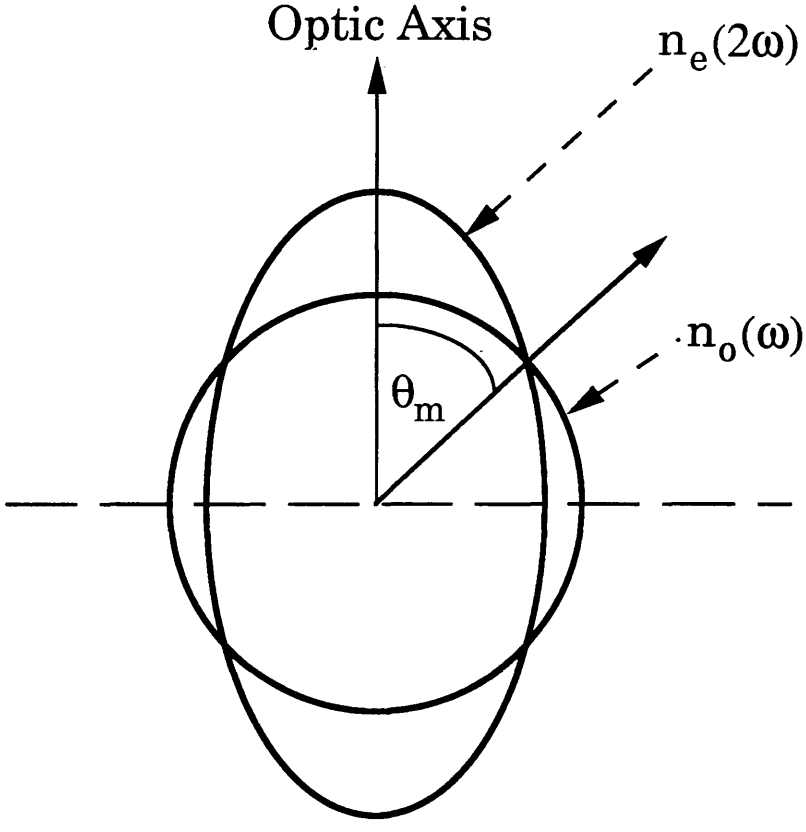

A closely related effect is THG. This occurs due to the third term of the expansion in equation 2.74. Generally, the size of the coefficient is very small and this leads to very low efficiencies (~10^{-4}). Where there is an advantage over frequency doubling is that the χ_3 component is in general non-zero for materials with inversion symmetry. This allows frequency trebling occur in most materials, including gases. This is useful since at very short wavelengths (<200nm) there is high absorbance of light in most non-linear crystals, whereas in some gases this effect does not occur (Becker 1990). The phase matching condition ($n(\omega_1)=n(\omega_3)$) is achieved by using a gas with anomalous dispersion between the two frequencies (Dermtröder 1981).

In SFG two photons of different frequencies are added to give a third of the sum frequency. This depends on χ_2 and consequently it restricts SFG to the same type of crystals as SHG. It can be shown (Shen 1984) that the phase matching condition in this case is

$$\omega_1[\, n(\omega_3)-n(\omega_1)] + \omega_2[\, n(\omega_3)-n(\omega_2)] = 0 \qquad (2.77)$$

where ω_1, ω_2 are the frequencies of the two incident waves and ω_3 is the frequency of the summed wave. SFG allows better efficiencies than frequency trebling (~10%) and where the fundamental and second harmonic wave are used it provides the same effect.

§6 Laser Ablation.

Introduction

Laser ablation is a complex and poorly understood phenomenon that has as yet relatively little theoretical underpinning. The description presented in this section relies on phenomenological descriptions rather than basic physical principles.

When a laser beam is incident on a solid surface, the photons in the beam interact with electrons in the material resulting in

the rapid transfer of energy to the lattice. This process results in two possible mechanisms for production of vaporised species

1) At low power density ($<10^9 W/cm^2$) the material evaporates with little or no ionisation.

2) At higher power densities a laser plasma may be formed by light absorption by the ablated neutrals. This can result in high net ionisation and multiply charged ions. Further increases in power density can result in shockwaves in the sample, resulting in very intense laser plasmas and ejection of bulk material (exfoliation) from the sample.

In RIMS it is desirable to operate in the former of these regimes. Instruments that utilise the ablation process (eg LIMA instruments (Bingham *et al* 1976))as their primary source of ions will operate in the latter, although below the power densities required for exfoliation.

Emission of Neutrals at Low Power Densities

From the perspective of RIMS, laser ablation is a method for the production of neutrals. In order to gain some understanding of the ablation process, it was desirable to model ablation plumes acquired experimentally. An ablation plume is the temporal and spatial distribution of neutrals produced by the laser. The model that was first tried was a Maxwellian fit to the data:-

$$f(v)dv \propto \sqrt{\left(\frac{m}{2kT\pi}\right)^3} e^{-\frac{m}{2kT}v^2} . v^2 dv \qquad (2.78)$$

where m is the mass of the neutrals, k is Boltzmann's constant, T is the (kinetic) temperature of the neutrals and v is the velocity of the neutrals. $f(v)$ and v can be measured experimentally. This allows the temperature of the plume to be fitted. This model proved to be unsuccessful as although the fit was good at short times, at longer times the Maxwellian curve was too high (see fig 6.4). However, by incorporating another term to allow for the expansion of the plume, this defect could be rectified. The modified Maxwellian model is:-

$$f(v)dv \propto \sqrt{\left(\frac{m}{2kT\pi}\right)^3} e^{-\frac{m}{2kT}v^2} . v^2 \left(\frac{v}{vs + \alpha v_p d}\right)^2 dv \qquad (2.79)$$

where s is the radius of the sample spot, d is the distance from the sample to the ionisation region and α is the plume expansion coefficient. v_p is the most probable velocity of the Maxwellian and is given by $v_p = \sqrt{\frac{2kT}{m}}$. The idea behind the last term is shown in fig 2.6. The plume is expected to expand from a radius of s to a radius given by $s + \alpha v_p t$ and consequently this term compensates for the decreased density in the directions parallel to the sample surface. This is the form that was used for modelling. There are two drawbacks to this model. The first is that s and d are not known very accurately. Consequently it is difficult to obtain a precise fit to temperature. Secondly α is a constant that was obtained by only one method. While it is possible to allow α to become a variable and fit to both α and T, in practise a change in α could be compensated by a change in T (figs 6.25 and 6.26).

These drawbacks may be overcome if it is known that the plume (ie. T, α, s and d) will be identical for two separate sets of results. This is the case if different isotopes of the same element are modelled using data taken at the same time. In this case only m would be different. Described below is a extension of the Maxwellian model developed to account for the variation of isotope ratio as a function of neutral velocity. Neutral velocity is best described by using the time taken for the neutrals to move from the sample surface to the ionising laser, hence $v=d/t$. By considering the cases of (1)$vs \gg \alpha.v_p d$ and (2) $vs \ll \alpha.v_p d$ equation 2.79 can then be written:-

$$g(t)dt \propto m^{\frac{3}{2}} e^{-\frac{m}{2kT}\left(\frac{d}{t}\right)^2} \frac{1}{t^2} dt \qquad (2.80)$$

for case (1) and

$$g(t)dt \propto m^{\frac{5}{2}} e^{-\frac{m}{2kT}\left(\frac{d}{t}\right)^2} \frac{1}{t^4} dt \qquad (2.81)$$

Fig 2.6: Plume Expansion used in Simple Maxwellian Distribution

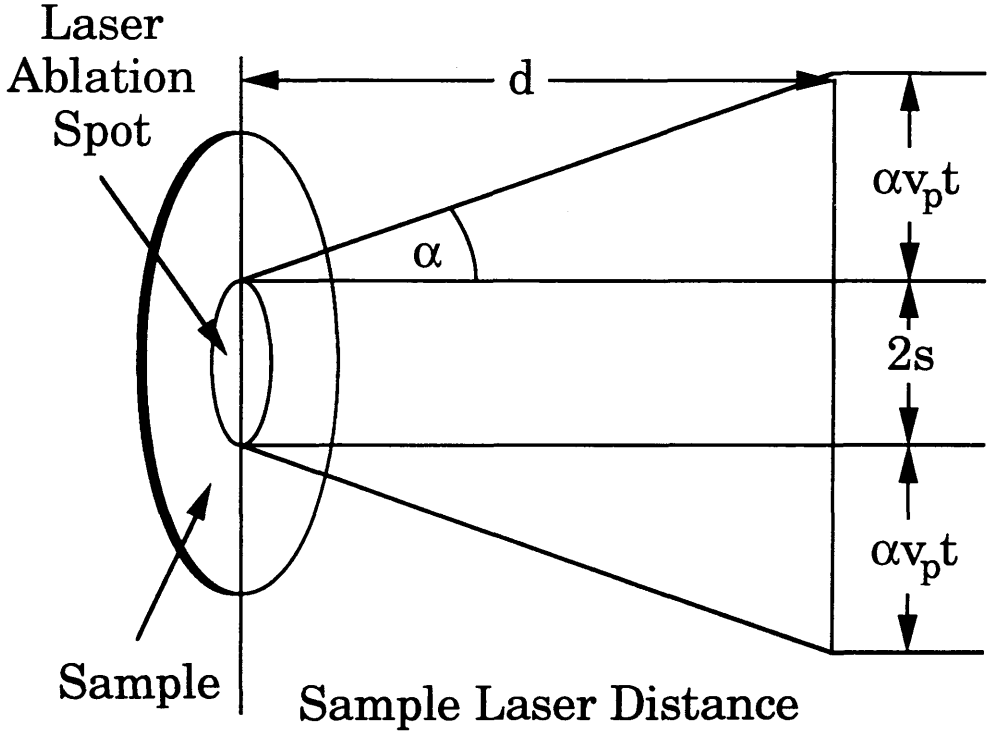

for case (2).

For two isotopes of masses m_1 and m_2 the isotope ratio for case (1) is given by:-

$$R(t) = \Re\left(\frac{m_1}{m_2}\right)^{\frac{3}{2}} e^{-\frac{\Delta m}{2kT}\left(\frac{d}{t}\right)^2} \qquad :\Delta m = m_1 - m_2 \quad (2.82)$$

for case (1) and

$$R(t) = \Re\left(\frac{m_1}{m_2}\right)^{\frac{5}{2}} e^{-\frac{\Delta m}{2kT}\left(\frac{d}{t}\right)^2} \qquad :\Delta m = m_1 - m_2 \quad (2.83)$$

for (case 2), where $\Re$ is the actual isotope ratio. In the ablation work performed at Glasgow, the values of the parameters d, s and α, and the experimental value of v_p are such that only case (2) is appropriate. Fig 6.14 shows the form of this curve. This analysis assumes that the neutrals are ionised in a very small volume (ie. with post-ionising lasers tightly focussed),in a very short time (ie. much shorter that the time taken to cross the ionisation region) and that the neutrals are produced from the sample very quickly (also much shorter than the transit time). In the experiments performed in this thesis these conditions were fulfilled. The experimental determinations of isotope ratios as a function of delay time are presented in chapter 6 §3.

More complex descriptions, such as Knudsen layer formation (Kelly *et al* 1988), have been employed to describe the laser ablation plume. These models assume some interactions between the neutrals within the plume. They are generally more complex to implement and give similar predictions about the shape of the plume as the Maxwellian description.

Chapter 3 : Instrumentation

§ 1 Introduction

The RIMS instrument used to perform the work for this thesis is a large and complex instrument. For ease of description the instrumentation used can be split into three parts: lasers and optics, mass spectrometer, and data acquisition and analysis. Each will be dealt with in turn

§2 Lasers and Optics

General Overview

Two main laser systems were used in the course of this work. The first is a dye laser system from Spectron which consists of a Nd:YAG (Eastham 1986) laser pumping two dye lasers (Schäfer 1973) which is used to generate the resonant laser light needed, and the other is a Quantel Nd:YAG which is used for ablation. The laser and optical layout is shown in Fig 3.1. Also required are beam measurement and beam steering optics to allow control of laser power and position. The details of these are given after the description of the lasers.

Spectron Nd:YAG

The dye pump laser is a Q-switched Nd:YAG (Fig 3.2). (Spectron SL2Q + SL3Q, Spectron Laser Systems, Rugby, UK). The laser consists of a flashlamp pumped laser oscillator, a dual flashlamp pumped laser amplifier rod and frequency doubling, tripling and quadrupling facilities. The laser operates multimode and the measured outputs of this laser are shown in table 3.1, together with the factory specification. These values are not constant over time and decrease gradually with the ageing of the flashlamps. The laser has an optimum repetition rate of 10Hz, which was used throughout this work. It can be made to operate at repetition rates of up to 30Hz by shortening the cavity length to compensate for thermal lensing, although this reduces the

Fig 3.1: Resonant Laser Optical Layout

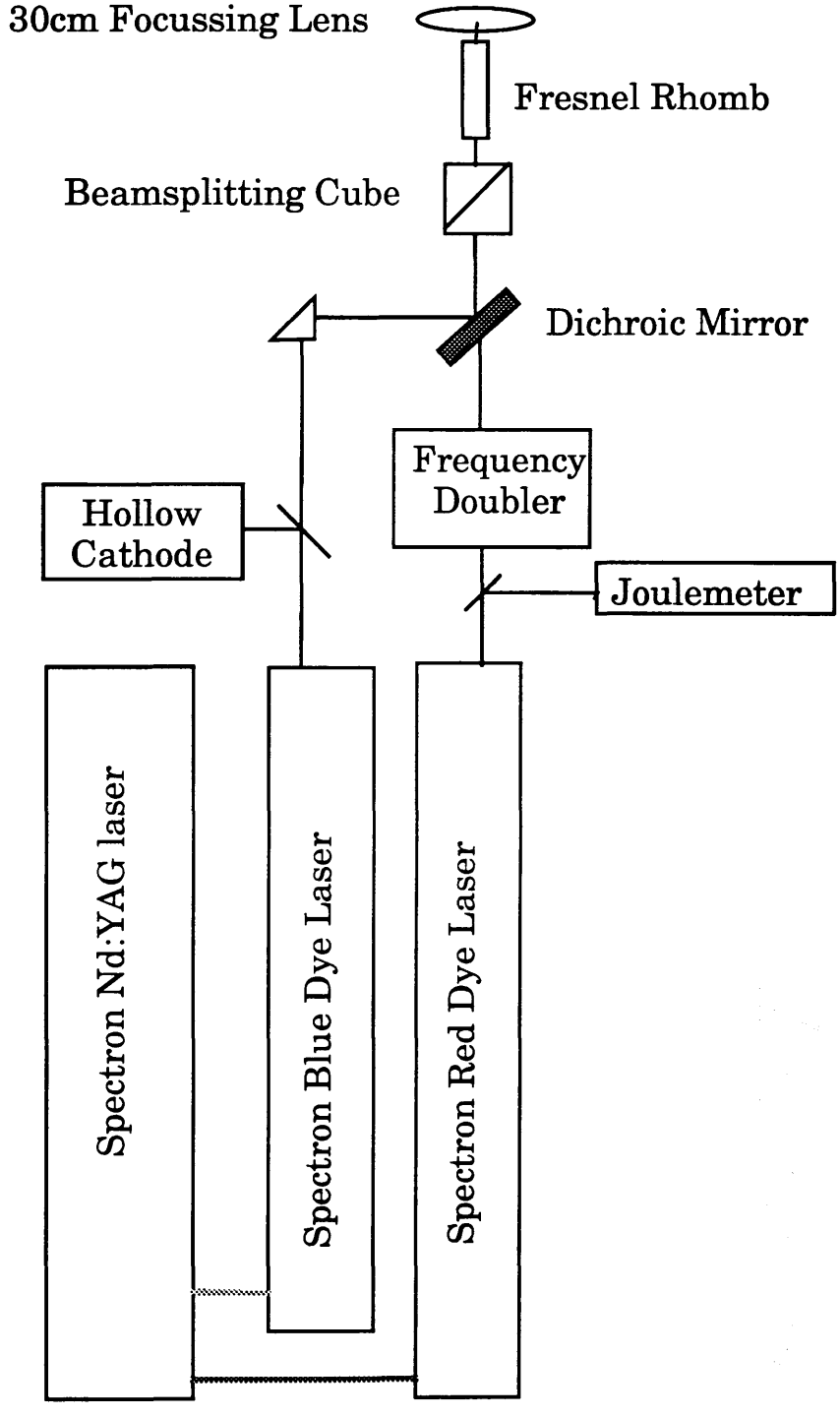

Figure 3.2: Spectron Nd:YAG Laser

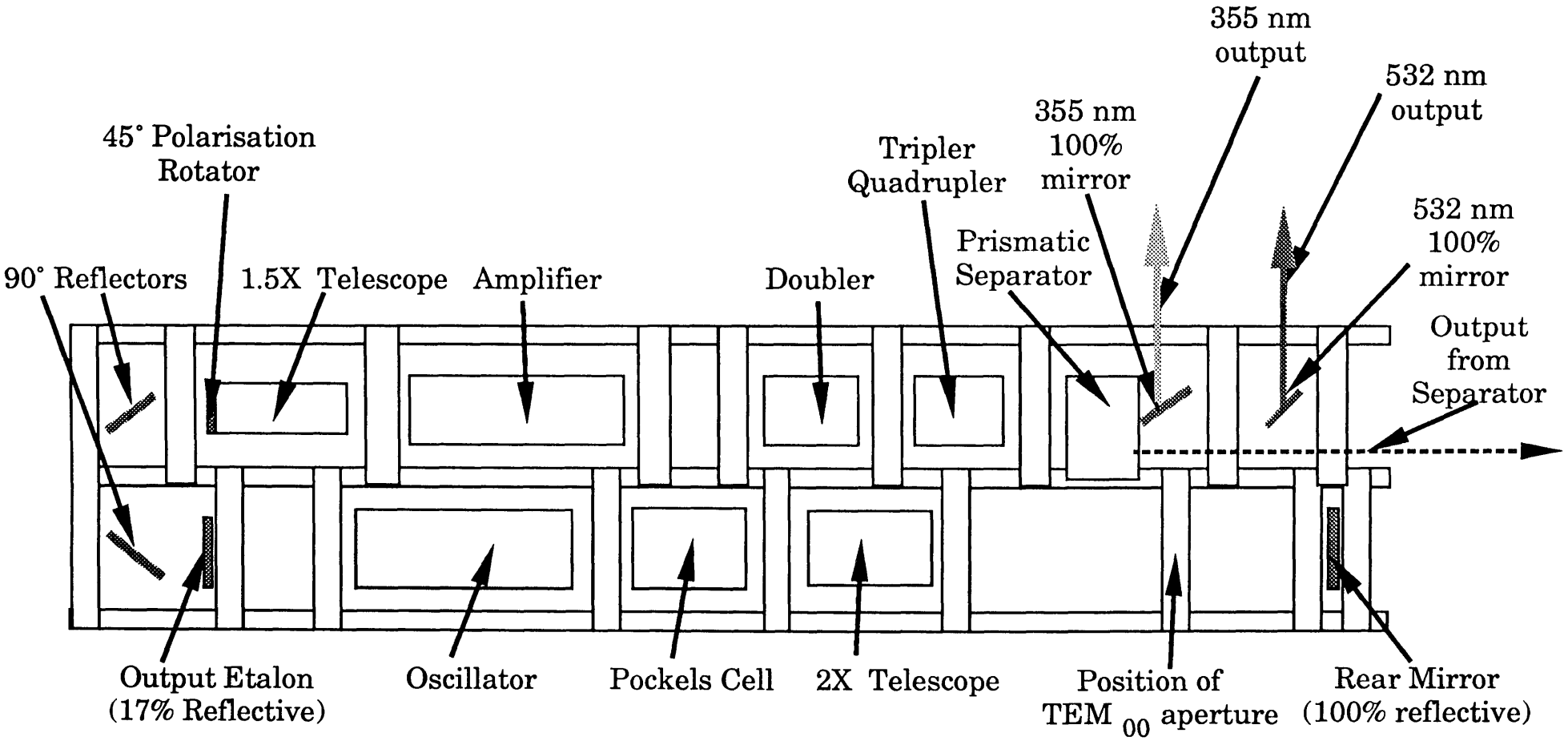

Table 3.1: Output Specification for Spectron Nd:YAG system

Factory Specification	(10 Hz Multi Mode)
1064nm	850mJ
532nm	310mJ
355nm	90mJ
266nm	50mJ
	(10Hz TEM_{00})
1064nm	50mJ
532nm	N/A
355nm	N/A
266nm	3mJ
Output pulse length	16ns

Table 3.2: Specifications for Dye Laser Systems

Output Energy with 532nm	>30% (spec) = 100mJ ~10% (actual) = 35mJ
Output Energy with 355nm	>15% (spec) = 10mJ ~5% (actual) = 3mJ
Pulse Duration	14ns
Tuning Range	750nm-540nm (Red Laser) 750nm-400nm (Blue Laser)
Linewidth	<6GHz (spec) ~40Ghz (actual)

laser power. The laser can also be made to operate in TEM_{00} mode by insertion of a ceramic disc in the oscillator cavity, again at the cost of reduced power. Power also decreases at repetition rates below 10Hz, due to changes in the optical characteristics of the laser rods caused by reduced heating. Beam telescopes are used to expand the laser beam to a size that makes best use of the laser medium. The telescope in the oscillator also helps to discriminate against high transverse modes by raising the degree diffraction per unit length of the cavity.

The internal harmonic generation crystals are all Potassium Di-deutrium Phosphate (KD*P) (Shen 1984) which is an angle tuned nonlinear optical crystal. For optimal power stability the crystals are maintained in a temperature controlled oven at a temperature of 55°C. This arrangement gives very good power stability as compared to non-temperature controlled crystals (see below). The output stability of the laser is ±5% in the 532nm and 355nm harmonics after the laser has been allowed time to stabilise.

Only one of the tripled or quadrupled outputs are available at once with the internal optics, although the 532nm output can be externally doubled to 266nm if both UV wavelengths are required simultaneously. The 266nm output usually takes a few minutes to reach peak power due to UV absorption and subsequent heating of the crystal.

The Nd:YAG harmonics are collinear after exiting the harmonic generating crystals and can be separated either by use of wavelength selective dichroic mirrors or a twin Pellin-Broca prism (Pedrotti 1987). The Pellin-Broca prism allows only one output to be used at a time, with the other outputs being dumped in beamdumps.

Spectron Dye Lasers

The tunable laser facility consists of two Spectralase 4000 dye lasers (fig 3.3). (Spectron Laser Systems). These lasers are almost identical, the only differences being the wavelength specific optics

in each and the use of two amplifiers in the laser pumped by the 532nm Nd:YAG output.

The dye laser cells are pumped transversely as shown in fig 3.4. The same design of cell is used for both oscillator and amplifier. Cylindrical lenses are used to focus the pump laser into a line inside the dye cell. Lasing action occurs along this line.

For the maximum possible wavelength coverage, different diffraction gratings have to be used. The two used cover the range are 540nm-750nm in one laser (The Red Laser) and 400nm-750nm (The Blue Laser). The red laser is exclusively pumped by 532nm, which can pump dyes down to 540nm, and the blue laser is pumped by 355nm, which can pump over the entire range of the grating but in practice is only used for dyes that lase below 540nm. The upper limit on the wavelength range is defined by the scan mechanism in the laser head. Upon leaving the oscillator the laser beam is expanded by a telescope and then enters the one-pass amplifier cells, two in the red laser and one in the blue laser.

Control of the laser is via the dedicated controller SL4000 SC. This controls the position of the mirror by means of a sine drive which is driven by an anti-backlash gearbox which is in turn driven by a five phase stepper motor. The dedicated controller is not interfaced to the computer and wavelength scans have to be started manually.

The laser power output depends on many factors, e.g. the age of the dye solution, the type of dye, room temperature and dye concentration. Due to these factors, and the lack of effective optical coatings on some components (eg. the beamspreader) the efficiency of these lasers is poor, reaching at best 10-12% when the dye is new, and usually falling to around 5%. Typical powers from the dyes used are given in table 3.2. Table 3.2 also lists the other important parameters of the lasers. The linewidth was measured by use of a hollow cathode lamp, which can also be used for absolute wavelength calibration (see "Beam measurement optics" below).

Fig 3.3 Spectron Dye Laser

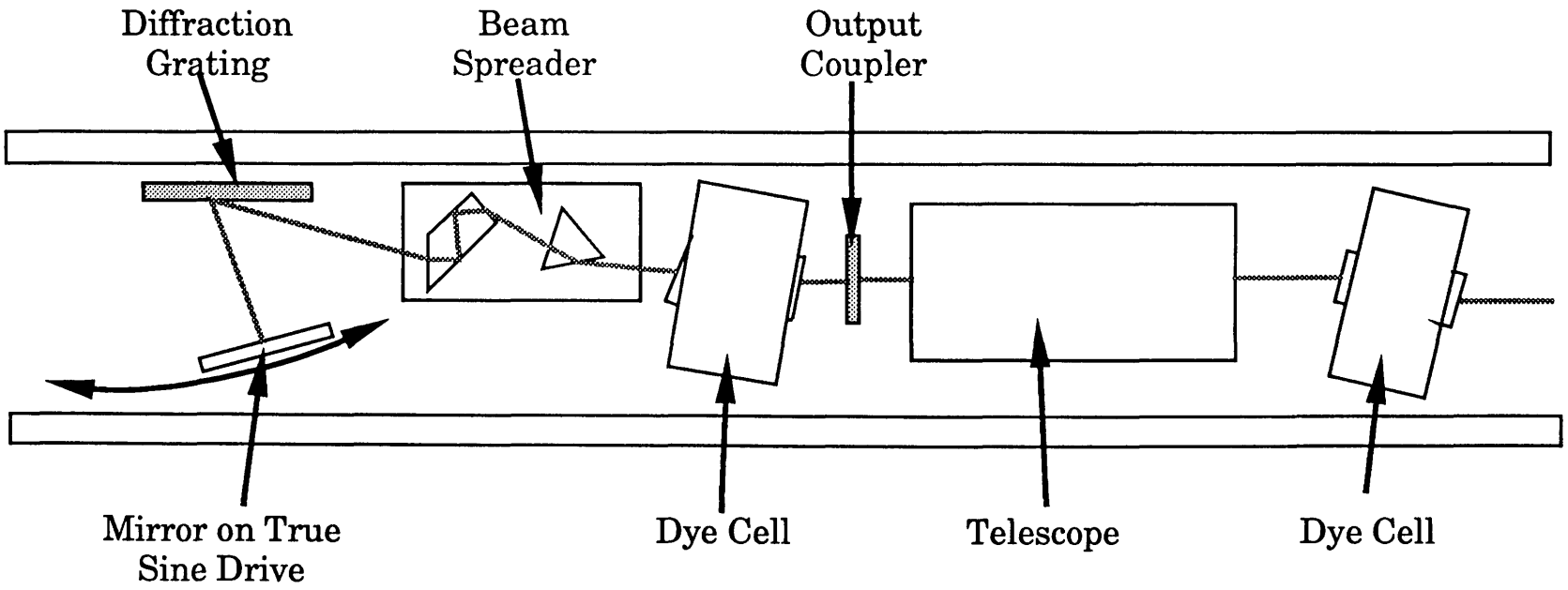

Figure 3.4: Dye Cell Configuration

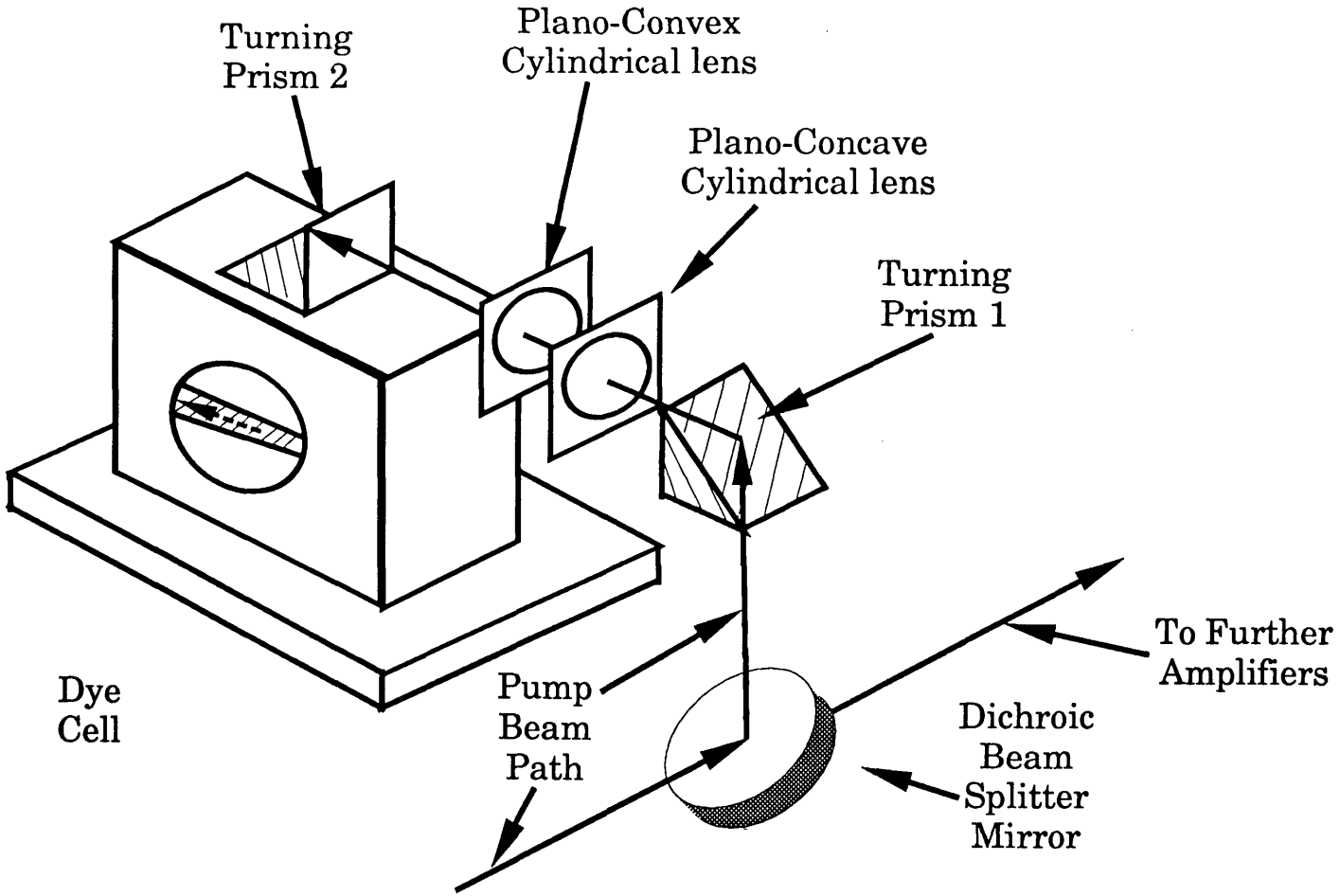

Quantel Nd:YAG

A second Nd:YAG laser (Quantel YG 585 "COMPACT", Quantel, Cedex, France) is used for laser ablation purposes. This laser, like the Spectron Nd:YAG, runs multimode and has a repetition rate of 10Hz. Similarly, it has doubling, tripling and quadrupling facilities, although only one of these wavelengths is available at any one time.

The laser is shown in fig 3.5. The harmonic generation facility is shown in fig 3.6.

One of the major problems with this laser is that the output is highly unstable. The output stability is 15%, and over a period of time the average output energy drifts by 25% over the first hour of operation. After this time the fluctuations and drift become less problematical, but still occur. The reason for this is thought to be the lack of temperature control of the harmonic generating crystals. The condition is exacerbated by the exponential dependence of the ablation process on the laser power (see Chapter 6), leading to variation in the ablation rate of orders of magnitude in the worst case. A possible wavelength for laser ablation is 266nm, but because of stability problems this is unusable on this laser. Generally the 532nm output was used instead for ablation. The laser also includes a built-in variable attenuator. The attenuator gives control of the average power of the 1.064μm beam, although the power fluctuations are still problematical.

There are two solutions to the power variation problem. The first is to take readings over many shots in order to average the power fluctuations out, and the second is allow the computer (§4) to decide if a particular shot is acceptable on the basis of the laser power. Both methods were used and the second was found to give more reproducible results, although this method did greatly increase the length of time required for an analysis. Generally, the first method was used for setting up and alignment of the instrument, and the second was used where accuracy was required.

Fig 3.5: Quantel Nd:YAG Laser

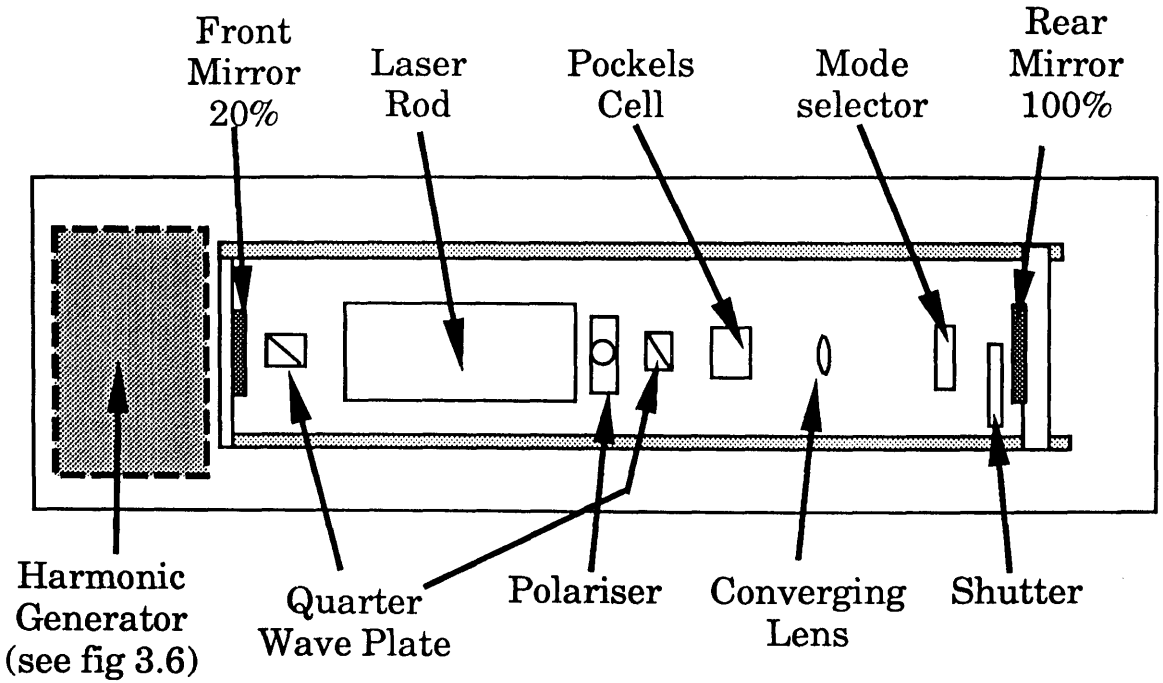

Fig 3.6 Harmonic Generation Facilities on Quantel YAG

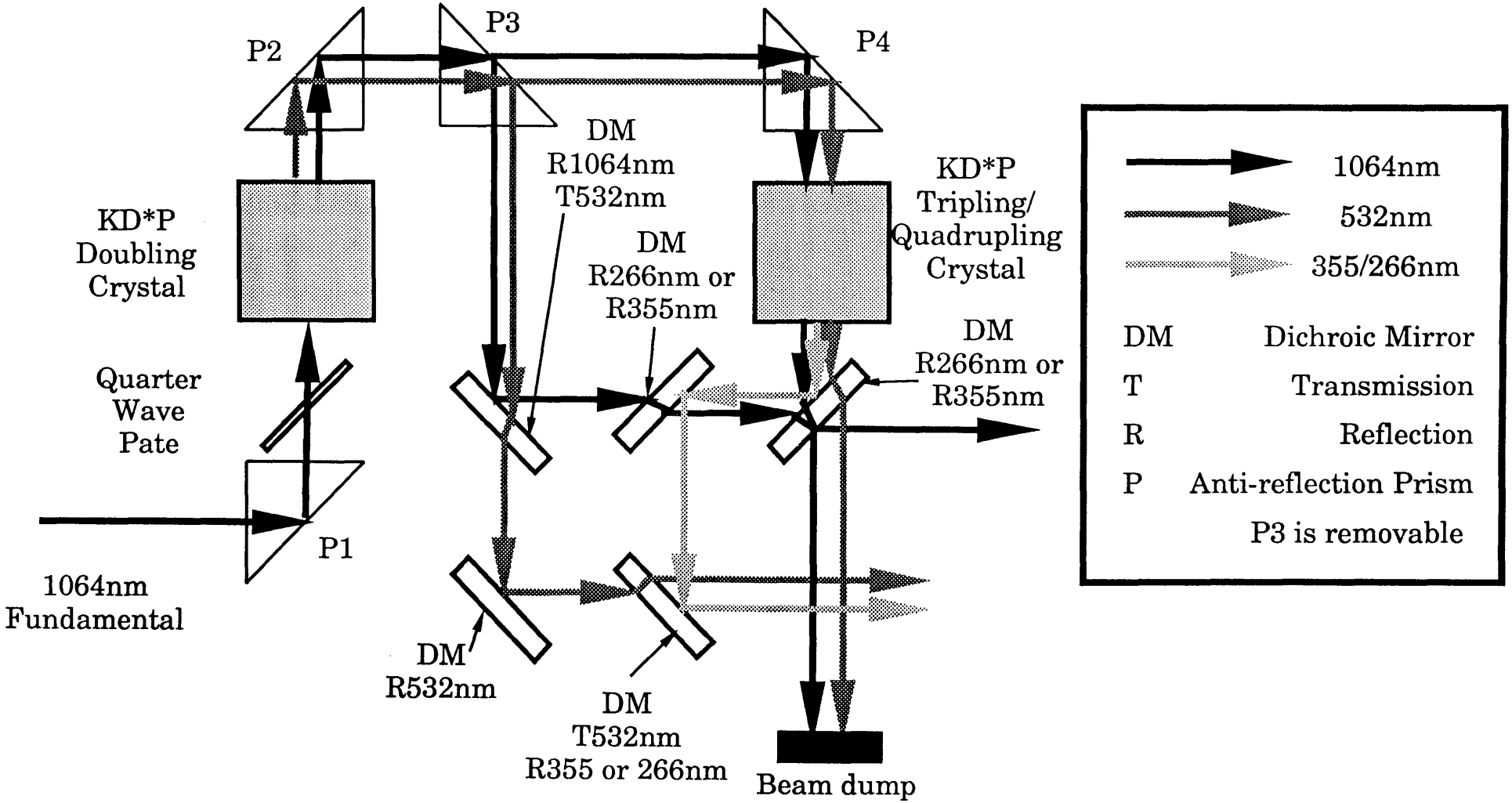

Pulse generator

To obtain the best overlap of the ionising lasers and the ablation laser the timing between firing of the lasers has to be carefully controlled. To achieve this end a custom delay generator was developed by Dr A.P. Land. This unit accepts a pulse from the 2261 Transient Digital Recorder(see below) and fires the laser flashlamps and Q-switches at the correct time. The time between the Q-switch firings is variable from between .25μs and 14μs. This delay is controlled by a front panel potentiometer. A calibration graph for the unit is shown in fig 3.7. Measurements of the delays between the lasers was measured by photodiodes and an oscilloscope. The firing sequence for the unit is shown in fig 3.8

Frequency Doubling of Dye Lasers

As mentioned in chapter 1, to obtain ionisation schemes for all the elements requires the use of harmonic generation. Two facilities were used. One is an angle tuned mount which allows the angle of the crystal to be altered for different laser wavelengths. This mount is not suitable for use when the laser wavelength is being continuously changed.

To achieve reliable frequency doubling when the laser wavelength is being scanned an Inrad Auto-Tracker is used.(Inrad J-12 "Autotracker", Interactive Radiation Inc, NJ, USA.) This device (fig 3.9) can continuously maintain an optimal tuning angle for a nonlinear crystal. Details of the autotracker range and crystals used are shown in table 3.3.

Beam Steering Optics

The ionising lasers are introduced into the mass spectrometer by the beam steering optics. The bulk of these are quartz 45° prisms which serve to guide the beam. For experiments where two lasers are necessary a broadband dichroic mirror may be used for beam combining (Newport Dichroic Edge Filters, Newport Corp CA, USA). After the final quartz prism a Glan-Taylor beamsplitting cube (Hecht 1987)

Fig 3.7: Pulser Calibration Graph

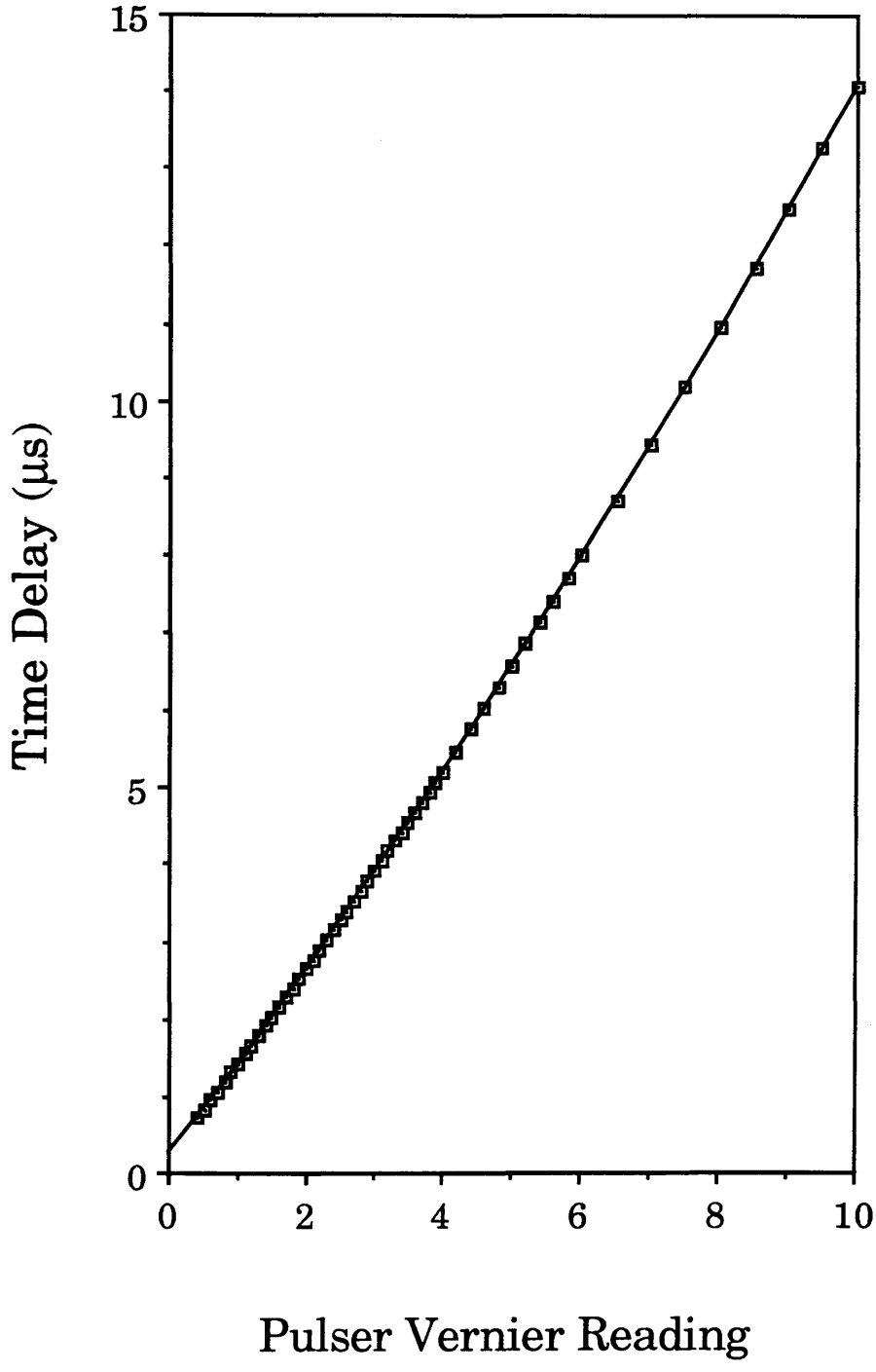

Fig 3.8: Pulse Generator Firing Sequence

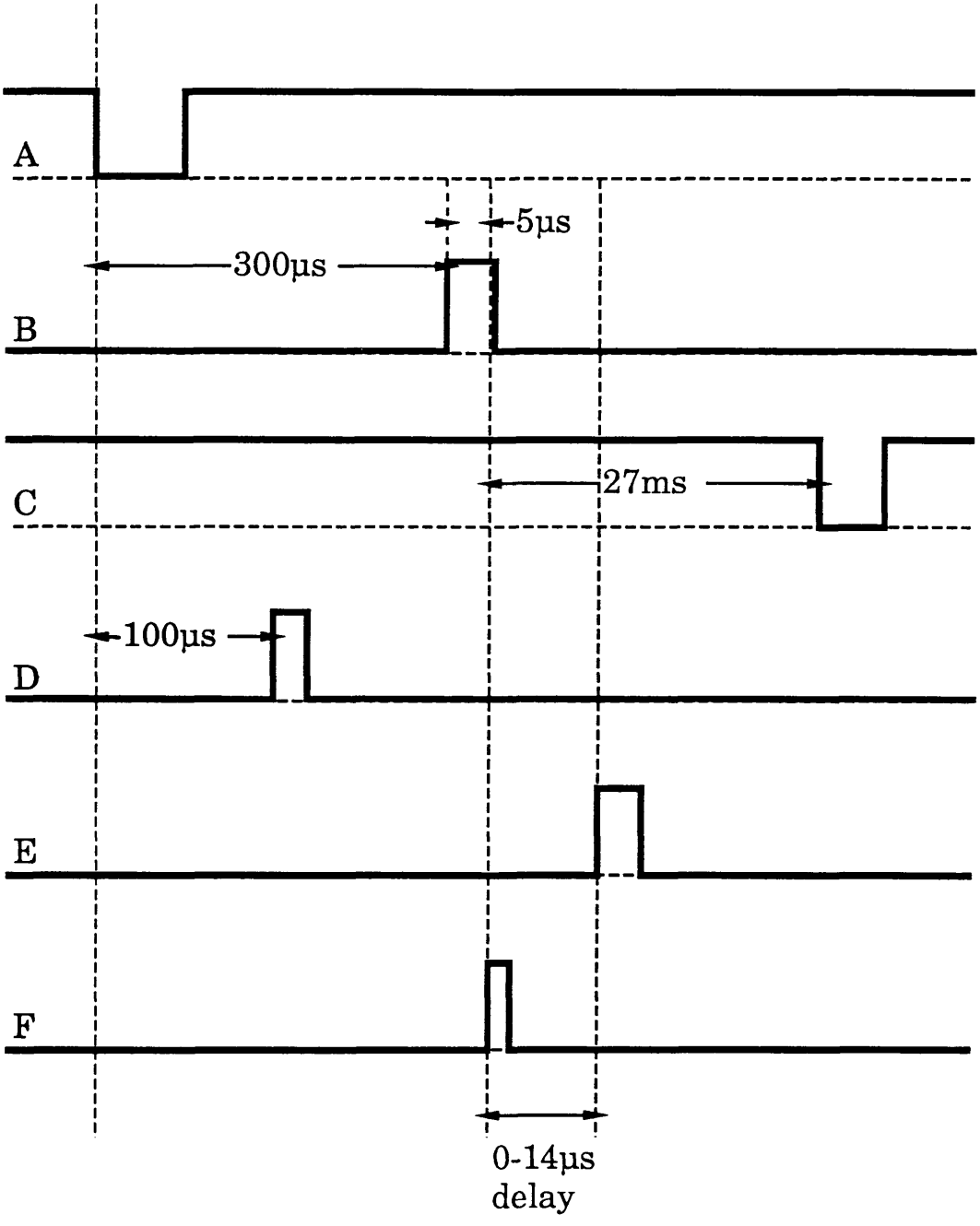

A	Quantel Flash lamps	B	Quantel Q-switch
C	Quantel Cap. Banks	D	Spectron Flashlamps
E	Spectron Q-switch	F	TTL ' zero' pulse

Fig 3.9: Inrad Autotracker

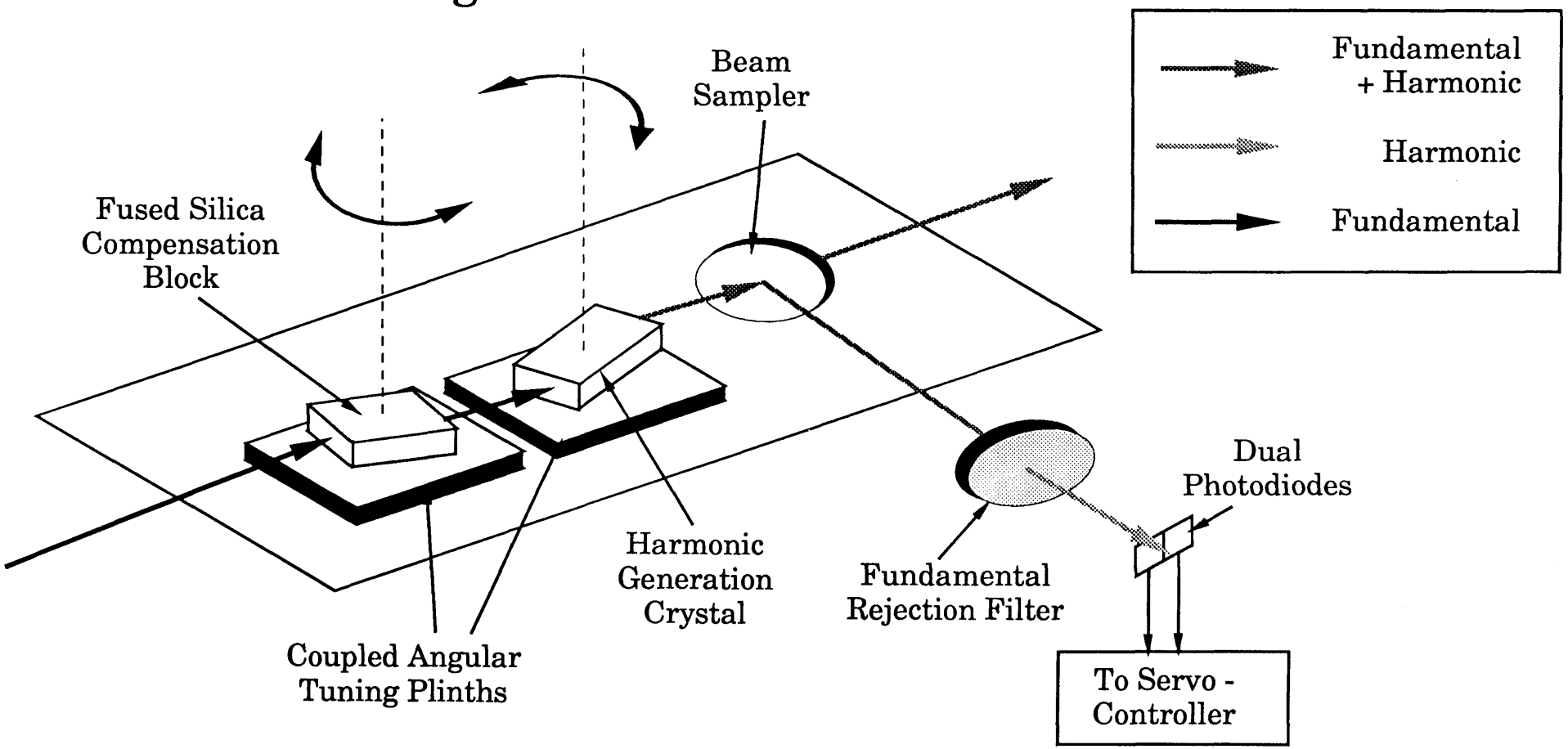

Table 3.3: Frequency Doubling Specifications

The specifications for the autotracker are:-

Conversion Efficiency	90% of static crystal
Scanning Rate	0.01 nm/s/Hz
	0.5 nm/s (max)
Wavelength Range	217nm-470nm
Output Stability	±1%
Laser Rep. Rate	5Hz - 10kHz
Bandwidth	<0.1nm
Beam Diameter	<4mm
Peak Power	>5kW

The crystals used for the frequency doubling varies with the wavelength as shown below:-

Species and Orientation	Fundamental Wavelength(nm)	Harmonic Wavelength(nm)
β–BBO	434 to 526	217 to 263
KPB "A"	434 to 443	217 to 222
KPB "B"	443 to 469	221 to 235
KPB "C"	469 to 518	234 to 259
KD*P "A"	518 to 534	259 to 267
KD*P "B1"	525 to 565	262 to 283
KD*P "R6G"	533 to 590	282 to 330
KD*P "C"	590 to 730	295 to 365
KD*P "D"	660 to 940	330 to 470

(Newport 10FC16PB.3) may be used to separate the polarisations, giving high quality linear polarisation. A Fresnel rhomb (Jenkins 1981) (Spindler and Hoyer 33-7852, Gottingen, WG) which functions as an achromatic retarder may be used to change to circular polarisation. A 30cm focusing lens then focuses the beam through a quartz window on the mass spectrometer into the ionisation region. The beam intensity can be varied using a precision variable optical attenuator (Newport 935-5).

Beam Measurement Optics

There are two main features of the lasers that need to be know for effective spectroscopy or spectrometry: wavelength and energy.

Although the lasers used have quoted resetability of .001nm and accuracy of .005nm, in practice it is necessary to calibrate them for wavelength from some external source. The ideal method for this would be a wavemeter such as the Burleigh pulsed wavemeter (Burleigh Instruments, St Albans, UK), but the financial restraints prohibited its purchase. A cheap and accurate absolute wavelength calibration for the dye lasers was needed. The most feasible method was the Optogalvanic Effect (OGE) (Dovichi 1982) in hollow cathode discharge lamps.

The lamp used is a uranium hollow cathode lamp. This was chosen because uranium has a large number of absorption lines which give coverage over the entire visible spectrum. For wavelength determination of frequency doubled light the fundamental was used in the hollow cathode lamp. A section of output from the hollow cathode lamp is shown in fig 3.10. This is taken from "An Atlas of Uranium Emission Intensities in a Hollow Cathode Discharge" (Palmer 1980). Although these are emission lines, it is applicable to apply them to absorption resonances since, as reported in Nestor (1982), there is a one to one correspondence with the emission spectra.

By comparing the output from the lamp when scanned across a resonance, an estimate of the linewidth of the laser can

Fig 3.10: Typical Output from an Uranium Hollow Cathode Lamp.

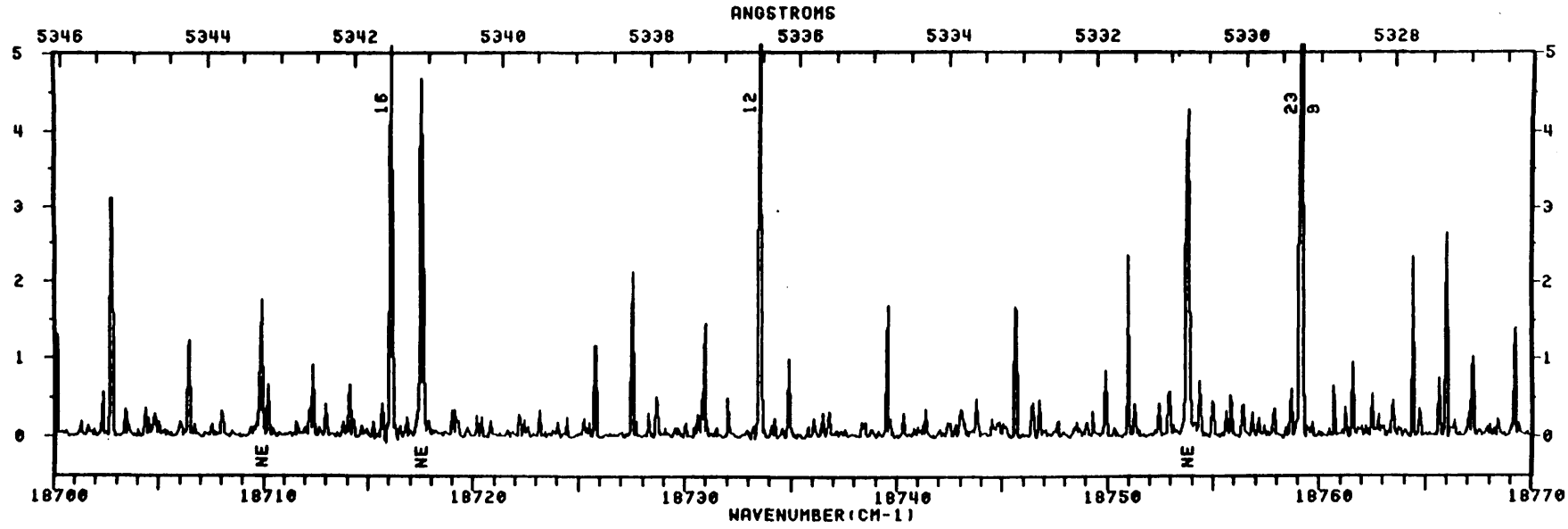

be made if the linewidth of the laser is wider than the linewidth of the hollow cathode transitions. For the system used (linewidth of transitions ~0.03cm^{-1} (Palmer 1980)) this is the case.

Pulse energies of the lasers were measured either by a Molectron J-09 joulemeter (Molectron Detector Corp, CA, USA) when the energy was less than 1mJ, or by a Gentec ED200 (Gentec, Ottawa, Canada) for energies greater than 1mJ.

§3 Mass Spectrometer

Overview

The mass spectrometer is shown in figs 3.11 and 3.12. It consists of a sample insert chamber, a 30cm diameter spherical chamber constructed of stainless steel (SS) in which the sample is analysed, and a 1.5 meter long SS time of flight tube. The system generally operates at a pressure of 10^{-9} torr.

The mass spectrometer is a time of flight instrument. It works by producing ions in an ionisation region, accelerating them into a field free region where the lighter ions, which are moving faster, arrive at the destination first. Chapter 5 gives more information on the operation of the instrument.

Main Chamber.

The main chamber is a sphere of radius 30cm constructed by Kratos Analytical, Manchester, UK. It has thirteen ports on to which instrumentation can be attached.

The top port houses an XYZ–θ sample manipulator (Kratos WG-194). The manipulator is used for the introduction and positioning of samples.

The neck has three ports attached. One port was used for a gas analyser (Edwards Anavac Gas Analyser, Edwards High Vacuum, Crawley, UK) which was used for analysis of the residual gases in the chamber. A titanium sublimation pump (Kratos XSAM 800) was also housed here, although this is no longer used due to excessive contamination of the chamber

Fig 3.11: Elevation of Kratos Machine

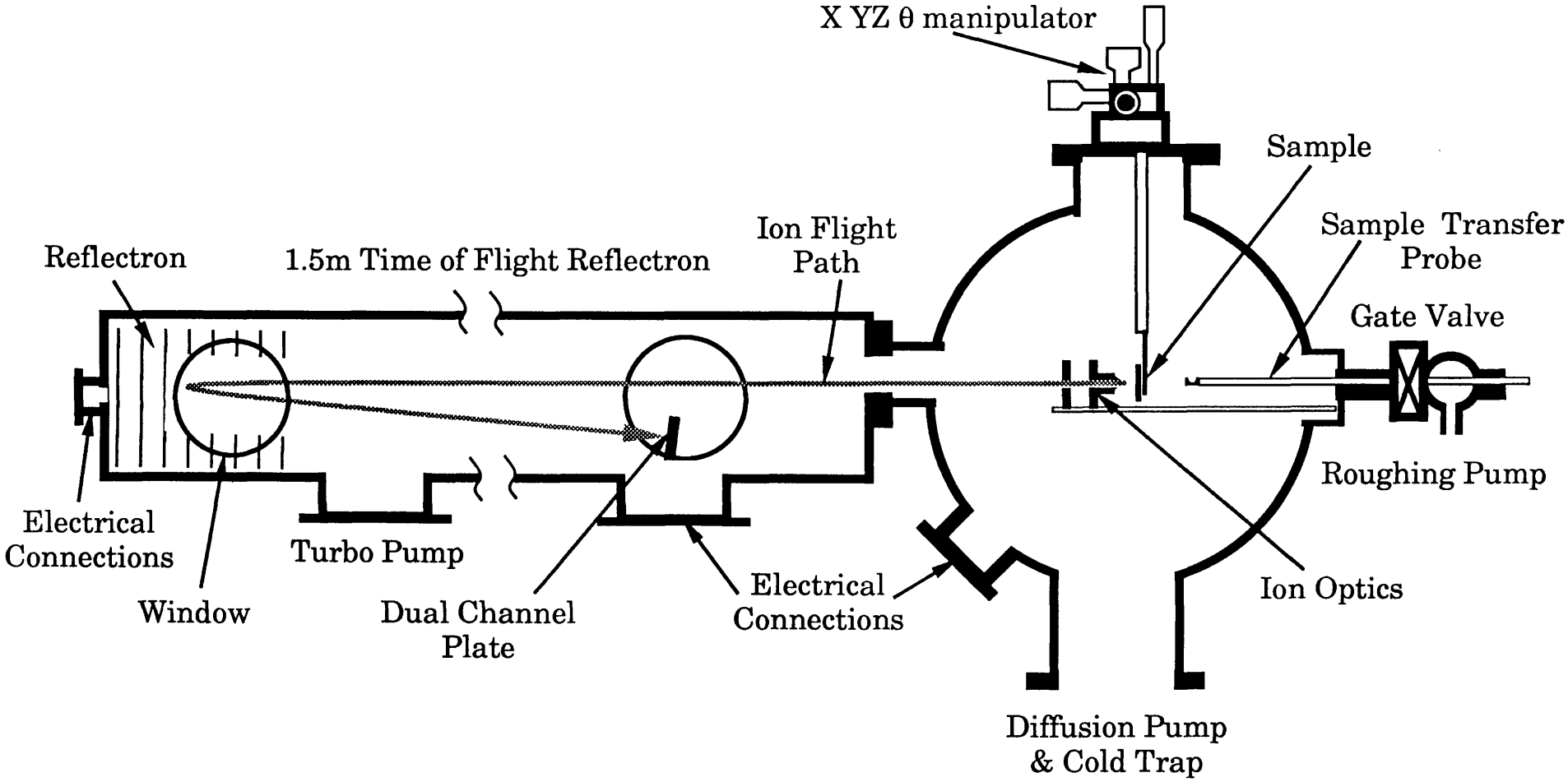

Fig 3.12: Plan View Of Kratos Machine

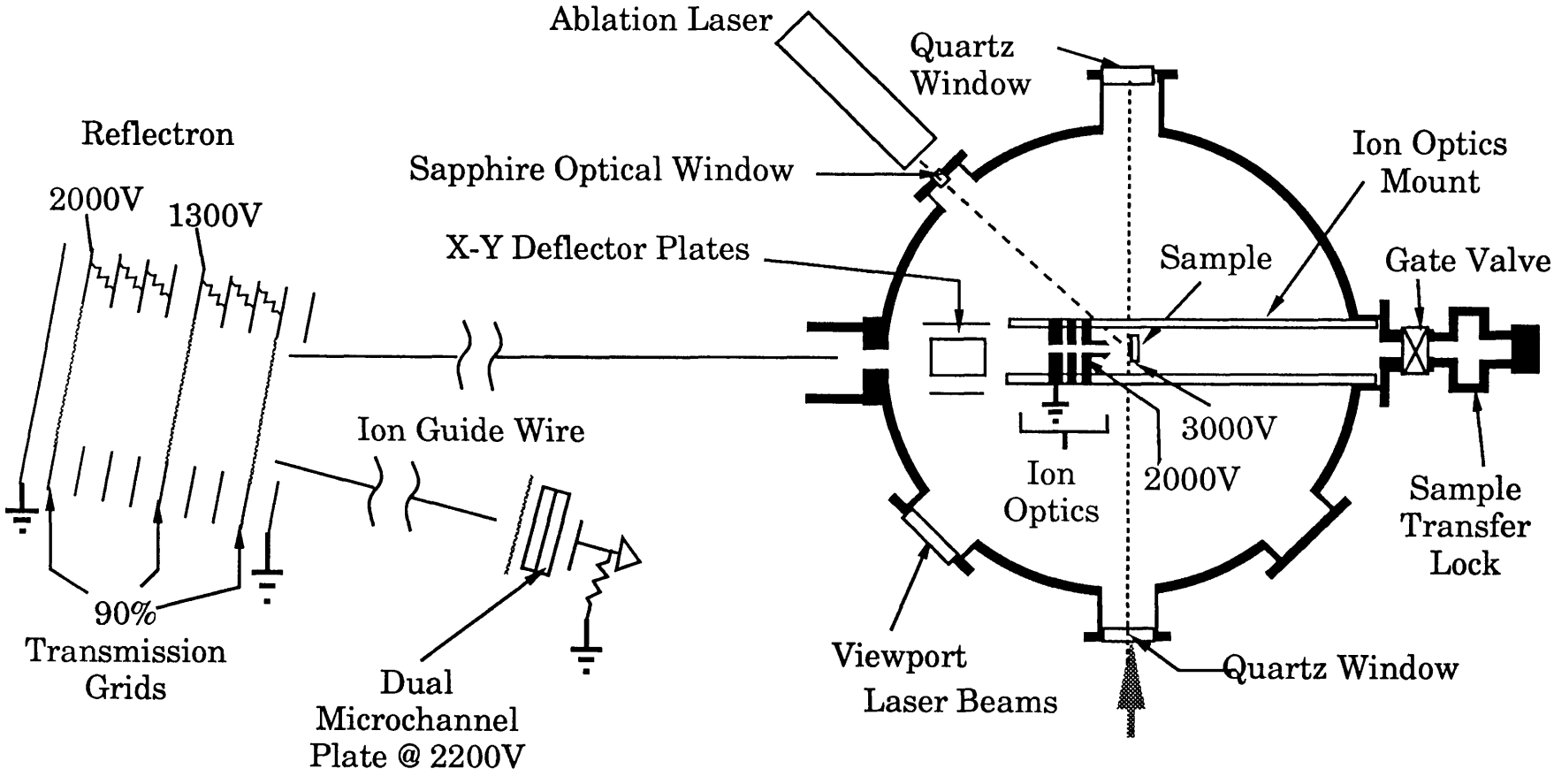

interior from the sublimated titanium. The third port housed the ionisation gauge (Kratos VC-22 IG) which monitored the pressure in the main chamber.

The main system pump, a diffusion pump equipped with a liquid nitrogen cold trap (Edwards Diffstak Mk2 model 160) with a pumping speed of 700 l s^{-1} is located in the neck. The diffusion pump was backed by an oil rotary pump (Edwards 2 stage rotary model E2M8). The time of flight tube was pumped by a turbo-molecular pump (Edwards ETP6, 200 l s^{-1}). The pressure attainable with these pumps was better than 10^{-9} torr, the limit of the ionisation gauge.

At the rear of the sample on the equatorial plane is the sample insertion port (Kratos WG-707). This allows samples to be exchanged and the chamber returned to operating pressure within 5 minutes. The port is pumped down by a rotary roughing pump (Edwards E2M5) to a pressure of 10^{-3} torr before the sample inlet valve is opened. The samples are introduced into the main chamber by the sample insert probe (Kratos WG-175). This has a tip that fits onto the rear grove of the sample and allows the sample to be transferred onto the sample manipulator in the main chamber.

The probe tip is equipped with a programmable temperature controller (Kratos WG-110) which allows a sample to be heated or cooled before insertion. This is useful for removing any water that may be present on the sample, and thus avoid perturbing the vacuum in the main chamber. The range of temperature is -150°C to 600°C.

Also on the equatorial plane are the laser ports. There are three in all; one for the ablation laser and two for the ionisation laser. The ablation laser window is made out of sapphire and the ionisation windows are constructed from quartz. A viewport is provided on the equatorial plane for visual aligning of the lasers with the sample.

Above the equatorial plane is another set of flanges. These are to allow future use of an ion-gun with the system. Viewports are

also provided for visual inspection of the chamber. Below the equatorial plane are ports for the electrical feedthoughs for the ion optics.

Samples to be analysed are introduced into the machine on the SS stubs shown in fig 3.13. Descriptions of sample preparation techniques are given in Ch. 5 §3.

Ion optics

The ion optics used (fig 3.14) are based on the Wiley-McLaren design (Wiley *et al* 1955) and were designed by Dr M. Towrie. These optics provide some energy compensation for ions produced over a finite volume ionisation region. After being accelerated from the sample region the ions enter a field free time of flight tube, of length 1.5m.

Resonant ions formed in the ion optic extract region as shown have an energy, in eV, between the voltage of the sample stub and the first optic. This energy will be dependent on where the ions are formed.

Only ions formed inside the ion acceptance volume will be transmitted to the detector. The ion acceptance volume was measured using the resonant ionisation of background organic impurities in the vacuum (see chapter 4). Fig 3.15 shows the acceptance volume. The acceptance volume in the z-direction is partially controlled by voltage settings on the rest of the instruments. The y-direction form is thought to be due to a slight misalignment of the ion optics with respect to the rest of the instrument.

Time of Flight Tube

At the end of the flight tube the ions reach a reflectron (Gonl *et al* 1983), fig 3.16 and plate 1 constructed by Cambridge Mass Spectrometry, which reflects the ions back along the flight tube to the detector. The reflectron also provides energy compensation for ions produced with different energies, allowing better time resolution. It works by providing a longer flight path for ions of higher energy, which allows ions of different energies to arrive at

Fig 3.13: Kratos Machine Sample Stubs

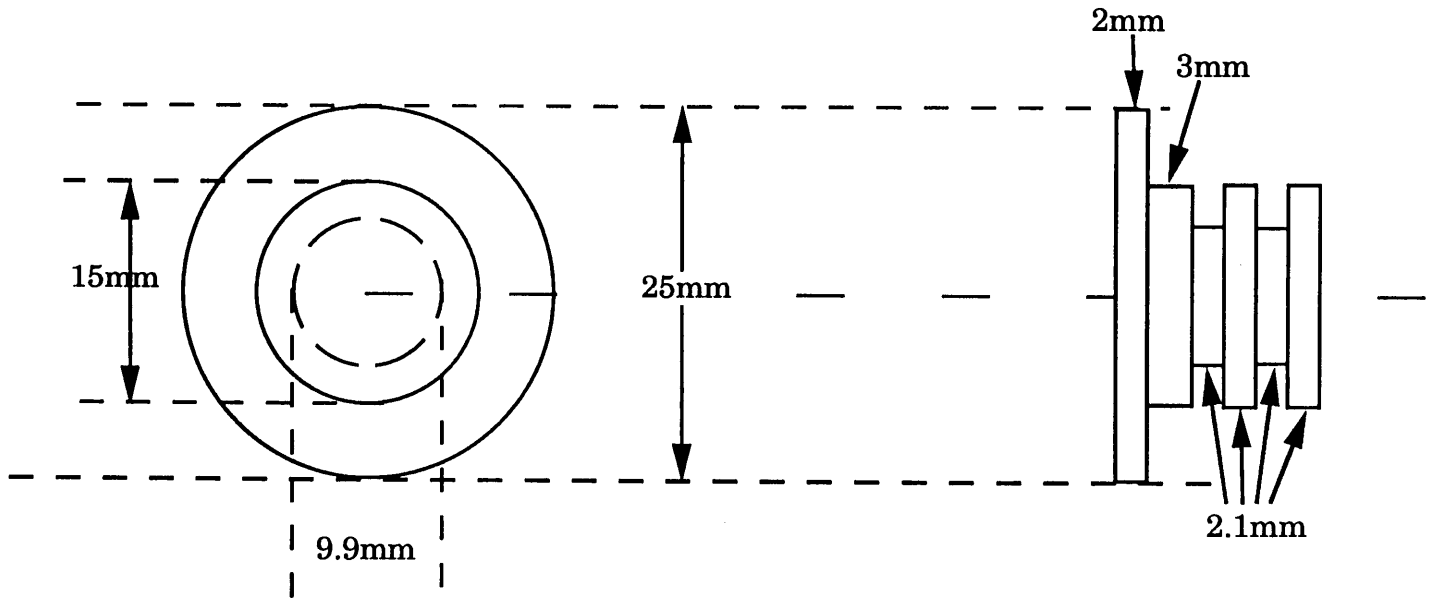

Fig 3.14: Kratos Machine Ion Optics

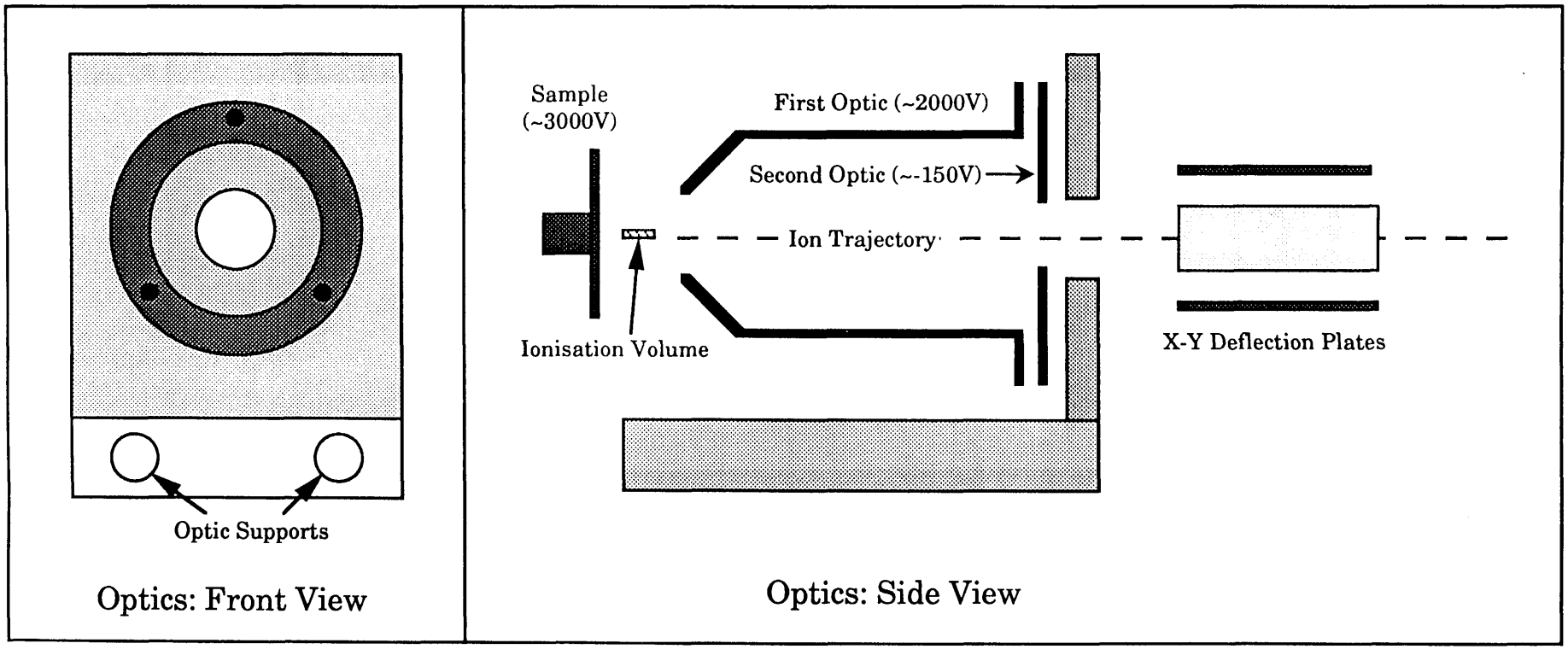

Fig 3.15: Ion Acceptance Volume

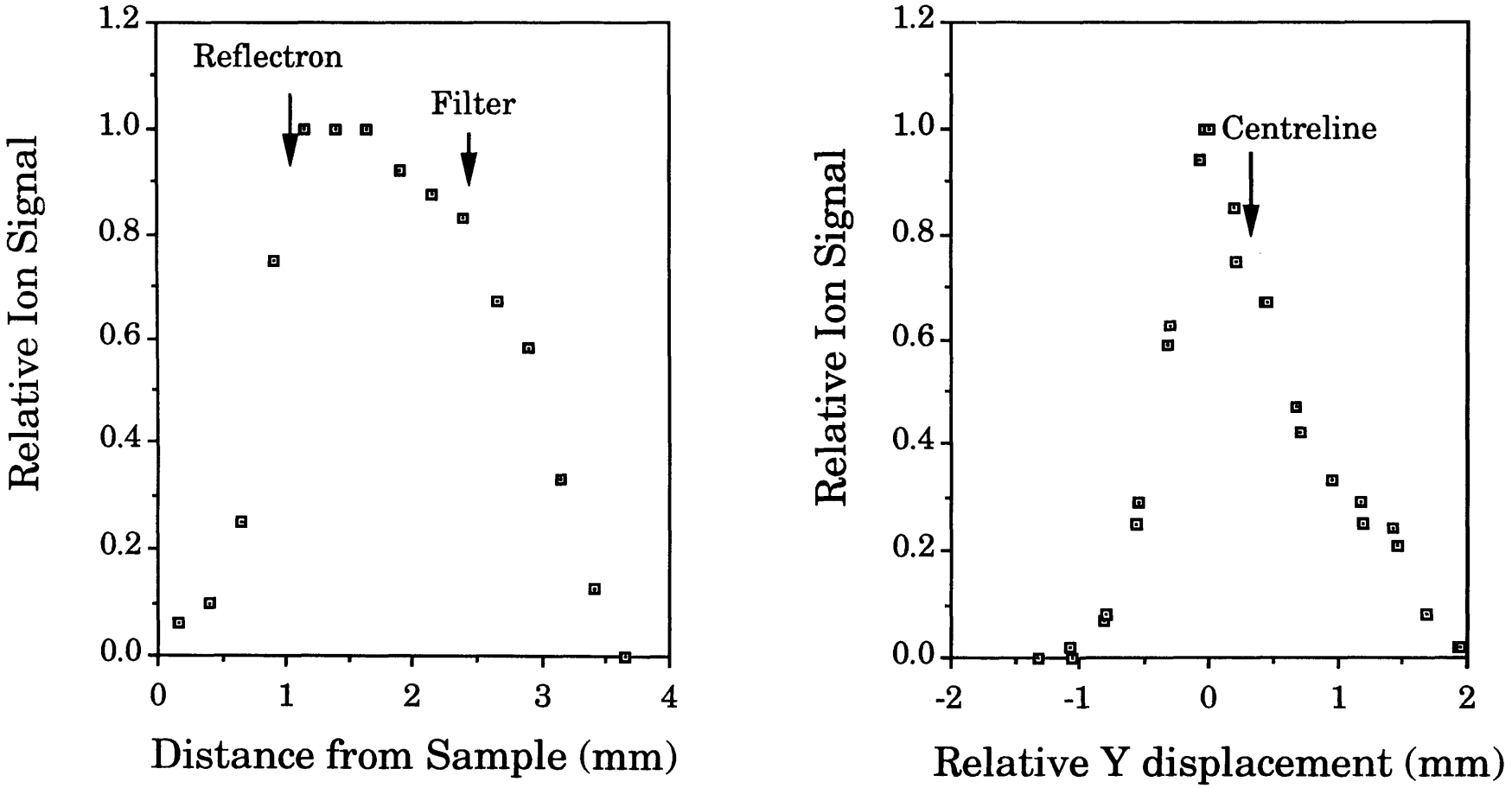

Fig 3.16: Reflectron Showing Paths of Low and High Energy Ions

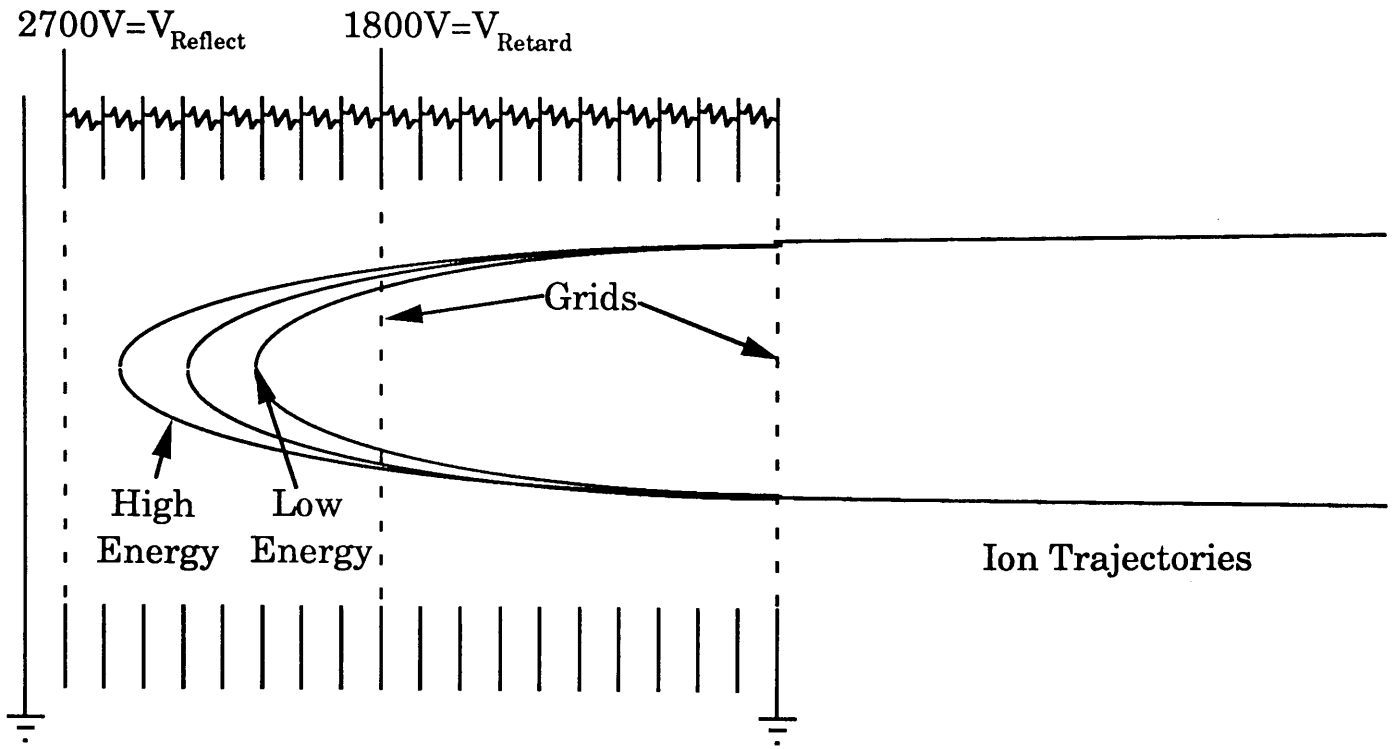

Plate 1. The CMS Reflectron electrostatic mirror

the detector simultaneously. It consists of ~20 plates connected by precision resistors to provide a smooth potential field. The reflectron utilises two voltages, $V_{reflect}$ and V_{retard}, which provide the reflection and the second order energy focussing voltages respectively

Besides energy compensation the reflectron can also provide discrimination between ions formed in the laser ablation process and those formed by resonant postionisation. By a suitable choice of voltages ($V_{sample} > V_{reflect} > V_{RIMS\ ions}$) the ions formed in the ablation process, which are accelerated by the sample voltage, have got too high an energy to be reflected by the reflectron and are rejected. Ions produced in the ionisation region have got a lower energy and are reflected by the reflectron.

The entrance to the flight tube is baffled to prevent any stray ions entering the region.

A thin guide wire runs from the baffle to the reflectron, and from the reflectron to the detector. This acts as an electrostatic ion guide (EIG) (Dingle 1987). This allows the mass spectrometer to be operated at reduced voltages if desired. At low voltages, when the EIG was at 0V no signal was observed, but when a small negative voltage ($\simeq$-6V) was applied signals could be obtained.

Linearity of the TOF can be measured using a carbon cluster spectrum (chapter 5). Fig 3.17 gives known cluster mass against experimentally measured mass. The experimental mass is calculated by assuming a quadratic relationship between mass and time and and an offset correction factor to be applied to each time.

Detector

The detector is a dual microchannel chevron detector made by Galileo Electro-optics (Wiza 1979). It is mounted in a housing built by Cambridge Mass Spectrometry.

The detector has a gain, when new, of 10^7. This decreases with age and currently the gain of the detector is estimated to be

Fig 3.17: Linearity of TOF using Carbon Clusters

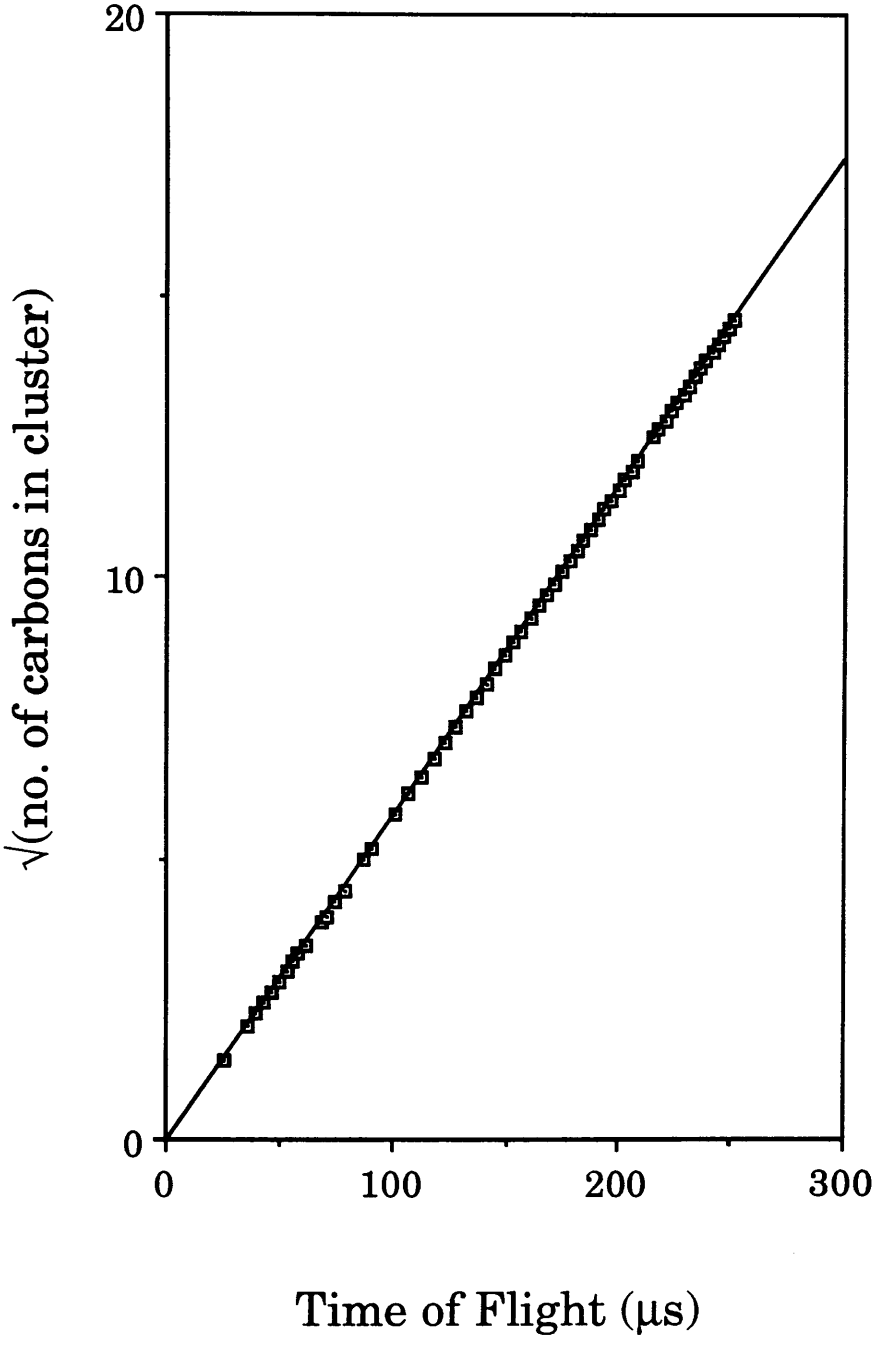

of the order of 10^5 (Towrie 1989). The detector has a specified rise time of 0.2ns.

As originally supplied the detector was biased as shown in fig 3.18a. This proved unsatisfactory (Land 1990) and the detector was rebiased as shown in fig 3.18b.

Early work on the spectrometer showed large background uncorrelated ion signals. These were determined to be due to low energy ions formed by signal ions scattering from eg. the grids in the reflectron. To remove this problem a low energy ion filter was attached in front of the detector. This solved the problem of the low energy ions but at the expense of decreasing the transmission of the spectrometer. Plate 2 shows the detector assembly together with the low energy ion filter.

§4 Data Acquisition and Analysis.

The data acquisition system is required to measure signals both from the spectrometer itself and from other ancillary equipment (laser joulemeters and hollow cathode lamps). The system must also control the timing and synchronisation of the lasers. The data acquisition equipment is shown in fig 3.19 The full timing of the experiment is shown in fig 3.20.

The equipment is controlled by a Compaq Deskpro 386/25 PC compatible (Compaq Computer Corperation, USA). This was connected via a GPIB interface (National Instruments, USA) (IEEE 1978) to a LeCroy 8901A CAMAC to GPIB interface (LeCroy, Spring Valley, NY, USA) (IEEE 1975) and a Stanford DG 535 Digital Delay/ Pulse Generator (Stanford Research Systems, Sunnyvale, CA, USA). The computer runs custom software which enabled data acquisition and analysis. This software was written by the author and is described fully in Chapter 4.

The LeCroy 8901A is housed in a LeCroy 8013 CAMAC crate, which provides 13 CAMAC slots (LeCroy 1984). Also housed in the 8013 is a LeCroy 2259B 12 channel 11 bit peak sensing analog to digital converter (ADC) and a LeCroy 2261

Fig 3.18a: Original Detector Biasing

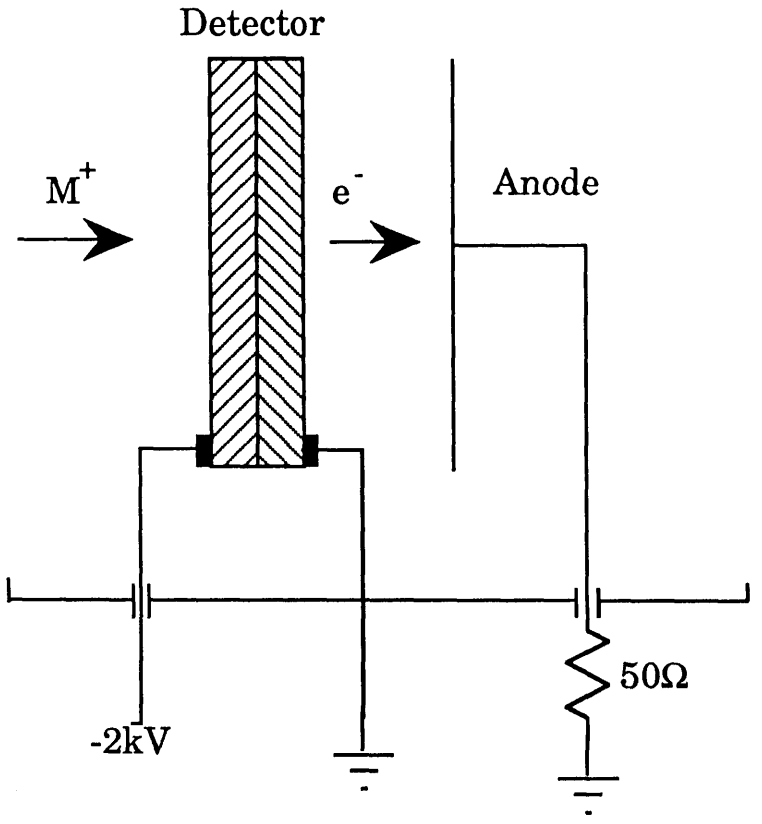

Fig 3.18b: Modified Detector Biasing

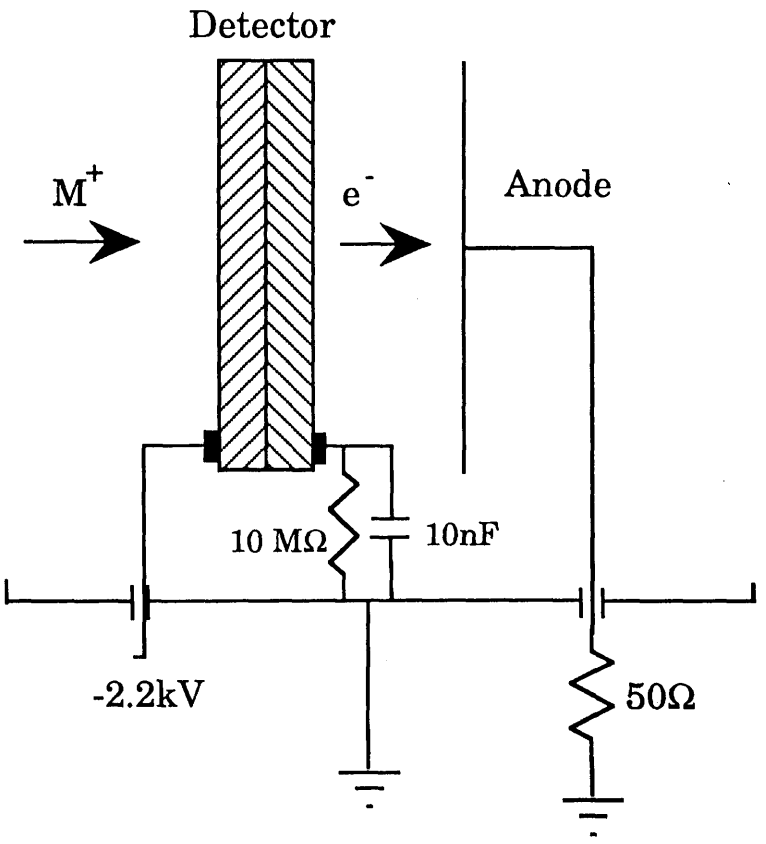

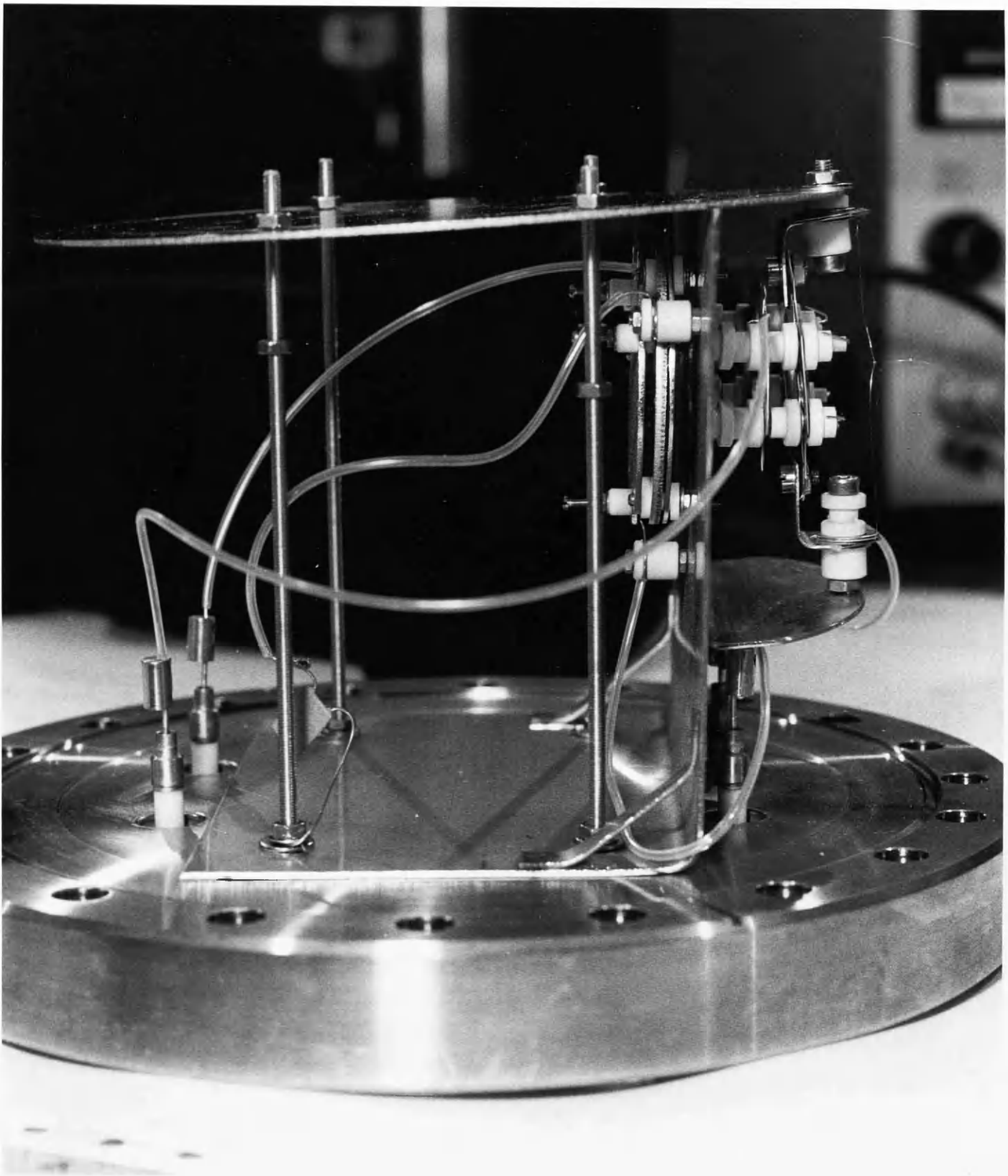

Plate 2. The dual CEMA detector and low energy filter assembly

Fig 3.19: Data Acquisition Equipment Layout

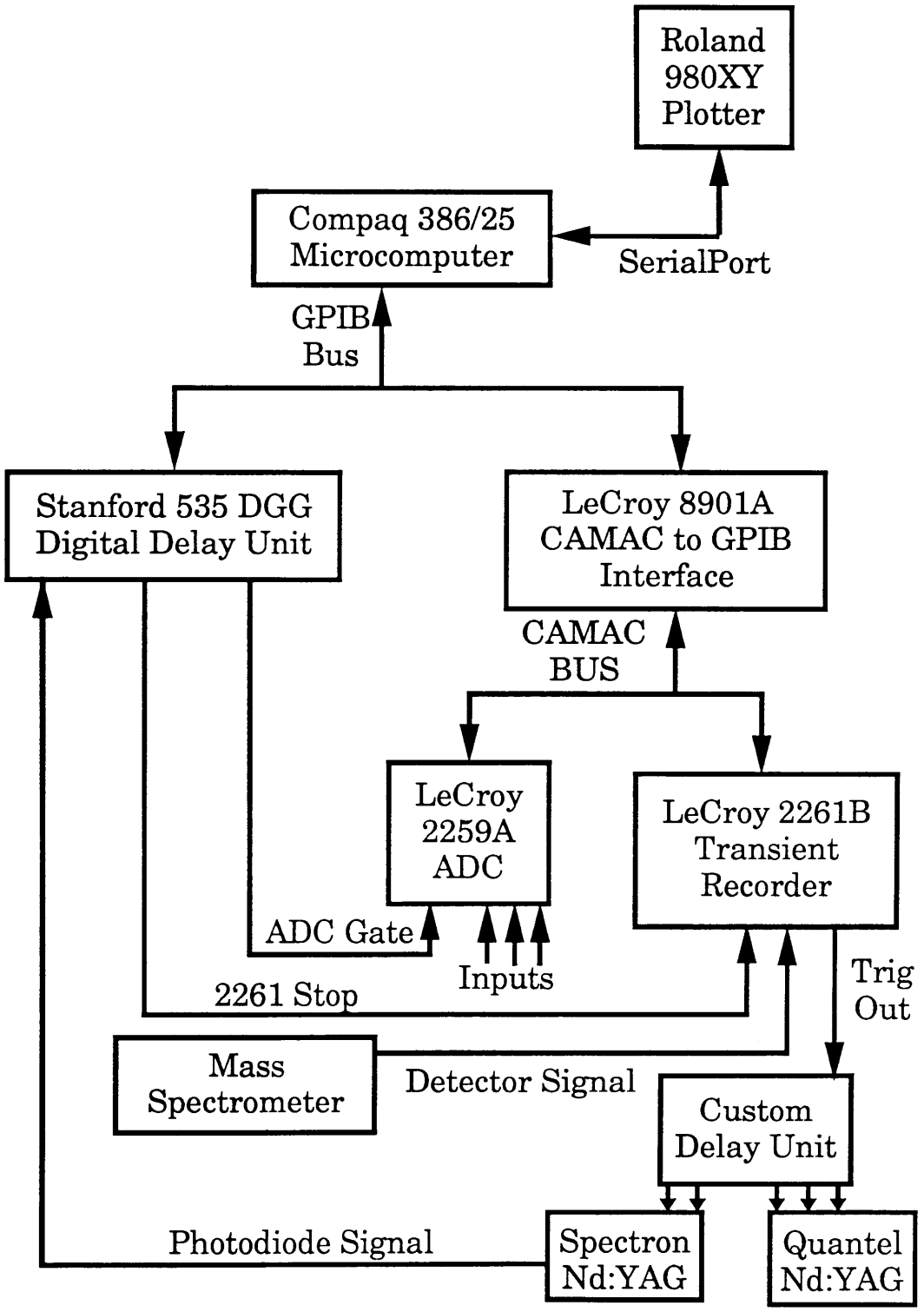

Fig 3.20: Data Acquisition Timing

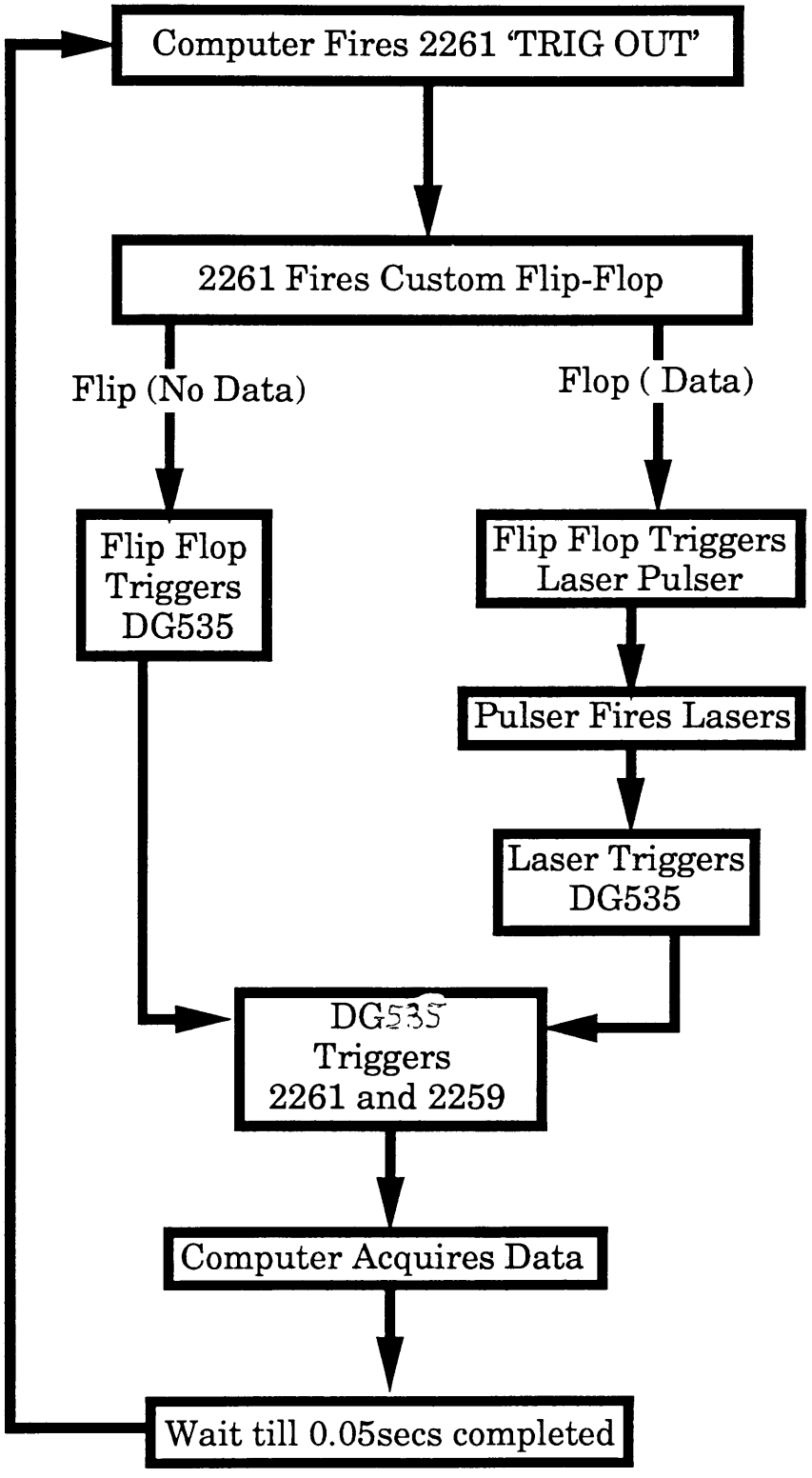

image chamber analyser, which operates as a transient digital recorder (TDR).

The Stanford DG is used to provide the timing required to operate the LeCroy ADC and TDR. This instrument has four outputs which can be used to give a precisely timed edge after a trigger pulse is accepted by the unit. The trigger pulse, and the zero time for the ADC and TDR, is provided by a fast photo diode operating from the resonant ionisation laser.

The 2261 was used to acquire signals from the spectrometer. If the signal was too small then amplification (LeCroy VV100B X10 pre-amp) could be used. The 2261 functions as a transient digital recorder, allowing 0.1 to -1.9V signals to be digitised with a resolution of 1mV and a speed of up to 100MHz. A time slice of 640 10ns bins is allowed in one shot, giving a window of 6.4μs at 100MHz operation. The device acts as an integrator, measuring total charge arriving in the 10ns time. The 2261 can also be run at 40MHz, 20MHz and 10MHz, allowing time slices of 16μs, 32μs, and 64μs but poorer time resolution. The 2261 'TRIG OUT' output is used to start the experimental cycle.

By using an artificially generated test signal and a precision variable attenuator (Hatfield precision 50Ω attenuator, Hatfield Instruments, Plymouth, UK) the response of the transient recorder was measured in two different modes (fig 3.21). The first method used involved taking a baseline reading (ie. reading the 2261 without no signal being input) at the start of a run and comparing all future readings to this. All signals below a operator defined level are rejected. The best dynamic range was given by the 2261 operating in 'flip flop' mode. This mode of operation is described fully in chapter 4. It involves running the 2261 at 20Hz and using one reading to take data and one to read the current 2261 baseline. The data is then corrected for the background by subtraction and the remaining signal accumulated. From these measurements the dynamic range of the 2261 was >60dB.

With this procedure, when the instrument is operating in an analogue counting mode the correction shot by shot gives superior performance. Correction using a background reading

Fig 3.21: Linearity of 2261 TDR

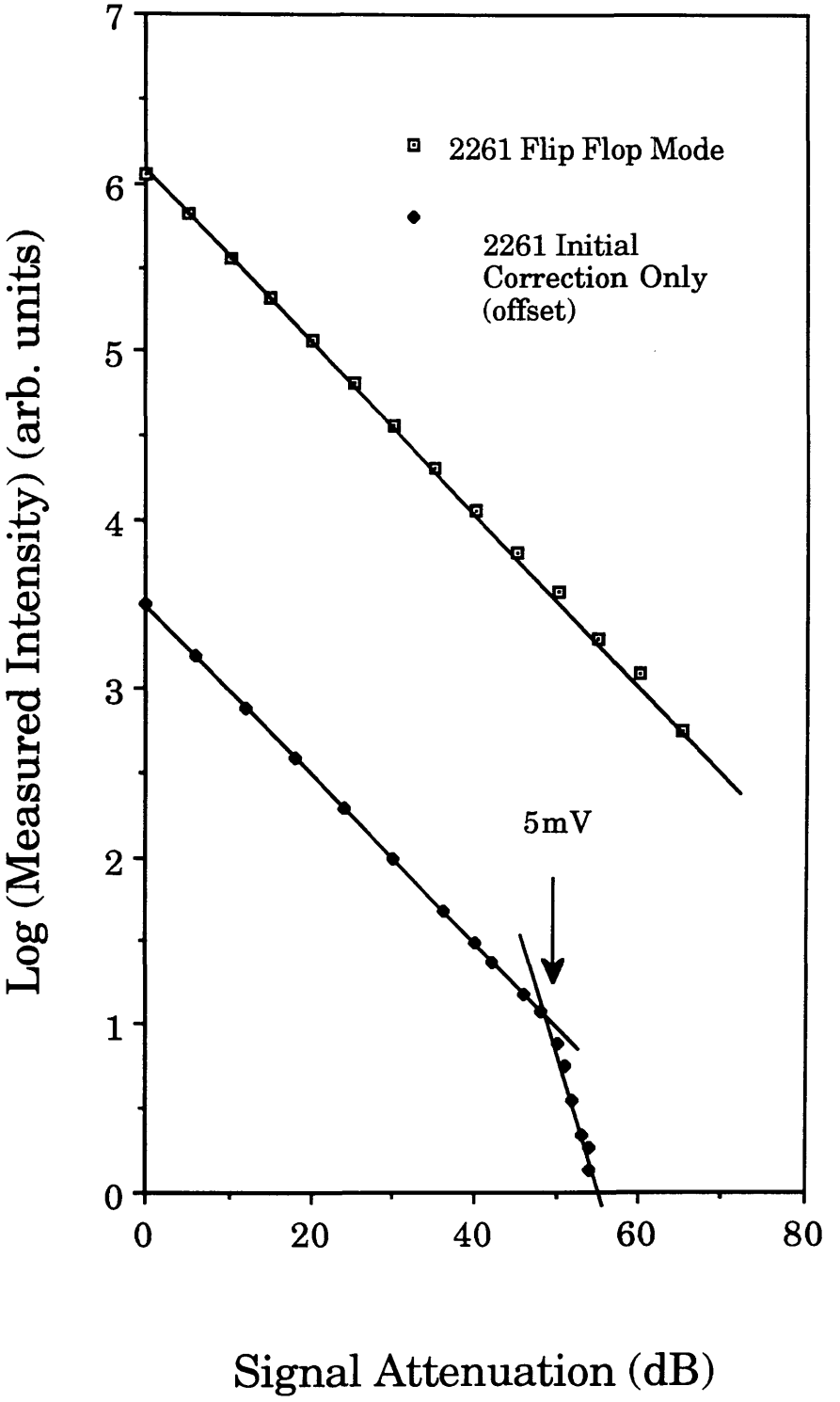

taken at the start of a run was only was used in the early stages of development before the 2261 was capable of operating at 20Hz.

By combining both methods, correcting each shot individually and using a digital discriminator, it is possible to operate in a digital pulse counting mode. This requires that the size of a single ion signal is larger than the discrimination threshold. This is only true when the detector is new and a single ion signal gives ~6mV from the detector. Presently the instrument is operated in an analogue counting mode only.

The 20Hz flip flop method is also preferred because of peculiarities in the 2261 behavior. To obtain data from the 2261 requires that each individual time bin be corrected for the baseline. The baseline is subject to not only random noise but to a large drift over a period of time. This results in a DC offset being added to the signal. The rate at which the unit is read is critical, as a difference of 1ms in the times of the 'flip' and the 'flop' parts of the measurements are readily apparent. The rate is controlled via computer, and the method used is described in chapter 4. The rate is constant to approx 50μs difference between cycle lengths.

The flip flop generator also contains a failsafe timing device. In the early work, the 2261 would display an intermittent fault, bringing the experiment to a halt. This was obviously undesirable. The problem can be solved by resetting the 2261 with an external pulse. The flip-flop unit, if it does not receive a trigger pulse from the 2261, will reset it after a small delay ($\sim\frac{1}{20}$ sec). The source of this problem is not known, but is thought to be caused by laser generated electrical interference affecting the computer/GPIB/CAMAC interfaces.

Two separate methods are currently used for data acquisition. One method, used in spectrometry, involves reading the 2261 and adding the data to a storage buffer. Data storage can be made conditional on eg. laser power. In this mode the 2261/computer combination acts as a digital storage scope acting in a summation mode. The second, used mainly for spectroscopy, involves using the corrected 2261 and integrating certain areas

of it. This gives the ion signal for that particular shot. This, together with data on laser power and hollow cathode signal, can be stored on disk. This allows a laser spectrum to be recorded. Both these mode will be fully described in chapter 4.

Data can then be analysed and hard copy obtained from the program. The analysis and hardcopy facilities are described in chapter 4.

Chapter 4: The Data Acquisition and Analysis Software

§1 Overview

The data acquisition and analysis program, called PLOT5, was written by the author during the course of his doctoral research. This chapter will detail the development of the program, provide a description of each of the major subprograms and provide operating instructions for the program.

PLOT5 is designed specifically for use with the Kratos Machine and is written in a combination of Fortran 77, machine code, and Halo '88 graphical extensions. It will run under DOS 3.3 on any 80386 based PC microcomputer containing a 80387 coprocessor, VGA graphics monitor and a mouse. Hardcopy output requires a HPGL compatible plotter.

To acquire data it requires a CAMAC crate containing a LeCroy 2261, a LeCroy 2259, a LeCroy 8901, and also have a Stanford DDG 535 digital delay generator. It is written in a modular form and can easily be extended to accept data from other instruments, such as digital oscilloscopes.

The source files for the program are contained in the diskette at the back of this volume.

§2 Development of PLOT5

The original data acquisition program was based on the LeCroy data-acquisition package CATALYST running on an IBM PC-AT. This had several disadvantages:

1) It operated too slowly (1.5Hz when the minimum requirement was 10Hz).

2) The transient digitiser (TDR) (a LeCroy 2261) and the ADC (a LeCroy 2259) were not supported by catalyst, although a user written module could be added.

3) The program operated on a single shot mode, whereas the acquisition system was required to work on a multishot summation mode.

4) Addition of non-LeCroy GPIB instruments caused unpredictable behavior of the computer, in addition to which these instruments could not be controlled by catalyst.

5) There were few facilities offered for the offline analysis of CATALYST data.

With these points in mind it was decided to write a new data acquisition and analysis program specifically for the RIMS instrument.

The first stage of the rewrite involved the writing of a program to allow the user to analyse data from the CATALYST program. This was written in IBM BASIC and was called PLOT. This was written in BASIC because the FORTRAN used (IBM Fortran V) had no provision for graphics programming, which is essential in such a user interactive program. BASIC had several disadvantages, such as a maximum of 64Kbytes for both code and data and, being an interpreted language, extreme slowness at certain points.

At this stage work was proceeding on a rewrite of CATALYST to enable the program to run at the required speed. This, in the end, proved impossible due to the slowness of the computer, and it was decided to purchase a faster micro-computer to enable the desired repetition rate to be achieved. To this end a COMPAQ 386/25 was acquired. It was also decided to upgrade the software tools at this point with the purchase of Microsoft Fortran v 4.1, Halo '88 graphics package and Borland's TASM Turbo assembler. A Roland D-XY 980 A3 8 pen plotter was also purchased to enable the production of high quality output.

A new version of the plot program was written at this point (PLOT2) which was a translation of the basic program into FORTRAN. This was originally run on the IBM-AT. When the

COMPAQ was fully functional the program was transferred and worked with little bother six times faster.

Once the COMPAQ was operational new programs, called READ2261 and SPEC, were written. These were stand alone programs and are described fully below.

PLOT3 added the convenience of a mouse interface to the program. This allowed for much greater user interaction, and made the program far easier to use.

One problem with PLOT3 was that it stored all of the current file in memory. Because of the limitations of DOS 3.3, this limited either the size of data files that could be handled or the facilities offered by the program. This problem was exacerbated by the decision to use the HALO graphics package to provide the plotter output. This offered higher quality output that could reasonable be obtained from within the program, but at the penalty of decreasing the maximum size of data file that could be handled. Another drain on the limited memory resources was the decision to integrate the two stand-alone programs, READ2261 and SPEC into the PLOT program.

This problem was circumvented in PLOT4 by using a combination of disk based and memory based storage. This allowed part of the data file to be stored in memory and part to be stored on disk, effectively removing the limit on the size of the maximum file which could be handled. Disk based access was not used exclusively for reasons of speed. PLOT4 also integrated the stand along programs into the one environment, giving more convenience to the user.

PLOT5, the current version, enhanced the speed of operation by optimising the disk access routines and tidying the user interface.

§ 3 Data Analysis Subprogram

The data analysis routines form the core of the program, from which all other functions are accessed.

Upon loading the program the user is presented with the option of either loading a file for analysis or acquiring either 2261 data or SPEC type data. If acquiring new data, the user is transferred to the appropriate subprogram, which are described below. If the user decides to load new data then he selects one of the directory files, which contain lists of related files. Each directory may contain 100 files, and there may be up to 100 directories, allowing a maximum of 10000 files. The number of current files in use at any time is usually less that 300. After selecting the the appropriate files from within the directory the file is then loaded into the machine.

Once loaded the file may be analysed. This occurs in a 'point and shoot' environment, using a mouse. In this environment, peaks may be integrated, and also characterised (ie. finding the height of the peak, the time of the peak, and the time resolution of the peak.). The area under analysis may be expanded in the X and Y directions. The plot may be calibrated with respect to the masses of the peaks.

For hard copy, the plot may be given a title, the X and Y axes can be labelled, and individual peaks may also be labelled. Hard copy may be made onto either A3, A4 or A5 paper.

Many of the facilities can be obtained via combinations of function keys instead of use of the mouse.

§4 Transient Data Recorder Acquisition Program

This section of the program is for acquisition of the data from the transient digital recorder (TDR). This was originally a separate program called READ2261. It is now incorporated into the data analysis program.

The transient recorder consists of an 11bit charged coupled device (CCD) which integrates the current arriving in each clock cycle (usually 100MHz). This conversion process happens continuously until the TDR receives a stop pulse (from the Stanford DDG). The TDR then digitises the stored integrated

current. This data is transferred to the computer via the GPIB bus.

Several problems with this procedure became apparent. Small changes in operating frequency would cause a large DC offset to be superimposed onto the data. The TDR would also stop intermittently in mid-conversion. This would also cause a DC offset, and would stop the laser systems from firing. Finally, zero volts on the input would not give a value of zero from the digitiser. The value was nominally 1024 counts, but different channels would give different values. Due to technical problems with the CCD's the signal would tend to ramp down towards the end channel, with the last channel giving a lower value than the first for the same signal.

After consideration of these problems, the following procedure was adopted:-

1) The 2261 would operate at 20Hz, with each alternate reading being a dummy or null reading (ie the 2261 would be read when the lasers did not fire).

2) The difference between an actual reading and the previous null reading would constitute the actual signal.

3) The timing would be controlled by the computer.

This procedure was successfully implemented and the program can operate at speeds of up to 20Hz. The functions that the computer carries out in the data acquisition loop are shown in fig 4.1.

Timing was the most crucial aspect of this implementation. After experimentation with software loops, which proved unsatisfactory, the timing was controlled by the computer's clock. This clock normally runs at 18.2065 Hz, but the rate can be changed by writing to the correct port on the computer. A rate of 20Hz was chosen. This has a side effect in that it makes the computer's clock run fast for the duration of the data run. Consequently the computer's time is corrected at the end of the

Fig 4.1: Functions During 2261 Read Loop

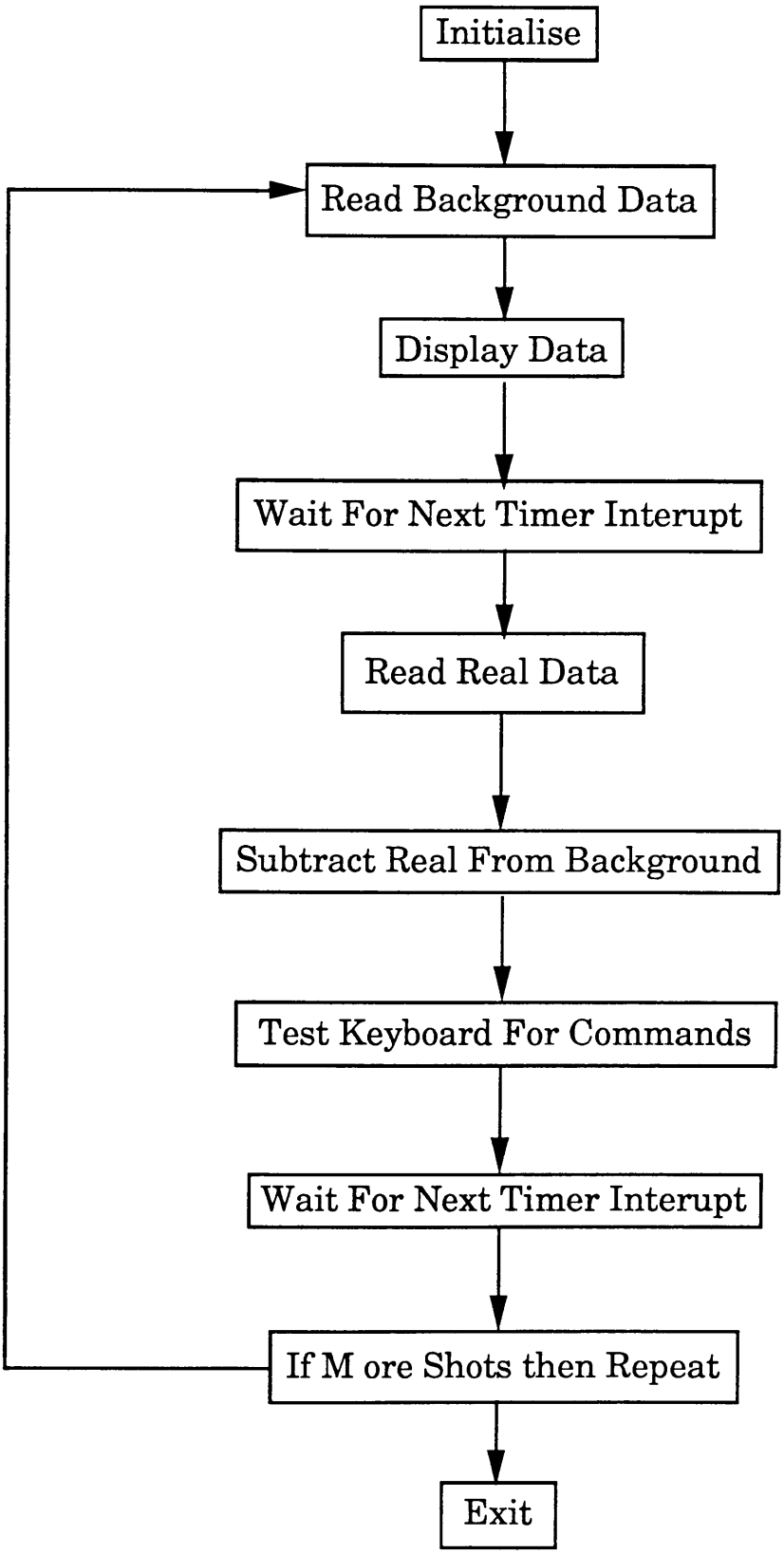

run. The routine to change to clock speed was written in assembly language.

Two other assembly language routines are required in the loop. The first corrects the raw data from the 2261 for the current baseline and adds the result to the accumulated data. The second plots the accumulated data on the screen in real time, allowing the user to see the data as it is being acquired.

§5 Spectroscopy Acquisition Program

Originally called SPEC, this was incorporated into the analysis program at the same time as READ2261.

The program takes corrected data from the 2261 as provided by the program above and, instead of adding the data to a store, adds together all of the channels of a specified peak to give an integrated signal for each shot. Thus the computer contains a record for each shot of the ionisation signal received for a specific peak. Also recorded are any other parameters that are important for spectroscopy, eg. laser power and the hollow cathode lamp signal (for wavelength determination), which are recorded from the CAMAC ADC module. The functions that are carried out during the SPEC acquisition loop are shown in fig 4.2.

The integrated signal and two channels of the ADC are displayed on screen in real time during the acquisition run.

At the end of the run the user is offered the opportunity to save the data to disk.

§6 Operating Instructions for PLOT5

To load the program select the subdirectory c:\data on the Compaq by typing CD C:\DATA. Then type PLOT5 <return> to load the program into memory.

The first screen presented shows a list of user directories and a list of options. Each user directories contains a user's files for a particular area. It is recommended that the directories are named with a name of the form **name.dir** to facilitate easy

Fig 4.2: Functions During Spec Read Loop

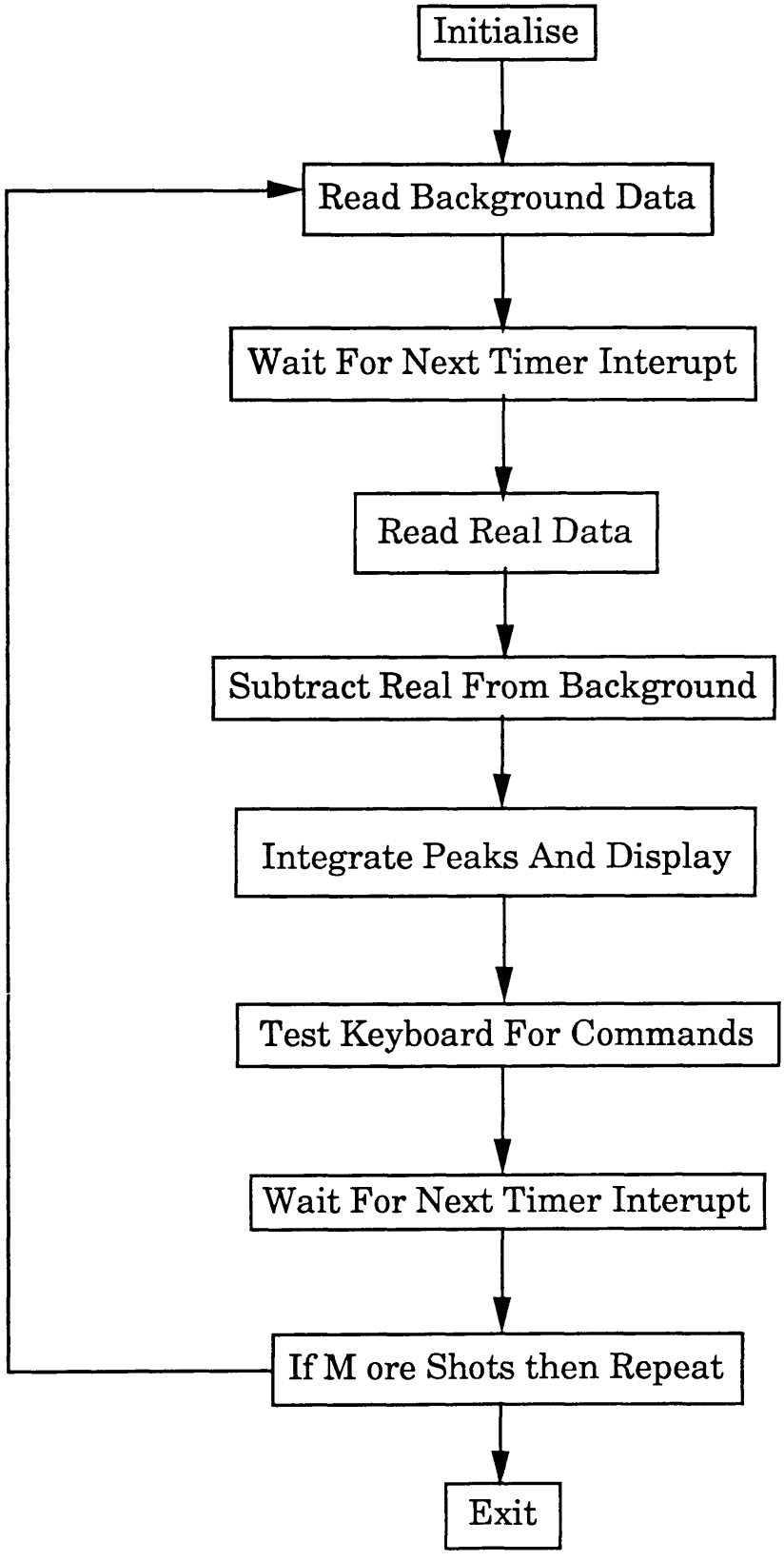

maintenance of the program. Each directory can contain 100 files and up to 100 directories are possible. The format of the screen and the options provided are shown in fig 4.3.

A mouse interface is provided. The current choice is highlighted and can be selected by pressing the left mouse button. Choices can also be selected by pressing an appropriate key on the keyboard. The key to press for any selection is shown to the left of that option.

If a directory is selected then it is opened and the list of directories replaced by the list of files from the chosen directory. As before an entry can be edited, added or deleted. The options to acquire data are replaced by an option to change to another directory and type of data to be loaded cannot be changed, otherwise operation is as for choosing a directory.

To load a file the file is selected by mouse or keyboard as above. The data is automatically loaded and the user moves to the analysis screen (fig 4.4).

The analysis screen is split into four sections: the menus bar, the data area, the access bar and the plot information area.

The menu bar lies at the top of the screen. It contains seven menu choices (PLOT, FILE, MAGNIFY, TEXT, MISC, SHOW and QUIT). Each of these produces a menu when selected and the left mouse button pressed.

The PLOT menu is a 'pop up' menu which appears in the center of the screen. The rest are pull down menus which appear below the menu bar at the position of the menu choice.

The PLOT menu contains the options for hard copy output. Plots may be made on the Roland plotter in A3, A4 or A5 sizes by selecting the appropriate icon on the menu with the mouse and pressing the left button. The colours that the plot will appear in can be changed by selecting the pen icons with the mouse and entering the new pen stall number. Since the software has no way of knowing if a pen is present the user must ensure that there is a pen in the stall or the plot will appear incorrectly.

Other options are to plot the data as either a time or a mass spectrum. To plot as a mass spectrum the spectrum must be calibrated by means of the CALIBRATE MASS option. Data only may be plotted so that multiple spectra can be plotted easily onto a single page.

All the following menus can be operated in "short cut" mode where function keys can be used to select options as opposed to using the mouse. The plot menu can be brought up by pressing <F1>, the file menu by <F2> through to the QUIT menu by <F7>. Except for the plot menu, each option can be selected by pressing the appropriate function key, eg the READ2261 option, which is the third option in the FILE menu, can be selected by pressing <F2> followed by <F3>. The plot menu can be brought up using <F1>. All other options have to be selected with the mouse but a plot can be made immediately with the current settings by pressing <RETURN>. In common to all menus is pressing <ESC> to abort the current action. The same effect can be achieved by clicking on the option in the main menu bar eg. clicking on FILE once will bring up the menu, clicking again will remove it.

The FILE menu contains options to load new data, change the channel if the current data type is SPEC, and to acquire either READ2261 or SPEC type data.

The MAGNIFY menu contains the options that change the Y magnification of the data. Most are self explanatory. The option MOUSE SELECT is used to allow the user to change the vertical magnification by means of the mouse. Usually this is not advantageous but it can on occasion be of use.

The next menu option, TEXT, allows the user to annotate plots. It only affects the plotter output. A title for the plot, an X axis label and a Y axis label can be entered. These are all placed in predefined positions outside of the data area. Labels can also be entered. When a label is entered the user is asked to give a position for it on the data area. These labels are typically used to

name peaks. Subscripts and superscripts are allowed. The label can be a maximum of 10 characters long.

The MISC (miscellaneous) menu is next. The first choice is to CALIBRATE MASS. This allows a true mass spectrum, as opposed to a time spectrum, to be plotted for time of flight data. To use two peaks must be selected, using the mouse, and the mass of these peaks must be entered. The computer can then calibrate the rest of the spectrum. the calibration works by assuming that the mass of a peak is proportional to "real time" squared which differs from the time associated with the peak by a constant time. ie

$$m = k(T+ t)^2$$

This means that two unknowns are present, hence the need for two peaks. This procedure works well up to masses of several kiloDaltons.

For SPEC type data linear wavelength calibration is required. The program operates as above except the relationship is assumed to be linear.

TEXT SIZE, as its name suggests, allows the size of the text appearing on the plot to be altered.

FONT SELECT allows different fonts to be used in plotting data. It is recommended to use the default text for two reasons: speed, as some of the other fonts take a long time to plot out, and clarity especially in the A4 and A5 sizes, since the other fonts are generally thicker and harder to read at small sizes.

DATA OFFSET is used primarily when plotting multiple files on one sheet to avoid overlapping different data.

SMOOTHING is used for SPEC type files for two reasons. It increases plotting speed by a factor of five and it enables easier interpretation of the data. The original idea for a smoothing routine was to have a Fourier transform routine acting as a low pass filter. This was impossible to implement within the program because of memory limitations. A simpler binomial smoothing is

used. Any odd order smoothing is allowed. The algorithm works by weighting each point by a binomial coefficient depending on how far away from the centre point it is eg.

$$n_i' = (n_{i+2} + 4n_{i-1} + 6n_i + 4n_{i+1} + n_{i+2}) / 16 \qquad (4.1)$$

where n_i' replaces each data point n_i. This is a quick solution, requiring very little data memory space and very little code.

The last option on the MISC menu allows the user to turn off the integrate feature. When the data file is longer than 16000 points then not all the data is stored in memory at once. When zooming in on a certain area of data it is sometimes the case that the section selected will contain more than 16000 points. In this case the program is continually accessing the disk in order to integrate the area selected.and this slows down the program unacceptably. By turning the integration facility off, the program speed is acceptable.

The SHOW menu allows the user to preview the plot output. Since the same graphics system is used for both screen and plotter the screen representation is accurate to the resolution of the screen. This option also allows the user to move labels on the plot area, allowing for more accurate labeling of peaks.

SHOW NEG DATA. Usually the bottom of the screen corresponds to zero. However it is sometimes desirable to see negative values. When this option is used the bottom of the screen becomes the lowest value data point, unless all points are greater than zero in which case the bottom remains zero. When selected the menu changes to SHOW POS DATA, which restores the base to zero. SHOW BASELINE, which appears on the menu after the SHOW NEG DATA is selected, shows the zero level on screen. When SHOW NEG DATA is on, the zero level of the data is always visible on screen, regardless of the magnification.

The QUIT menu contains just two options: QUIT and DONT QUIT. These are self-explanatory.

At the right hand end of the menu bar are four arrows. The "up" and "down" arrows control the magnification of the data. Selecting "up" will increase the magnification by 2, "down" decrease by 2 ie "up" changes 10X to 20X, and "down" 10X to 5X. The "left" and "right" arrows allow the position user to change the data viewed. Selecting one of these moves the view on the appropriate direction by the width of the window. ie if the data being viewed is from 40μs to 50μs, selecting the "left" arrow will change the view to 30μs to 40μs, and the "right" to 50μs to 60μs.

The main data area shows the data versus time. The individual data points are joined up to facilitate easy viewing. When the mouse is on the data area the time that the position of the mouse corresponds to is shown in the information panel at the bottom. Mass or wavelength are also shown if calibration has been carried out.

The plot can be expanded along the time direction by use of the mouse. Firstly, position the mouse at one side of the section to be expanded. Hold the left mouse button down. When the mouse is moved a rectangle appears on screen. Move the mouse until the section to be expanded is within the rectangle. Then press the right mouse button. The expanded area is shown in the data area. If the MOUSE ON option is selected in the magnify menu the rectangle is expanded to fill the screen, with expansion in both the X and Y directions.

A similar procedure is used for peak integration. The peak to be integrated should be enlarged to a convenient size using the procedure above. A rectangle is then drawn under the peak. The peak integral given is the area above the lower horizontal line and between the vertical lines. Also given is the width of the integrated area. This information is given at the bottom of the screen in the information panel.

By positioning the mouse under the peak and pressing the right mouse button the 'peak parameters' are shown. These are the maximum height of the peak, the full width half maximum

Fig 4.3: Load Data Screen

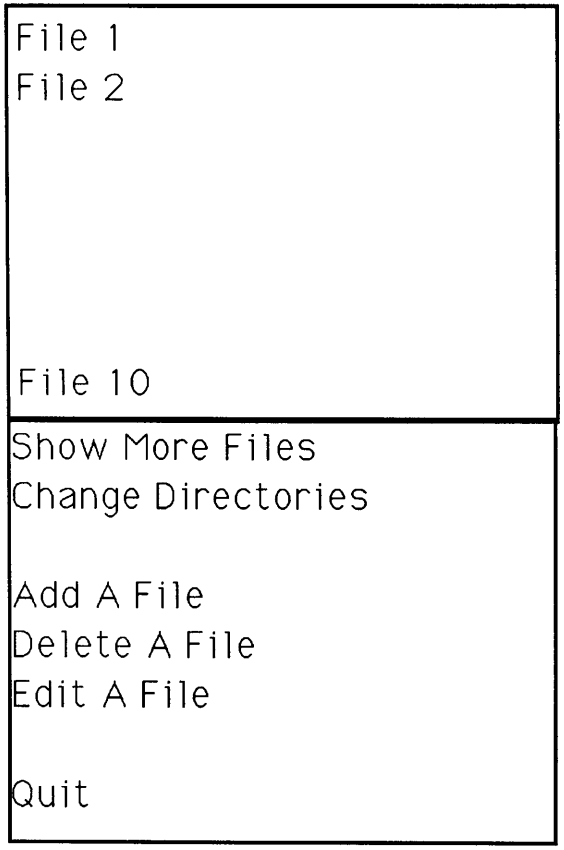

Fig 4.5: Read2261 Option Screen

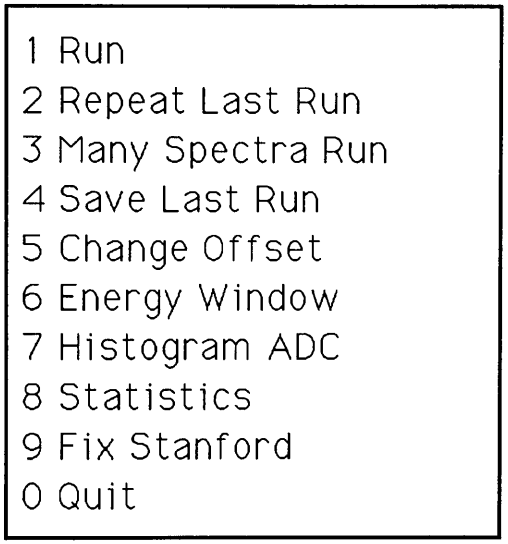

Fig 4.4: Plot Analysis Screen

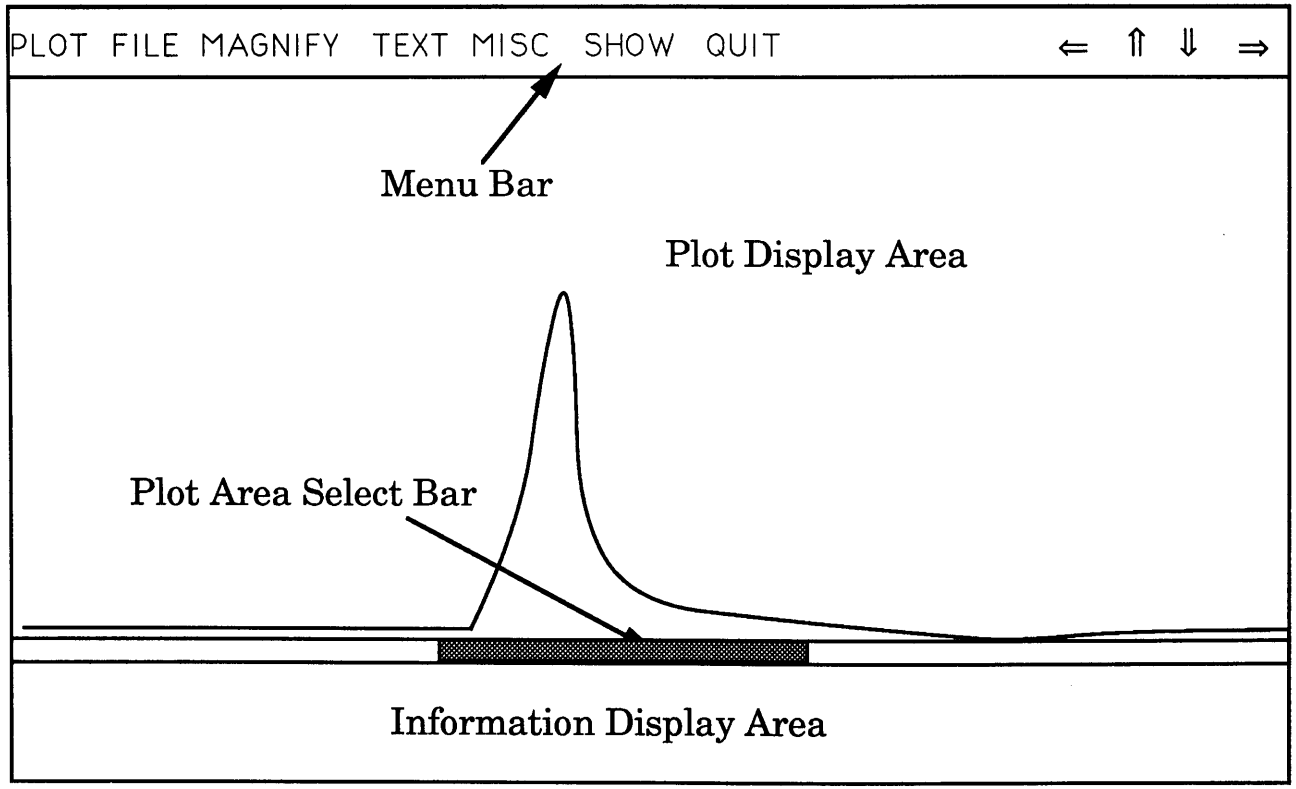

of the peak and the resolution of the peak (defined as time of peak divided by FWHM). This is displayed in the information panel.

The area immediately below the data area is the access bar. This shows the area of the plot currently displayed as a proportion of the entire file. If the mouse is moved onto this bar, any time in the file can be selected by pressing the right button. This allows zooming out from a peak.

The bottom of the screen is occupied by the information panel. This contains, from left to right, the filename and the start and finish times of the file, the start and finish times of the current window, the largest and smallest data values, data from integration and peak statistics and on the right the current magnification, time and mass.

Access to the data acquisition functions is controlled from the file menu. When one of these functions is selected the screen is cleared and a new menu is presented.

The READ2261 menu is shown in fig 4.5. The first option is RUN. This prompts the user for the number of shots to be acquired. A reminder to reset certain equipment is then shown. The data is then acquired. Two hundred shots are taken before acquisition of the data to allow for warm up of the lasers. The screen is cleared and the data acquired is shown in real time during acquisition. The vertical scale can be magnified to show low level features and recontracted to show the full scale. Rescaling can be carried out automatically by pressing <a> and disabled by pressing <d>. Pressing <shift> + <z> will clear the current buffer. The run can be terminated at anytime by pressing <t>.

Upon completion of the run the final data is shown. Pressing any key will advance the user to the file menu screen. This is the same as the file menu for loading data except the only options are to save the file just acquired to a directory or to add a new directory. The screen may be quit by pressing <esc> or selecting the exit option, in which case the file is not saved. When a directory is selected then the user is asked to type in a file name.

The second option is to repeat the last run. This saves any repetitive entering of the same options.

The MANY SPECTRA RUN option is third. This allows a series of spectra to be acquired one after another. There are two main uses for this option. The first is to acquire a long time of flight spectrum. Since the transient digitiser is limited to a 6μs window under normal conditions to acquire a long spectrum it is necessary to acquire several spectra consecutively, with the time of each spectrum advanced on its predecessor by 6μs. This can be accomplished automatically by the program. The second use of this function is to acquire data repetitively from the same time, but changing an external variable eg the time delay between the ablation and post ionising lasers, or laser power.

A series of questions is asked before the commencement of the run. First the time increment between spectra is asked. This is to ensure that the time is incremented properly by the computer on the Stanford DDG. The number of spectra and number of shots per spectra are asked for next. The clock rate of the 2261 is also required for reconstruction of the data. A file name for the data is required at this point as the data is saved to disk as the run proceeds. Finally the user is asked if the Stanford DDG timer should be incremented after each run. This is to enable repetitive taking of the same data. The data taking proceeds as before.

An option to change the offset is next. The offset is the amount that the data has to exceed to be considered relevant. It is only used where the size of a single ion signal from the Kratos machine is larger than 10mV. Otherwise it acts to filter out low signals. The problems caused by this are described in chapter 3 §4.

The next option is ENERGY WINDOW. This allows the user to input a signal into channel 11 of the ADC, and a decision to add data to the store or not is taken on the basis of the signal size. This option lets the user enter the lower and upper values for this decision. If the channel 11 signal is outwith these limits then the data acquired for that shot is not added to the store. This was

provided to try and eliminate inaccuracies caused by variations in ablation laser power.

HISTOGRAM ADC is an option that lets the user collect data from the ADC to find the range of values that the ADC channel normal returns. It works in conjunction with the next options, STATISTICS, which allows rudimentary analysis of the ADC data.

The last option QUIT returns the user to the main file selection screen.

The SPEC program is similar. Upon entering this section, the user is asked a series of questions about the data to be acquired. The information required is the clock speed of the 2261, stop time of the spectra, the time of the center of the peak to be integrated, and the width of this peak.

Most of the options are as READ2261 (eg RUN, REPEAT LAST RUN, MANY SPECTRA RUN). DISPLAY SCREEN shows the last acquired spectrum, SAVE LAST RUN saves the spectrum and CHANGE PEAK allows the peak parameters to be changed. QUIT operates as in READ2261.

§7 Technical Details of the Program.

Table 4.1 on the following pages gives a list of subroutines and functions in PLOT5. A parameter calling list is given, together with the use. Also given are the data formats for all the files used by PLOT5.

Data Formats

In the discussion that follows some abbreviations and symbols are used. These are

«variable»	The value of a program variable
I4	Four byte integer
I2	Two byte integer
R4	Four byte real number (short real)

A full description of file types (ie. record binary etc can be found in any decent FORTRAN manual eg. Microsoft Fortran Language reference (1986))

Each data file stored on disk is stored in blocks of four bytes as a binary record file. The first twenty bytes are reserved as a header to allow reconstruction of the data. The header is shown in the table 4.1 below. All variables are I4 or R4.

Table 4.1: Header Formats

File Offset	2261	SPEC
1	-1 or -3 (1)	-2
2	length	length
3	biggest	num chans
4	smallest	numshots
5	clock	clock
6	stoptime	stoptime
7	mass cal	wave cal
8	**const**	**const**
9	**corr**	**corr**
10	numspec	NA
11	numshots	Big#1 (B1)
12	N/A	Small #1 (S1)
13	N/A	B2
14	N/A	S2
15	N/A	B3
16	N/A	S3
17	N/A	B4
18	N/A	S4
19	N/A	B5
20	N/A	S5

(1) -1 is used when a single mass spectrum is stored, -3 when multiple spectra from the 2261 are stored.

The header is followed by data in specific format for each file type:

1) A Mass Spectrum has a one block of I4 data giving a total of «length» data points.

2) Multiple Spectra has «numspec» blocks of 640 I4 data points each.

3) SPEC data depends on the number of channels.

2 channels (1 record, all I2)	Peak, ADC11
3 channels (2 records, all I2)	Peak, ADC10, ADC 11
4 channels (2 records, all I2)	Peak, ADC9, ADC10, ADC11

4) During the acquisition the SPEC data is saved after each shot and data is stored in a file with format as 3) above without a header. This file is stored on the fast virtual disk.

5) Data file used in Data Analysis. This file has no header and is stored on the fast virtual disk.

«Length» data bins (all I4)

Full source code for the program can be found in the diskette at the rear of this volume.

Table 4.2: Subroutines and Functions in Plot 5

Name	Parameters	Functions		Notes
abtime	m x	displays absolute time when mouse is on access bar	Fortran	
addfil	thisdir, fname	adds a directory to a master directory	Fortran	
alpnum	code	Tells if a ASCII code is a character or number	Fortran	
amort	t	Changes a mass or time to a data position	Fortran	
annot1	none	Displays the information panel (IP)	Fortran	
binomial	m,b	calculates binomial coefficients	Fortran	
ccqrd	CAMAC vars	quick read data from CAMAC crate	Fortran	1
ccrd16	CAMAC vars	reads a word from CAMAC crate	Fortran	1
ccwr	CAMAC vars	write instructions to the CAMAC crate	Fortran	1
cheight	m y	changes mouse pos to height	Fortran	
chgoff	isig	change the offset in Read2261	Fortran	
chngplot	none	allows alteration of plot image	Fortran	
cmode	mode, exist	type of cursor for cposit	Fortran	
collect	none	collect SPEC data	Fortran	
cposit	mode, cpos, exist	Shows a cursor for getlab	Fortran	
ctime	m x	changes mouse pos to time	Fortran	
dat	i	returns value of data for point i	Fortran	
dirop	choice	Shows the options on the select file menu	Fortran	
disdir	i	shows the files in current dir. on select file menu	Fortran	
disnum	*	displays a number	Fortran	
emansp	n n	displays menu in SPEC	Fortran	

enddis	none	shows SPEC data on screen in SPEC	Fortran	
endmen	n n	Displays menu in Read2261	Fortran	
endview	store, itest	shows data at end of 2261 run	Fortran	
ewindow	none	gets energy window in Read2261	Fortran	
facts	none	peak facts for integrate in SPEC	Fortran	
fimenu	action	Shows file menu on screen	Fortran	
fonttype	none	changes plotter fonts	Fortran	
gdat	flag,select	controls the load data procedure	Fortran	
getatt	none	Finds attributes of data	Fortran	
getdir	name	loads a directory	Fortran	
getlab	super, normal, sub	entry of labels	Fortran	
getnam	name, namtype, numchr, row ,col	Controls entry of text	Fortran	
getnum	numout,row,col	entry of number	Fortran	
gmouse	mf,mx,my,mb	returns mouse position and state	Assembly	
goffset	none	get offset for data	Fortran	
histadc	none	histograms ADC data	Fortran	
ilnabs	x1,y1	Fixes a bug with Halo and MS Fortran	Fortran	2
imovabs	x,y,z	Fixes a bug with Halo and MS Fortran	Fortran	2
imovhca	x1,y1	Fixes a bug with Halo and MS Fortran	Fortran	2
inddg	none	initialises the DDG via gpib	Fortran	
ingpib	none	initialises GPIB bus and devices	Fortran	
initdat	none	initialises plotter pens	Fortran	
integ	funct,mx,my	integrates peak	Fortran	
iptabs	x1,y1	Fixes a bug with Halo and MS Fortran	Fortran	2
irbox	x1,y1,x2,y2	Fixes a bug with Halo and MS Fortran	Fortran	2
isetstext	x,y,z	Fixes a bug with Halo and MS Fortran	Fortran	2

loadms	file,test	loads a READ2261 file	Fortran	
loadst	file2	loads and converts old SPEC data file	Fortran	
makeplot	action	Calls external program to provide plotter output	Fortran	
mamenu	none	Shows misc menu on screen	Fortran	
manmas	const, correct	calibrate mass	Fortran	
manyspec	store, isig	many spectra control	Fortran	
menu1	none	Shows the menubar	Fortran	
menuwork	menu choices	handles the menu control	Fortran	
mgmenu	none	Shows magnify menu onscreen	Fortran	
mort	bin	Changes a data position to a mass or time	Fortran	
mouse	row	returns a user choice to option	Fortran	
movcur	coords	shows cursor onscreen	Fortran	3
mrange	coords	limits mouse movement	Fortran	3
newdir	name, comment	makes a new directory	Fortran	
option	mess, dir numf,i	reurns user input to gdat	Fortran	
outst	ch, nx,rx	output a character to plotter	Fortran	
pand	action	alters variables that control plot size	Fortran	
PARRAY	Store, Blank	Quick plot routine for raw 2261 data	Assembly	
peakstat	mx,my	calculates peak parameters	Fortran	
plotpop	action	Shows plot menu onscreen	Fortran	
plxc	i diff	changes screen x coord to plotter coord	Fortran	
plxchange	mx	changes plot from access bar	Fortran	
plyc	i	changes screen y coord to plotter coord	Fortran	
PTOTAL	Store, Blank, Divider	Quick Plot for summed 2261data	Assembly	
putdir	name	saves the current directory	Fortran	
putext	text, row, col, col, back	display text on screen	Fortran	

putlab	labplot px py	allows labels to be moved	Fortran	
putmse	none	Shows if MOUSE MAG. is on	Fortran	
putstim	cnum pow	output x times to plotter	Fortran	
putstroke	text, x, y	displays stroke text	Fortran	
puttim	m x	shows the current time of mouse on IP	Fortran	
qumenu	action	Shows quit menu on screen	Fortran	
r2261	none	Top level of Read2261 part of program	Fortran	
read2261	store, isig, numshots, test	Controls the reading and diplaying of 2261 data	Fortran	
readdat	order, ar22261, ar2259	reads instruments via GPIB	Fortran	
ready	none	initialises GPIB intruments	Fortran	
restore	coords	restores highlighted menu option	Fortran	
reverse	coords	highlights a menu option	Fortran	
revs	coords	Combines restore and reverse for the menu bar only	Fortran	
RSETCT	none	Resets the PC clock Speed	Assembly	
savadc	none	saves SPEC type data	Fortran	
savdat	store, shots	saves single 2261 data to disc	Fortran	
savmany	fname	saves many spectra to disc	Fortran	
selchan	chan	changes SPEC channel	Fortran	
seldir	thisdir flag	chooses a directory in datacq	Fortran	
SET_PC	none	Sets colour for PTOTAL and PARRAY	Assembly	
SETCNT	none	Sets the PC clock speed to 20Hz	Assembly	
sethal	none	initialises halo environment	Fortran	
setvars	none	initialises data variables	Fortran	
shbox	coords	Used by plot menu for box drawing	Fortran	
shmenu	action	Shows show menu on screen	Fortran	3

showplot	output	preview plotter output on screen	Fortran	
smooth	none	performs smoothing of data	Fortran	
spec	none	Top level of spec subprogram	Fortran	
spload	file test	loads a SPEC file	Fortran	
splot	none	displays data on screen in data area	Fortran	
start	none	readys the 2261	Fortran	
SUMIT1	2261 data, Store, Offset	Fast add routine for odd 2261	Assembly	4
SUMIT2	2261 data, Store, Offset	Fast add routine for even 2261	Assembly	4
temenu	none	Shows quit menu on screen	Fortran	
textput	iaction	controls input of all text	Fortran	
uikey	none	returns keyboard input	Assembly	
waits	none	controls timing of data acq. loop	Fortran	
warmup	num	warms up lasers in read2261	Fortran	
wrdat	none	changes data values used by program	Fortran	
xpand	coords	expands the plot in x dirn by use of mouse	Fortran	3
ypand	action	changes vertical magnification	Fortran	
yplace	none	shows magnification on IP	Fortran	

Notes

1) CAMAC variables. The variables passed to the subroutine that call the CAMAC crate must contain three variables

n the slot number of the addressed device in the crate
f the CAMAC function
a the subaddress in the slot

Other variables are supplied to tell the subroutine the type of data and amount of data and for transfer of CAMAC data back to the main program as required.

2) Some HALO functions have no fixed data type to be passed ie they will accept floating point or integer depending on the settings of internal variables. Microsoft Fortran on the other hand expects consistancy in all functions called, which precludes calls to the same function with different variable types in the same source file. This can be circumvented by compliling a set of dummy functions in a seperate file to call the functions in one fashion, and to use the alternative call in the main source files.

3) Coords. Several functions take a list of coordinates and act upon them. These are passed as (x1,y1,x2,y2...xn,yn).

4) Fast sum routines. Two different fast sum routines are used. Each performs the same task but because of there being two different ways that the 2261 can return data, two routines are needed; one for each case. For each channel in the 2261, there are two CCDs. which are used for digitising. One converts half of the data (every odd channel) and the other every even channel. When reading the 2261 these are interleaved to give 640 consecutive data bins. To correct the data the interleaving order of these must be known, as each CCD has different characteristics. There are two possibilites: first that the CCDs were in the same order for the null reading as for the data reading, and secondly that the readings were in the opposite order. In the first case SUMIT1 is used, and in the second case SUMIT2 is used.

Chapter 5: Operation of The RIMS Instrument and Early Results

§1 Introduction

The operation of the Kratos Machine is complex. There are a large number of parameters which can be varied, and optimisation of the instrument can take several hours for a new type of sample. For samples of a similar type generally the machine is robust and does not need any optimisation between sample changes.

Basic principles of time of flight mass spectrometry are discussed in §2.

One of the most important facets of the machine's performance is the behavior of the ion extract optics. As previously mentioned optimal performance depends on the sample being either small enough not to perturb the fields if the sample is insulating, or the sample being, or being made to be, conducting. Large insulating samples lead to the field being distorted, ion acceptance and resolution being seriously degraded. The method of making samples conducting and its consequences are discussed in §3 and §4.

Another potential problem, especially where UV lasers of wavelength less than ~270nm are being used, is background ionisation of residual gases. Work was carried out to determine the background signals from the gases prevalent in the machine. This is presented in §5.

Finally, in §6, early results from the instrument are given which show some of the capabilities which are not presented later in the body of the work.

§2 Operation of the Spectrometer

As previously mentioned, the spectrometer is a time of flight instrument. The ion time of flight depends on the ion's mass and the acceleration voltage. This can be derived as follows:-

$$eV=\frac{1}{2}mv^2$$

for a singly charged ion, where

V _____ accelerating voltage
e _____ electronic charge
m _____ mass of ion
v _____ velocity of ion

So for a flight distance d the time of flight for velocity v is

$$t=\frac{d}{v}$$

so $$t=d\sqrt{\frac{m}{2\,eV}}\propto\sqrt{m}$$

Hence time of flight is proportional to $\sqrt{m}$.

The resolution of the mass spectrometer can be defined as

$$R=\frac{t}{\Delta t}=\frac{2m}{\Delta m}$$

where

R _____ resolution of spectrometer
Δt _____ FWHM of peak at time t
m _____ mass of peak
Δm _____ FWHM of peak at mass M

For a conventional Wiley-McLaren (1955) linear TOF the resolution will be ≃ 200. A reflectron system will have resolution ≃ 2000, although resolutions of up to 10000 (Boesl *et al* 1987) have been reported. The Kratos machine has a normal resolution of ~500. This can be increased to ~1500 under certain conditions, with 2000 being the upper limit.

There are several limits to the resolution of any TOF instruments. Two important limitations in this case are the 10ns temporal resolution of the data electronics and the ~10ns pulse length of the resonant lasers. The pulse length of the post ionising laser is the most fundamental and cannot be overcome. The temporal resolution of the data electronics can be overcome by the use of more expensive digitising equipment with a faster clock speed, but since the laser pulse length is 10ns this would not significantly improve the resolution.

Three other factors degrade the resolution are present:-

The first of these is the finite ionisation volume. This can be corrected in two ways. Firstly the ionisation volume can be made smaller by focussing of the post-ionising lasers. This however decreases the geometrical overlap (ie. the proportion of the plume which is interrogated by the ionising laser) and decreases the size of the signals. This can also cause additional problems with the determination of isotope ratios as is explained in chapter 6. The second method for compensating the finite ionisation volume involves the use of Wiley McLaren type optics, which are used in this machine. These work by introducing a potential gradient in which the ions are formed. Ions formed (fig 5.1) in position A have further to go to reach the detector the ions formed at position B but are accelerated through a greater potential difference. By choosing the correct gradient the ions from A and B can be made to arrive at a detector simultaneously.

Secondly, not all ions have the same energy when formed, due to a distribution of energies in the vaporised plume. This spread of energies can be compensated for by the reflectron. The operation of the reflectron is described in chapter 3.

Thirdly, space charge effects and other consequences of a high ion density. If a large number of ions are present at any part of the ion flight path they will interact with each other and spread out temporally before reaching the detector. A similar problem occurs at high ablation laser powers. At high powers ($>10^9 Wcm^{-2}$) the formation of large numbers of ions at the sample can act to

Fig 5.1: Wiley McLaren Optics

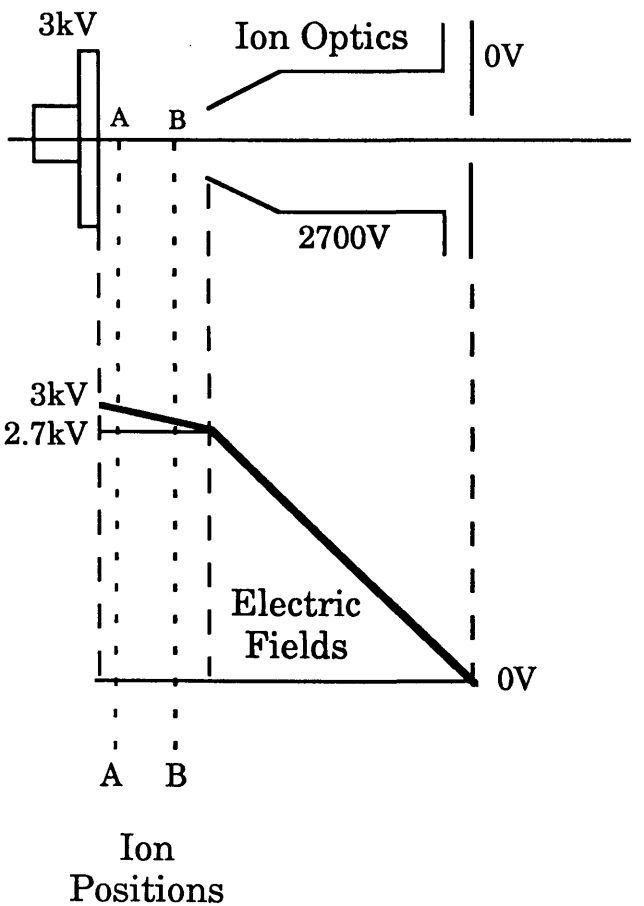

Fig 5.2: Sample Mounting for Small Metal Samples

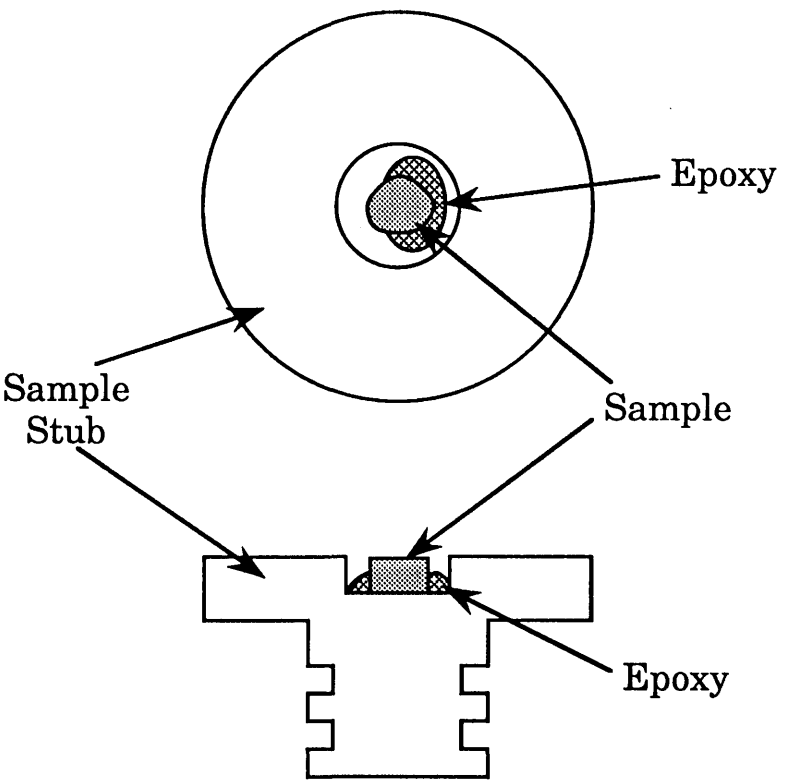

lower the effective voltage of the stub. This leads to the peaks produced being shifted in time, due to the change in accelerating voltage. Since the number of ions produced by the ablation laser varies considerably with each shot at these powers, this has the effect of changing the positions of the peaks for each shot. In accumulating data these peaks are summed and this leads to an effective lowering of the resolution of the instrument, despite the fact that the actual resolution in a single shot can be considerable better.

Mechanical misalignment problems can also lead to impaired resolution (eg the detector not being normal to the ion flight path, leading to ions in the same packet hitting at different times.).

§3 Sample Preparation

Samples were prepared for the machine in several different ways. The metallic copper samples used later in this work (described fully in chapter 7) are prepared as shown in fig 5.2. The bonding agent in this case is non-conducting epoxy. This requires that some part of the metallic sample be kept in contact with the sample stub surface. Normally conducting epoxy would be used, but the copper samples had equal amounts of trace gold and silver implanted and since conducting epoxy is loaded with silver, it was impractical to use in this instance. Samples would be cleaned before insertion into the instrument with methanol, and in the instrument by laser ablative cleaning before being used for analysis.

Large metal samples, eg foils as used in chapter 6, are attached to the surface as shown in fig 5.3. by the use of double sided sellotape. This method, despite its relative simplicity, was extremely effective, providing a easy, quick and secure method of sample mounting without noticeable charging effects.

Large nonconducting samples are ground into a powder and mixed with high purity graphite, to a proportion of 10% to 50%, depending on the sample. This allowed the sample to be conducting, although one drawback was that the concentration

Fig 5.3: Sample Mounting For Foil Samples

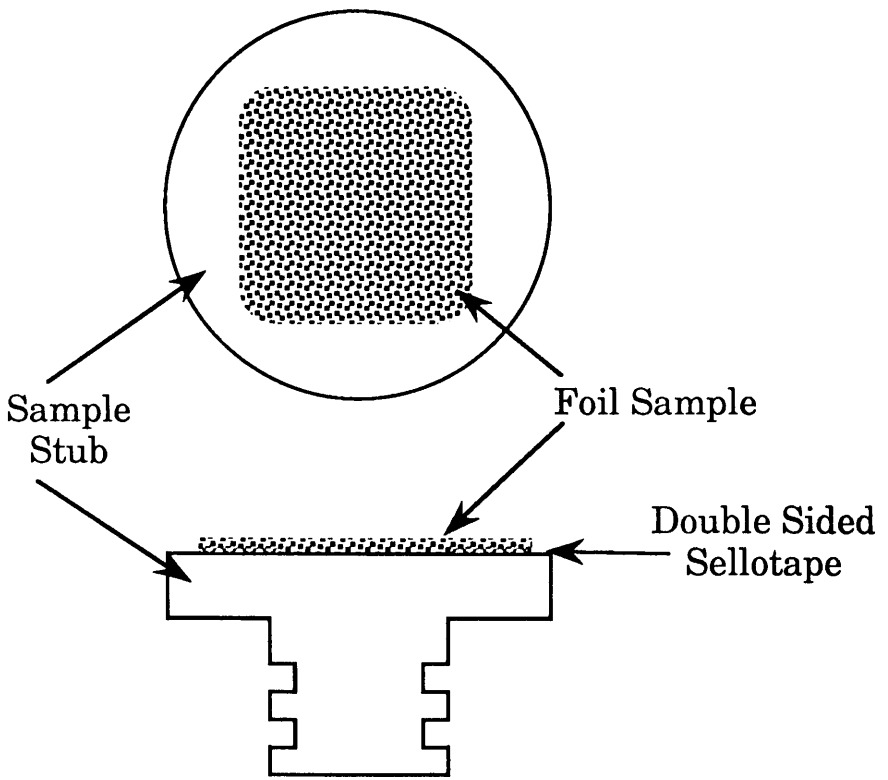

Fig 5.4: Sample Press

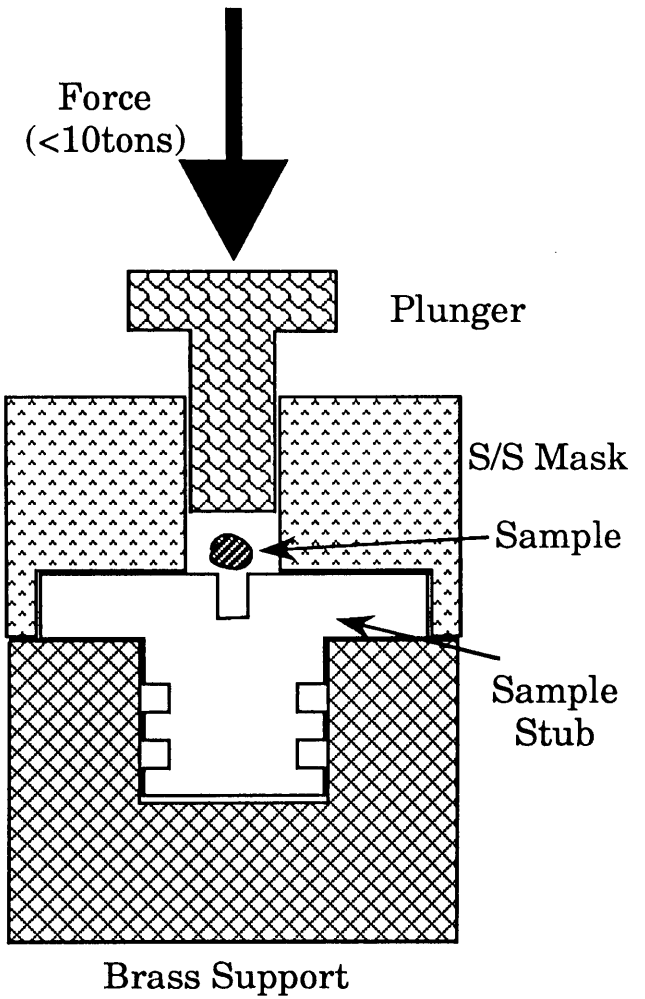

of the elements of interest was reduced. Another drawback, the formation of carbon clusters, will be discussed in the next section. The sample/graphite powder was then compressed, using either a 10-ton press or, for easily pelletisable materials, a hammer (Stanley Steelmaster 20oz, Stanley Tools, UK) in a compressor specially made for the purpose (fig 5.4), into a drilled indentation in the sample stub.

Where bulk metals were required a thin section of the metal was placed on the surface using double sided sellotape, or if the metal was soft (eg lead, calcium), the metal was compressed in the same way as a powder.

§4 Graphite Problems: Carbon Cluster Formation

One side-effect of the method used for the preparation of non-conducting samples is the formation of carbon clusters. These are shown in fig 5.5 and 5.6.

Carbon clusters are formed when the laser interacts with graphite. They are formed in the ablation process and usually only leak through to the detector in the manner described in chapter 3 §3. These spectra were taken with the machine operating in a 'primary ion mode' ie the reflect voltage being higher than the sample voltage so that the laser ablation ions reach the detector directly. The carbon cluster distribution is distinctly bimodal. The early part of the spectrum (clusters 1 to 32) are spaced one carbon apart, implying clusters of C_n where $1 \leq n \leq 32$. The second part of the distribution is carbon clusters with $n>32$ but with only even n.

The reason for the bimodal distribution is straightforward. For the monatonic clusters the structure is believed to be of the form shown in fig 5.7, with alternating triple and single carbon carbon bonds, but for the higher clusters the form is believed to be as shown in fig 5.8, with the carbon atoms forming closed polyhedra consisting of hexagonal and pentagonal rings. The closure condition restricts the clusters to even numbers of carbons. The C_{60} shown has the specific name Buckminster Fullerene (Kroto *et al* 1985, Zhang *et al* 1986, Liu *et al* 1986)

Fig 5.5: Complete Carbon Cluster Mass Spectrum

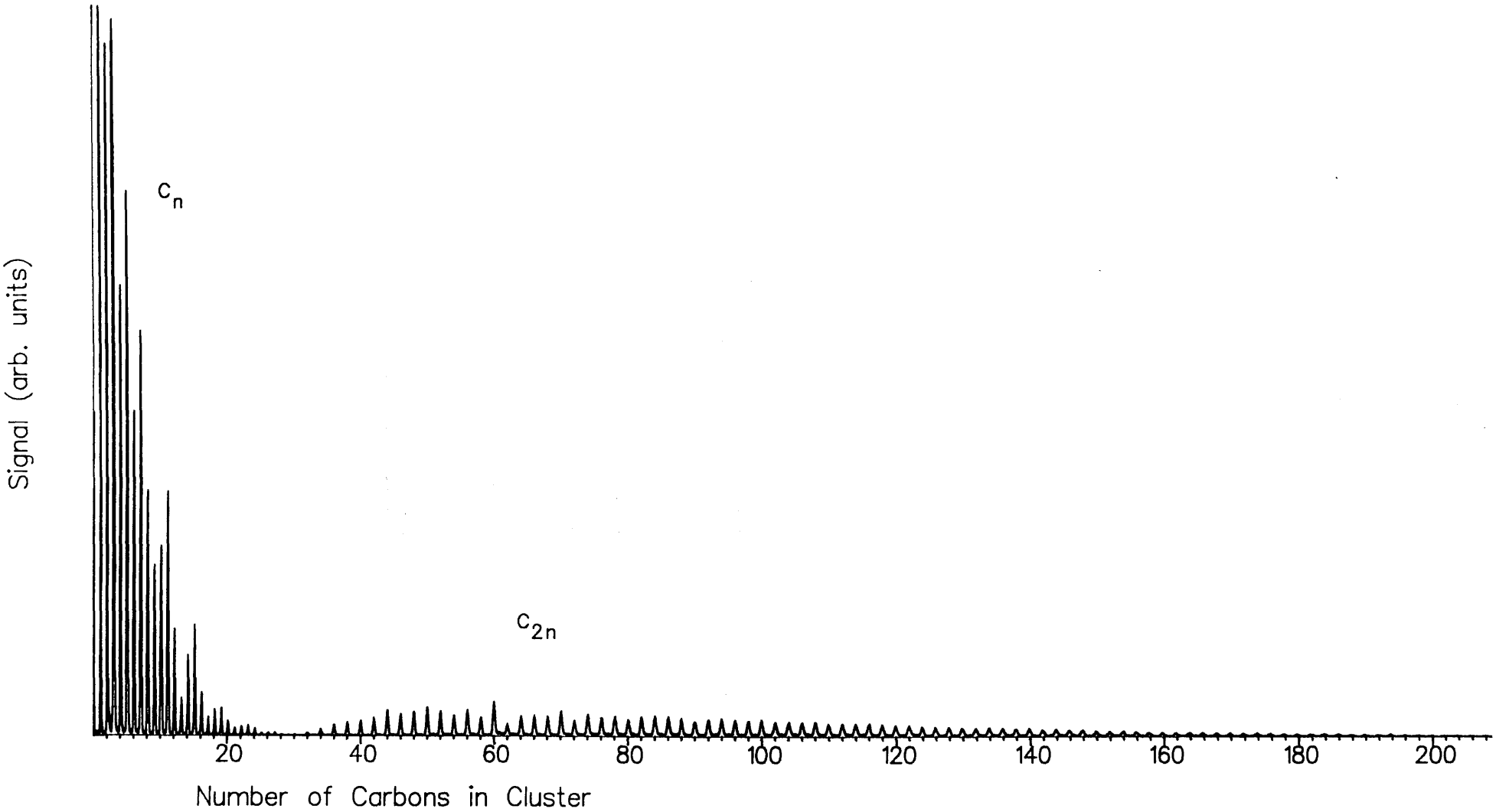

Fig 5.6: Closed Shell Carbon Clusters (Fullerenes)

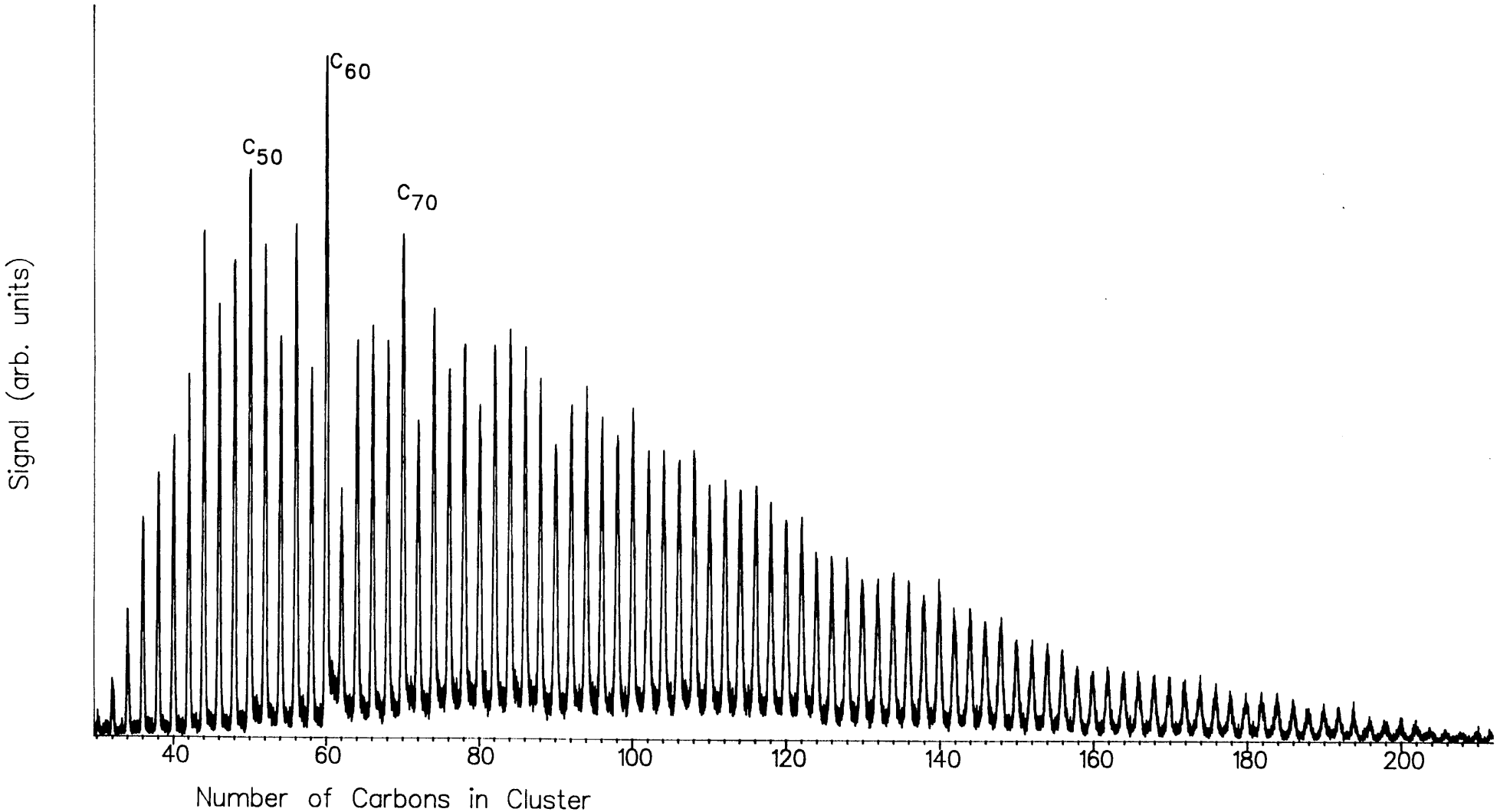

Fig 5.9: Proposed Structure of Low Number Cluster (10<n<30)

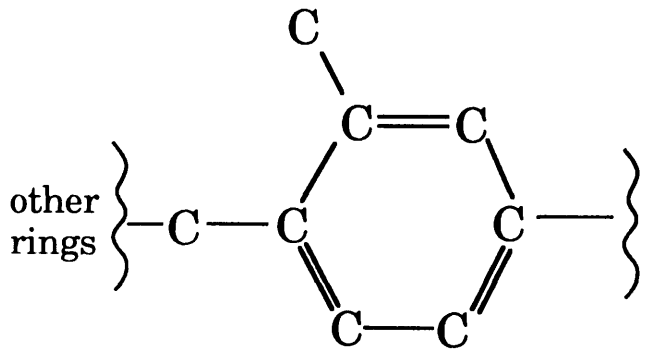

Structure is proposed to consist of a combination of ring and linear strucures

Fig 5.10: Structure of C_{60} Buckminsterfullerene

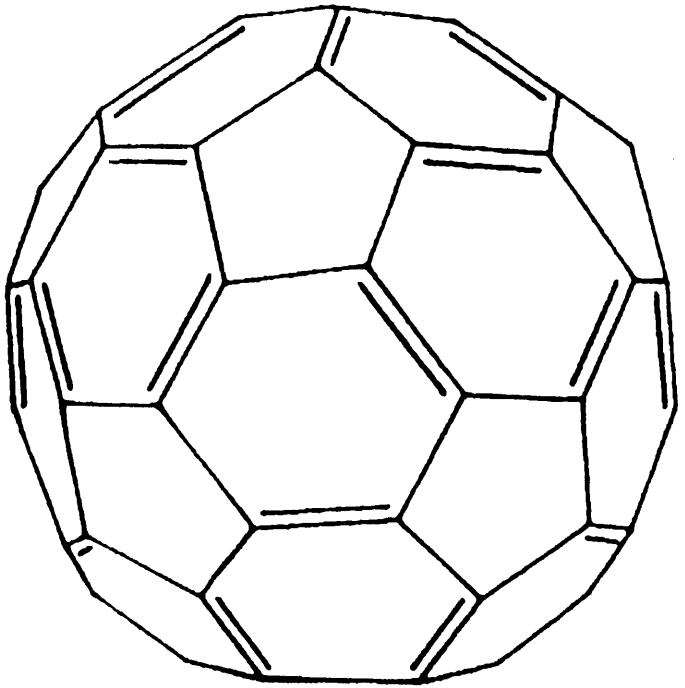

(after the originator of geodesic domes which these clusters mimic) and the family as a whole has the name Fullerenes. C_{60} is also known as footballene. C_{60} has recently been manufactured in near gram amounts (Krätschmer *et al.*1990) and their structure, as determined by X-ray and electron diffraction, appears to correspond with the predicted structure described above. C_{60} crystals (known as fullerite) have also been prepared by Krätschmer's group and are apparently stable. Thus C_{60} represents a new stable allotrope of carbon. Two other closed structure are thought to have a similar stable structure. These are C_{50} and C_{70}. These can be thought of oblate (C_{50}) and prolate (C_{70}) forms of the C_{60} structure. These clusters are indicated in fig 5.6.

The problem with the formation of the carbon clusters is the wide peaks that are formed may mask any low level signals from the element of interest. With careful selection of voltages, and by the use of low ablation powers, it is possible to eliminate these peaks almost entirely since the clusters are formed in the ablation process. Another novel solution to this problem, and to the general problem of ions produced in the ablation process, is discussed more fully in Chapter 8: Conclusions and Appendix B: Inverting Ion Optics.

§4 Background Spectra.

Background spectra in this case are the spectra that are accumulated from the residual gases in the chamber. Many of these residual gases are aromatic and they absorb laser radiation strongly in the region of 260nm. This causes ions which cause unwanted signals in the spectrometer. The effect of the gases was assessed by tightly focussing 266nm quadrupled YAG radiation of varying power and looking at the signals produced. Typical spectra are shown in figs 5.9, 5.10, which used post-ionising 266nm radiation at fluences of $4mJmm^{-2}$ and $0.4mJmm^{-2}$ respectively. This shows the change in fragmentation produced as the fluence increases. The greater the fluence the more pronounced the fragmentation. As it was desirable to determine the source of these contaminants a sample of each of the oils that

Fig 5.9: High Power 266nm Ionisation of Residual Gases

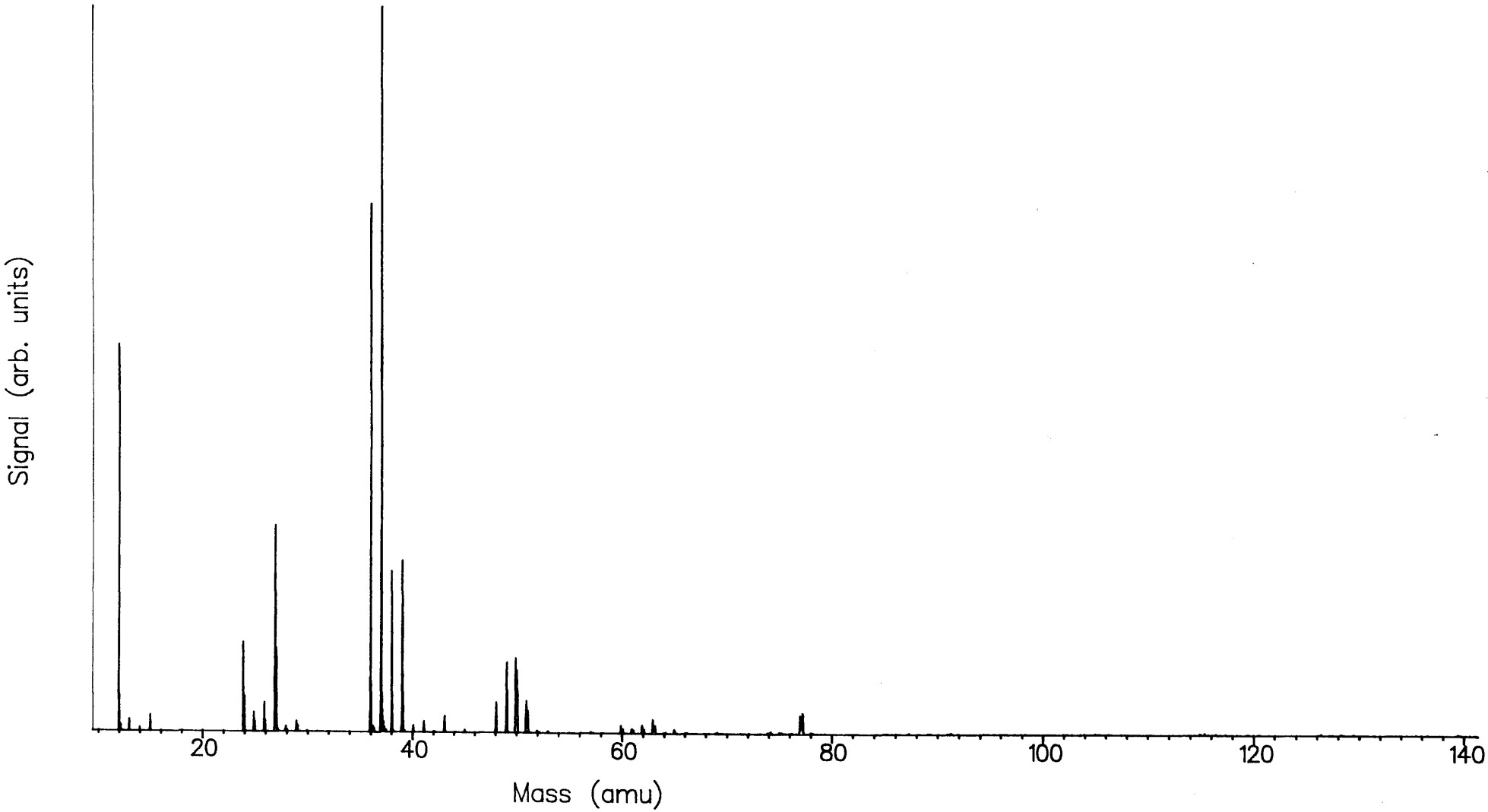

Fig 5.10: Low Power 266nm Ionisation of Residual Gases

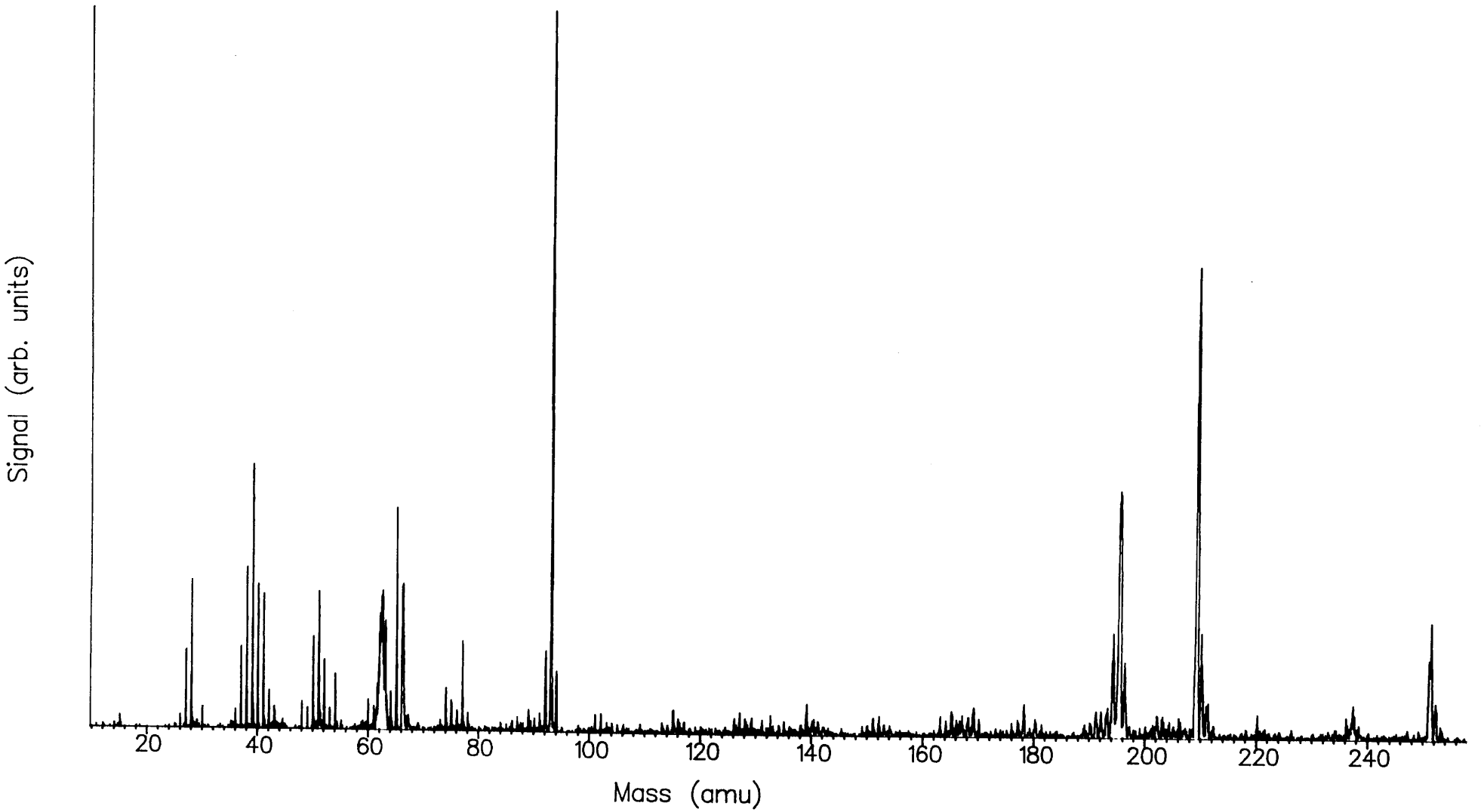

would be present in the chamber was placed in the sample insert chamber and the valve opened until the main chamber was at 10^{-7} torr pressure. The analysis of the background gas would proceed as usual. Figs 5.11, 5.12 are results from diffusion pump oil and 5.13 and 5.14 are results from rotary pump oil. Fig 5.15 shows post-ionisation of diffusion pump oil using 532nm at $250mJmm^{-2}$. As can be seen there is very little ionisation despite the extremely high power levels.

When the instrument is operating at its operating pressure and the ionisation of the background gases is very small, and is usually neglected in this work.

With the machine operating at a known pressure of a given contaminant it is possible, if the laser ionisation volume is known, to determine the transmission of the instrument, since the number of molecules being ionised is known. This assumes saturation of the ionisation process is occurring. For this experiment nitrobenzene [$C_6H_5N0_2$] was used as it was known to absorb strongly at 266nm (Fig 5.16). It was calculated that the transmission of the instrument was of the order of 0.1% (Towrie 1988).

§5 Early Studies with the Kratos Machine.

The early work on the Kratos machine was performed using two different elements: rubidium and calcium. The rubidium was chosen because it is an easy element to ionise using RIS and had been previously studied in the LIS group. Calcium was chosen because it offers a wide mass range of isotopes of greatly different concentrations.

Rubidium was the first sample to be analysed in the Kratos machine. The sample was a NBS standard coal (standard 1632a - table 5.1) mixed with 50% graphite in the process described above. The sample was ablated using Nd:YAG 532nm radiation at $1mJ/mm^2$. The ablation spot size was approximately $1mm^2$. The rubidium isotopes were not evident at this stage. The laser was tuned to 420.7nm at $120\mu J/mm^2$, which corresponds to the $5s_{1/2}$-$6p_{3/2}$ transition in rubidium (fig 5.17). The excited rubidium

Fig 5.11: Mass Spectrum of Diff. Oil with High Power 266nm

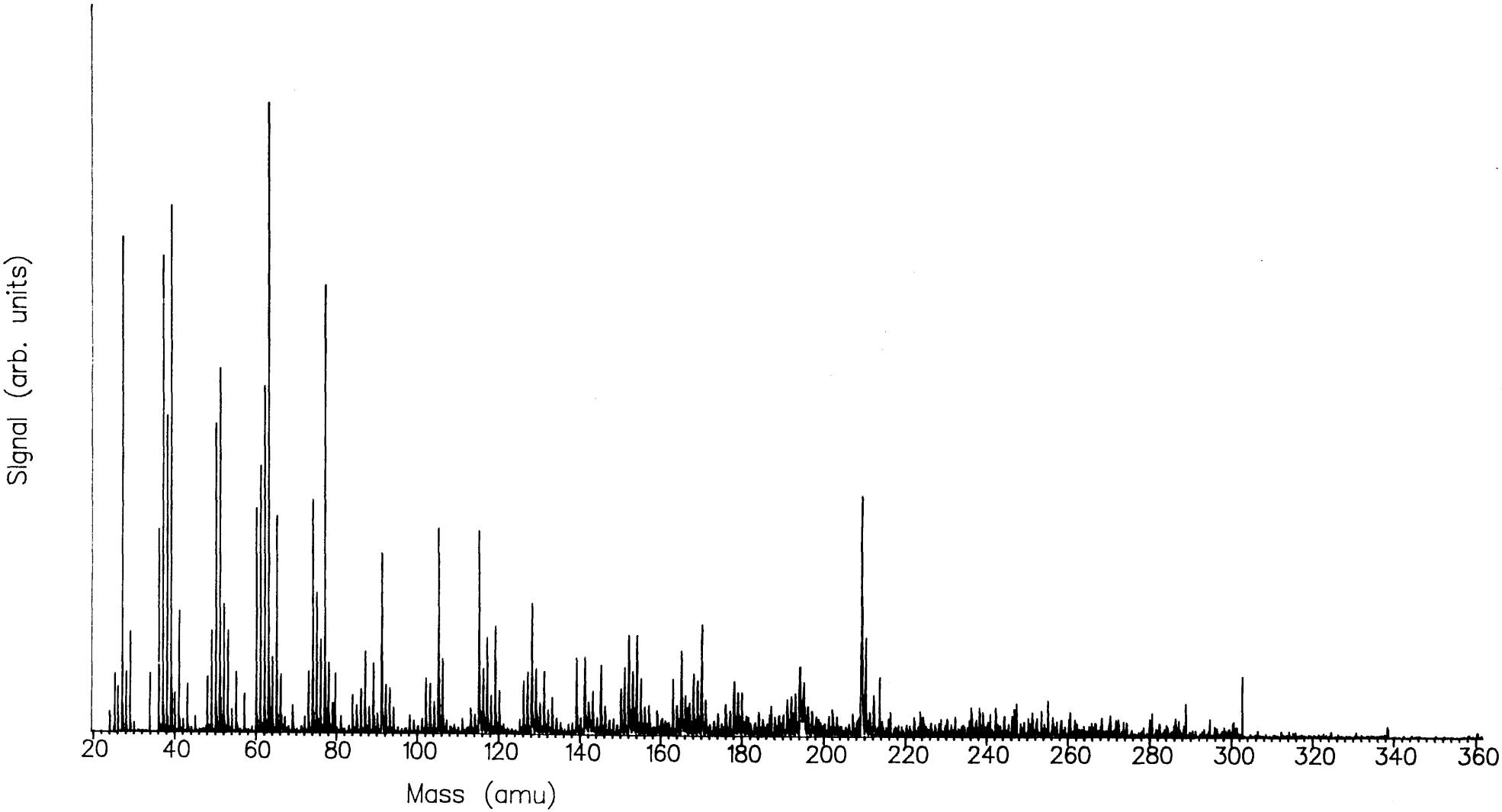

Fig 5.12: Mass Spectrum of Diff. Oil at Low Power 266nm

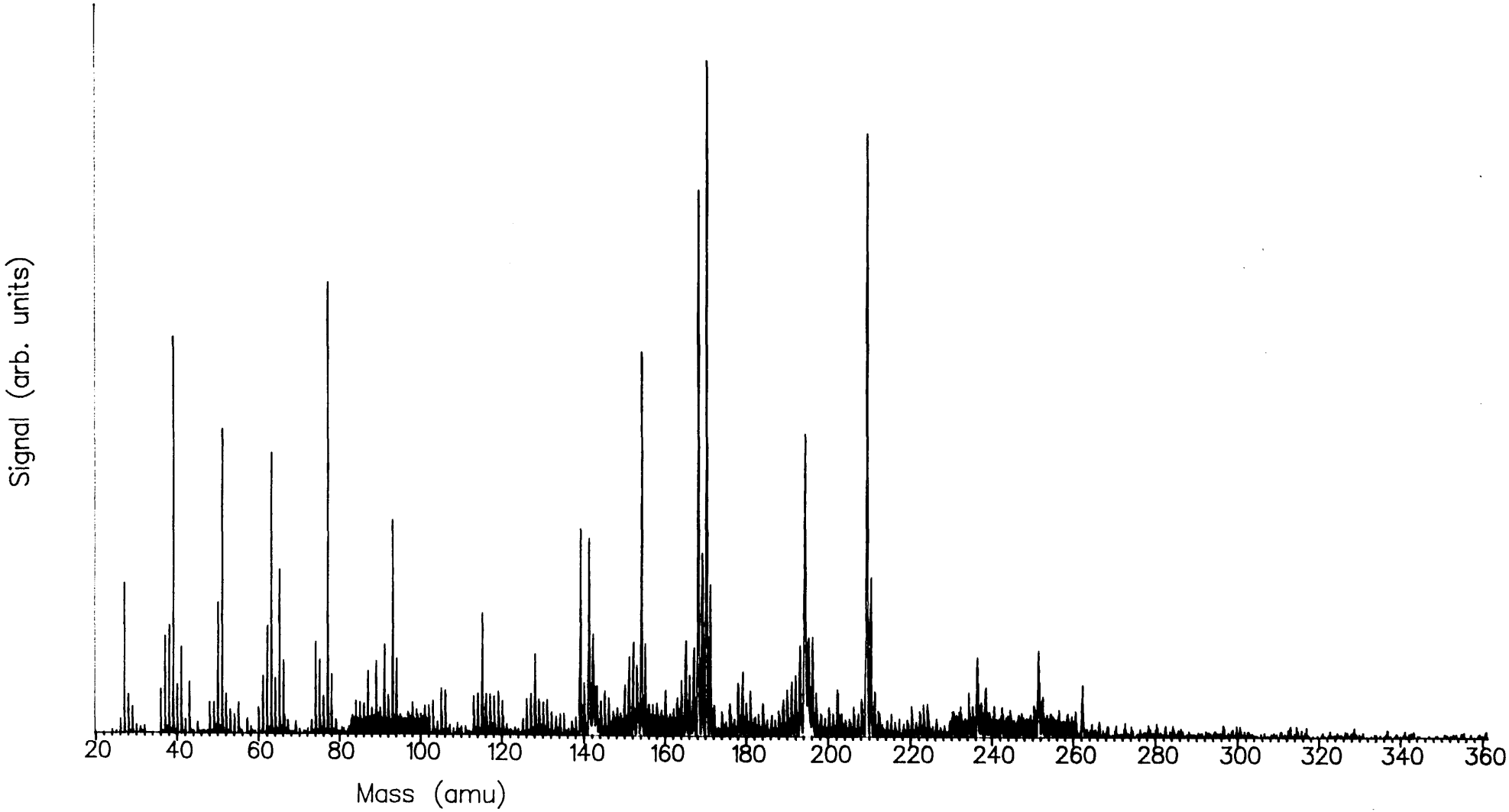

Fig 5.13: High Power 266nm Ionisation of Rotary Pump Oil

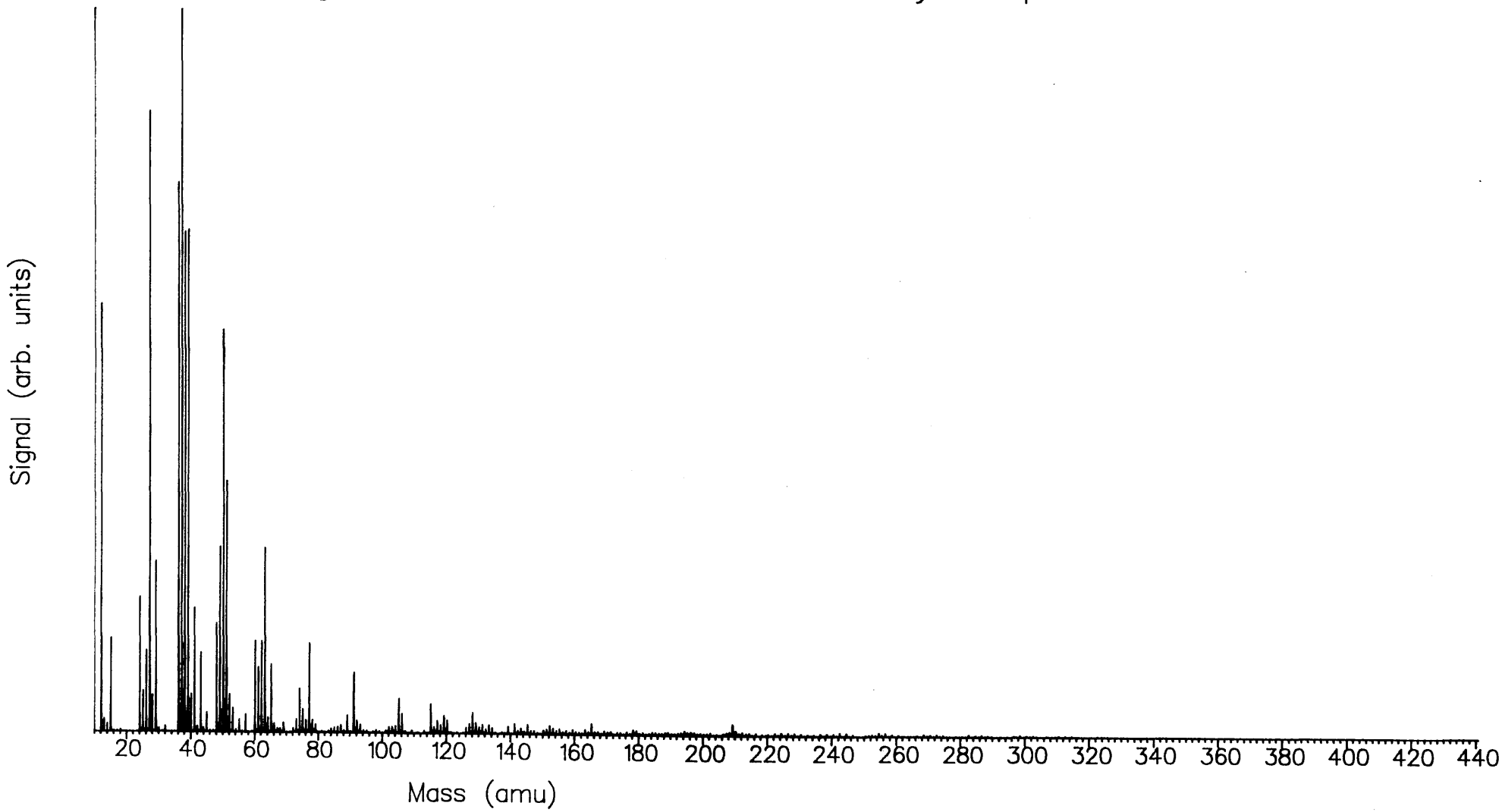

Fig 5.14: Low Power 266nm Ionisation of Rotary Pump Oil

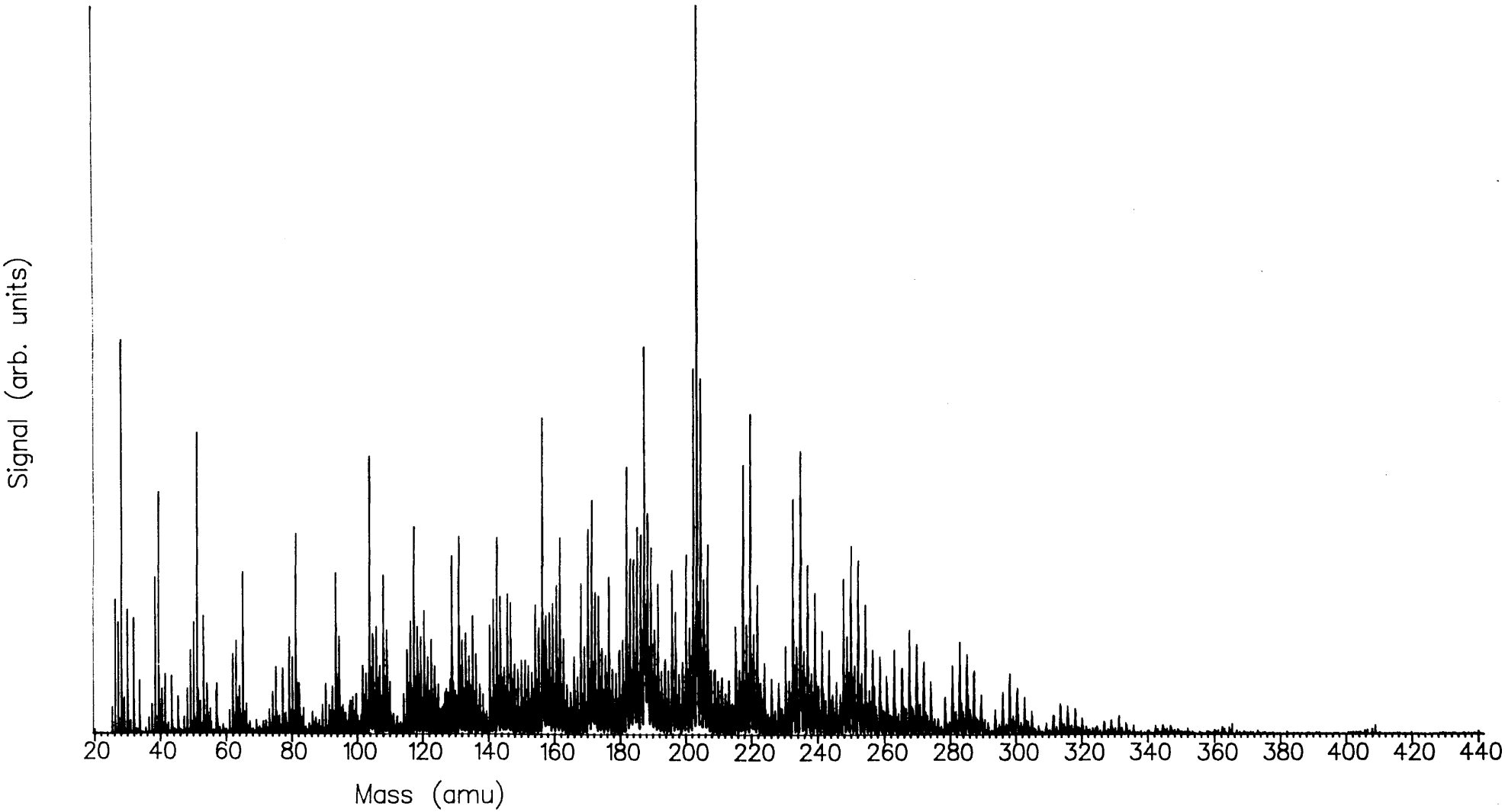

Fig 5.15: High Power 532nm Ionisation of Rotary Pump Oil

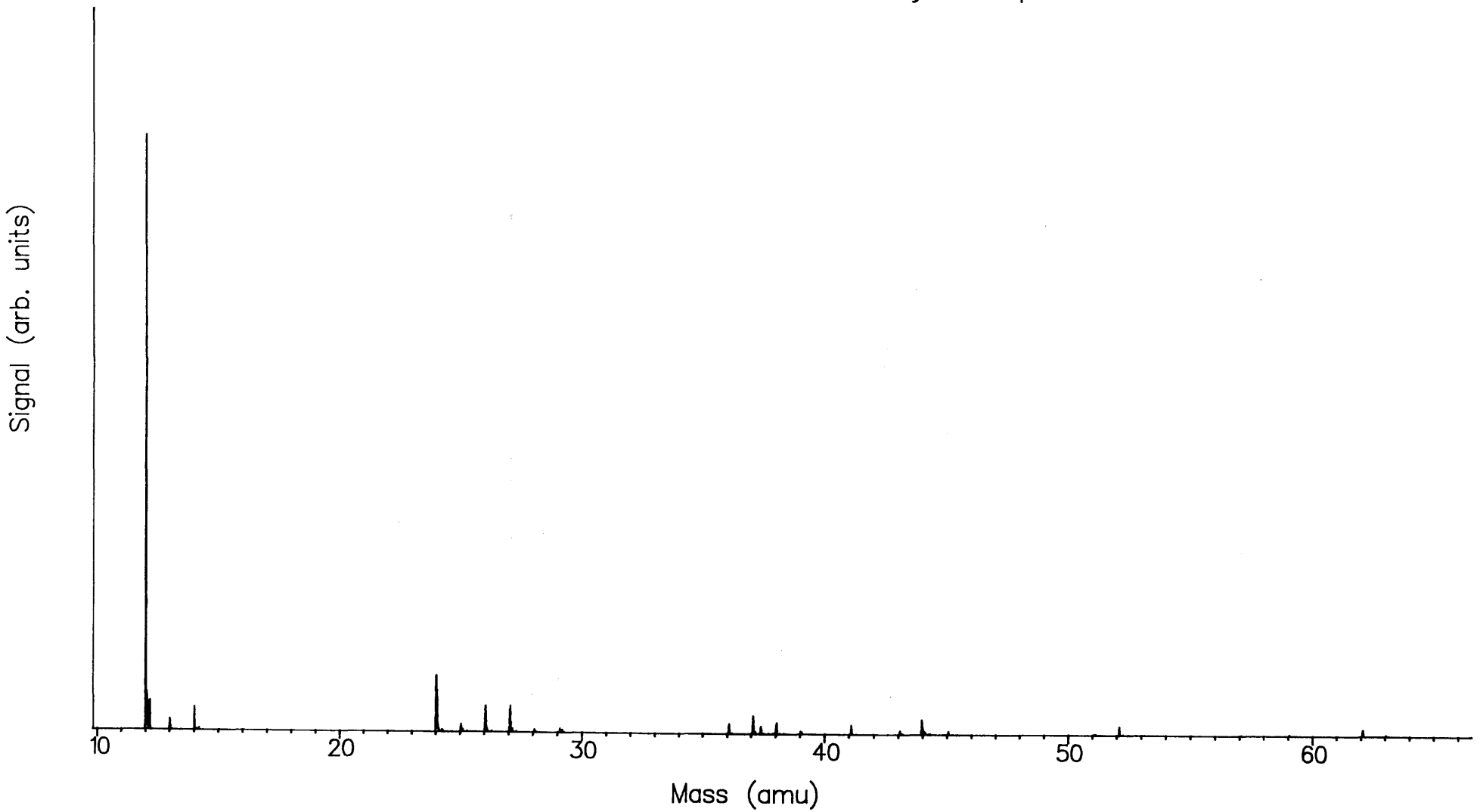

Fig 5.16: Mass Spectrum of Nitrobenzene using 266nm

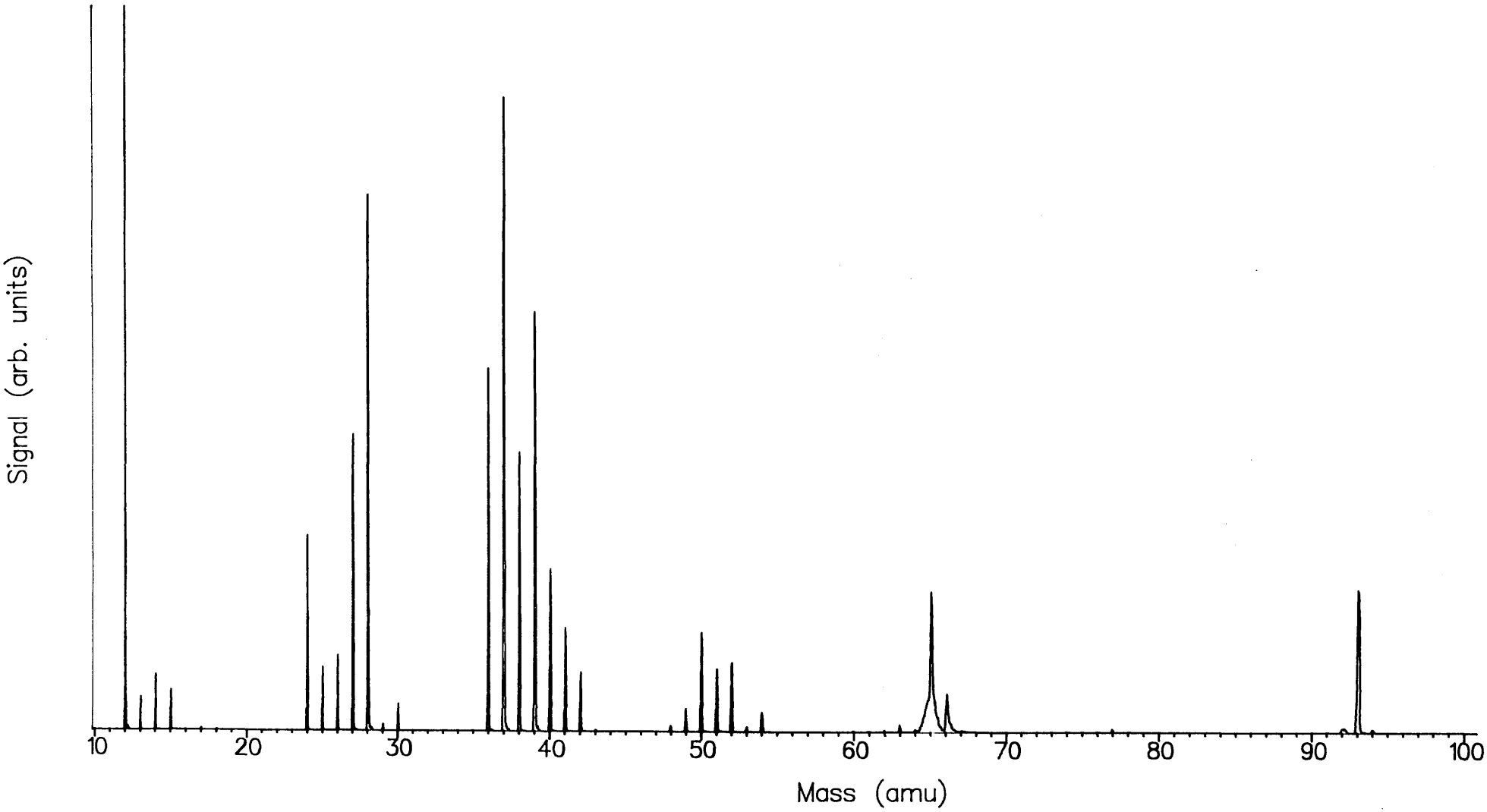

Fig 5.17: Energy Level Diagram for Neutral Rubidium

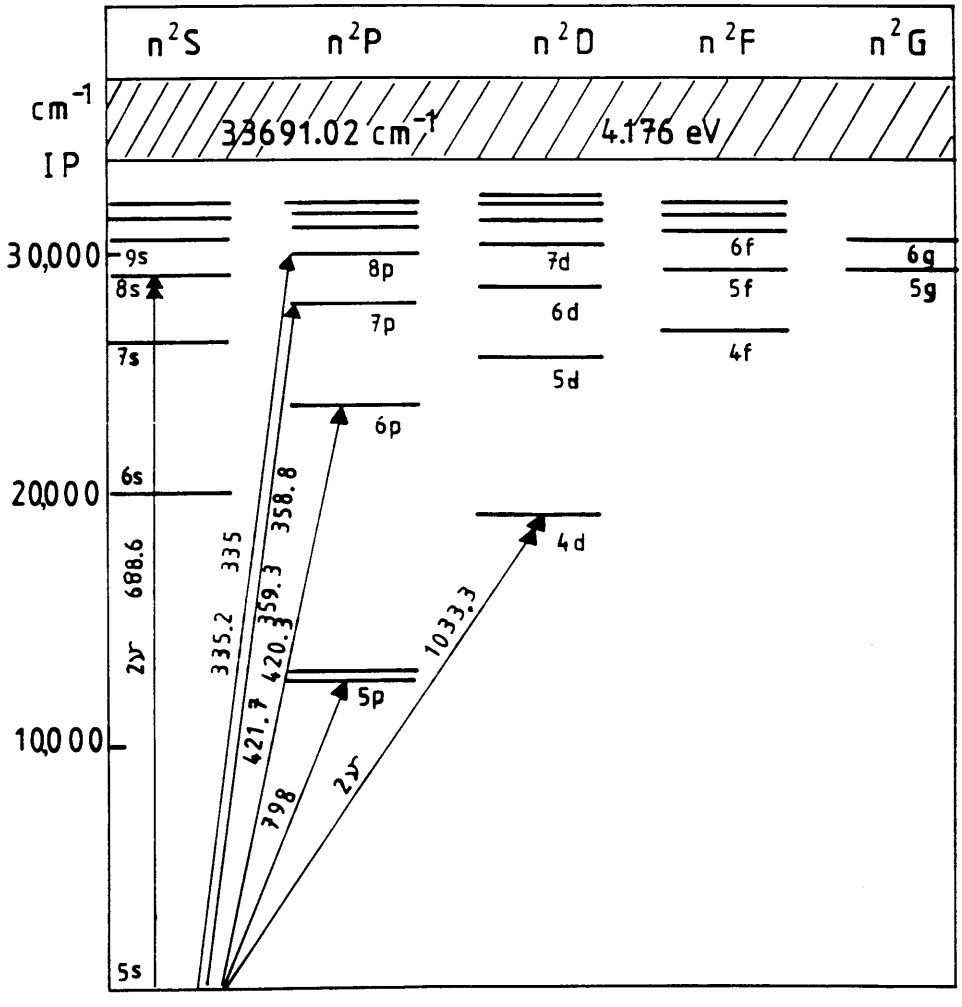

Table 5.1: NBS Coal Standard 1632a

Element	Composition(ppm)
^{6}Li, ^{7}Li	18.1
^{10}B ^{11}B	26.5
^{23}Na	380
^{27}Al	1.485%
^{28}Si, ^{29}Si, ^{30}Si	2.95%
^{39}K,^{41}K	2050
^{40}Ca	1150
^{52}Cr, ^{53}Cr	17.5
^{54}Fe, ^{56}Fe	0.56%
^{63}Cu, ^{65}Cu	7.95
^{75}As	4.9
^{85}Rb,^{87}Rb	15
^{88}Sr	44
^{121}Sn	0.35

atoms were ionised using unfocused 532nm Nd:YAG at 7mJmm^{-2} (fig 5.18). The effects of strongly focussing the 532nm to 30mJmm^{-2} laser is shown in fig 5.19. The rubidium signals have increased in size, but also visible are two more sharp peaks corresponding to ^{88}Sr and to a hydrocarbon at mass 84. With the lasers as in fig 5.19 but with the 420.7nm resonant laser detuned off resonance at 418nm no signal is seen (fig 5.20), thus confirming the selectivity of the RIMS process.

Also visible in these spectra is the problem mentioned earlier with the carbon clusters. The two broad peaks are due to C_7 and C_8. These are fortunately not coincident with the rubidium peaks or much of the sensitivity would be lost.

Calcium spectrometry was also performed. Calcium, as mentioned, has a very wide range of isotopic abundances. Details of calcium are shown in table 5.2. One sample was prepared from calcium carbonate with 50% graphite, and compressed as described above. This contains 10% calcium. Another sample of pure metal calcium was used, and this was prepared as described above for soft metals.

Calcium has a very complex spectroscopic structure. Fig 5.21 shows the energy levels. The left hand side of the diagram shows the single electron excited states, which converge towards the ionisation potential, producing the Ca^+ ion in its ground state. To the right are the two electron excited states, which converge to excited states of the Ca^+ ion.

Spectroscopic studies of calcium verified the existence of the expected one photon transitions. In addition, several two photon transitions with very large cross-sections were discovered (fig 5.22 and table 5.3). Further details, together with an explanation of this effect, are given in Land (1990).

A mass spectrograph of calcium is shown in fig 5.23. This was obtained using a one colour '2+1' scheme using a wavelength of 421.5nm. Fig 5.24 shows the same spectrum with the vertical scale expanded. Clearly seen are all the stable isotopes. The least

Fig 5.18: Rb Mass Spectrum using 420.7nm and 532nm

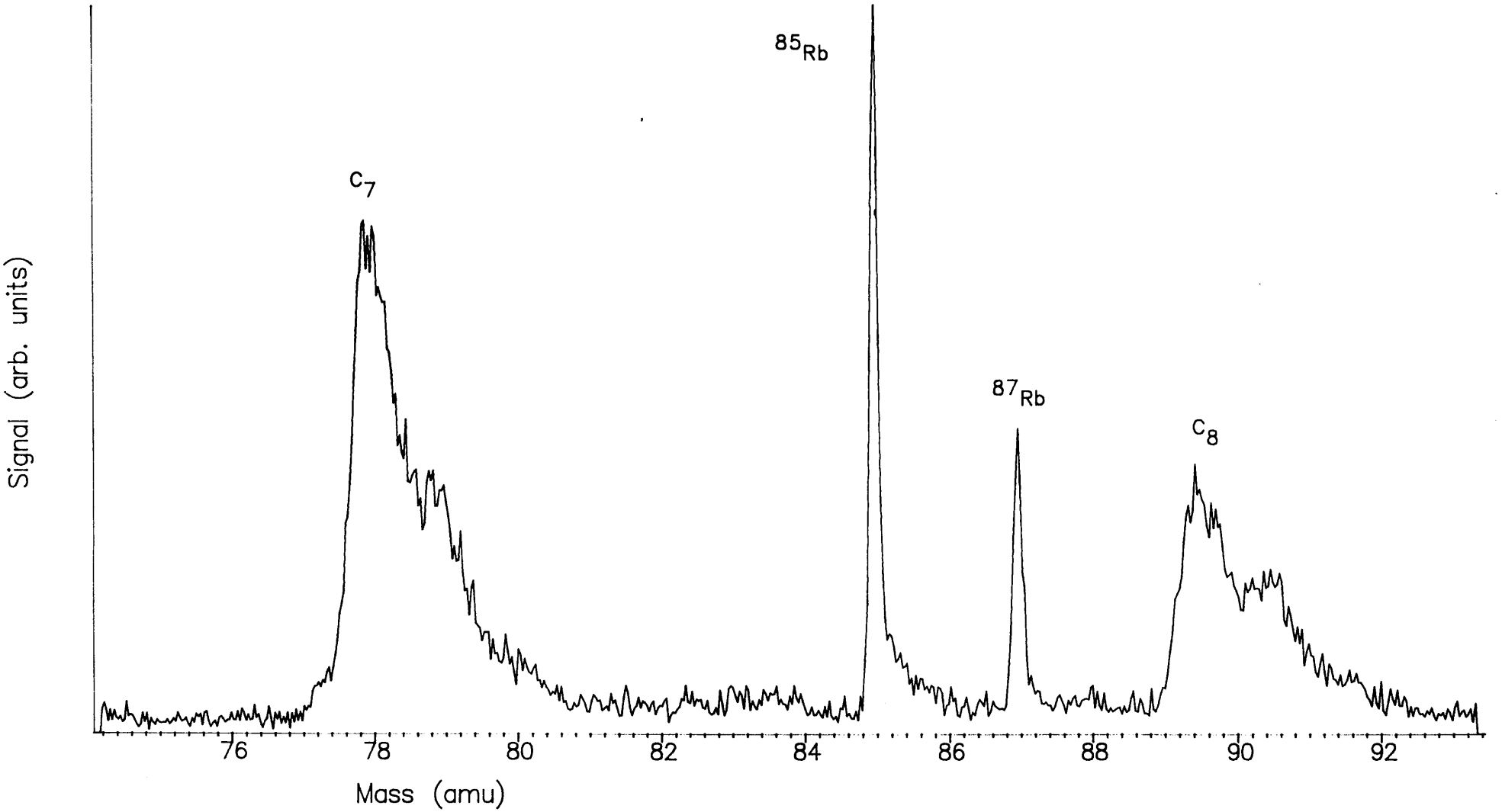

Fig 5.19: As Fig 5.18 with 532nm tightly focussed

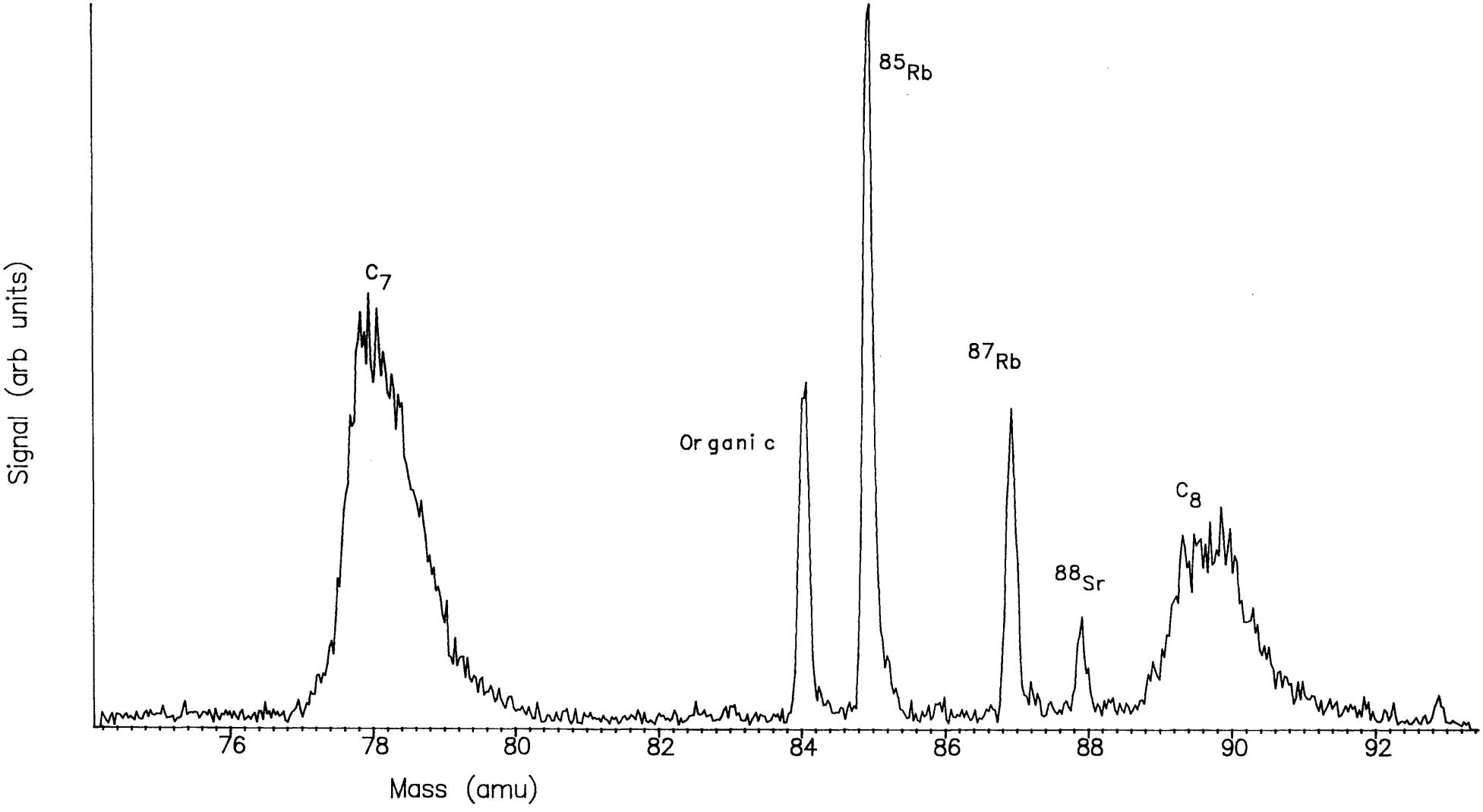

Fig 5.20: As Fig 5.18 with 420.7nm laser retuned to 418nm

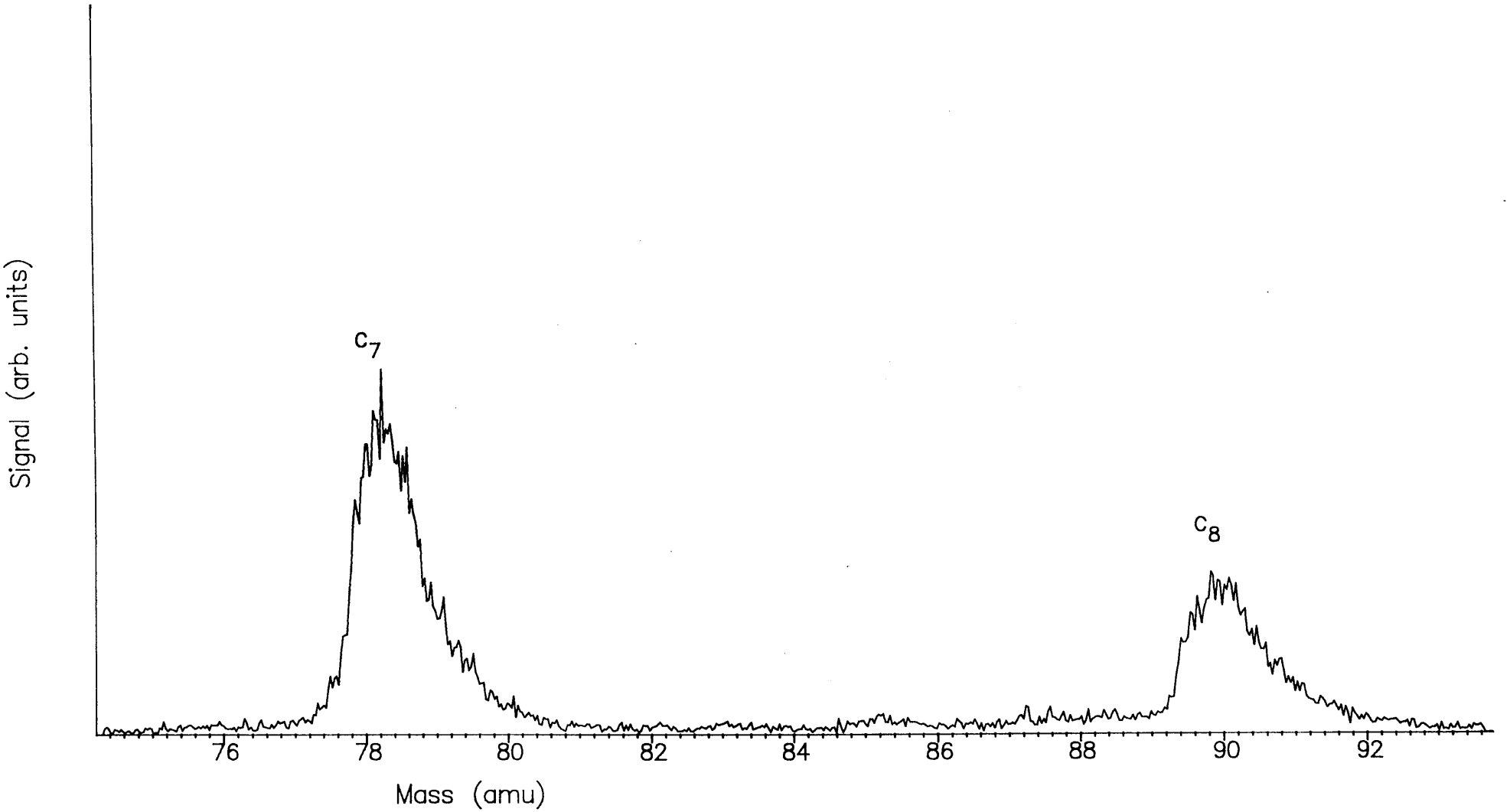

Table 5.2: Calcium Data

Atomic Number	20
Atomic Weight	40.08g/mol
Density	1.54 gcm^{-3}
Oxidation Number	+2
Electronegativity	1.0
Atomic Radius	0.196nm
Ionic Radius	0.099nm
Melting Point	1120K
Boiling Point	1760K

[From *Science Data Book*, ed R.M. Tennent, Oliver Edinburgh, 1971]

Atomic Ground State	$4s^2\ ^1S_0$
Ionic Ground State	$4s\ ^2S_{1/2}$
First Ionisation Potential	6.115eV
	$=49{,}306.1cm^{-1}$

Isotopic Data

Isotope	Mass (amu)	%Abundance
40	39.96	96.982
42	41.96	0.642
43	42.96	0.133
44	43.96	2.057
46	45.95	0.003
48	47.95	0.182
	$T_{1/2}$	
41	1.03×10^5a	
45	165 days	
47	4.54 days	
Nuclear Spins	Even	0
	Odd	7/2

Fig 5.21: Energy Level Diagram for Neutral Calcium.

(From White H.E. (1934))

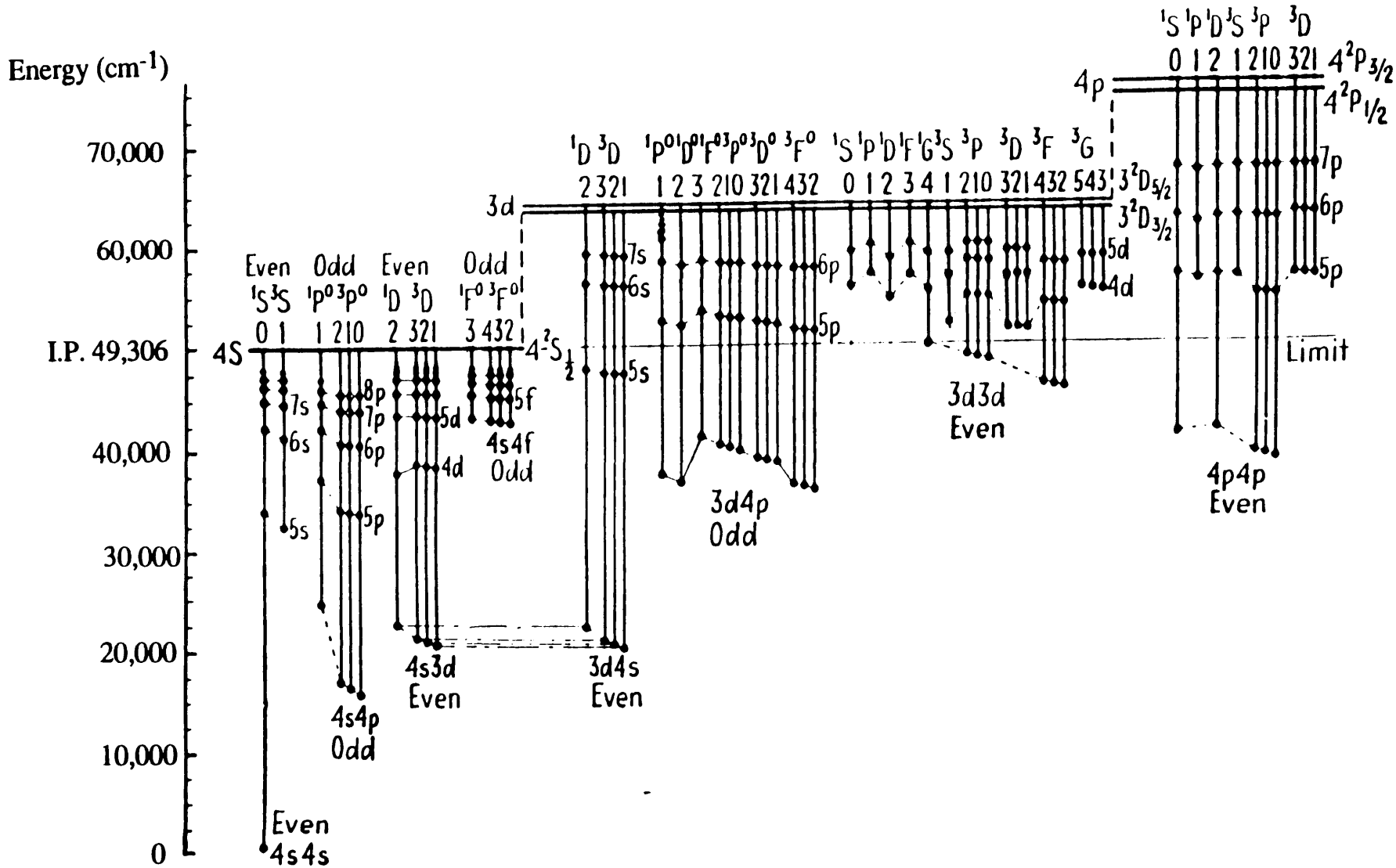

Table 5.3: Two Photon Resonant Transitions in Calcium

Transition	λ(nm)
$4s^2\ {}^1S_0 \rightarrow 4s8s\ {}^1S_0$	435.7
$4s^2\ {}^1S_0 \rightarrow 4s9s\ {}^1S_0$	426.9
$4s^2\ {}^1S_0 \rightarrow 4s10s\ {}^1S_0$	421.5
$4s^2\ {}^1S_0 \rightarrow 4s11s\ {}^1S_0$	417.9
$4s^2\ {}^1S_0 \rightarrow 4s12s\ {}^1S_0$	415.4
$4s^2\ {}^1S_0 \rightarrow 4s13s\ {}^1S_0$	413.6
$4s^2\ {}^1S_0 \rightarrow 4s7d\ {}^1D_2$	432.8
$4s^2\ {}^1S_0 \rightarrow 4s8d\ {}^1D_2$	425.9
$4s^2\ {}^1S_0 \rightarrow 4s9d\ {}^1D_2$	418.2
$4s^2\ {}^1S_0 \rightarrow 4s10d\ {}^1D_2$	415.8
$4s^2\ {}^1S_0 \rightarrow 4s11d\ {}^1D_2$	414.0

Fig 5.22: Two Photon Transitions in Calcium

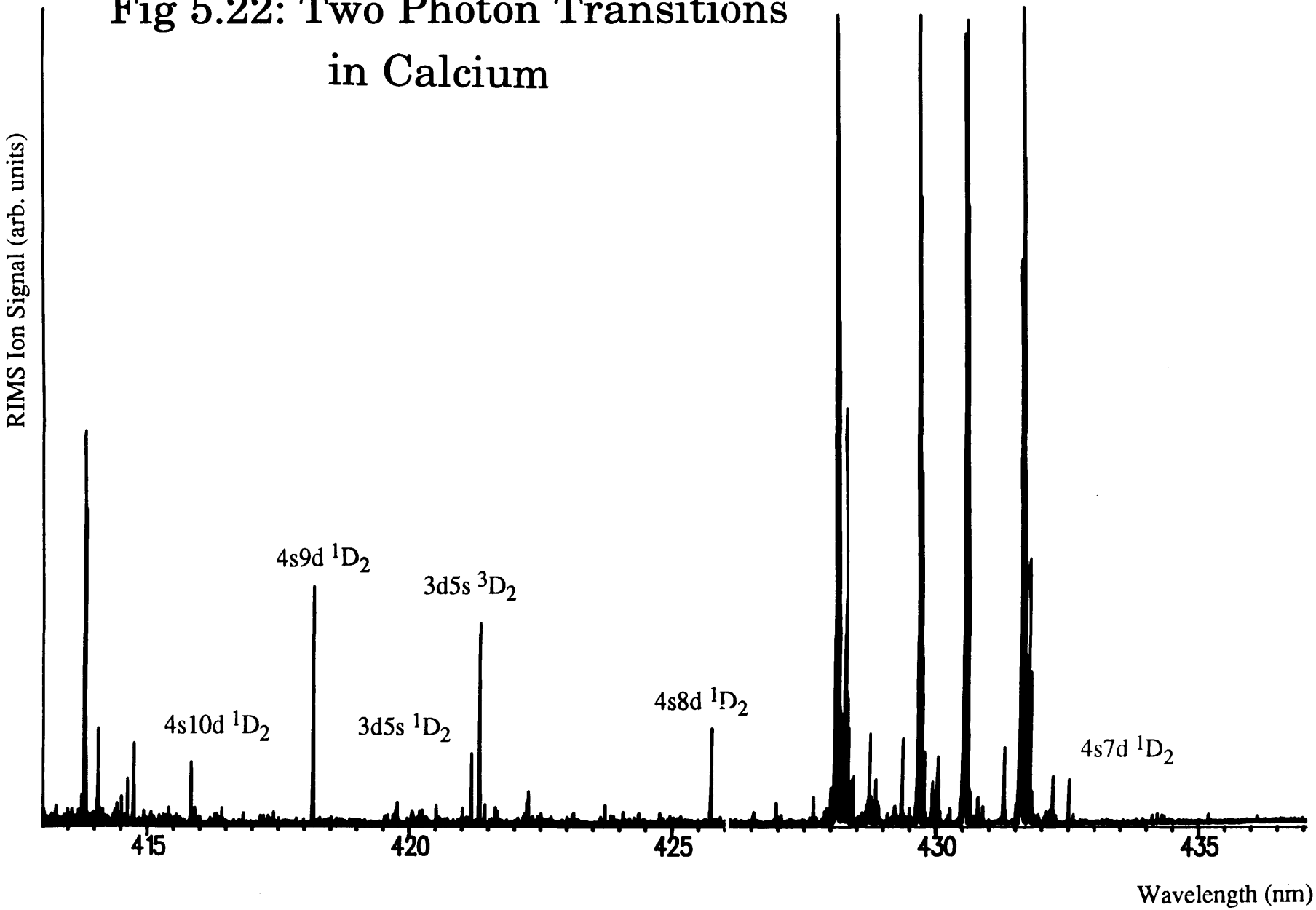

Fig 5.23: Mass Spectrum of Calcium at 421.5nm

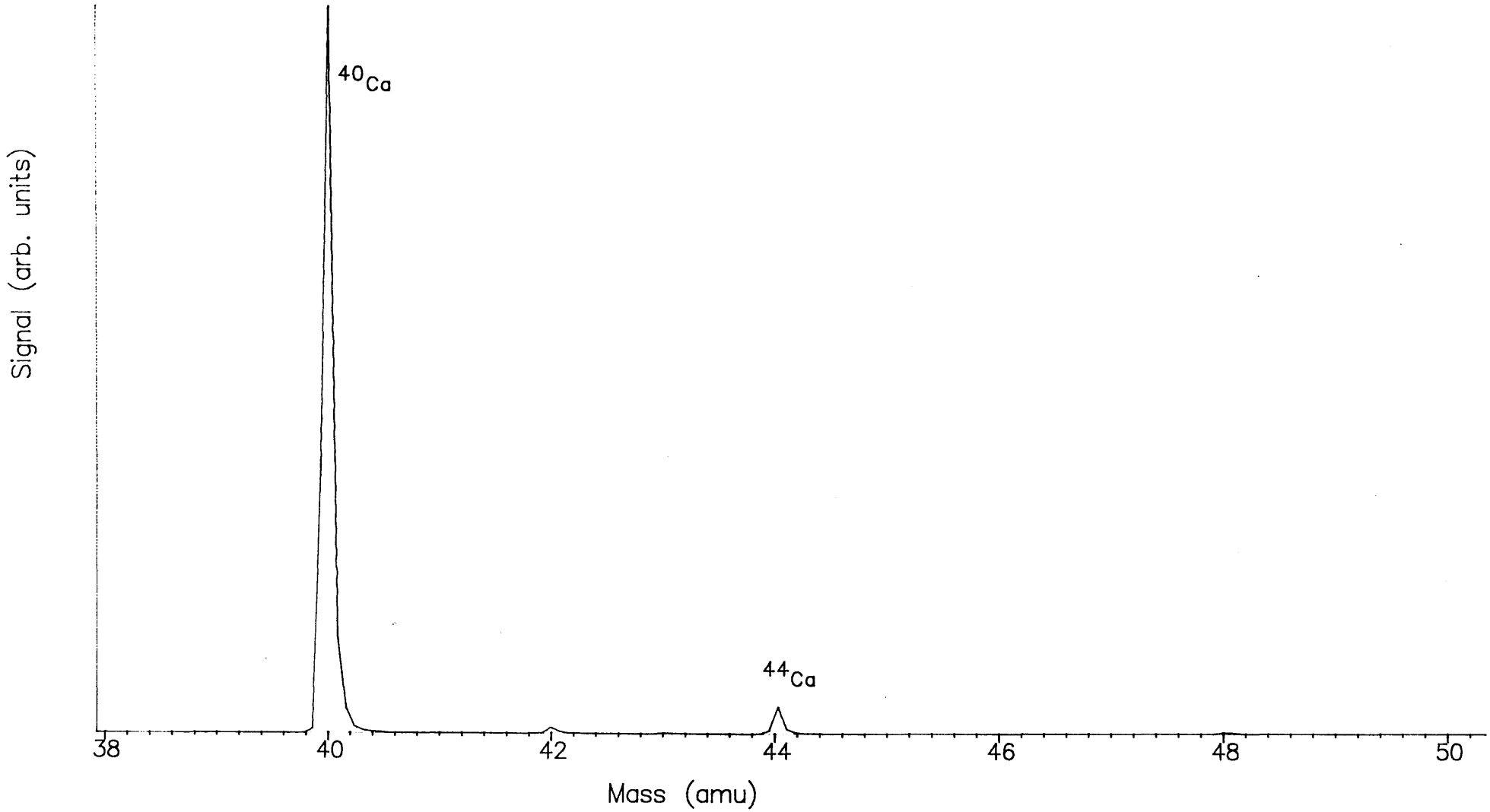

Fig 5.24: Mass Spectrum of Calcium at 421.5nm (X 100)

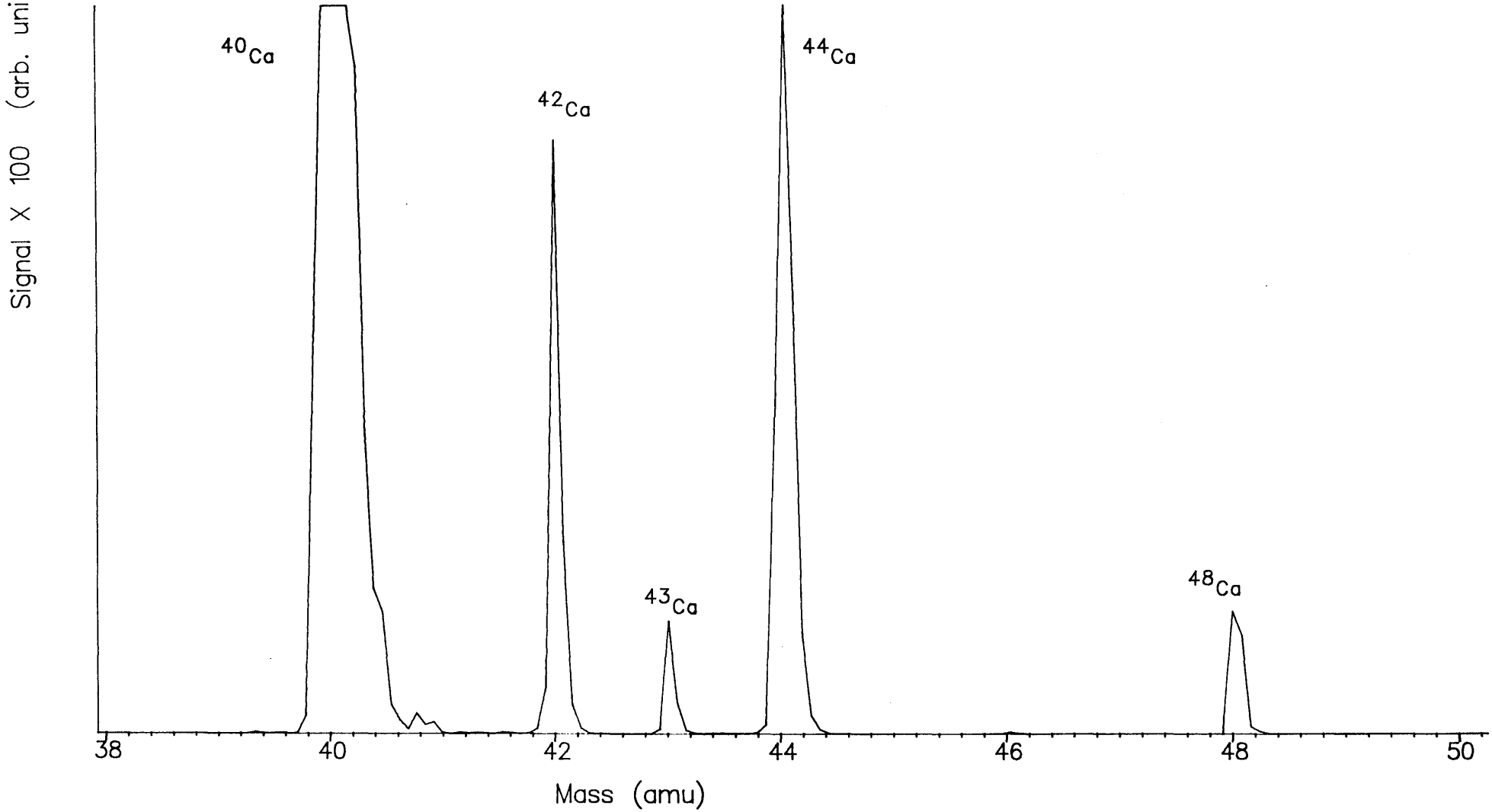

Fig 5.25: Mass Spectrum of Calcium at 421.5nm (X 10000)

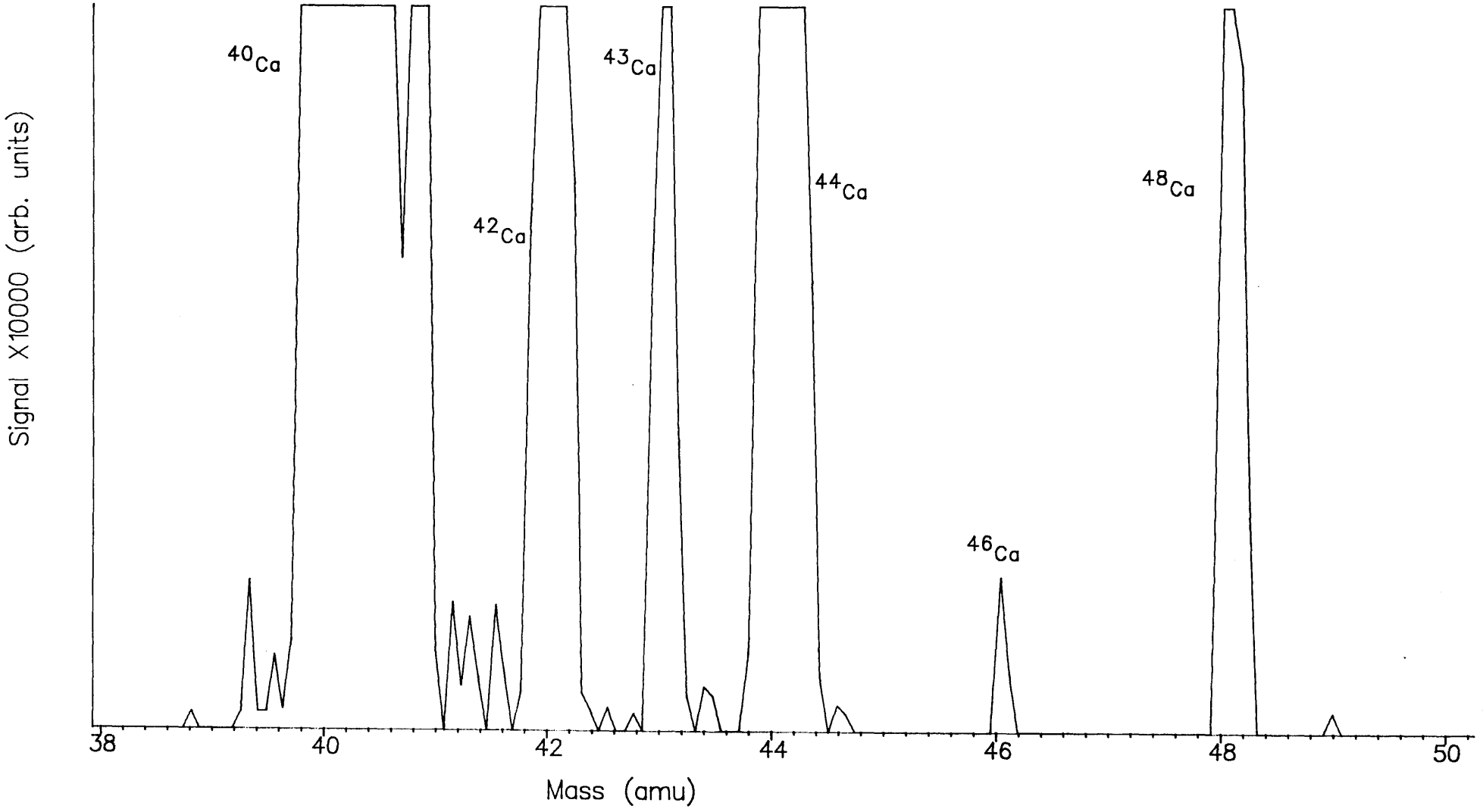

abundant isotope (^{46}Ca), present at 3ppm, is visible above the noise level.

One flaw in this result is that the isotope ratios for the different isotopes are not as expected. When repeated many times the isotope ratios would vary in an apparently random fashion. Changing to a pure metal calcium sample did not alleviate this problem. The problem was greatly improved when the detector biasing was corrected, but still inherent inconsistencies remain. Walker *et al* (1986), using thermal evaporation, managed to get very close to the expected ratios, the limitation being the counting statistics. The problem, and some of its possible causes, is discussed in Land (1990). A further discussion of this problem is given is chapter 6.

Chapter 6: Laser Ablation

§1 Introduction: Vaporisation Techniques

The analysis of solid samples by RIMS requires a desorption or evaporation process as resonant ionisation is performed on gas phase atoms.

The ideal evaporation method for RIMS would have the following properties:-

1) Be matrix independent (ie the composition of the desorbed plume is the same as the composition of the sample)

2) All desorbed atoms are neutral and in their ground state.

3) A high number of neutrals.

4) Provide 100% geometrical and temporal overlap with the resonant ionisation laser.

5) Remove atoms at the same rate for all samples.

Several methods of evaporation have been used for RIMS. The most common are thermal evaporation from wires (Fassett *et al* 1988; 1989, Travis *et al* 1986, Krönert *et al* 1985; 1989, Gerke *et al* 1988) and graphite and electrothermal furnaces (Bekov *et al* 1983; 1985; 1987b, Bushaw *et al* 1988), ion sputtering (Robinson 1984, Garrison 1982, Winograd 1989) and laser desorption/ablation (Beekman *et al* 1980; 1983, Mayo *et al* 1982, Williams *et al* 1984, Nogar *et al* 1985). The work in this thesis was performed exclusively using laser ablation as a source of neutrals. Disadvantages and advantages of each of these methods are shown in table 6.1 and discussed below.

Laser ablation occurs when a material is irradiated by a laser and some of the material is removed (Vertes *et al* 1990, Conzemius *et al* 1980). In this context laser ablation is used to cover laser-solid interactions at all fluences. It can be used for

Table 6.1: Comparison of Common Atomisation Methods

Method	Advantages	Disadvantages
Ion Sputtering	Able To Profile Basic Physics Understood	Expensive Much Lower Neutral Number Density than Laser Ablation (10^9 per pulse) Pulses Very Low Current or Poor Time Profile
Thermal Evapouration	Cheap	Needs Chemical Preprocessing Poor Duty Cycle with Pulsed Lasers
Laser Ablation	Easy to Install Very High Neutral Density Possible ($>10^{12}$ per pulse) Well Defined Short Time Profile of Pulse	Basic Physics Not Understood Unable to Profile

most vacuum compatible solid samples without any preprocessing.

Thermal evaporation is used with samples on filaments or in furnaces. The first technique involves chemically depositing a sample onto a wire from which it is evaporated by the heating of the wire. The other major thermal sources involves chemically prepared samples being placed in a furnace. One major disadvantage of these techniques, when pulsed ionising lasers are used for RIMS, is the difficulty of obtaining pulsed thermal sources (Fassett*et al* 1984). As continuous neutral sources they give very low duty cycle with pulsed lasers (2×10^{-4} at best with copper vapour pumped dye lasers (Young *et al* (1989)), although this can be alleviated to a degree by using enclosed furnaces (Magnusson *et al* 1986). The species of neutrals emitted from a thermal source depend on the temperature of the source. The need to preprocess the sample limits the range of applicability (Moore *et al* 1984, Apel *et al* 1987c, Walker *et al* 1986). The method of preparation and matrix effects can also be problematical (Zilliacus 1989).

Ion sputtering occurs when a high energy ion beam is incident on the sample surface. This causes analyte to be ejected from the surface. Ion sputtering can be either pulsed or continuous. For the purposes of RIMS it is the neutral component of the ejected plume which is used. A method which uses the neutral plume produced from ion sputtering can be termed secondary neutral mass spectrometry (SNMS), as opposed to secondary ion mass spectrometry (SIMS). The use of ion sputtering with RIS is generally known as SIRIS (Sputter Initiated Resonance Ionisation Spectroscopy).

SIRIS's major disadvantages as a technique are the relatively small number of neutrals produced in the sputtered plume and the possib le occurance of matrix effects. The former imposes a limitation in the sensitivity since a 1μA ion current incident on an area of $1mm^2$ yields 1.2×10^8 neutrals (Nogar *et al* 1990).

The possible matrix problem in SIRIS has been investigated by several authors. Matrix effects do not seem to be a major problem in surface studies using SIRIS, unlike SIMS matrix effects (Kimock *et al* 1983, Oechsner *et al* 1978). Arlinghaus *et al* (1989) and Downey *et al* (1990) report near matrix independence for semi-conductor profiling studies. However, Hutchinson *et al* (1987) and Goeringer *et al* (1988) have reported major problems with matrix effects in the SIRIS analysis of uranium from uranium containing solids.

Duty cycle is a problem with ion guns. It is difficult to obtain ion guns with a pulse length comparable to those of pulsed lasers used for RIMS. Any ion guns which do have a pulse length this short (<20ns) are generally limited in the current that they can be supply, and consequently in the flux of neutrals they can delivered.

Ion guns have some advantages in comparison with laser ablation. One advantage is that the ion sputtering process is well understood and can be modelled successfully (Winograd *et al* 1990). The mechanisms behind the laser ablation process are very poorly understood in comparison (Winograd 1989). Rastering of a laser is awkward, which makes ion guns the preferred method when rastering is required. Finally, laser ablation at higher fluences is not restricted to the surface layers but penetrates for hundreds of monolayers (Nogar *et al* 1990). This restricts laser ablation to surface analysis at low fluences or to bulk material analysis at higher fluences. Depth profiling, such as that required for advanced semiconductor devices, is not feasible using laser ablation (Ralston *et al* 1987) (Fig 6.1).

§2 Investigation and Modelling of the Ablation Process

Two phenomena are investigated in this chapter. Firstly the temporal profile of a laser ablation plume is examined. From this can be found the energy distributions of the neutrals produced by laser ablation. Secondly the fluence dependence of the number of neutrals is investigated. This can be used to indicate the optimum ablation laser flux for neutral production.

Fig 6.1: Lattice Mixing by Laser Ablation

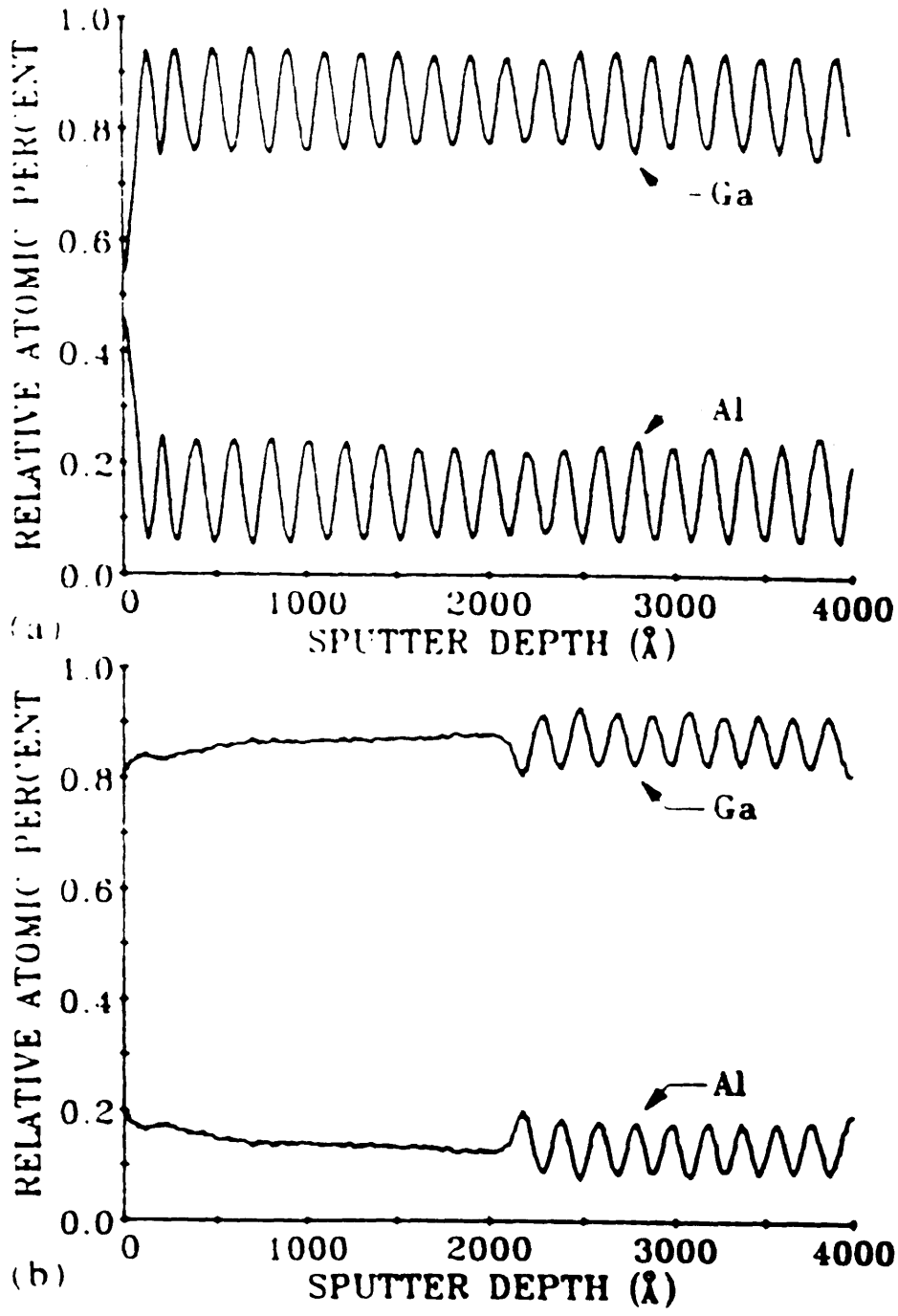

The upper diagram shows a depth profile of AlGaAs before laser ablation. The lower shows the depth profile after 1 laser pulse of $2.2 mJmm^{-2}$ at $\lambda = 248nm$.

As mentioned above, the underlying mechanisms of laser ablation are very poorly understood. For the purposes of this work it was decided to use the simplest model that was consistent with the data. This was the Maxwell-Boltzmann model described in chapter 2 §6. The reason for this modelling was to find the optimum time delay between ablation and post-ionising lasers for a given sample-ionising laser distance, and to investigate whether the time delay would vary with element, and possibly with isotope. Although it was not applicable to all fluences used, this model was adequate for the low laser fluences which were used for all trace analysis work presented in this thesis.

It was also desirable to find the optimum laser properties for the analysis of materials using laser ablation. This involved the investigation of two parameters:-

1) Wavelength of ablation laser.

2) Energy and fluence of ablation laser.

Some parameters were impossible to investigate with the experimental arrangements, such as pulse length, pulse temporal profile and angle of incidence of the ablation laser.

For all experiments in this chapter the ablation laser was used in TEM_{00} mode. Early experiments using the laser when operating in multiple transverse modes gave results which were generally irreproducible.

Laser power densities (fluxes) are usually given in units of Wcm^{-2}. Laser fluences are usually quoted in $mJmm^{-2}$. The discussion of the experimental work at Glasgow uses fluence whereas some other authors use flux as a measure of laser ablation. A conversion factor is $10^7 Wcm^{-2} = 1 mJmm^{-2}$ for a pulse length of 10ns. It should be noted that for meaningful comparisons between different work to be made the time taken for the energy to be deposited onto the sample should be similar.

§3 Experimental Investigations of Calcium Ablation Plumes

The laser ablation of calcium was the first to be investigated at Glasgow. Calcium spectroscopy was being investigated by Dr A.P. Land, and in order to optimise the spectrometer these studies were undertaken.

The calcium sample was compressed from pure calcium metal granules (Laboratory reagent, Hopkin and Williams, Chadwell Heath, England.) in the manner described for soft metals in chapter 5. This sample was used for all experiments in this section. The energy of the post-ioni sing laser used in all experiments in this section was 200μJ at the instrument. Ionisation scheme was as fig 6.10

Angular Distribution of Calcium Ablation Plume

The angular distribution can be described by the ratio of the neutral velocity normal to the surface and the neutral velocity parallel to the surface. This ratio is called α.

The angular dispersion of the calcium plume was measured using a method devised by Dr M. Towrie of the Laser Ionisation Studies Group. This is shown in fig 6.2. A glass plate was positioned 10mm away from the sample and the ablation laser was focussed onto the sample surface for 72000 shots. The fluence was ~5mJmm^{-2}. This provided a circular deposit of ablated calcium on the glass. Measurements on the size and thickness of the deposited circle allows an estimation of the transverse velocities of the plume, and hence the angular dispersion, to be made. The method assumes that the calcium deposited on the glass is proportional to the calcium that is available to be ionised by the resonant laser. From this method an estimate of $\alpha = 0.075$ was made.

Plate 3 shows a photograph of the calcium ablation plume. This provides support for the low angular dispersion measured above. The (blue) glow is thought to be due to a decay of a metastable state in calcium. The ablation laser wavelength was 1064nm and the fluence was ~10mJmm^{-2}.

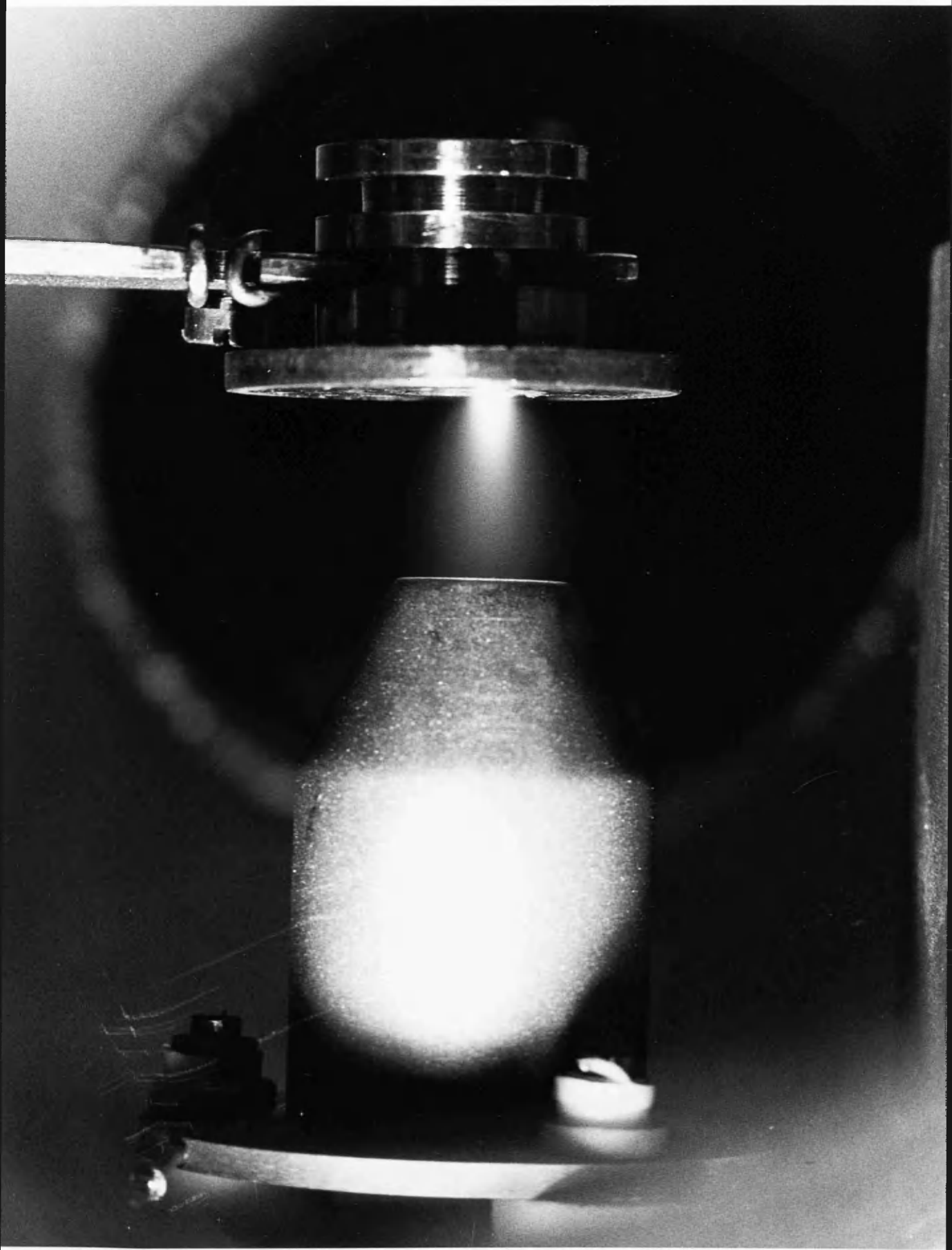

Plate 3 : 1064nm ablation of Calcium

Fig 6.02: Calcium Plume Dispersion Experimental Set Up

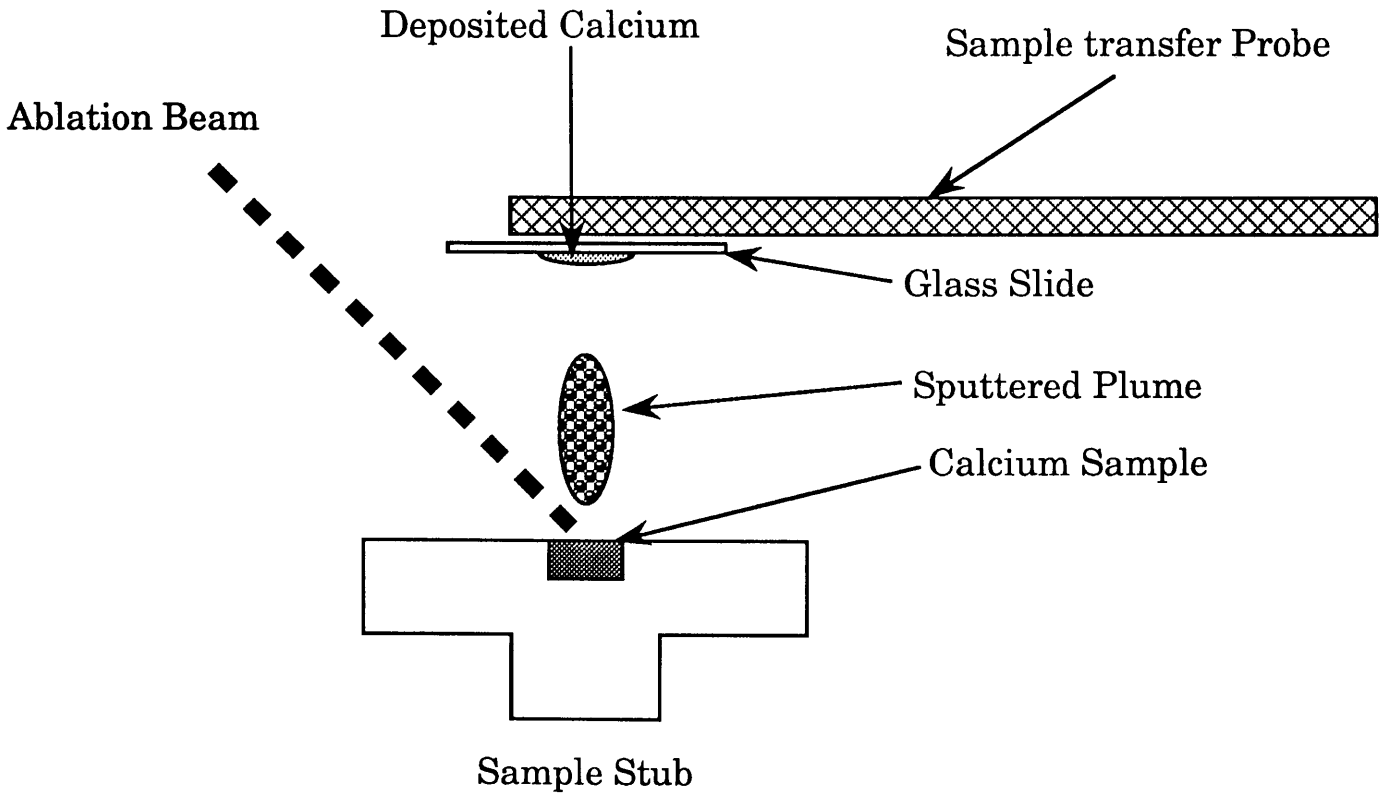

Another way of obtaining the angular distribution is to permit α to be a variable in the equations describing the plume. Generally this was ambiguous as the effects of varying α can be compensated for by a change in another unknown parameter, the plume temperature. This will be discussed in §6 below.

α, while only measured for calcium, was assumed to be approximately equal for all samples and at all energy densities.

Temporal Profile of Calcium at Low Fluences

The experimental arrangement for the measurement of the calcium temporal profile is shown in fig 6.3. The post-ionising laser was fixed at 2mm from the surface of the sample for these runs. It was tightly focussed (~0.1mm) to eliminate as much as possible contributions to the distribution caused by the finite size of the ionising laser volume. The ablation laser was apertured by a plate with a circular hole of area $1mm^2$.

The temporal profile was measured by the varying the delay between the ablation laser and the post-ionising laser. In the case of calcium for each different time delay, a one thousand shot spectrum was taken. This was to minimise the uncertainties due to energy fluctuations of the ablation laser. Up to 40 spectra are taken consecutively at different delays. From each of these the area of the peak corresponding to the signal of interest is taken. These areas plotted against time delay give the temporal profiles shown.

For each different profile a new area of sample was used, although for any one profile the same area was used.

Three ablation wavelengths were used:- 1064nm (fundamental Nd:YAG), 532nm (frequency doubled Nd:YAG) and 355nm (frequency trebled Nd:YAG). The 266nm wavelength (4 × Nd:YAG) was unusable because of excessive energy fluctuations. The laser energy was adjusted, using the in-built attenuator, to 1.5mJ per pulse for all wavelengths.

Fig 6.03: Arrangement for Temporal Profile Experiments (not to scale)

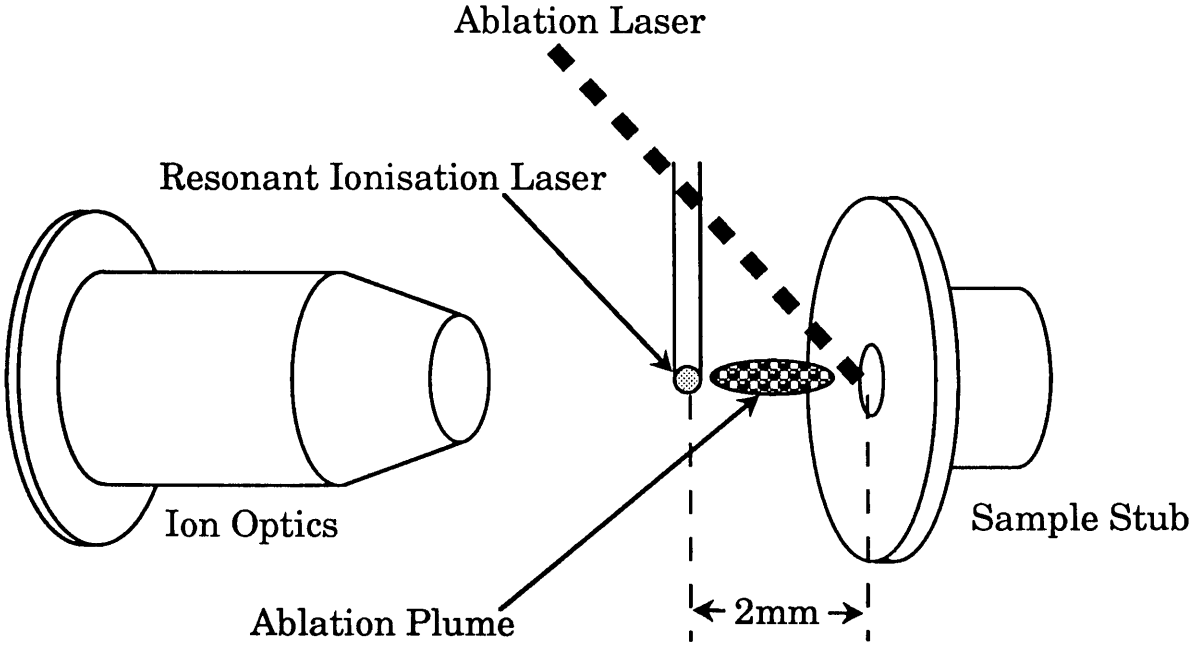

Fig 6.4 shows the results from all three wavelengths. Each data set is normalised for comparison. The ionisation scheme used was as shown in the inset to fig 6.4. This scheme was not saturated. The curves correspond to a Maxwell-Boltzmann fit with zero angular dispersion (broken line) and the measured angular dispersion (solid line). The temperature of the Maxwell-Boltzmann fit was 1700K. The Maxwell-Boltzmann fit was calculated using software developed by Dr R.P. Singhal of the Laser Ionisation Studies Group. The software requires the plume dispersion and plume temperature to be entered. The program calculates a distribution based on these parameters.

From this it appears that calcium is evolved thermally from the surface in the laser ablation process. There is no apparent variation of the ablation process with wavelength over the wavelength range covered.

Calcium Temporal Profiles at High Fluences

The experimental arrangement for this experiment was as for the low energy calcium experiment (above), with the exception of the 355nm ablation laser being tightly focussed instead of a passive aperture being used. The fluence was $100mJmm^{-2}$. Only the 355nm component could be used due to the focussing conditions required. The ionisation scheme was as above for the low fluence calcium experiment.

A very different profile from low fluence ablation, as shown in figs 6.5 and 6.6 for Ca^{40} and Ca^{44}, was obtained. Here, instead of a one peaked distribution corresponding to a Maxwell-Boltzmann, there are two peaks on the graph. The profile shows significant signals at long times in comparison to the profile for low fluence calcium ablation. Fig 6.7 shows a logarithmic distribution of the Ca^{40} signal for easy comparison with the work below.

Fig 6.8 shows a similar type of distribution, this time from GaAs. This work was done by Scheuler *et al* (1987) and used a similar fluence to the calcium work presented here. As can be

Fig 6.4: Temporal Profiles of Calcium Plumes at Three Different Wavelengths

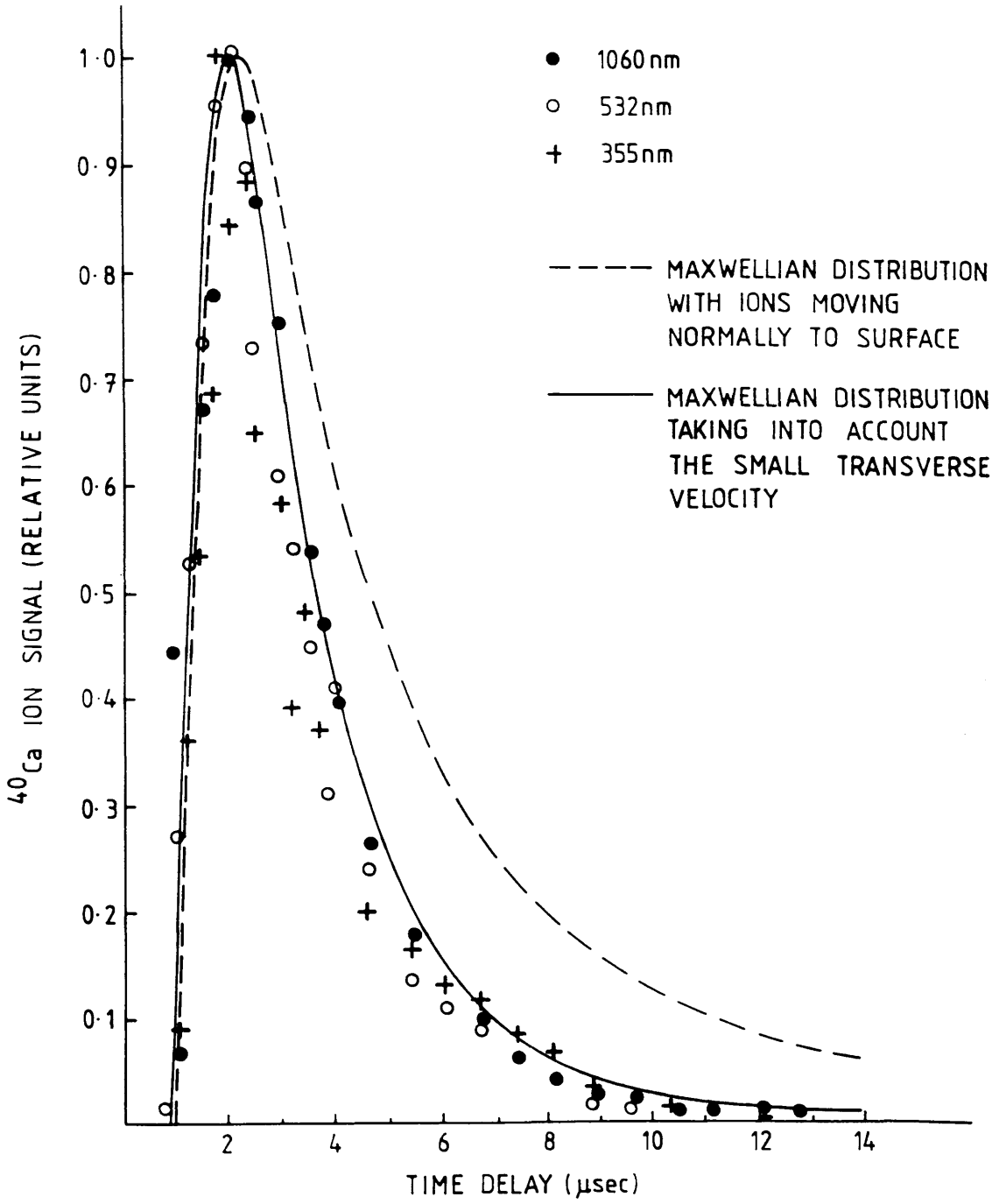

Fig 6.05: Temporal Profile of Calcium 40 Ablation at 100mJmm^{-2}

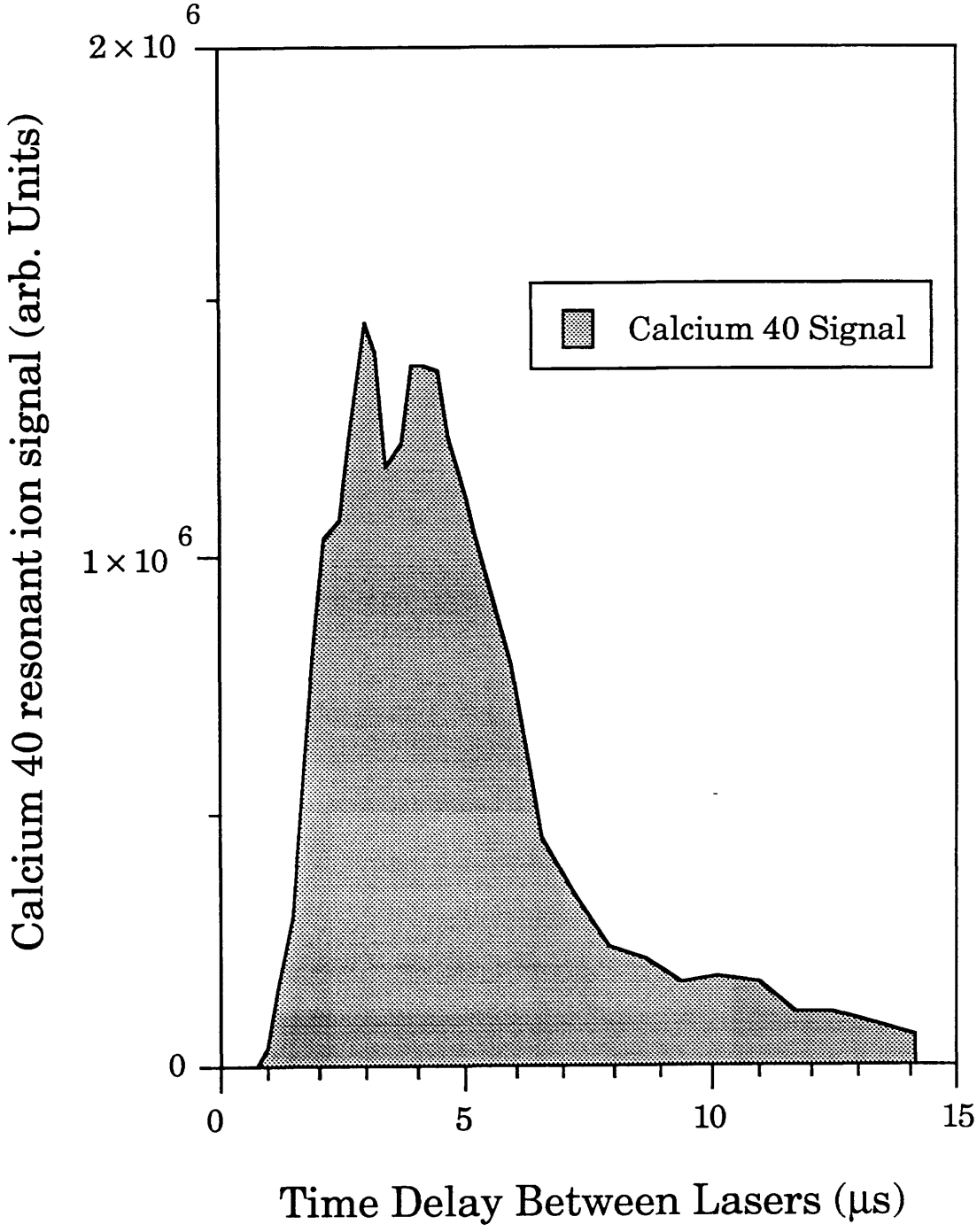

Fig 6.06: Temporal Profile of Calcium 44 Ablation at 100mJmm^{-2}

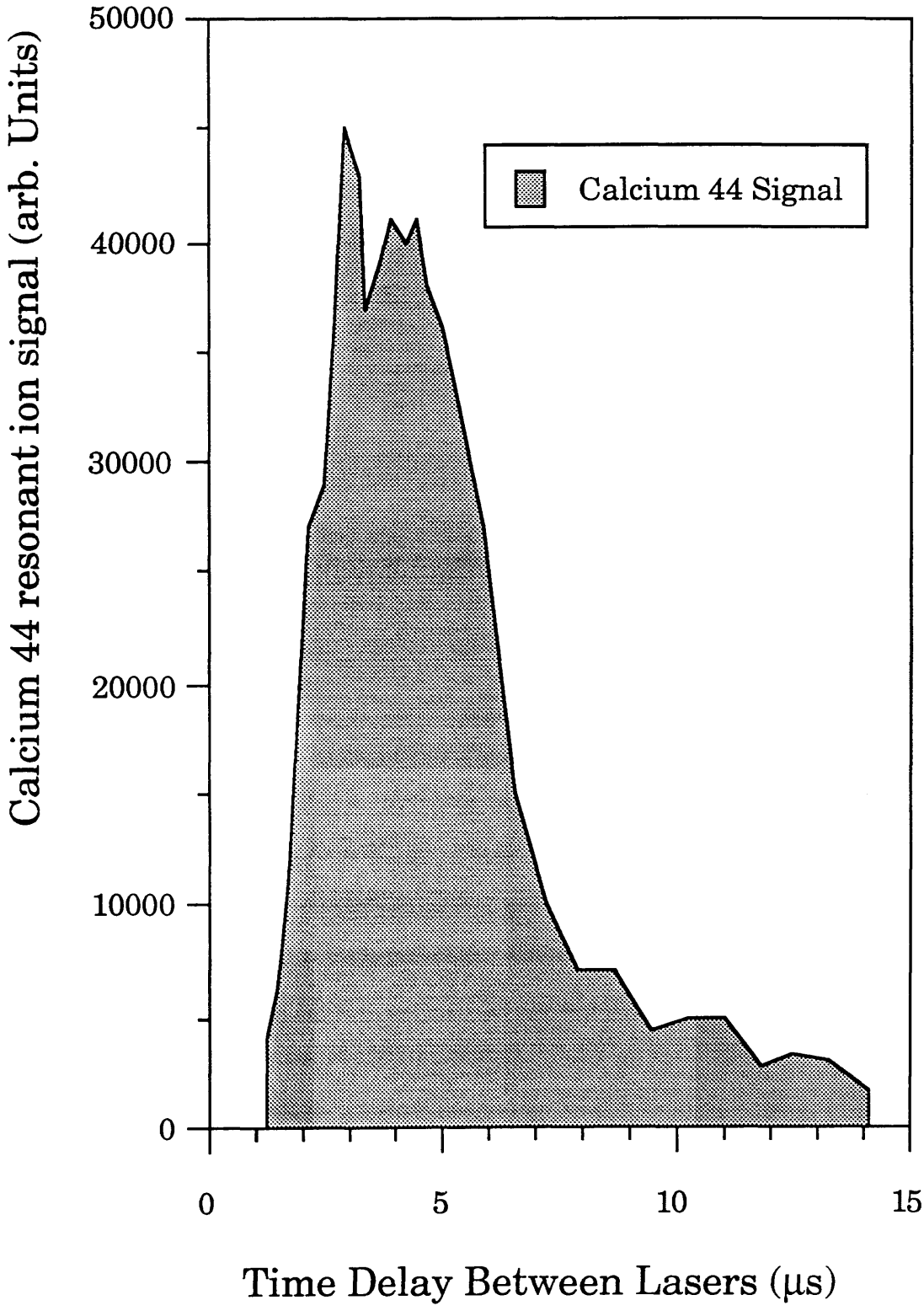

Fig 6.07: Logarithmic View of 100mJmm^{-2} Calcium 40 Ablation Temporal Profile

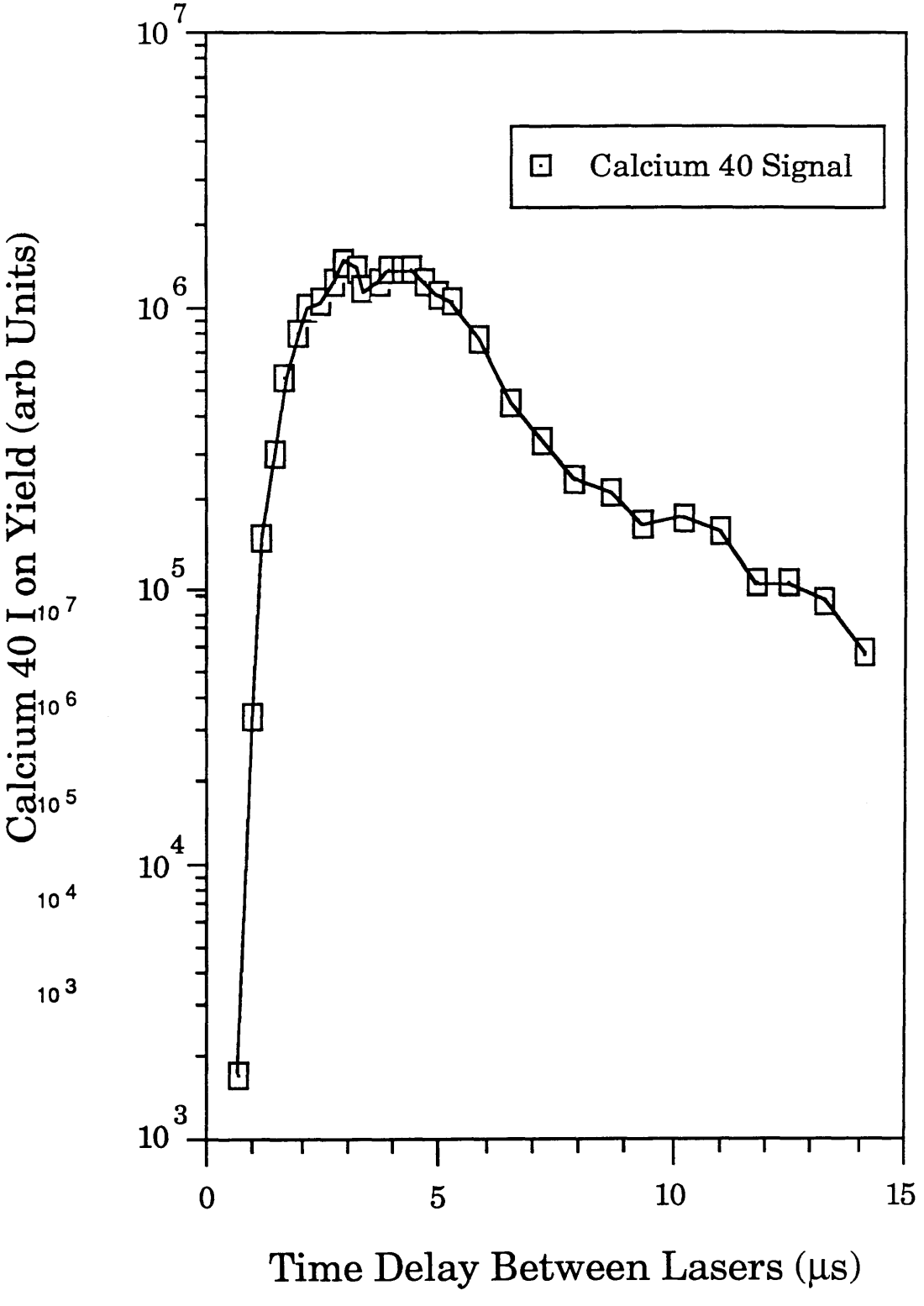

seen the shape of the curve is similar to the high fluence calcium curve. This demonstrates that the effect is not unique to calcium. Other papers (Apel 1987b, Estler 1987) have also reported similar phenomenon for calcium ablated from calcium flouride.

The mechanism for the production of the two peaks is unknown. One explanation proposed (McCombes *et al* 1990) was that calcium clusters were being produced. Calcium in its ground state is anti-bonding, so clusters would have to be formed with calcium atoms in excited states, or between calcium ions and calcium atoms. Even with this consideration it was impossible to produce the shape of the distribution using summed Maxwellian curves, with each curve corresponding to a different cluster.

The times of the first peak for both calcium isotopes at high fluences were similar to the times of the calcium peak at low fluences. This implies that the calcium, assuming a thermal emission process, is being emitted at a similar temperature in both cases. This in turn implies that the second peak is due to calcium being emitted at lower temperatures or at later times.

Apel (1987b) proposed that the double peaks seen in such spectra were due to multi-photon absorption. In this case (fig 6.9) the first peak appears at shorter times, with the second peak coinciding with the first peak of the low fluence spectrum. This ablation wavelength was 266nm from a Nd:YAG with a fluence of 250mJmm^{-2}.

The contrasting results at high and low fluences clearly indicates that different mechanisms are occurring at these two different fluences.

Fluence Dependence of Calcium Neutral Production

The fluence dependence for calcium was performed in a similar way except that the ablation laser - ionisation laser delay was set to correspond to the peak of the calcium temporal profile. Instead of the time delay being varied the fluence was varied. Only 1064nm laser light was used. Fig 6.10 shows the results.

Fig 6.8: Laser Abaltion of GaAs.

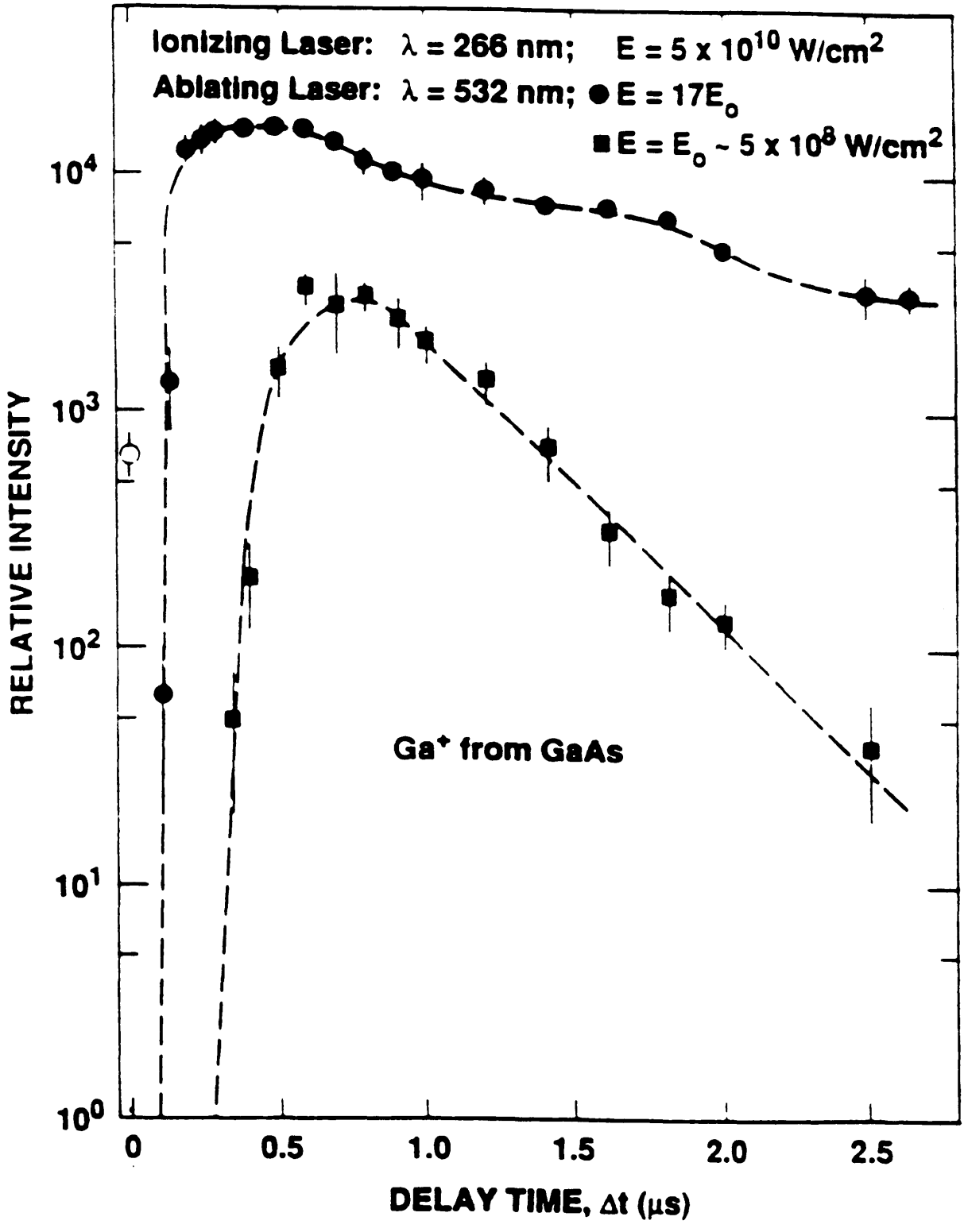

Fig 6.9: 250mJmm-2 Ablation of Calcium Fluoride.

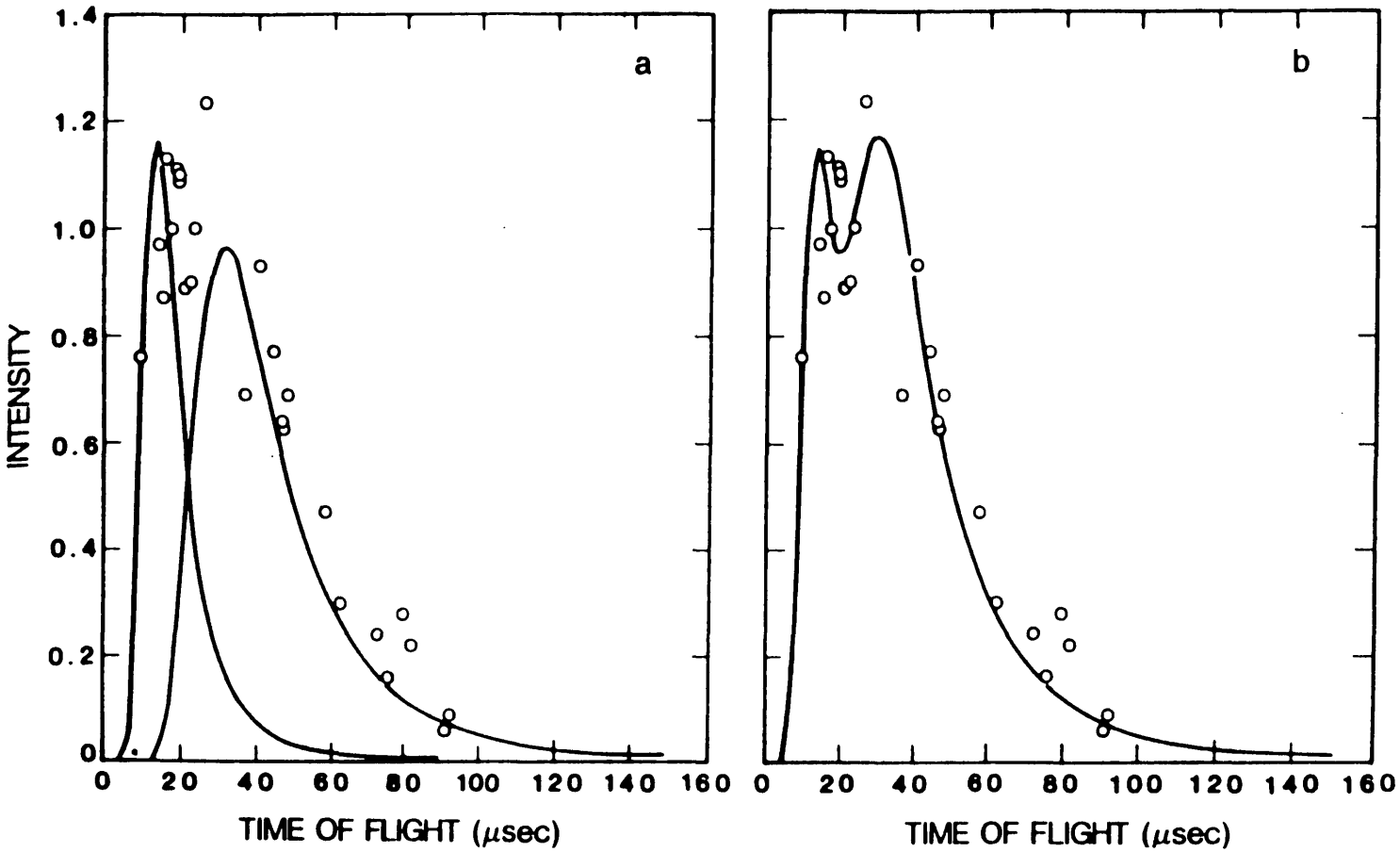

a shows the modelled components seperately whereas **b** shows the modelled fit

Fig 6.10: Variation in Calcium Neutral Yield with Increasing Abaltion Laser Fluence

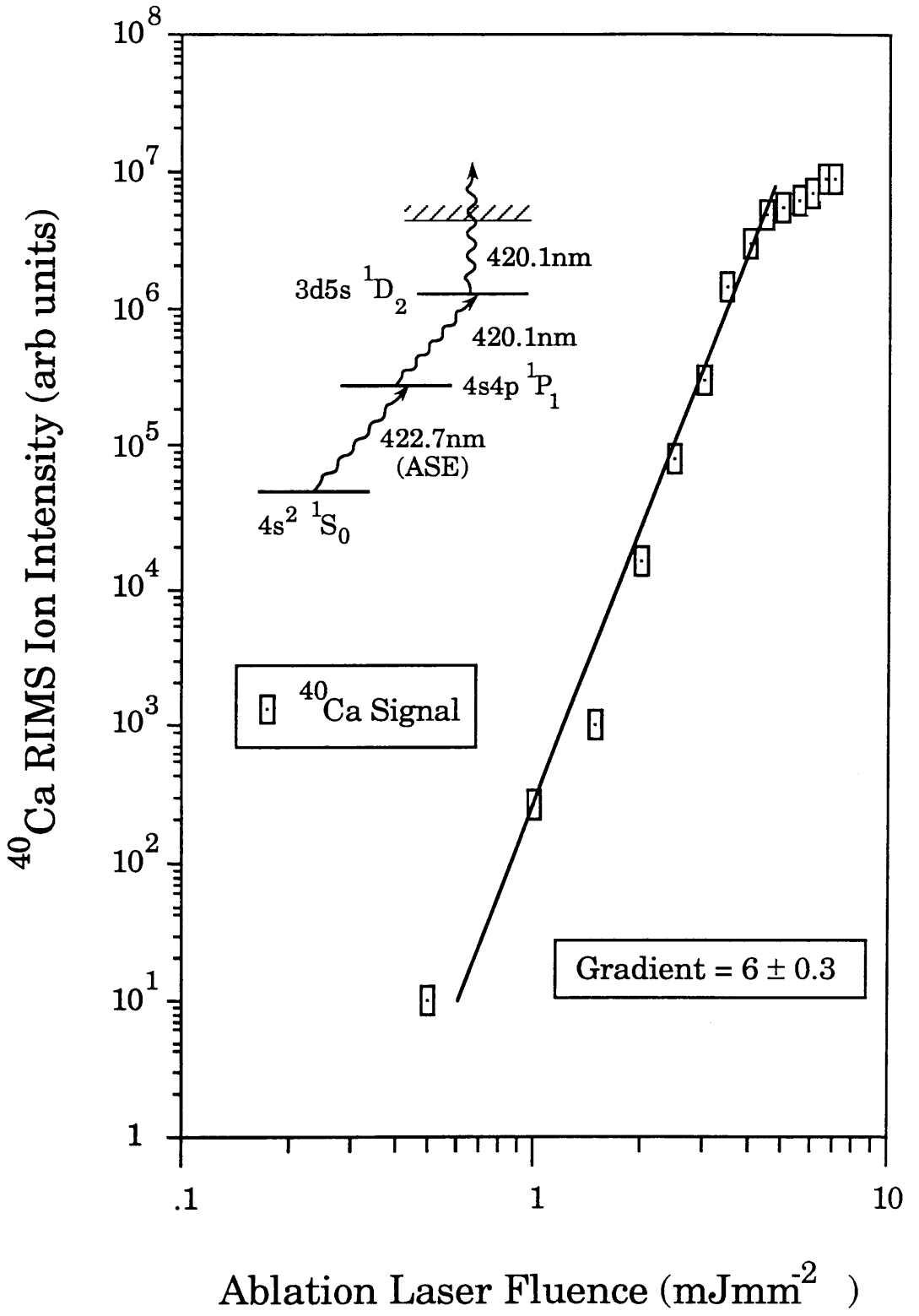

The resonant ionisation scheme used is shown in the fig 6.10 inset. As in the temporal work above, the calcium resonant ionisation scheme was not saturated.

This curve has two main features. There is an exponential rise in the neutral flux with laser fluences from 1mJmm^{-2} to 4mJmm^{-2} . Above 4mJmm^{-2} the neutral flux apparently levels off.

The rise when plotted on a log-log graph has a gradient of ~6 ± 0.3 ie:-

$$N_0 \propto I^{6 \pm 0.3}$$

where I is the laser energy and N_0 is the number of neutrals in the ground state. No explanation for the magnitude of the gradient is known.

Levelling off above 4mJmm^{-2} is thought to be due the saturation of the instrument, caused by space charge effects due to the large numbers of ions produced, rather than any physical mechanism in the sample-laser interactions. This is supported by the deterioration of the shapes of the calcium peaks at high fluences (fig 6.11 shows a normal peak and 6.12 shows a peak having undergone distortion typical of space charge effects).

Despite a literature search there seems to be no other group investigating the effects of laser flux on the number of neutrals produced. Most work investigates the number of ions produced. Antonov *et al* (1981) gives a quadratic intensity dependence at low fluxes (10^5 Wcm^{-2}) rising 'sharply' at high fluxes for organic molecules desorbed by UV lasers while Helvajian *et al* (1989) gives a intensity dependences of 12.5 at 248nm and 17.7 at 351nm with fluxes of 10^6Wcm^{-2} for iron and silver. Spengler *et al* (1989) quote a rise of 12 for the number of neutral molecules desorbed at 248nm and a irradiance of ~10^6 Wcm^{-2}. Rief *et al* (1989) quote a figure of 10 for the gradient of the Ba^+ signal from BaF_2 with fluxes above 3 MWcm^{-2}.

Fig 6.11: Normal Calcium Peak

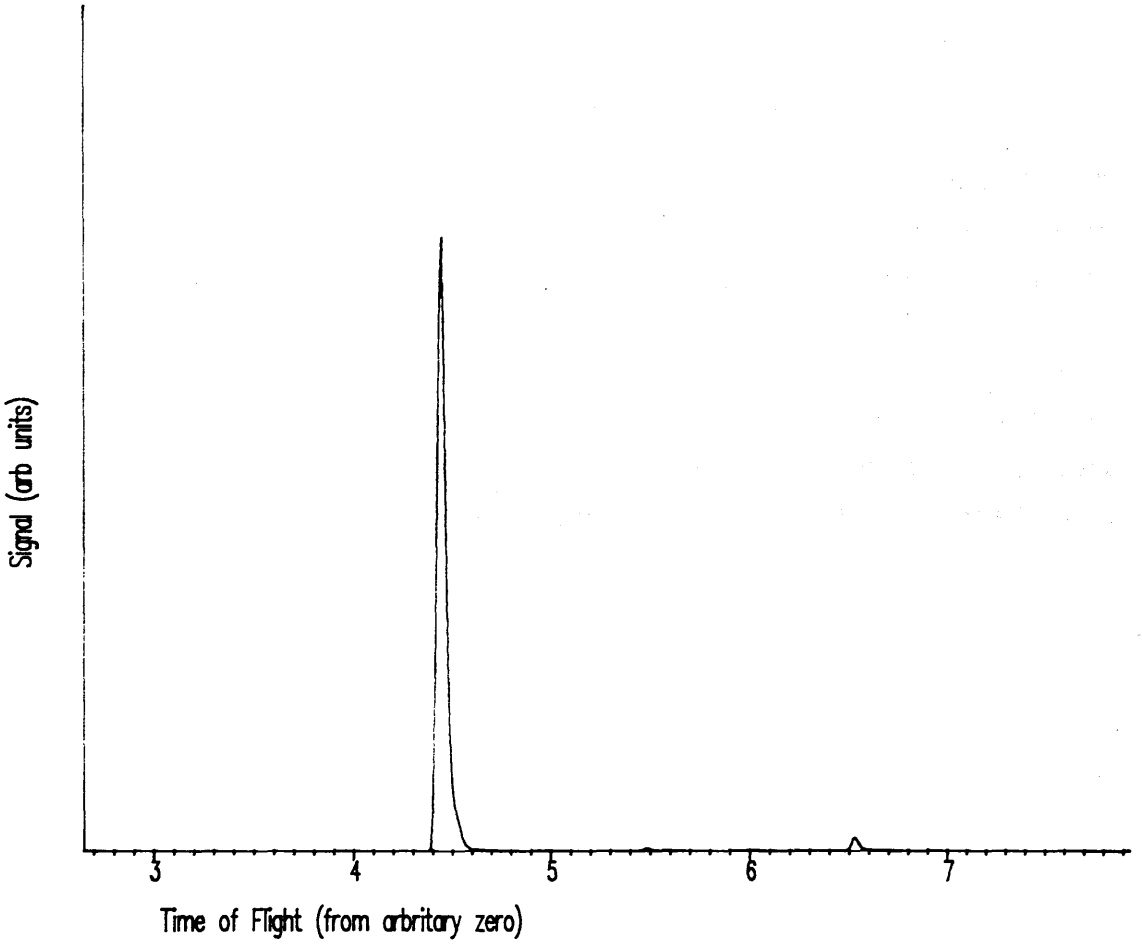

Fig 6.12: Severely Space Charge Affected Cacluim Peak

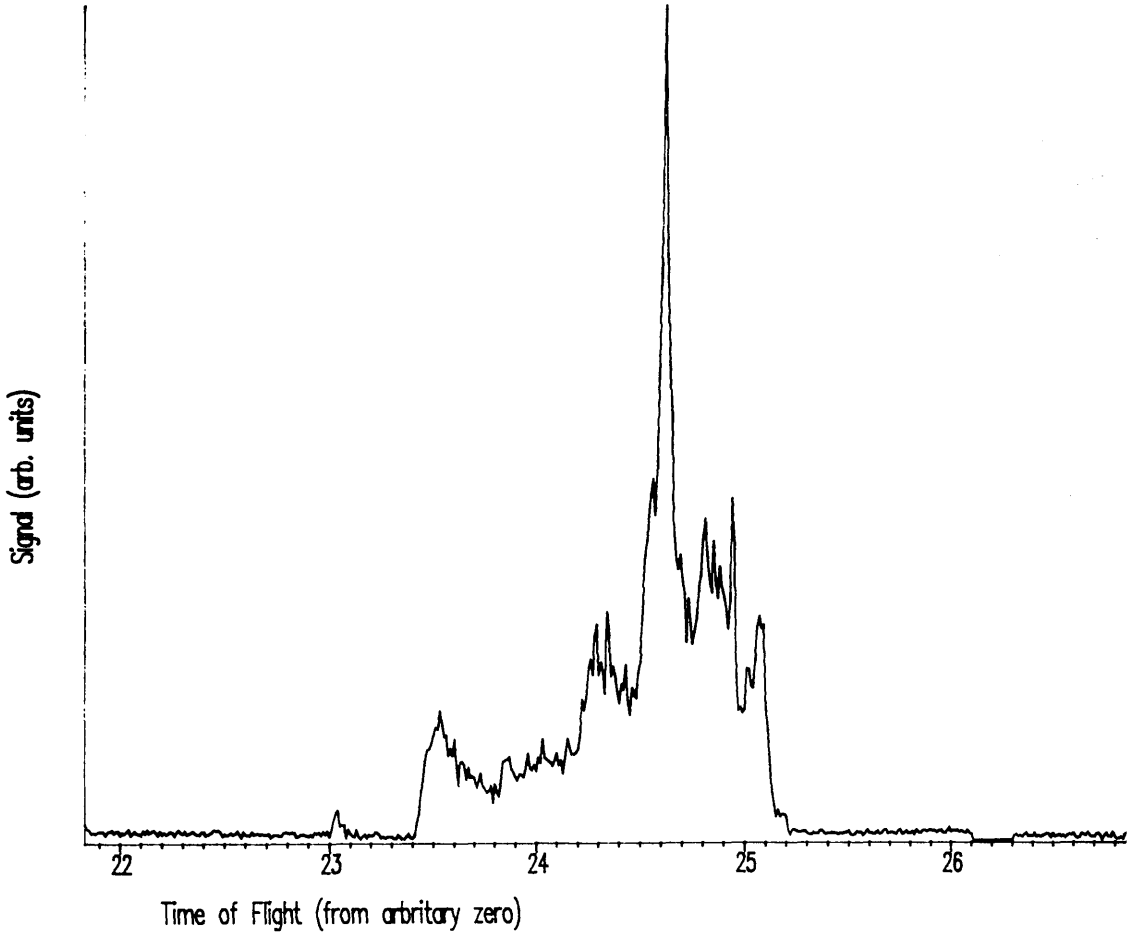

Temporal Dependence of Calcium Isotope Ratios.

As mentioned in chapter 5 the calcium isotope ratios obtained in all experiments on the Kratos machine were in poor agreement with the expected values. Discrepancies occured with the ratios being both too high and too low. These discrepancies are thought to be due to the poor optical quality of the ionising laser. Laser quality, on the Kratos machine, provides the limit on the accuracy of isotope ratio measurements. However, isotope ratio discrepancies can still occur when using laser ablation even with ideal optical quality from the post ionising laser.

This is because laser ablation, as shown above, can be modelled approximated as atoms being emitted thermally from a surface instantaneously. Each different isotope is be described by a different profile. Due to the different masses of the isotopes the profiles will not overlap but be slightly seperated. This is shown in fig 6.13.

Fig 6.14 shows the temporal dependence of the isotope ratio for the calcium isotopes ^{40}Ca and ^{44}Ca. This is from the same set of 1.064μm data that was used to produce fig 6.4. Shown also is the curve expected from the simple thermal model. It can be seen that such a model provides a reasonable description of the data, showing both the rapid fall at short delay times and the approach to an asymtotic value. Similarly shaped curves are seen with all wavelengths at this fluence (fig 6.15 and 6.16). This effects is also apparent at high fluences (fig 6.17).

A similar effect is seen for all pairs of calcium isotopes. As predicted, the greater the mass difference between isotopes the more pronounced the effect. One important ramification of this effect is that the correct isotope ratio for each pair is only obtained at one delay time, and furthermore this delay time is different for different pairs of isotopes.

The effect is pronounced in these experiments because the post-ionising laser was tightly focussed and was situated further than necessary from the sample surface. Thus only a small

Fig 6.13: Ablation Profiles for Neutrals of the Same Temperature and Different Masses

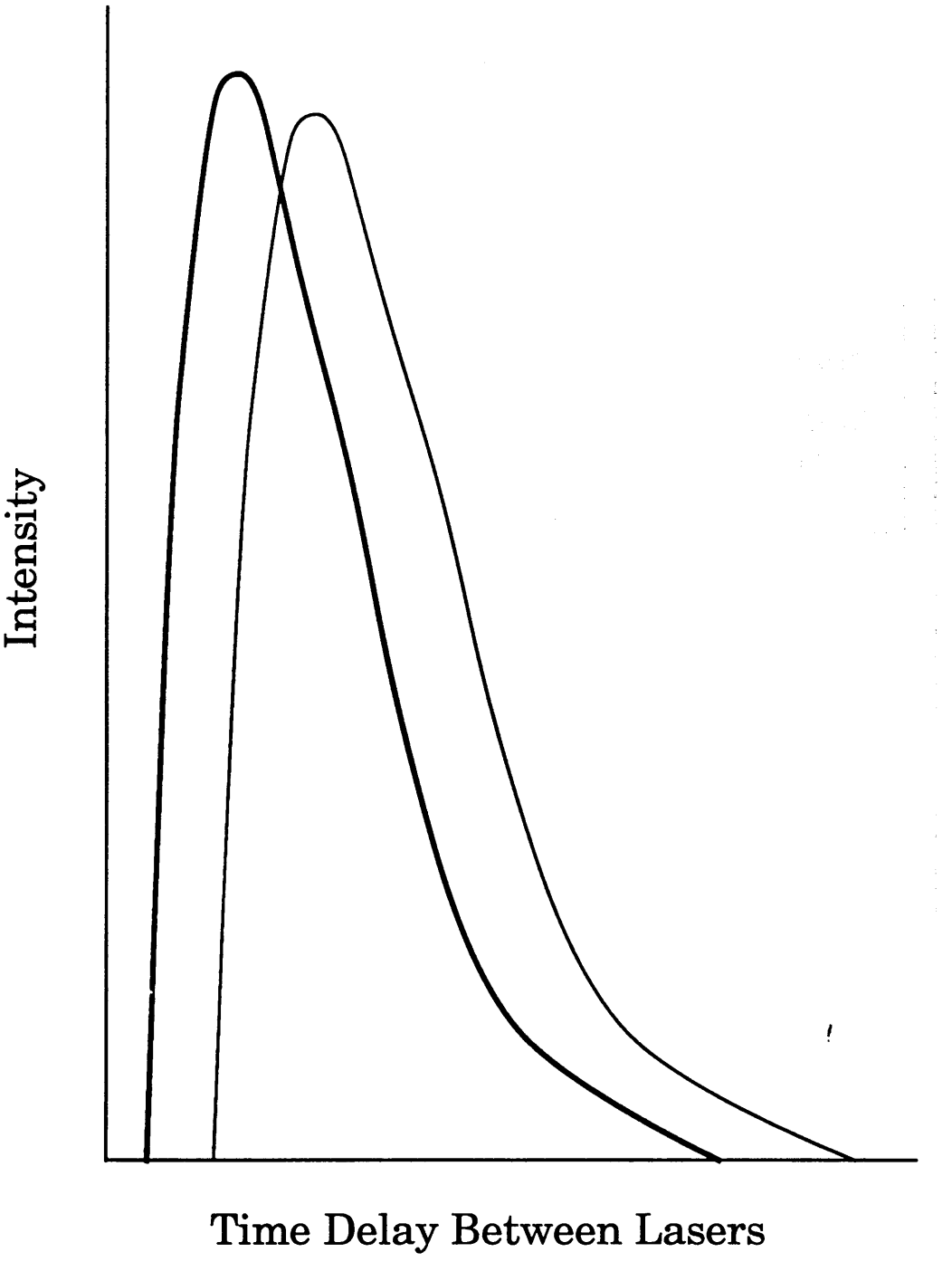

Fig 6.14: Normalised Calcium Isotope Ratio vs Time for 1.064μm Low Fluence Ablation

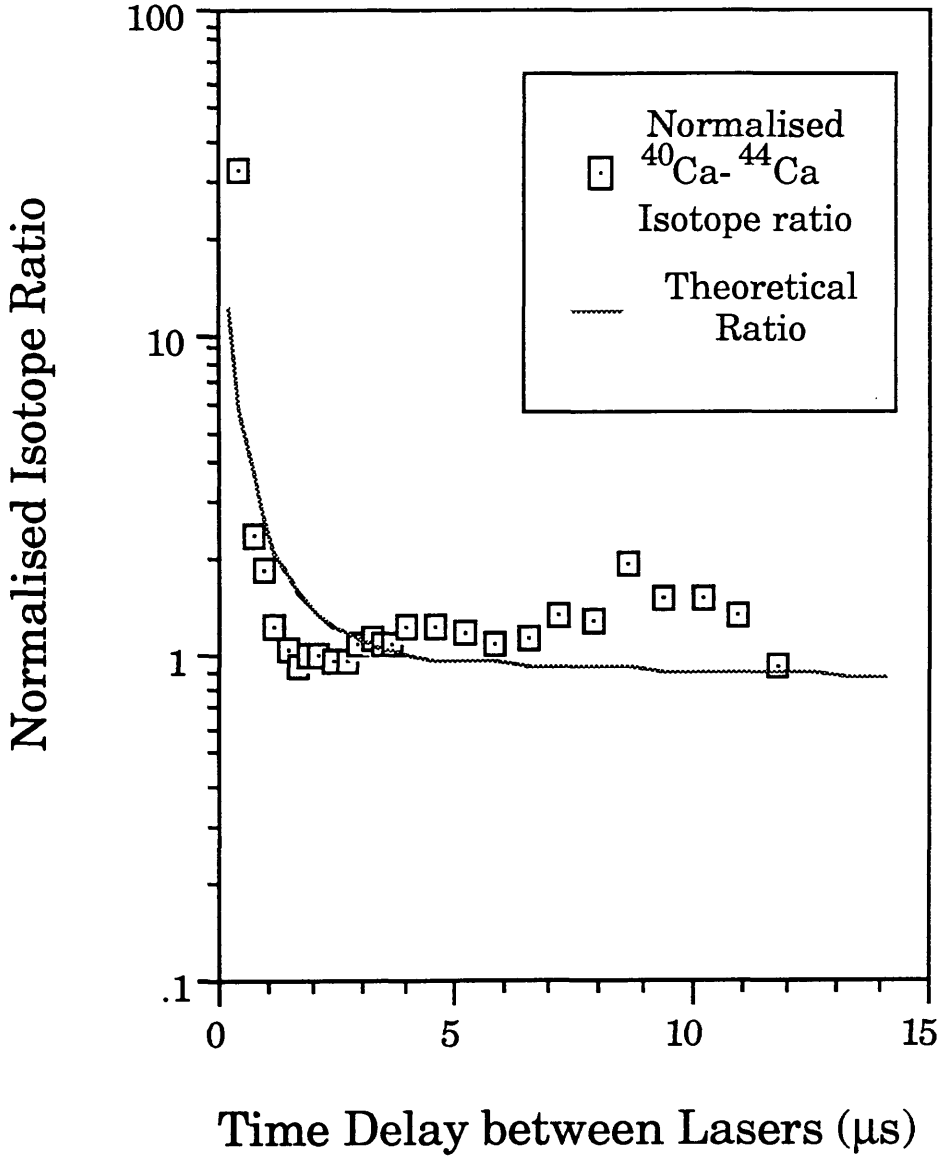

Fig 6.15: Calcium Isotope Ratio vs Time for 532nm Low Fluence Ablation

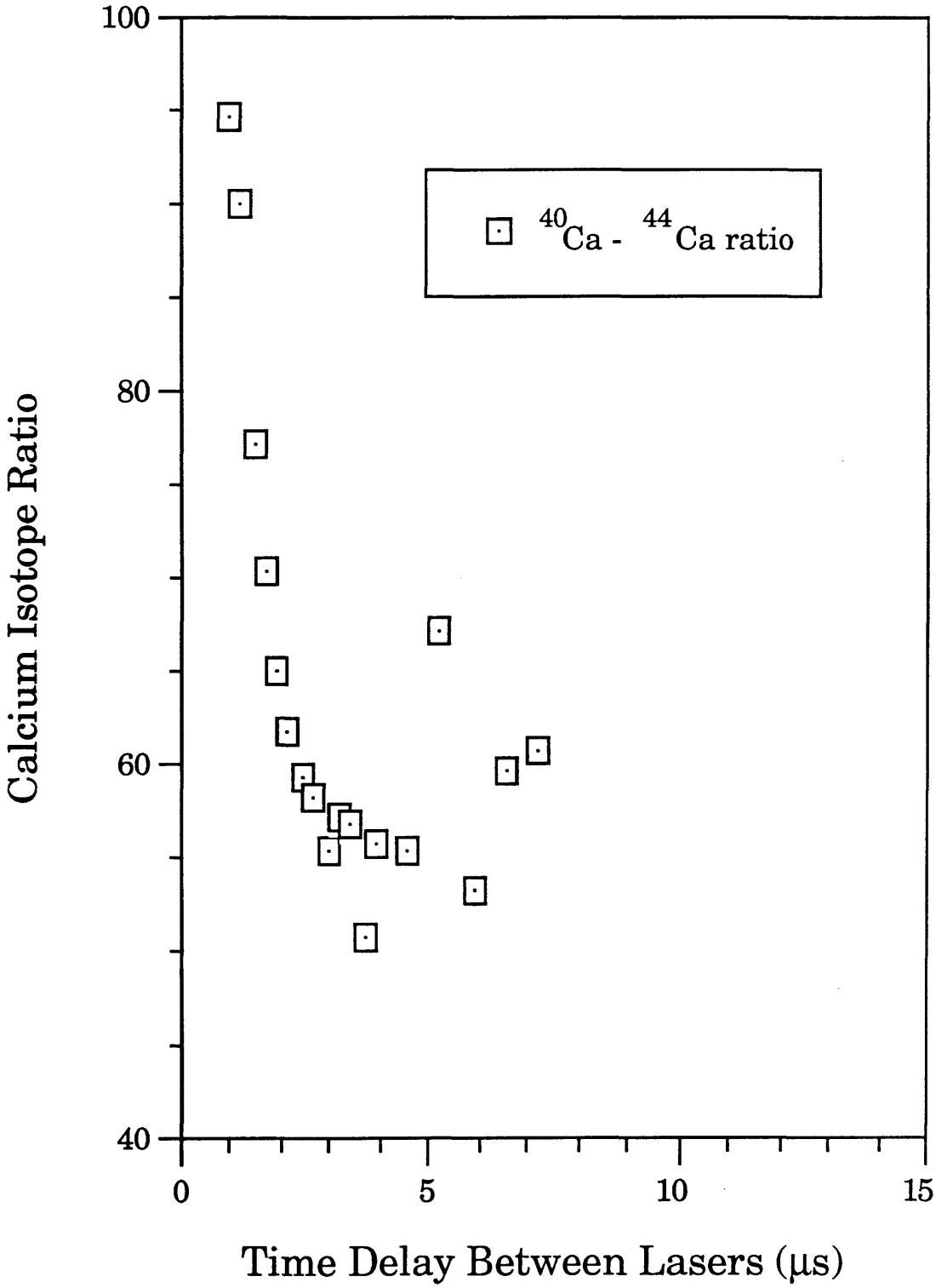

Fig 6.16: Calcium Isotope Ratio vs Time for 355nm Low Fluence Ablation

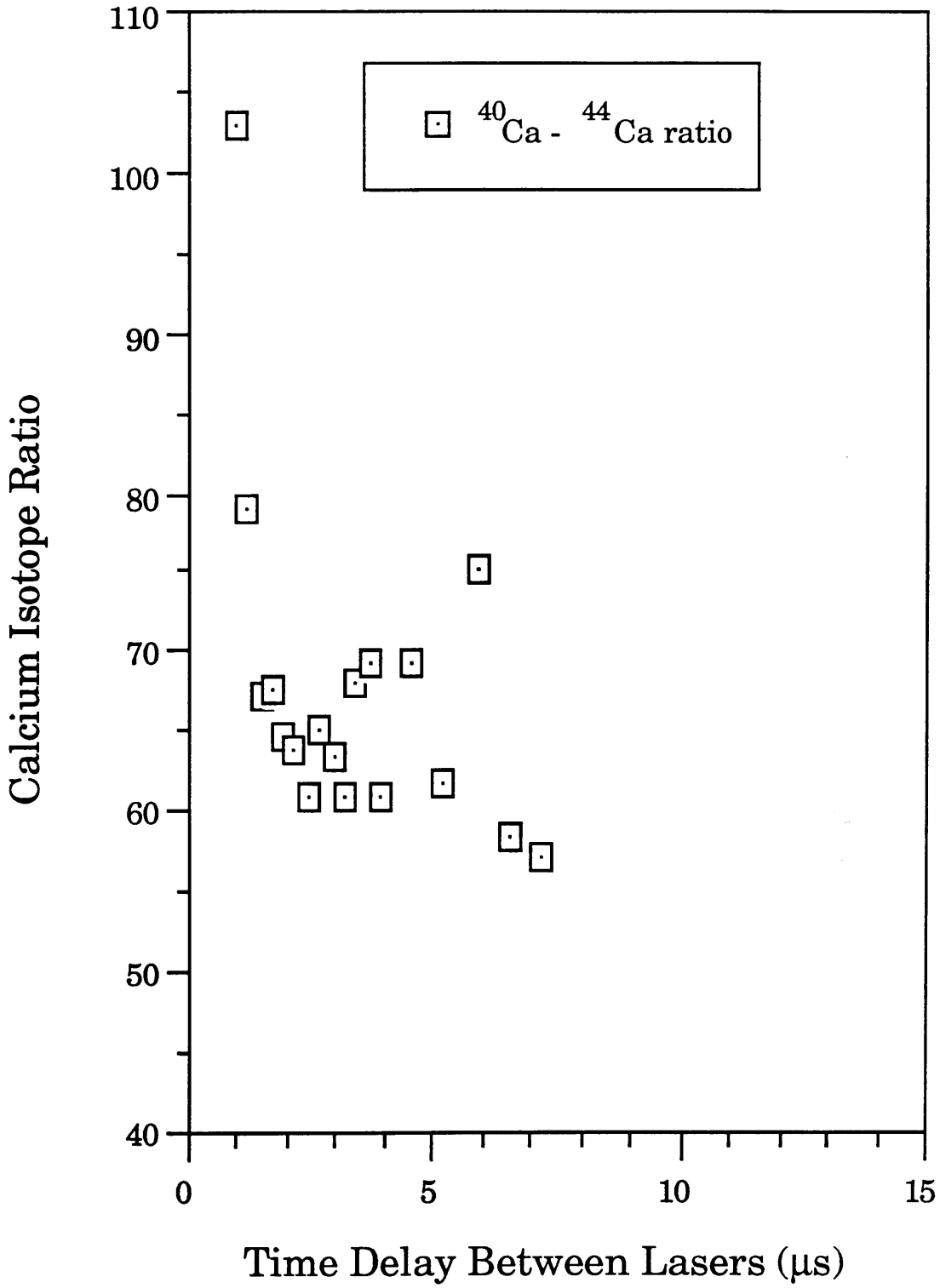

Fig 6.17: Calcium Isotope Ratio vs Time for 355nm High Fluence Ablation

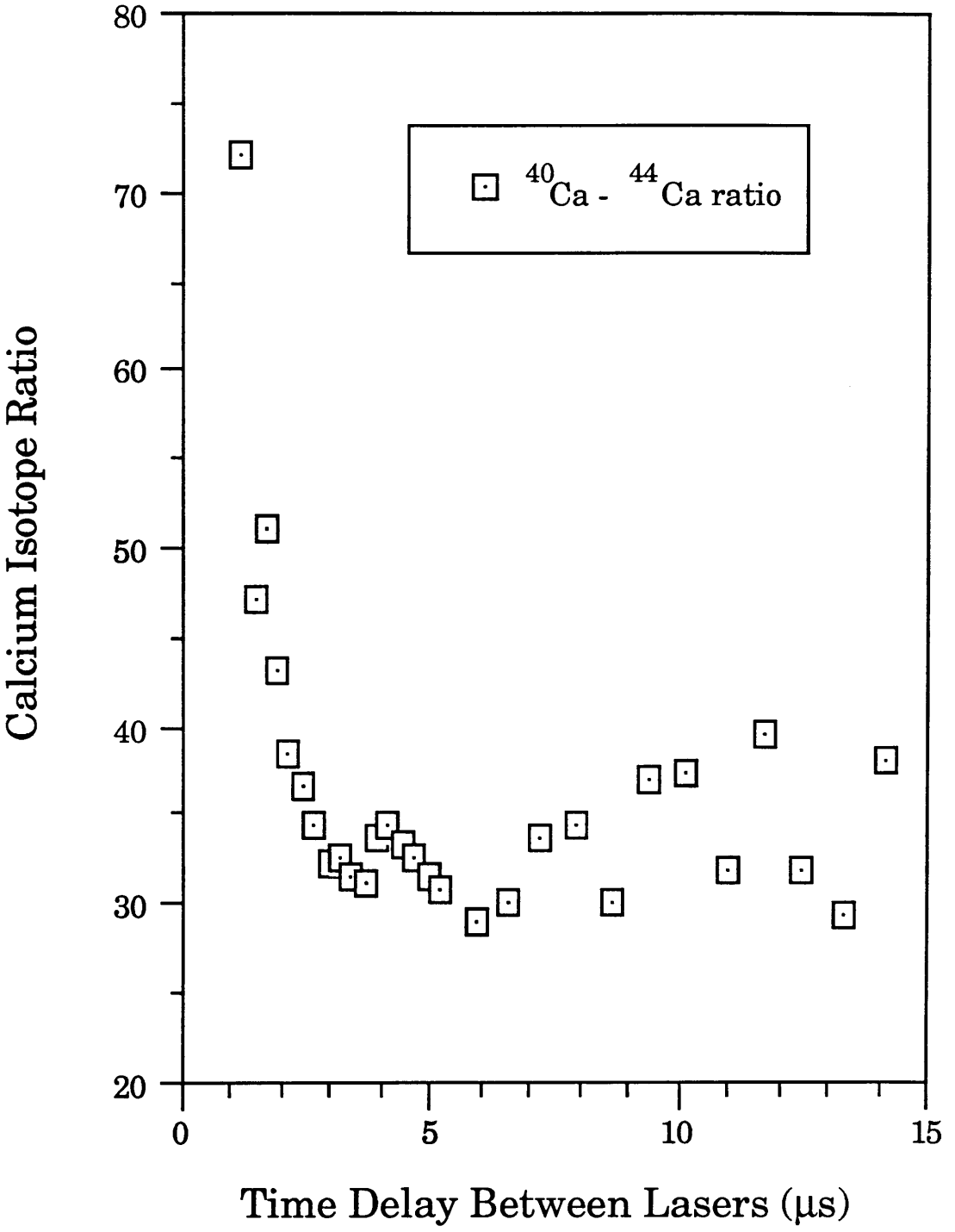

proportion of the plume was interogated at each delay. By increasing the ionisation volume or decreasing the distance to the sample the post-ionising laser will intecept a greater proportion of the plume and the bias in the isotope ratio would be expected to decrease.

Under some circumstances increasing the ionisation volume is impossible. For example sulphur, which is ionised using Hurst's scheme 5 (see chapter 1), requires tightly focussed post-ionising lasers to saturate the RIS scheme. Expanding the ionisation volume will mean losing saturation and could lead to possible problems associated with the optical quality of the lasers as discussed in chapter 5 and in the conclusions to this chapter.

§4 The Temporal and Fluence Dependence Of Gold using Non-Resonant Ionisation

Gold was the next element for which a temporal profile acquired. It was examined since the author was planning to perform trace analysis of gold. The results from these studies are presented in chapter 7.

The sample used in this case was gold foil (Goodfellow) mounted in similar way to other foils (chapter 5). Ablation was only carried out at 532nm. The UV wavelengths (355nm and 266nm) were too unstable and gold is highly reflective at 1064nm. The 532nm ablation laser was loosely focussed to $1mm^2$ to give fluences of between of $3mJmm^{-2}$ and $6mJmm^{-2}$. The gold was ionised non-resonantly using 266nm tightly focussed ($\sim 0.01mm^2$.) giving a fluence of around $50mJmm^{-2}$. Otherwise the experimental procedure was similar to that for calcium at low fluence.

Figs 6.18-21 show the variation of the temporal profile of the plume at fluences of 3, 3.5, 4, 6 $mJmm^{-2}$ respectively. It can be seen that the shape of the curve over this range of fluences is essentially unchanged. In comparison with the calcium peak shapes, despite being in the lower energy regime (fig 6.4) the peak width is closer to the high energy peak width (fig 6.5, fig 6.6). Also present on the profiles are large unexplained spikes,

Fig 6.18: Temporal Profile of Gold Ablation Plume at 3mJmm.$^{-2}$

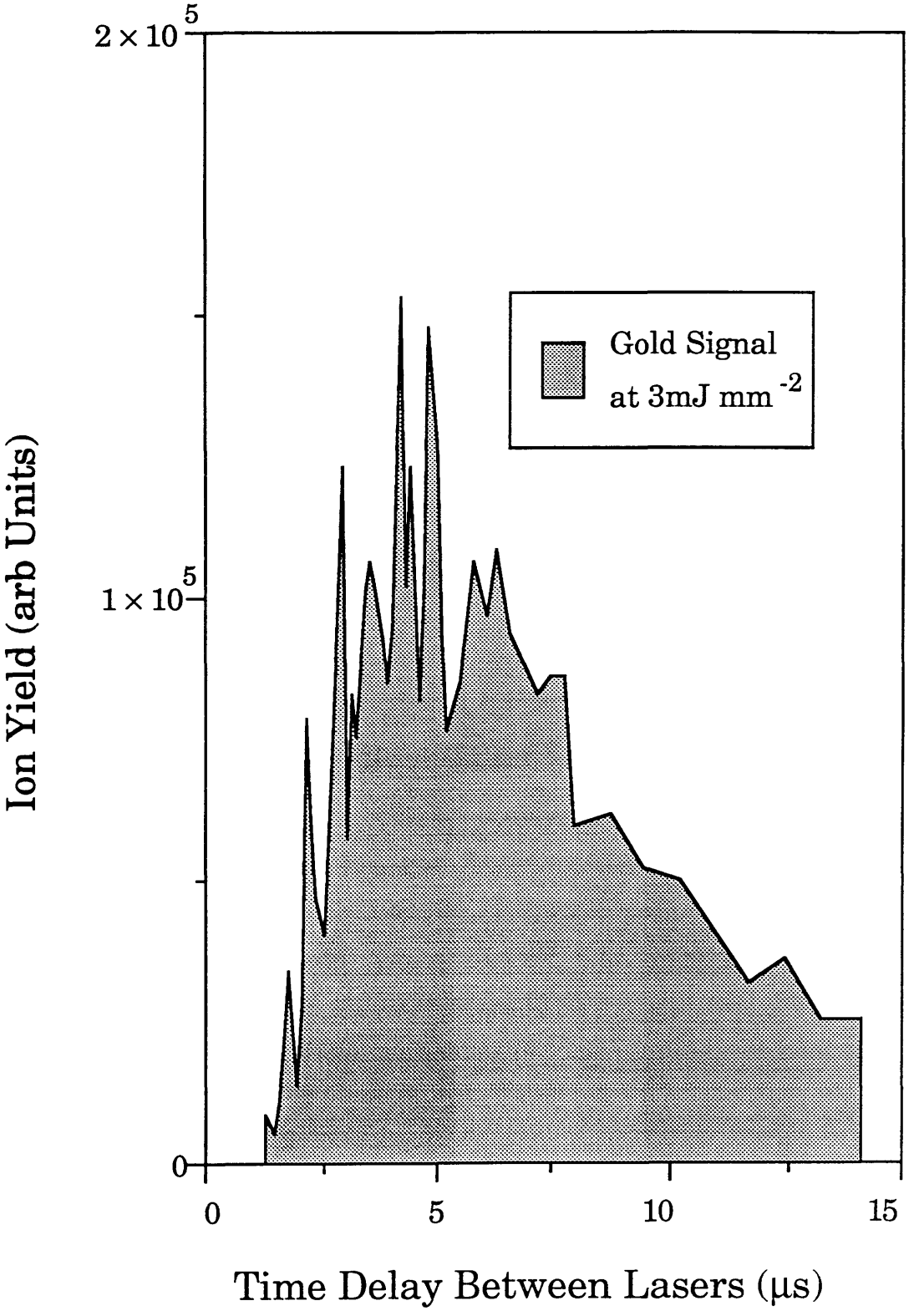

Fig 6.19: Temporal Profile of Gold Ablation Plume at 3.5mJmm^{-2}

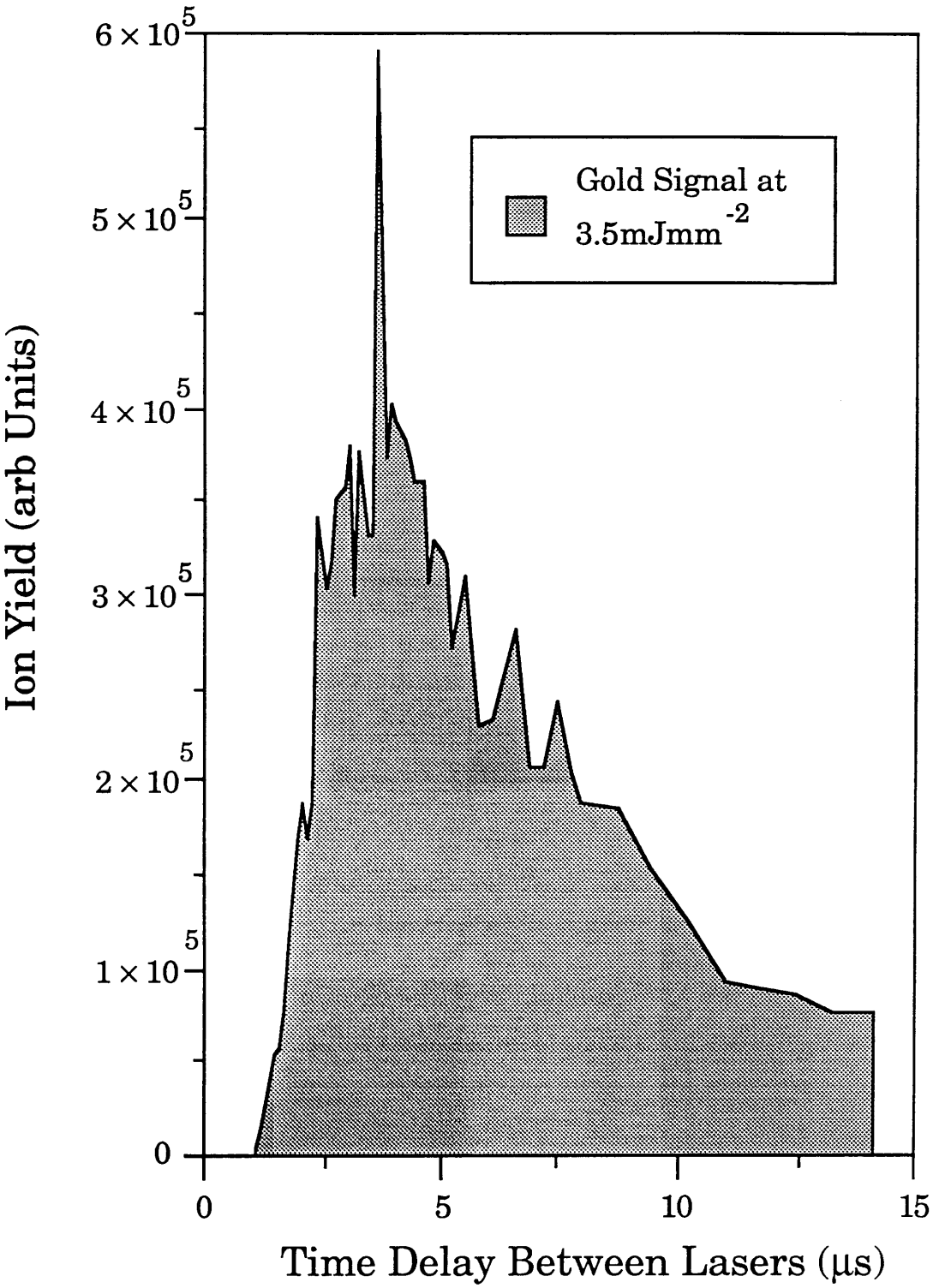

Fig 6.20: Temporal Profile of Gold Ablation Plume at 4mJmm^{-2}

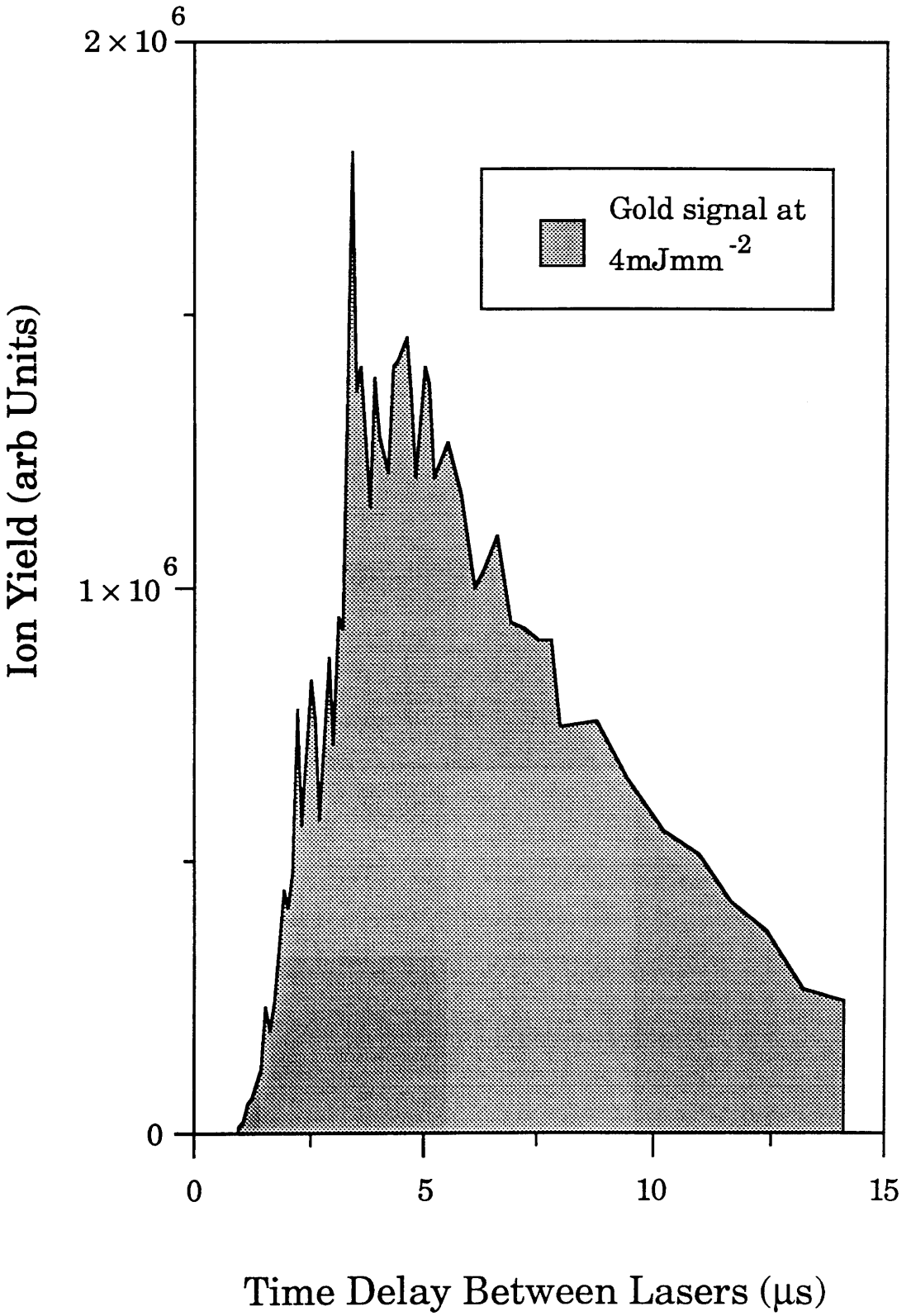

Fig 6.21: Temporal Profile of Gold Ablation Plume at 6mJmm^{-2}

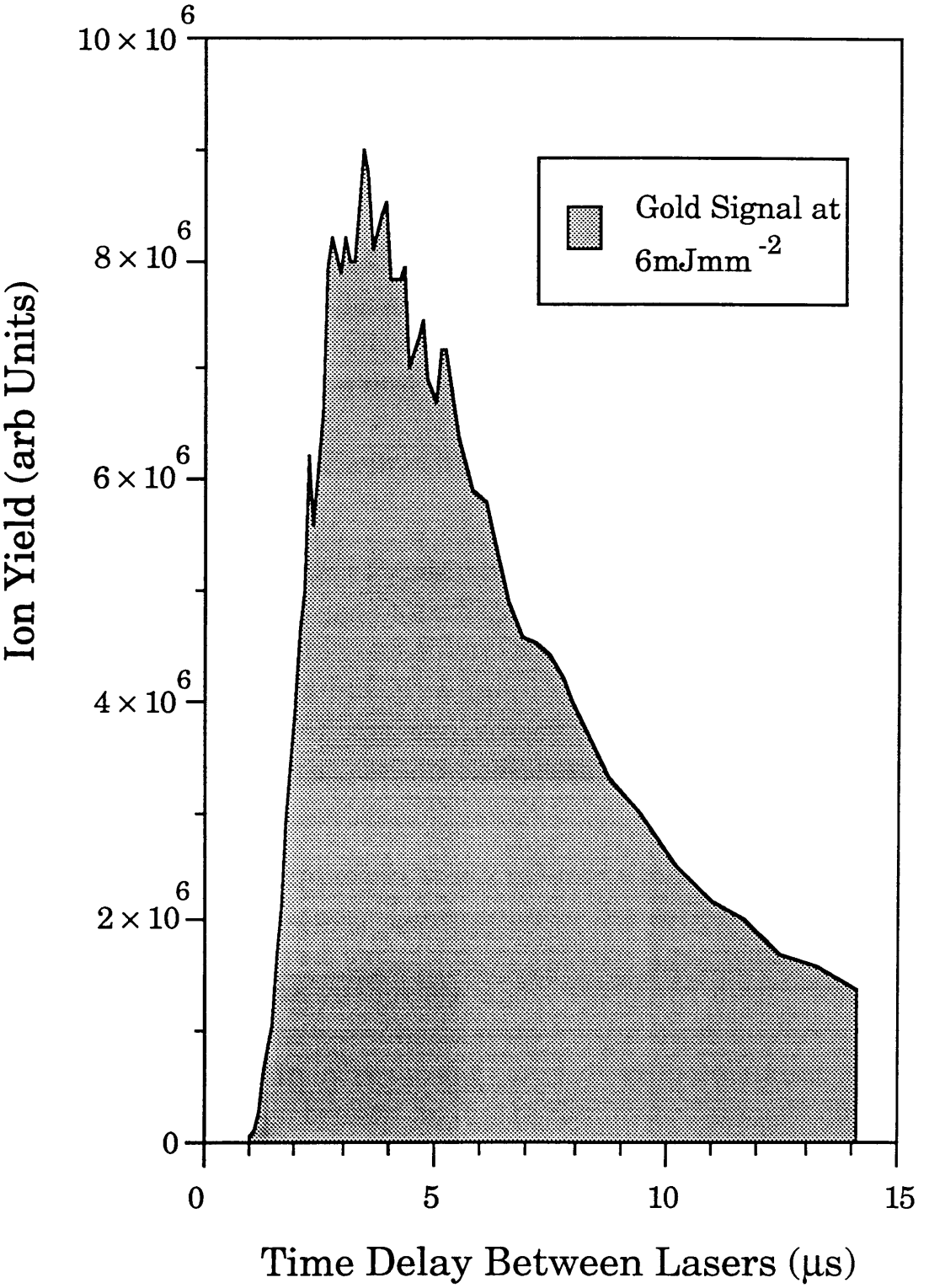

sitting on top of the a Maxwell-Boltzmann distribution. These will be discussed below. Fig 6.22 shows all peaks plotted together on a logarithmic scale. It can be seen that the peak widths do not change appreciably with ablation laser energy. The temperatures for all of these profiles are ~2000K. Consequently the temperature of the neutral component of the plume does not change measurably over the range of fluences used.

Fig 6.23 shows a log-log graph of neutral yield as a function of fluence. This has a gradient of 6.1 ± 0.3, which is consistent with the calcium dependency.

The spikes mentioned above are one of the most intriguing features of the gold temporal profiles. These spikes are similarly positioned in all the profiles, with only the magnitude varying. They are thought to be due to the break up and subsequent ionisation by the 266nm ionising laser of gold clusters formed in the ablation plume. Each different spike corresponds to a different cluster.

The spikes were most apparent at a fluence of $3.5 mJmm^{-2}$. Several repeated runs gave qualitatively the same structure. The heights of the spikes did not follow the intensity relationship of the 'mono-atomic' gold but grew more slowly. The clusters must be ejected with a well defined velocity, since the spikes are narrow compared to the 'mono-atomic' gold distribution underlying them.

No spikes were apparent when resonant ionisation was used on trace samples (chapter 7) but, due to the different nature of the samples, this was expected. A further test would be the acquisition of a temporal profile using resonant ionisation of a gold foil. If the clusters are broken up by the high fluence of the 266nm used then in a resonant ionsiation experiment these clusters would not be broken up due to the lower fluences used. If the clusters were short lived then spikes should be apparent on a resonant ionisation profile.

Fig 6.22: Logarithmic Display of Temporal Profiles of Gold Showing Variation with Fluence

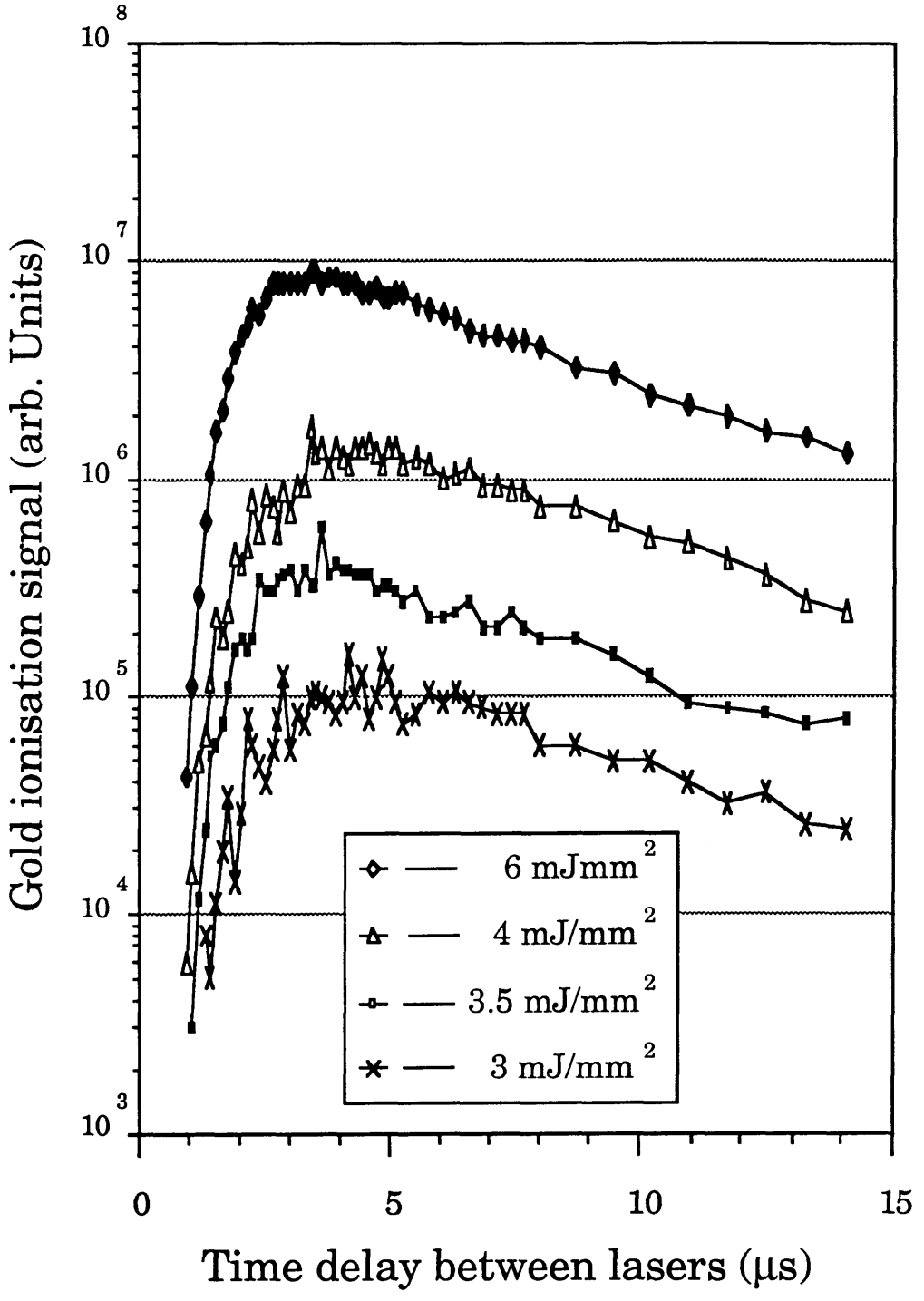

Fig 6.23: Log-Log Graph of Gold Yield versus Ablation Fluence

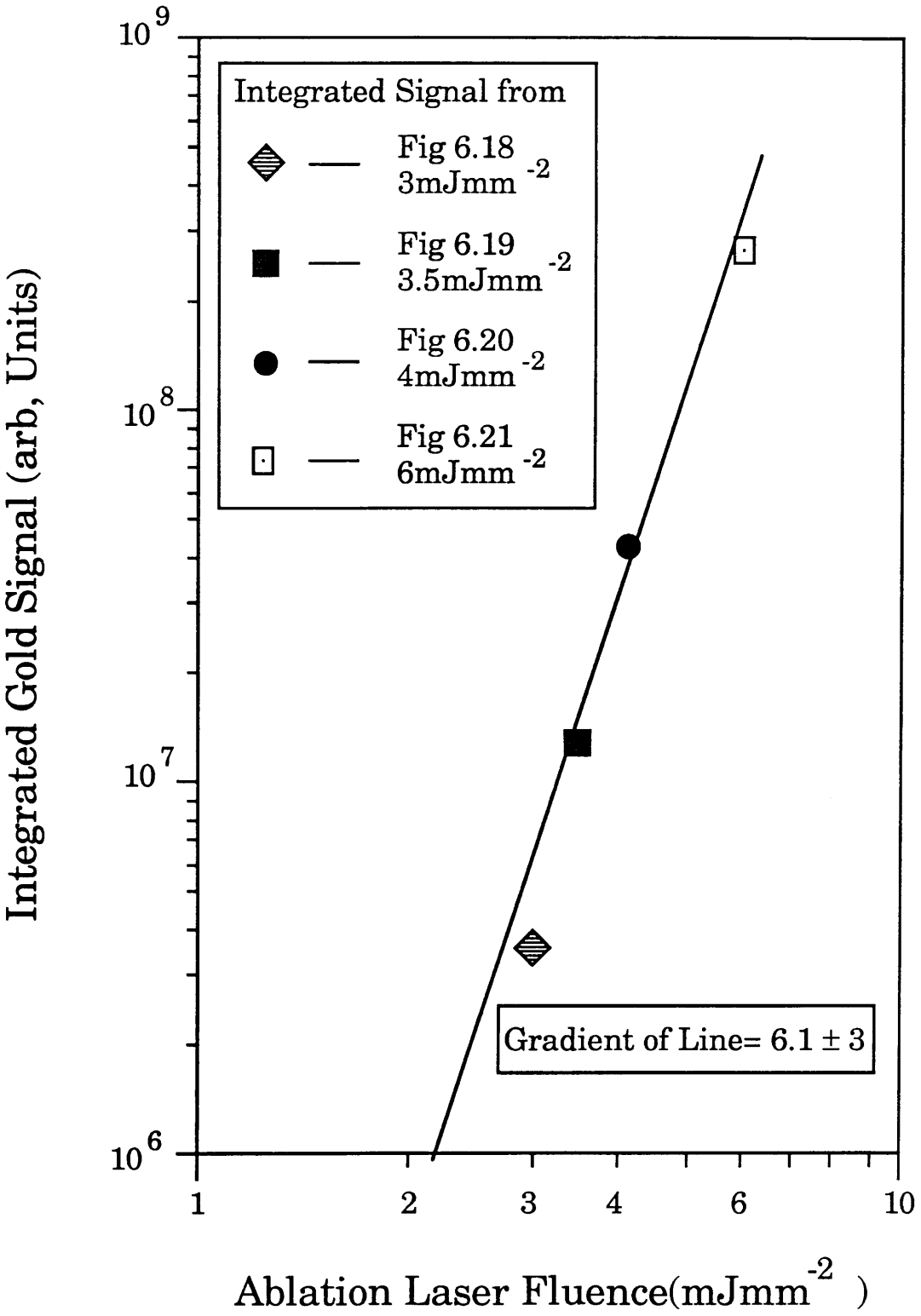

§5 Temporal Dependence of Gold using Resonant Ionisation

This was performed in a similar manner to the non-resonant ionisation experiment above with the difference that the gold sample was not a pure foil but a sample with 100ppm gold in a copper matrix. These samples are described in chapter 7. The method of taking data was different in that instead of 1000 shots data runs being taken at each delay time, three 300 shot runs were taken. This was to allow an estimate of the uncertainties in the peaks to be made since the absolute sizes of the peaks were much smaller than peaks obtained from pure metal samples.

The gold sample was ablated with 532nm Nd:YAG output with a fluence of $3mJmm^{-2}$ in the same manner as for non-resonantly ionised gold.

The fluence of the resonant post-ionising laser was $100\mu Jmm^{-2}$. The laser had an ionisation area of approximately $1mm^2$ and the wavelength used was 267.2nm. This fluence was sufficient the saturate the bound-bound resonant gold transition but not to saturate the ionisation transition. Full details of the gold spectroscopy used are given in chapter 7.

Fig 6.24 shows the distribution obtained. The width of the distribution is similar to the distribution from the non-resonant gold. This indicates that the width of the earlier gold work is not due to the foil sample used or to the post-ionising method. The distribution is estimated to have a temperature of 2000K, which is comparable to the temperature of non-resonantly ionised gold.

§6 Temporal Profile of Lead by Non-Resonant Ionisation

After analysis of the temporal profile of non-resonantly ionised gold, it was decided to perform an experiment with an element of similar atomic weight to try to determine if the width of the gold distribution was due to its high atomic weight. Lead (Goodfellow foil sample) was chosen for this purpose. Lead was non-resonantly ionised in the same manner as gold.

Fig 6.24: Three Temporal Profiles of Trace Gold using Resonant Ionisaiton

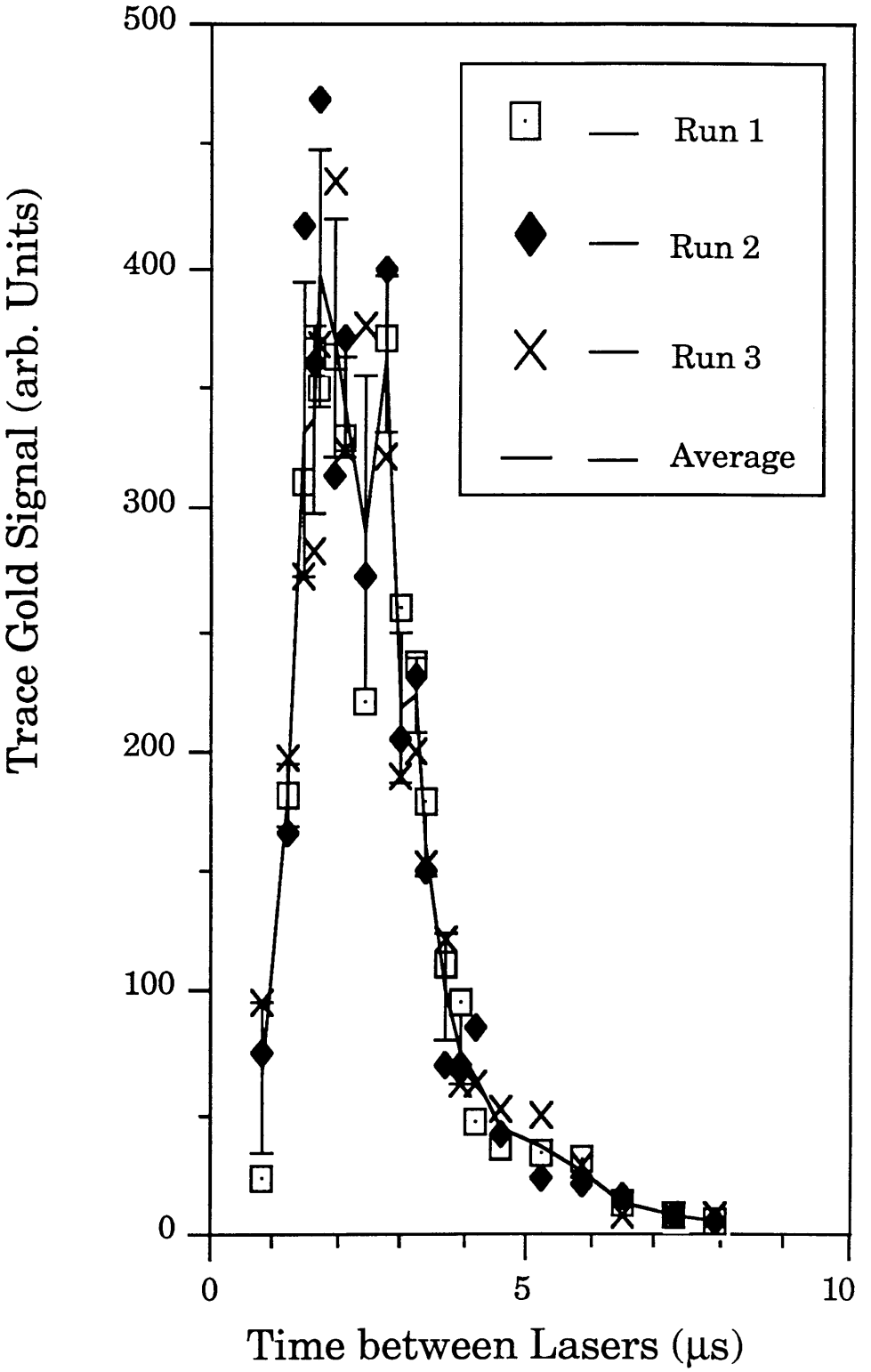

The lead was ablated with a fluence of $3mJmm^{-2}$ in the same manner as for the non-resonant gold experiment.

Fig 6.25 shows the temporal profile obtained. It is apparent that the lead distribution is not as intense at long delay times as the gold distribution at the same fluence.

Fitting a Maxwellian curve gives a temperature of 1600K with the usual angular dispersion being assumed (fig 6.25). By decreasing the angular dispersion to zero and increasing the temperature to 1800K a similar fit can be made (fig 6.26). This illustrates why attempting to calculate the angular distribution from the acquired data was not successful.

Also visible on fig 6.25 is some fine structure. This experiment was repeated several times and, unlike non-resonantly ionised gold, no reproducible structure was visible.

§7 Aluminium Ablation

Temporal Profile of Aluminium Ablation

Experiments with aluminium were conducted because if differences in the ablation process were connected with the atomic mass of the ablation material then the differences would be expected to show up most dramatically if aluminium and lead were compared. Lighter metals were possible (eg beryllium and lithium) but, for reasons of toxicity and reactivity, these were not used.

A sample of aluminium foil (Goodfellow 99% pure 1.02mm thick) was used as the sample. The experimental procedure was as for low energy calcium. A 532nm ablation laser of fluence $1mJmm^{-2}$ and a 266nm tightly focussed post-ionising laser ($50mJmm^{-2}$) were used.

Fig 6.27 shows the temporal profile obtained. Also shown is a Maxwell Boltzmann fit to the data. The temperature of the fit is 900K.

Fig 6.25: Temporal profile of Lead at 3mJmm^{-2}

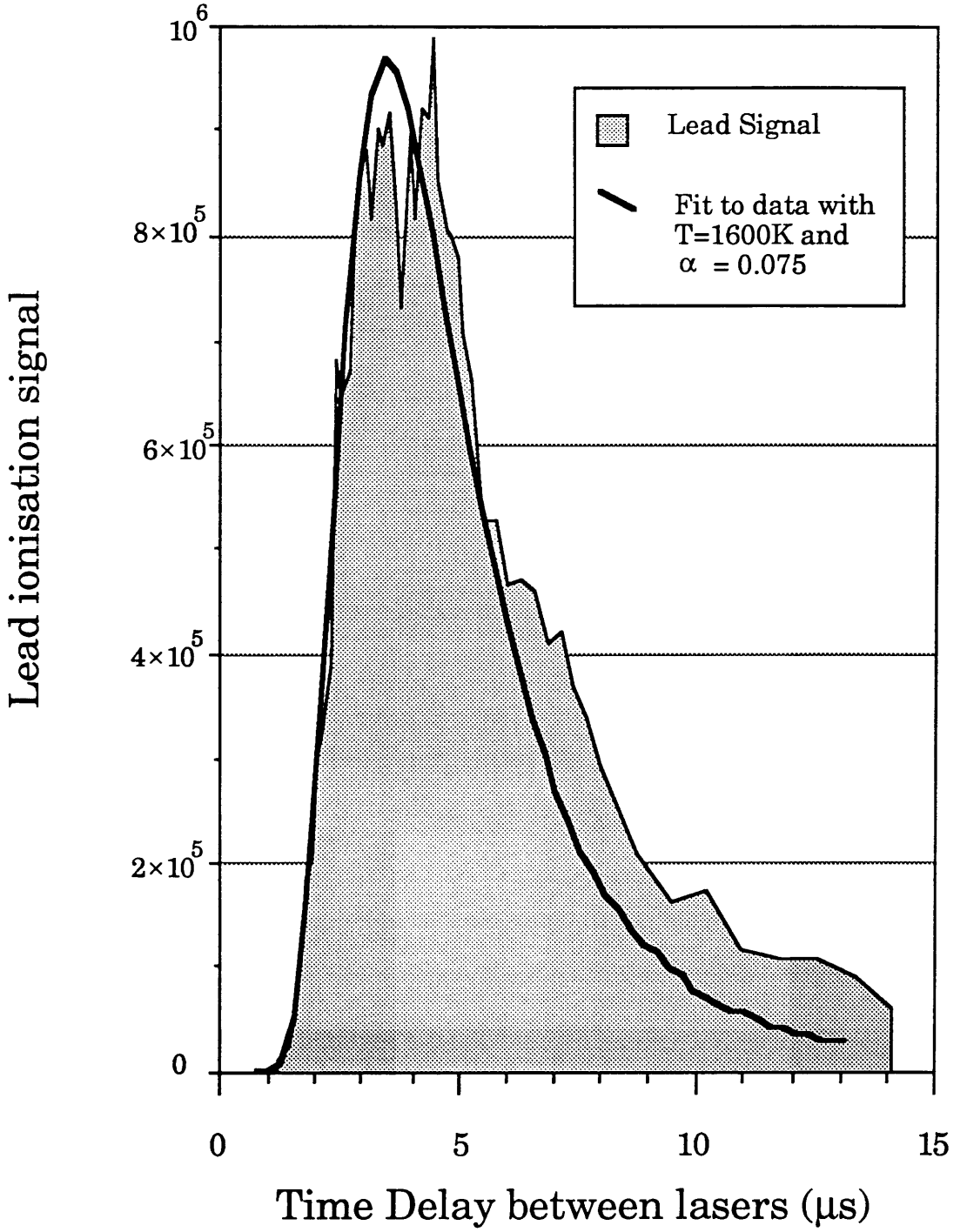

Fig 6.26: Temporal Profile of Lead at 3mJmm^{-2}

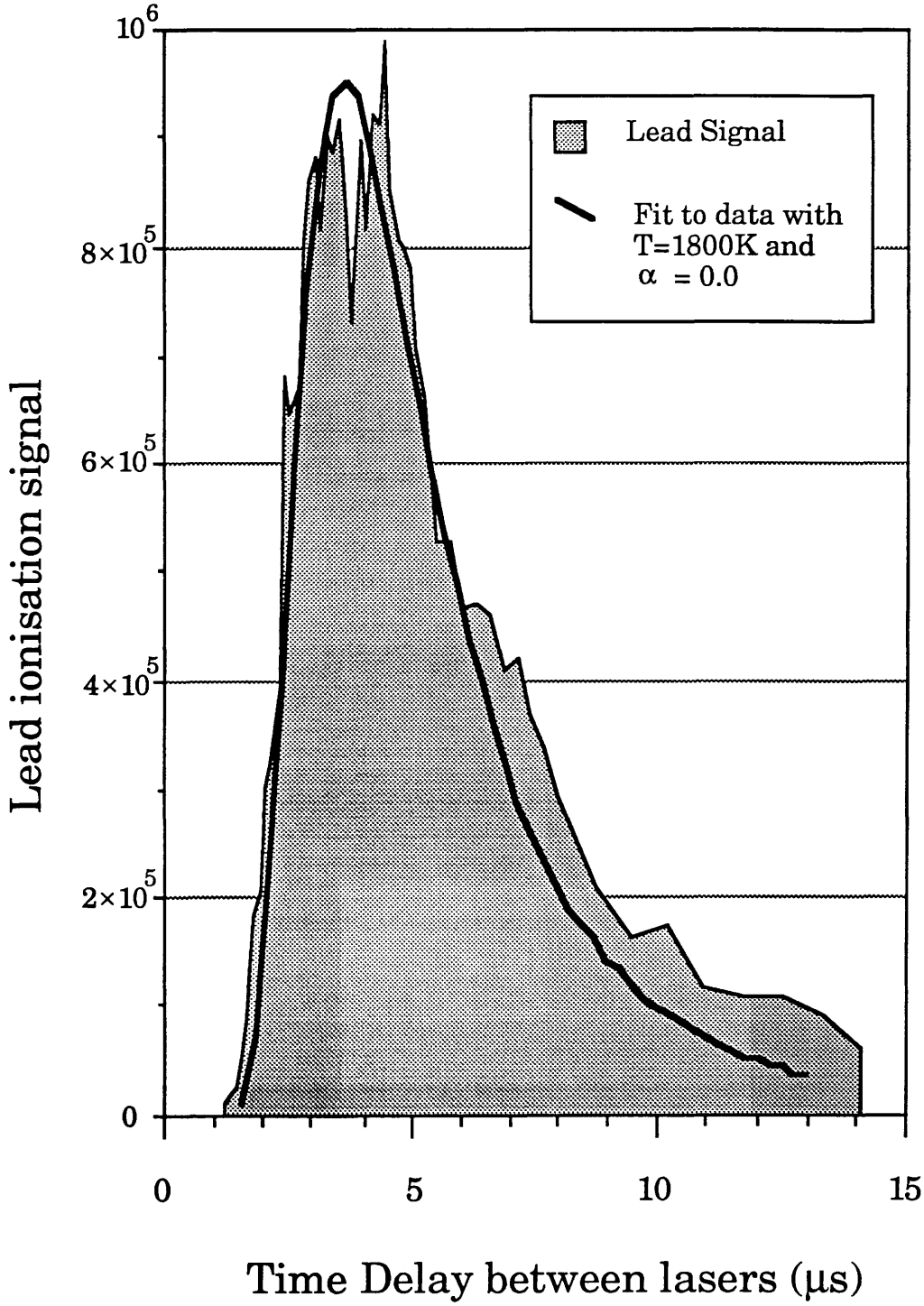

Fig 6.27: Temporal Profile of Aluminium at 1mJmm^{-2}

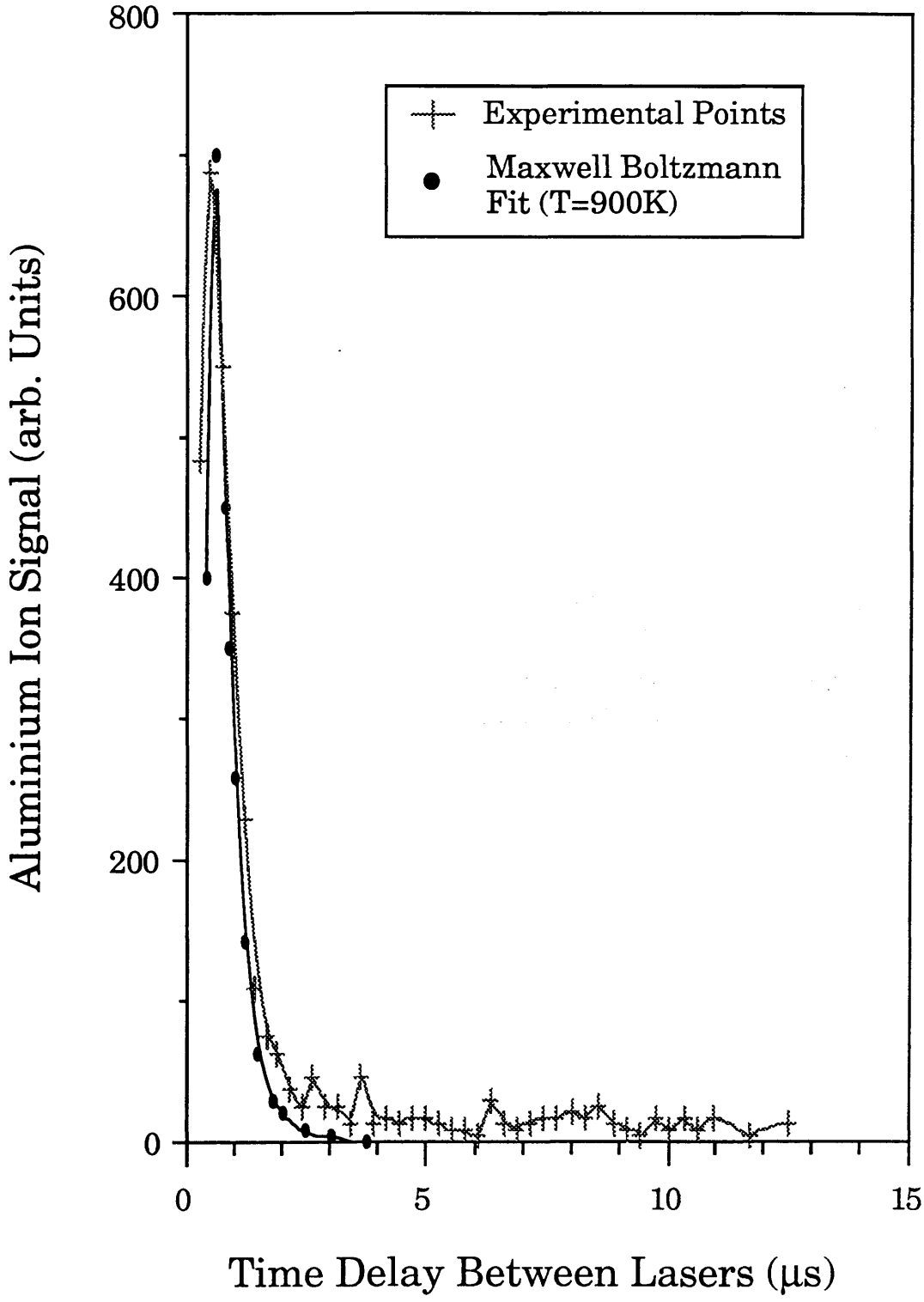

Aluminium, like gold, has significant signal at long times at low energies.

Fluence Dependence of Aluminium Neutral Production

In the same fashion as for calcium a fluence dependence for aluminium was obtained. The time delay between lasers was set to the peak of the temporal distribution and the fluence of the ablation laser was varied. The aluminium was post ionised non-resonantly ionised using 266nm fourth harmonic Nd:YAG. The fluence dependence is shown in fig 6.28.

The dependence is similar to the calcium dependence except the the post-ionisation signal saturates at lower fluences. The coefficient, estimated from the rising part of the graph, is ~6. The low number of points makes a precise calculation impossible. This is consistant with the values obtained for calcium and gold.

§8 Stainless Steel Ablation

The final sample which was analysed in this manner was a stainless steel NIST standard sample. The elemental composition of this standard is shown in table 6.2 below. This was selected to examine the differences in the ablation rates and temporal profiles for different elements in the sample. The method was as for the non-resonant gold profile.

Since different elements were to be simultaneously ionised, resonant ionisation was impossible. By using tightly focussed 266nm Nd:YAG it was possible to non-resonantly ionise several of these elements simultaneously.

Three elements were chosen: iron, which is the matrix, chromium and manganese. These were the elements for which statistically significant temporal profiles can be obtained in a 6μs time window around iron. A typical spectrum from which the temporal profiles were obtained is shown in fig 6.29.

Fig 6.30 shows six temporal profiles of Fe^{56} taken at three different fluences. Two profiles were taken at each fluence with

Table 6.2: NBS Cr-V Steel Standard 1263a

Element	Percent (by weight)
Carbon	0.62
Manganese	1.5
Phosphorous	0.02
Sulphur	0.005
Silicon	0.74
Copper	0.09
Nickel	0.32
Chromium	1.31
Vanadium	0.31
Molybdenum	0.03
Tungsten	0.046
Cobolt	0.048
Titanium	0.05
Aluminium	0.24
Zirconium	0.05
Tin	0.1

Fig 6.28: Fluence Dependence of Aluminium Ablation Neutrals and Ablation Ions.

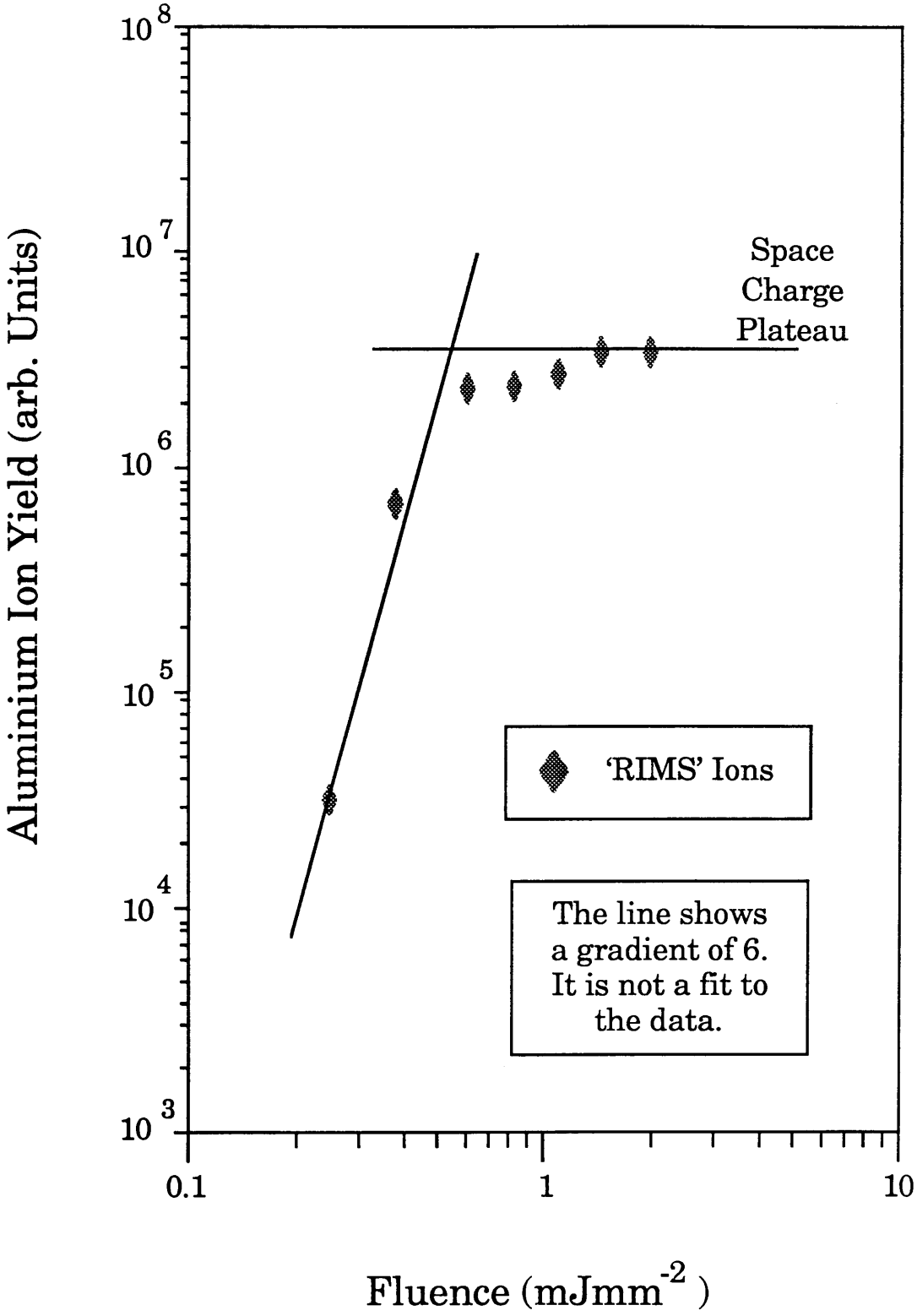

Fig 6.29: Typical Stainless Steel Spectrum

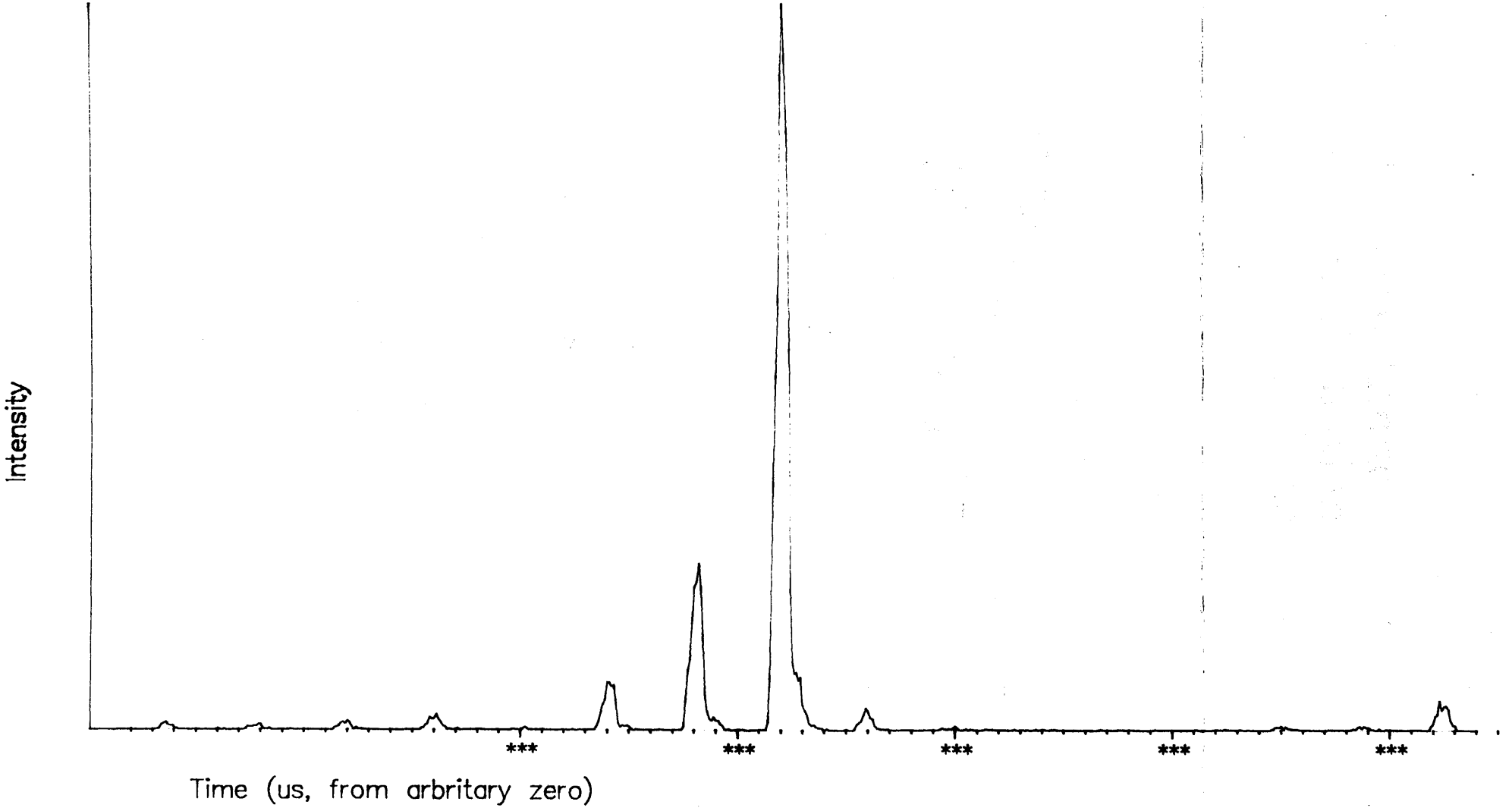

Fig 6.30: Logarithmic Display of Iron 56 Distributions from Stainless Steel at Three Fluences

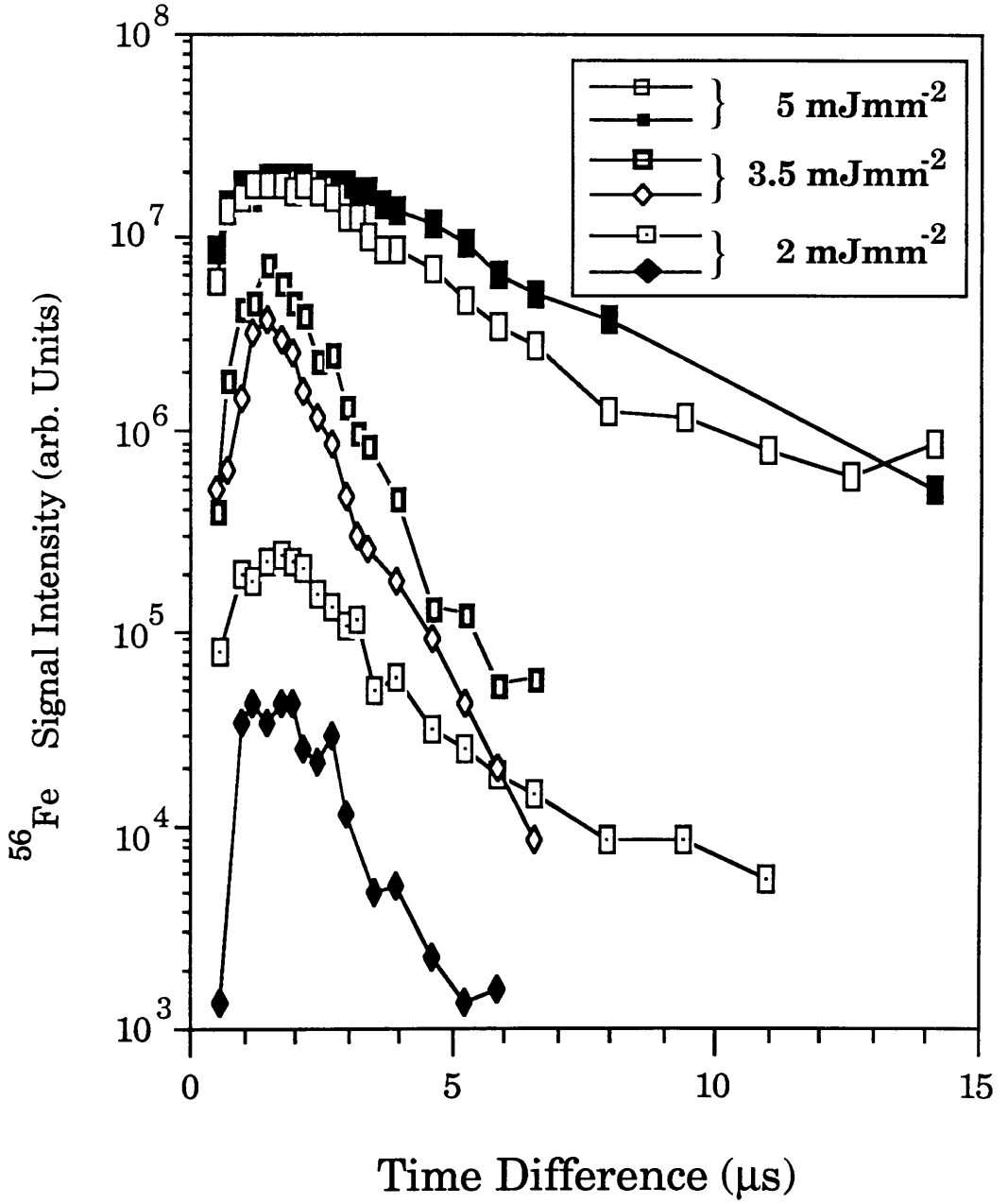

a new area of sample being used. In each case the lower of the two profiles was second to be acquired. Figs 6.31-6.33 show each pair of profiles on a linear scaled graph. Except for the highest fluence, there was a large difference between the repeated runs. The reasons for this are not known.

Another important feature of these spectra is that the height of the temporal profile at long times (as compared to the maximum of the profile) changes from the type of behavior seen in calcium at low fluence (ie. small at large times) to the type of behavior seen in gold at low fluence (ie. large at large times).

In line with the results from gold and calcium ablation the iron signal increases with laser intensity. Since only three different fluences were used, and because of the large variation of yield at constant fluence, it is impossible to calculate a coefficient for the dependence in the same manner as for calcium and gold.

Fig 6.34 shows the two iron isotope signals (Fe^{56} and Fe^{54}), together with manganese and chromium profiles. At this fluence the manganese was higher than the Fe^{54} signal despite the iron being approximately three times more abundant. The chromium signal also shows a large difference from the manganese, although manganese and chromium were present in similar quantities. Fig 6.35 and 6.36 show these temporal profiles at medium and high fluences. All other parameters were as for the lower fluence experiment. These shows an increase in Fe^{54} in comparison with Mn, although the Mn signal is still to large. The Cr/Mn ratio is as for the lower fluence profile. Thus, laser ablation exhibits clear matrix effects for stainless steel.

§9 Discussion and Conclusions

For all elements analysed, the peak of the temporal profile occurred, for a laser sample distance of 2mm, at approximately 2μs. This implies that the delay between the ablation laser and the ionising laser is not critical, and can be left unchanged for a wide range of elements.

Fig 6.31: Linear Display of Iron 56 Temporal Profile at 2 mJmm $^{-2}$

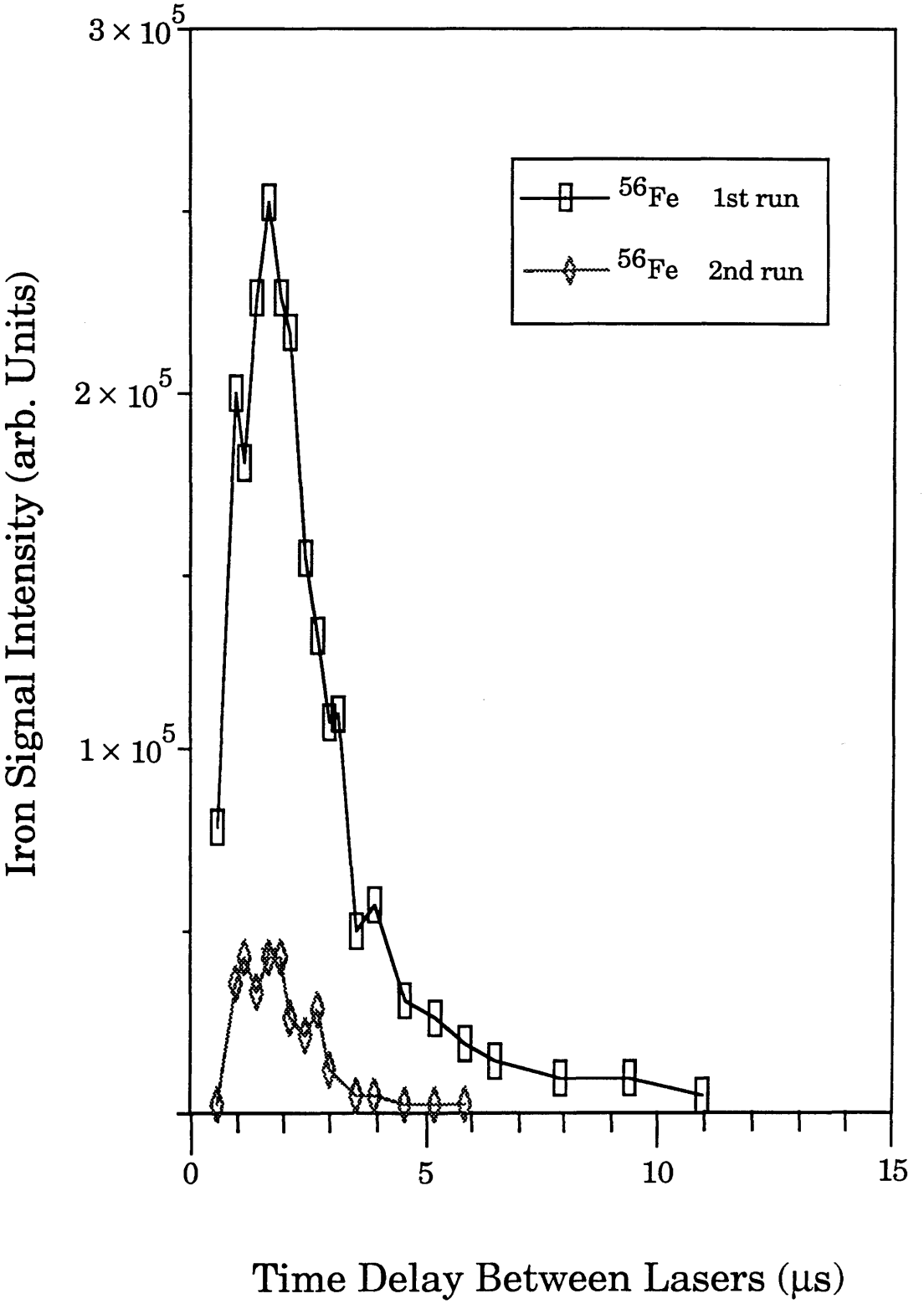

Fig 6.32: Linear Display of Iron 56 Temporal Profile at 3.5 mJmm $^{-2}$

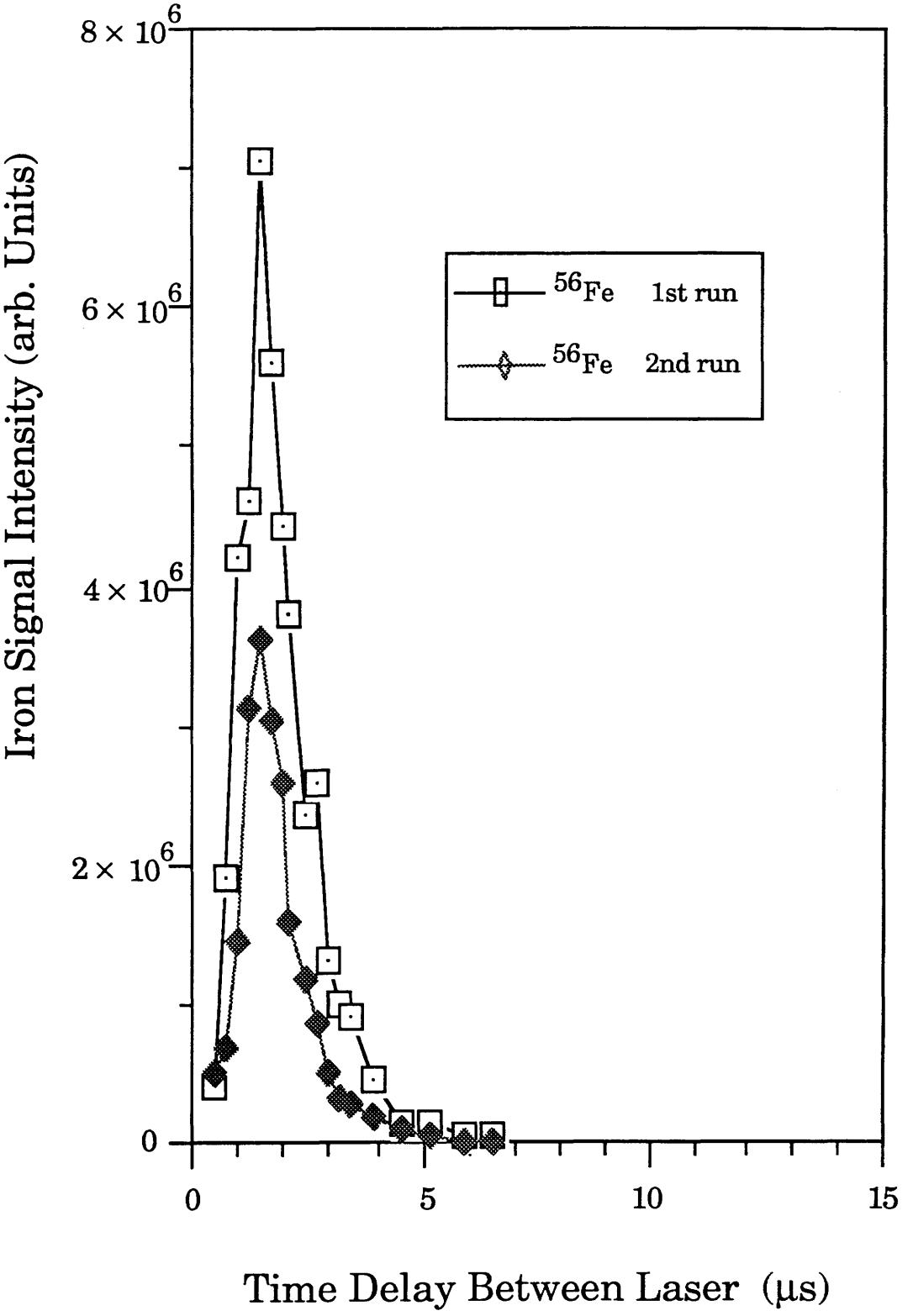

Fig 6.33: Linear Display of Iron 56 Temporal Profile at 5 mJmm^{-2}

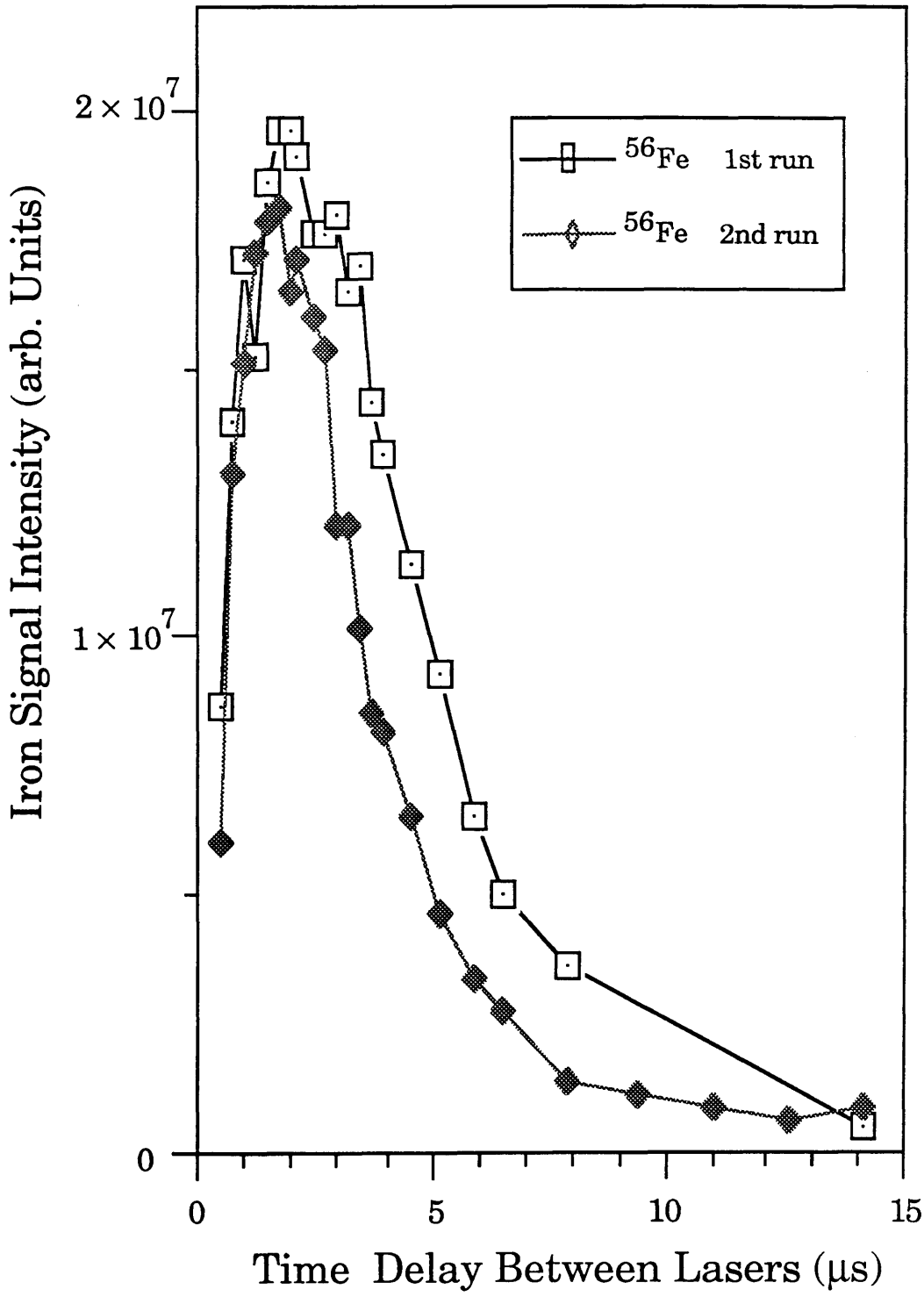

Fig 6.34: Logarithmic Display of Temporal Profiles of Stainless Steel at 2 mJmm^{-2}

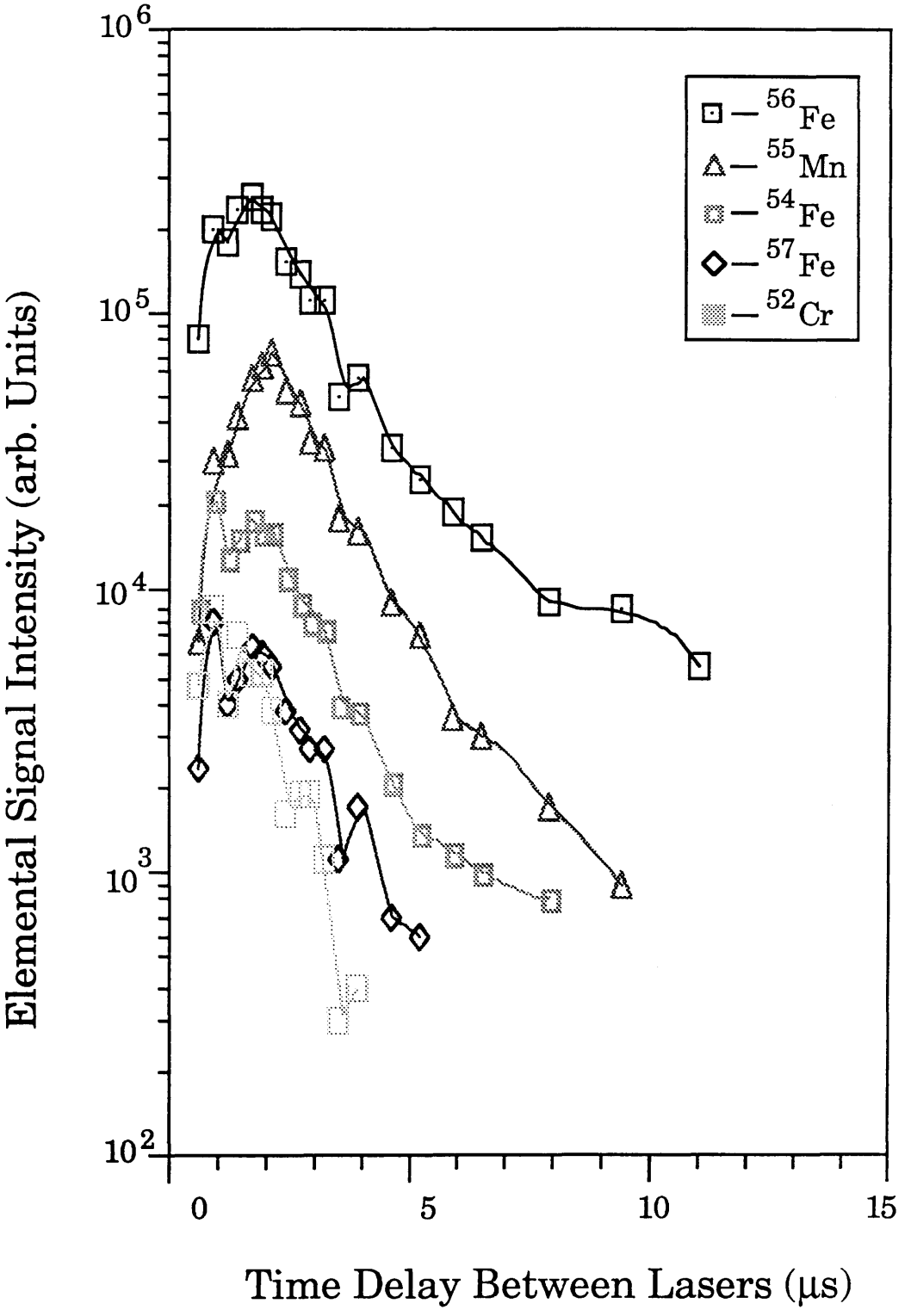

Fig 6.35: Logarithmic Display of Temporal Profiles of Stainless Steel at 3.5 mJmm^{-2}

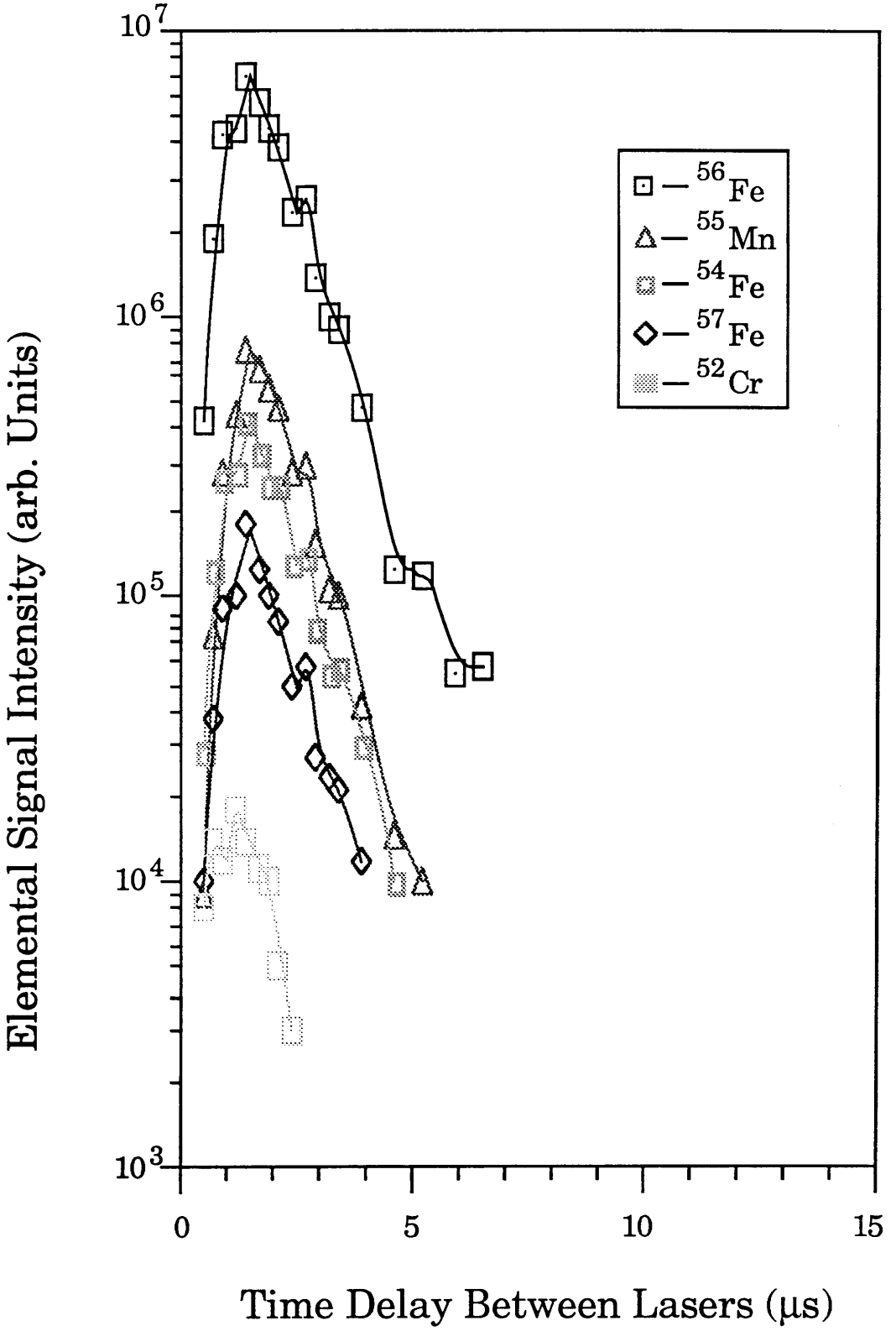

Fig 6.36: Logarithmic Display of Temporal Profiles of Stainless Steel at 5 mJmm^{-2}

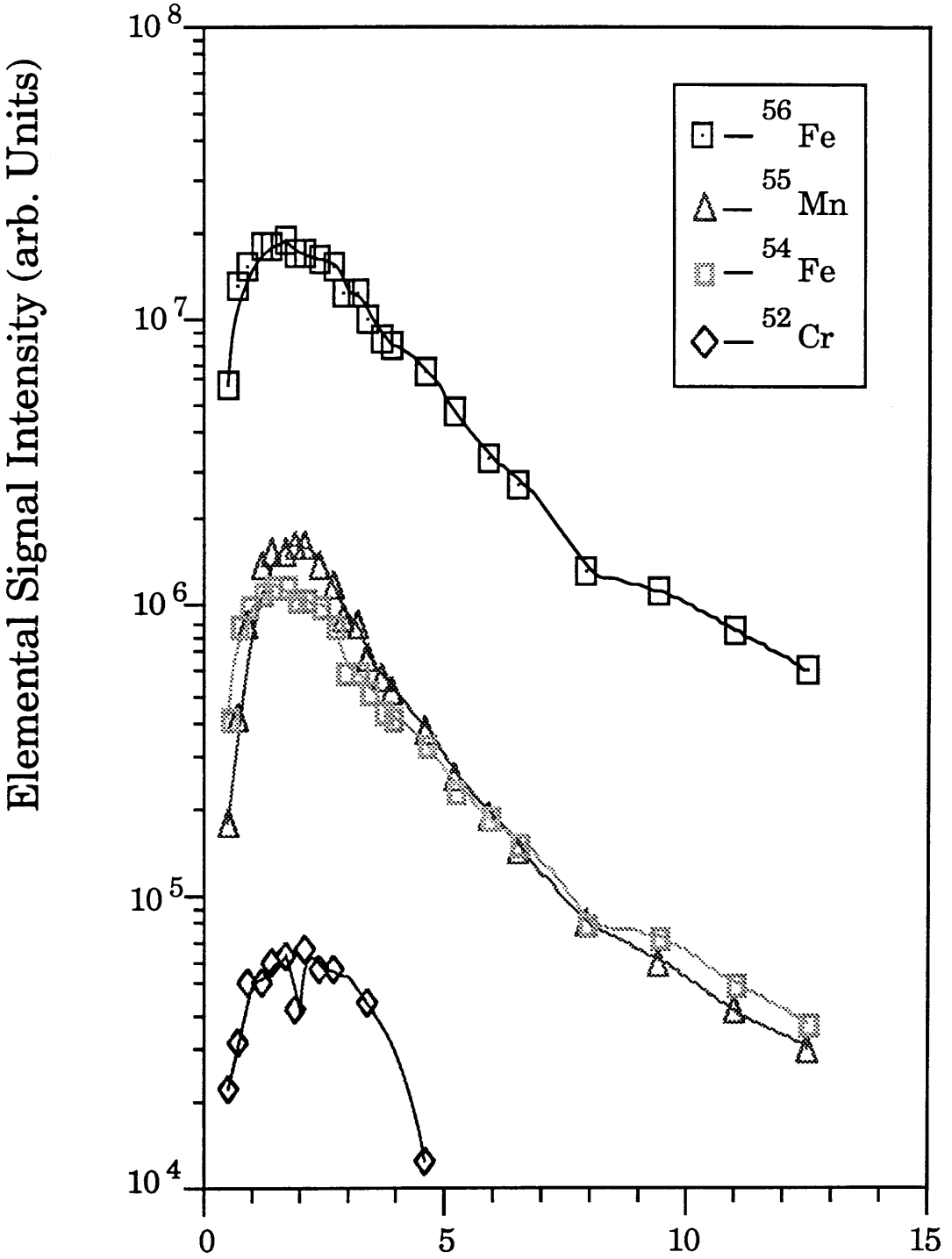

The isotope ratios as measured in all calcium experiments were not accurate. For different experiments the calcium ratio would vary from ~30 to ~70 for a delay time of 2μs. The actual value for the ratio is ~47. There are several possible reasons for this discrepancy. These are: saturation effects in the digitising electronics, preferential evaporation effects from the ablation process, and hyperfine effects where different isotopes are ionised with different efficiencies (Lamdropoulos 1990, Whitten *et al* 1990).

Preferential evaporation occurs when the lighter of two isotopes is preferentially ejected from the surface. An analogous phenomenon is well known in SIMS (Schwarz 1987). Since the Ca^{44} signal is would vary from being too large to too small in comparison with the Ca^{40} signal this can be discounted. Saturation effects are though to be unlikely as care was taken to ensure that the size of signals from the detector were not greater than 2V. Further comfirmation may be obtained by examining the isotope ratio as a function of delay for a calcium ablation profile. As can be seen there is no noticeable change in the isotope ratio when the Ca^{40} signal is large (fig 6.37).

Hyperfine effects are therefore the most probable cause. These effects depend on the properties of the ionising laser, and on the resonant ionisation scheme being unsaturated. In earlier studies (Land 1990) the laser was regularly adjusted which would have the effect of changing the optical properties of the laser, and consequently the relative ionisation probabilities of the different isotopes. In these early studies the isotope ratio was found to vary in an unpredictable manner, as would be expected with such an effect.

As a result of the unknown difference in the ionisation probabilities for the two isotopes it becomes impossible to make any definite statement on the utility of laser ablation for sensitive isotope ratio measurements. This problem may be overcome in future work by using sufficient laser fluence to saturate the transitions used, and consequently obtain 100% ionisation efficiency for all isotopes. However, laser ablation still has the

Fig 6.37: Calcium 40 vs Calcium 44 at low ablation fluences

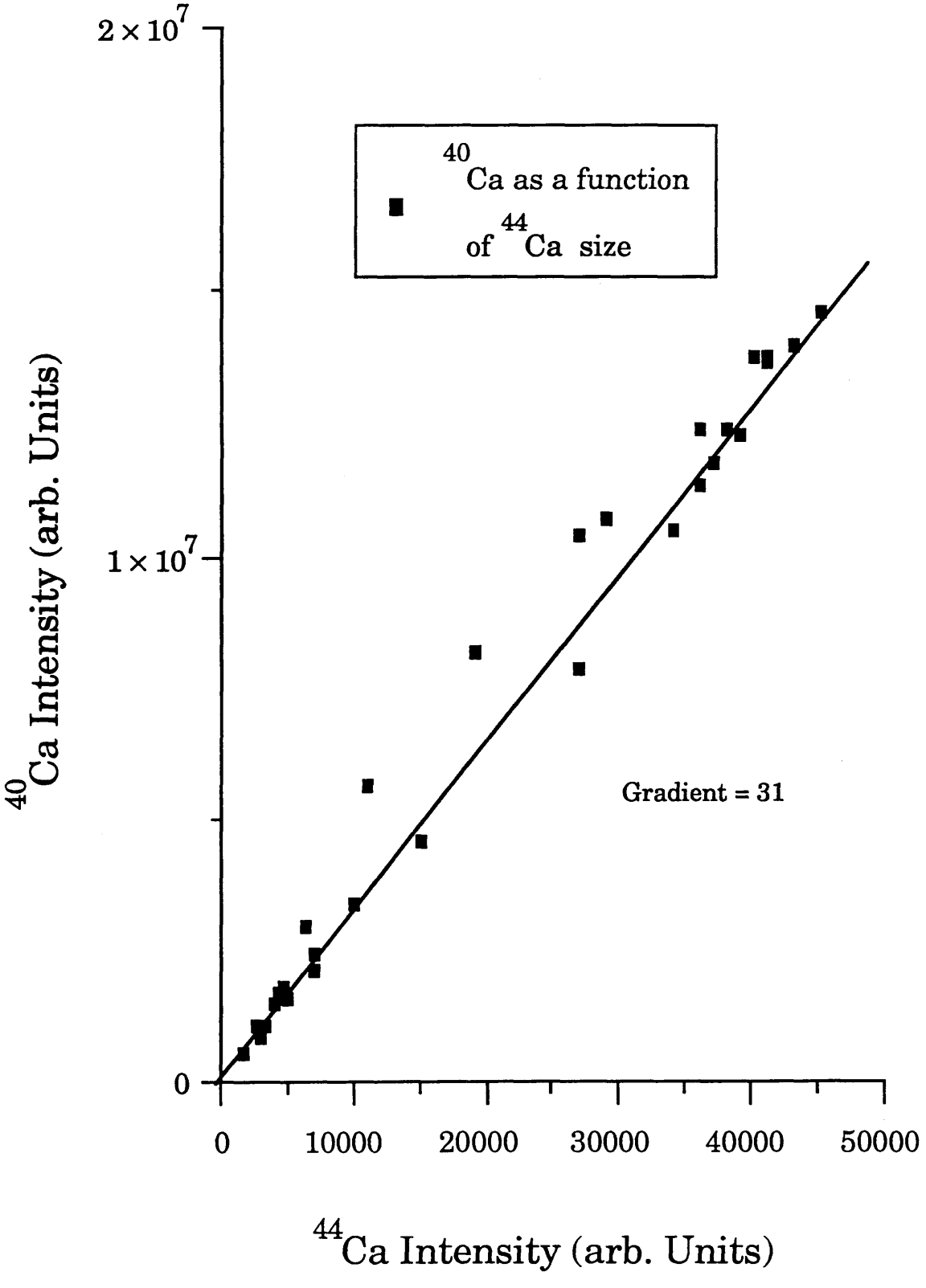

problem of isotope ratio bias caused by the different thermal velocities of the different isotopes in the ablation plume. Eliminating this would require a very large geometric overlap of the plume with the post ionising laser whilst maintaining saturation. As mentioned previously, this is in some cases impossible.

The "best" laser wavelength to use depends strongly on the sample and the properties of the laser. If the sample is highly reflective at one wavelength, as gold is at 1064nm, then this wavelength should not be used. From a practical point of view, when using a Nd:YAG system, the longest available wavelength that is absorbed by the sample should be used. The reason for this is that the stability of ablation beam energy decreases with laser wavelength. If an excimer system is used this consideration is not relevant.

The different absorbances of different samples at the same wavelength could prove to be a major problem with laser ablation. It would be very difficult to compare two samples of different reflectivities in any quantitative fashion. This is because the number of neutrals emitted is a function of energy absorbed, and not the energy of the ablation laser. The variation of reflectivity with laser intensity (Ready 1971) only serves to exacerbate the problem.

For the samples analysed in chapter 7 (trace gold and silver in a copper matrix) the problem above is not a major consideration, since the samples are essentially copper, and appear to an ablation laser as identical. It would however be very difficult to compare eg. trace gold in copper and trace gold in stainless steel at low fluences ($2mJmm^{-2}$).

Matrix effects appear in laser ablation of stainless steel. These effects are summarised in table 6.3. At fluxes of less than 5 $mJmm^{-2}$ there is a significant difference in the abundances of manganese and chromium from the stainless steel sample compared to their reference concentrations.

A possible reason for these matrix effects is the preferential evaporation mentioned earlier in this section. In this case, due to the large differences in melting points for the various components (table 6.3), any preferential evaporation is expected to be far more prominent. As can be seen from table 6.3 the more volatile elements have their signals enhanced relative to the less volatile.

Table 6.3: Melting Points

Element	Melting Point (K)	Ref Conc.	Low Fluence	Med Fluence	High Fluence
^{54}Fe	1808	1	1	1	1
^{55}Mg	1517	0.2	3.5	1.75	2
^{52}Cr	2160	0.28	0.4	0.05	0.07
		Relative to ^{54}Fe			

A possible mechanism for avoiding this problem is to raise the temperature on the surface to far above the melting point of the least volatile component. This would allow all components to be ejected with similar efficiencies. This has a side-effect in that a small high fluence laser spot will produce large amounts of laser ionisation. This will eventually limit the fluence that can be used for neutral production, as at very high fluences almost 100% ionisation occurs (Bingham *et al* 1976).

In the analysis in chapter 7 this consideration is not important since the same element (gold) is being analysed in all cases. Under the reasonable assumption the gold is emitted with the same efficiency from all the samples then any matrix effects will be similar.

In summary, for analysis of metallic samples on the Kratos instrument using RIMS an ablation laser fluence of between $1mJmm^{-2}$ and $4mJmm^{-2}$ and a spot size of $1mm^2$ should be used, the exact value depending on the specific sample.

Chapter 7 : Trace Analysis of Gold Using Resonant Ionisation Mass Spectrometry

§1 Introduction

The trace analysis of gold presented here was pursued with a very definite aim in mind. The object was to demonstrate the use of RIMS as a fast and accurate method for the quantitative analysis of precious metals (eg gold, silver and platinum) in mineral samples.

The work was performed as part of a feasibility study for Surface Science Western (SSW) (a Canadian analysis group attached to the University of Ontario). Kratos Analytical, the industrial partners in the author's CASE award, were approached by SSW and asked to investigate new analytical methods, especially those suitable for trace analysis of mineral samples. Several conditions were laid down:-

1) The samples should need little or no preprocessing.

2) Analysis times should be less than four minutes.

3) A sensitivity of <1ppm should be obtained in this time.

4) Any technique should be transportable.

The reasons for these conditions were as follows: 1) was that in order to keep the delay between the mining of the sample and its analysis as short as possible, preprocessing had to be avoided. 2) was to allow a high throughput of samples. 3) represents the concentration of these precious metals at which commercial mining becomes feasible. This condition is also why accurate quantification is required. The last condition reflects the need to perform the analysis on site.

Several other restrictions on possible analytical methods were provided by the nature of the 'real' samples that would be

Fig 7.1: Distribution of Gold Samples in Rock

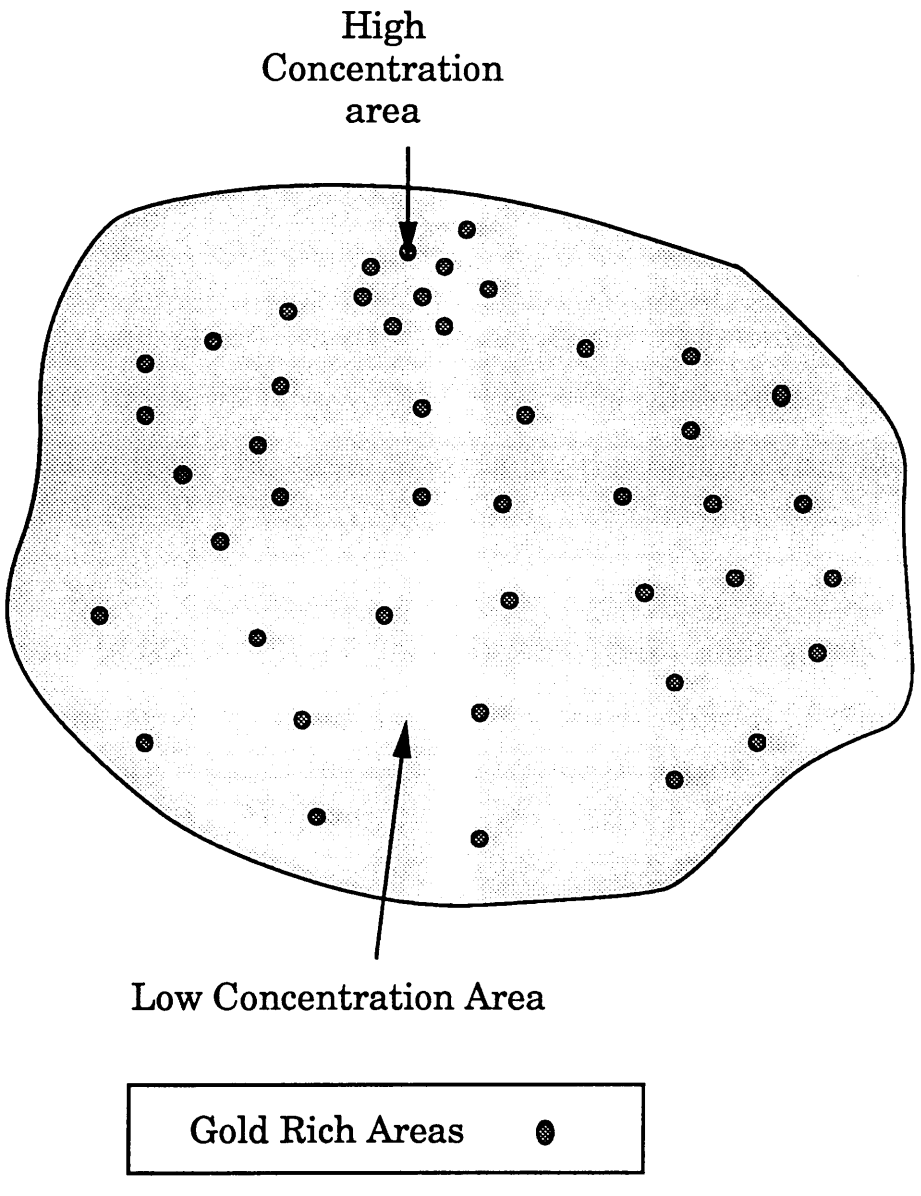

used. Gold, in particular, tends to be found in small deposits of high concentration embedded in low concentration material (Fig 7.1). This rules out the direct application of microprobe techniques, as these techniques could analyse a high gold concentration spot, giving a positive result for a negative sample, or conversely analyse a barren spot in a good sample, thus giving a negative result for a gold rich sample. This can be overcome by analysing many spots on a sample, but this greatly increases the analysis time, in violation of condition 2 above.

§2 Resonant Ionisation Spectroscopy of Gold

A Grotrian diagram (fig 7.2) shows that, although Gold has a comparatively simple atomic structure, there are a large number of resonant schemes that can be applied to it.

RIS and RIMS has been applied to Gold several times previously. Lee (1986) used the 267.6nm transition from the ground state to the 6p $^2P^o_{1/2}$ level followed by photo-ionisation by a second photon from the same laser (a '1+1' scheme). This was the method used for all of experimental work in this chapter.

Other methods that have been used include excitation via a virtual state to the 7s $^2S_{1/2}$ level using 367.0nm photons, followed by photo-ionisation by absorbance of a third photon of the same wavelength (Apel 1987) (a '2+1' scheme). A three color scheme has also been used (Wallmeroth 1987) with a 267.6nm photon exciting to the 6p $^2P^o_{1/2}$ level, followed by a 406.5nm photon to the 6d $^2D_{3/2}$ state. From this level the atom is ionised by 532nm doubled Nd:YAG laser light ('1+1+1'). Krönert (1987) used a similar scheme except the last step was replaced by a 591.9nm transition to an auto-ionising level.

One method not mentioned in the literature is the possibility of using a 242nm photon to excite from the ground state to the 6p $^2P^o_{3/2}$ level. From this level the ionisation methods mentioned

Fig 7.2: Grotrian Diagram for Gold

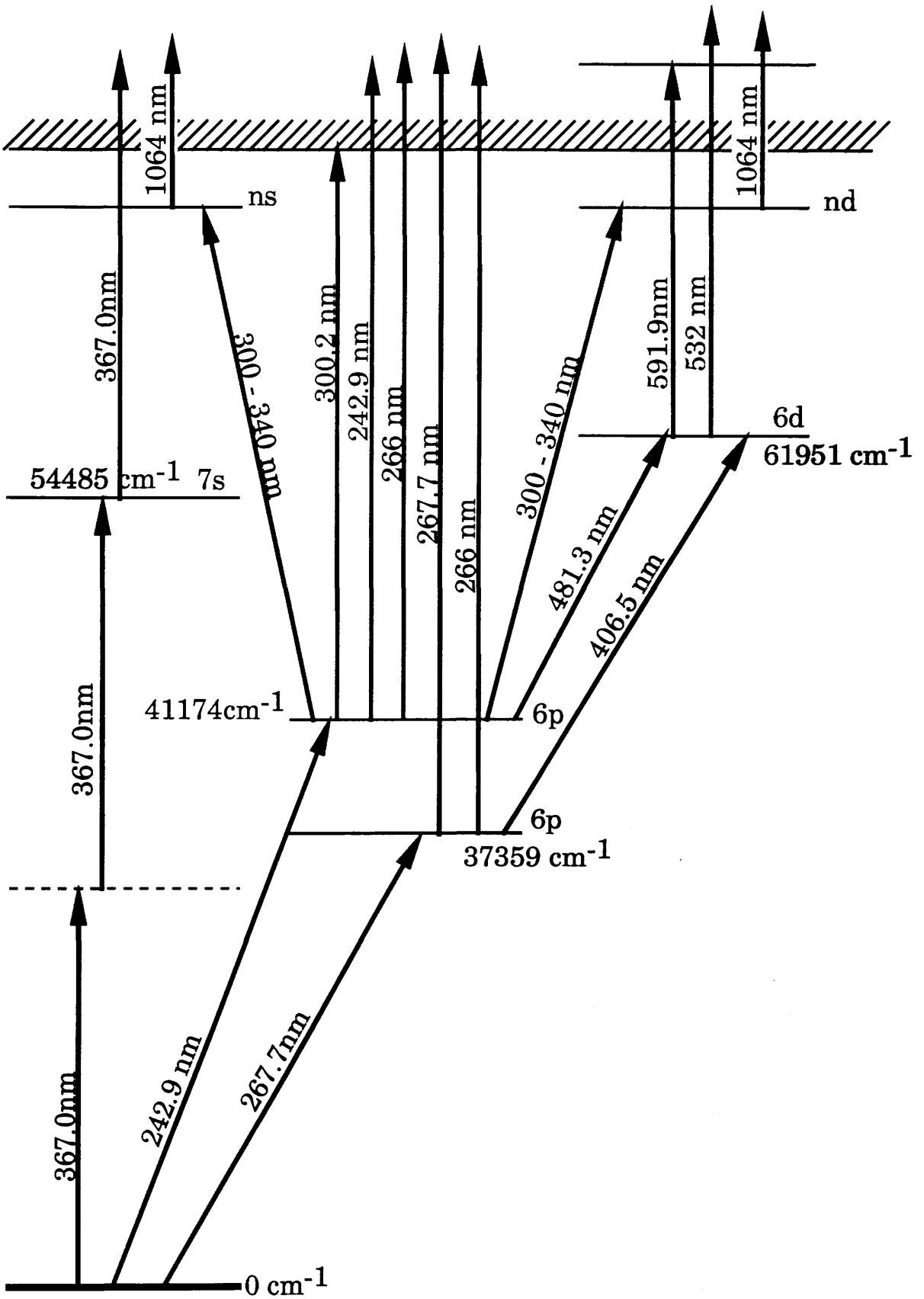

above can be used. Another option, field ionisation, is a possibility if a second photon of wavelength ~300nm is used to excite the electron into a high lying Rydberg state. The 242nm transition has not been previously used because the introduction of efficient frequency doubling crystals which operate in this range is relatively recent.

§3 Wavelength Dependence of Gold Signal

The wavelength required for excitation to the 6p $^2P^o_{1/2}$ state of gold from the ground state is 267.6nm. To obtain this wavelength with the laser system at Glasgow coumarin 522A dye was used in the blue laser. This gave an output power of ~2mJ at 533nm. This was frequency doubled using KDP crystals to give the 267.6nm required. The efficiency of the doubling was ~10%, giving 200μJ of UV radiation. After losses in the optics directing the laser to the spectrometer the energy delivered to the instrument was 100μJ. The wavelength scanning to find the gold resonance was carried out using the Inrad autotracker. Once the resonance was located the autotracker was replaced by an angle-tuned mount.

Initial wavelength calibration was carried out using an uranium hollow cathode lamp. From this spectrum the region of the resonance was obtained.

To align the system a gold foil sample (Goodfellow) was inserted into the chamber and the ablation laser activated. The ablation laser, which was operated at a wavelength of 532nm, was loosely focussed to provide a fluence of 3mJmm^{-2} at the sample surface. The ablation laser was operated so that the fluence was as constant as possible. To achieve this the laser was operated for several hours before any analysis to allow the temperature of the optics within the laser to stabilise. In this way the best stability could be achieved. The frequency doubling crystal was not operated at the full laser power since the stability was enhanced when the fundamental beam was attenuated to around half its maximum power.

With the ablation laser fluence constant the post-ionising laser beam was directed through the ablation plume. For this purpose the post ionising laser was tightly focussed, which allowed a small non-resonant ionisation signal resulting from the doubled light to be visible. This allowed alignment of the ablation and the post-ionising lasers without the post-ionising laser being tuned onto the resonance. That the ionisation was due to the UV, as opposed to the undoubled light, was easily verified by turning the doubling crystal until no UV was emitted. No post-ionisation signal was then observed.

The wavelength of the ionisation laser was scanned across the transition region and the gold ionisation signal recorded (fig 7.3). This clearly shows the 267.6nm gold resonance. The resonance was wider than expected, indicating that the laser was not optimally aligned as required to obtain the specified bandwidth(30GHz). However, the laser was working at a higher efficiency than expected for the dye, and it was decided that any gain from the reduction of bandwidth would be more than offset by a reduction in the laser output power. Hence the laser was left operating in a wide bandwidth mode.

The wide bandwidth also had the effect of eliminating the temperature drift of the laser wavelength. The temperature drift, caused by temperature variation in the laboratory, was less than the bandwidth of the laser. Over the period of time that resonant ionisation was performed on gold (about two months) it was unnecessary to retune the laser onto the transition. Periodically the laser would be wavelength scanned to determine whether the transition was occurring in the wings of the laser output, but in every case the laser output was still cent-red satisfactorily. This contrasts with the calcium analysis performed earlier, where the laser was operated with a narrower bandwidth. In this case almost daily tuning was required to maintain resonance.

The ionisation yield was unchanged when the undoubled light was removed with a bandpass filter, except for a small reduction attrtibuted to UV absorption by the filter. Thus the 533nm wavelength made no contribution to the ionisation

Fig 7.3: Wavelength Scan of Gold Resonance

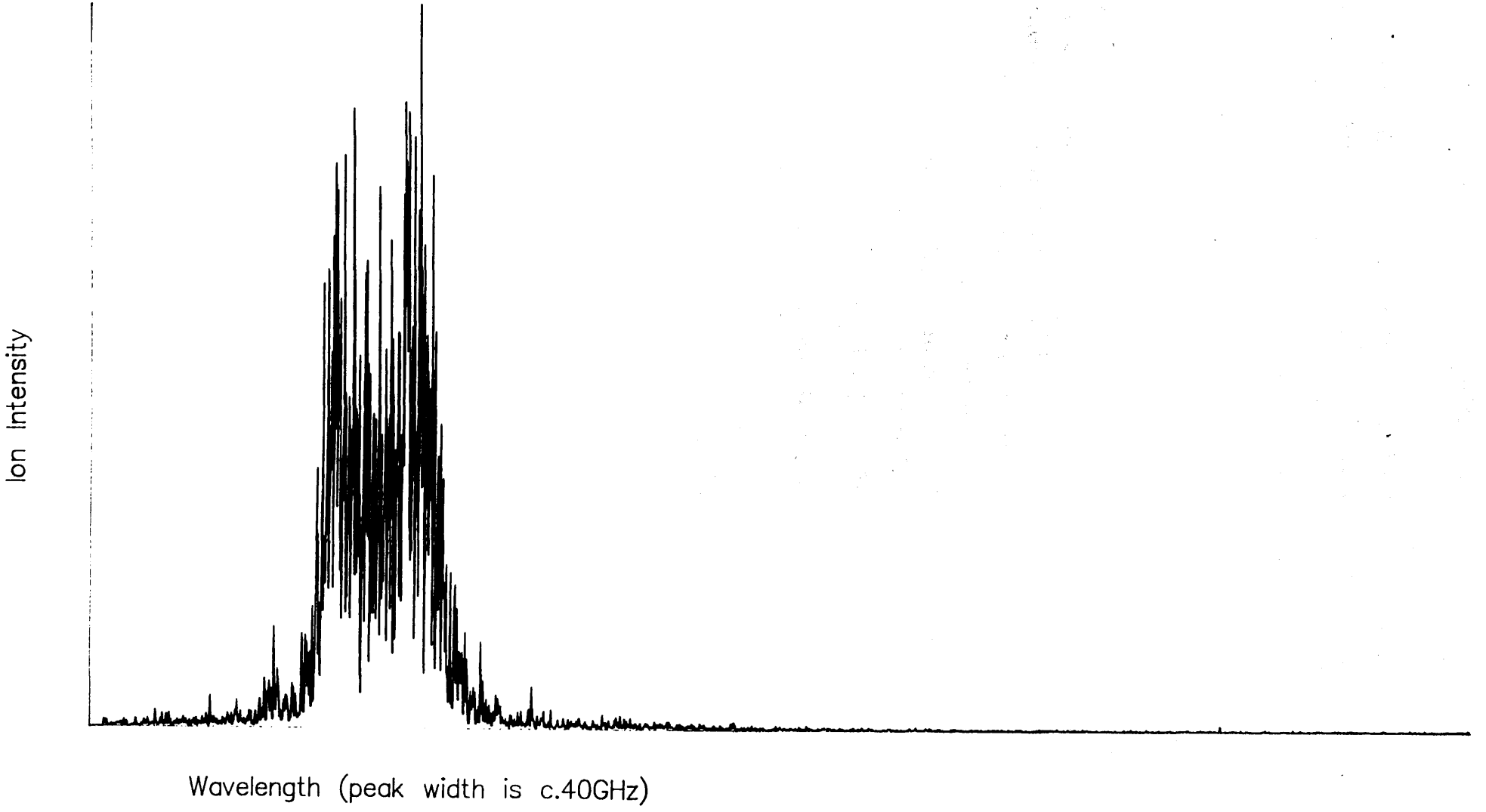

process. The filter was removed from the beam for the rest of the experiments in this chapter and both colours were directed into the chamber. The filter was placed in front of a molectron joulemeter (chapter 3) to allow the UV energy to be monitored during the experiment.

The tight focusing of the post-ionising laser resulted in relatively low ionisation efficiency due to the poor geometric overlap with the ablation plume. It was possible to direct the 267.6nm beam into the ionisation region without focusing and still achieve an ionisation signal but it was difficult to align the ionising beam properly. However, using the lens to align the laser in the interaction region without focussing removed this problem. This was the procedure adopted in §4 of this chapter. The ionising laser had a cross sectional area of ~1mm^2 when intercepting the ablation plume, giving a fluence of 100μJmm^{-2}.

§4 Dependence of Gold Yield on Post-ionising Laser Power

It was necessary to determine the effectiveness of the ionisation process. This was achieved with the post-ionising laser arranged as described in §3 above and the gold foil sample. A variable attenuator was put into the beam path and the ion yield measured as a function of laser power. This was performed using the program SPEC (see chapter 4), with the laser energy recorded using a molectron joulemeter. The ablation laser was operated in the manner described in §3 above.

Figs 7.4 and 7.5 show a log-log plot of ion yield against laser fluence. As can be clearly be seen the gradient changes from > 2 to 1, indicating that the bound-bound transition is being saturated at fluences above ~60μJmm^{-2}, whereas the ionisation step does not reach saturation (chapter 2 §3). From Lee (1986) it is estimated that 10% of the gold atoms irradiated are being ionised.

The fluence of 60 μJmm^{-2} required to saturate the bound-bound transition is higher than that reported by Krönert *et al* (1987) who needed 10 μJcm^{-2}. However the laser used by Krönert had a bandwidth of 0.5 GHz, compared with the bandwidth of >30 GHz of laser used for this work. The pulse lengths of the

Fig 7.4: Log-Log Plot of Gold Ion Signal Vs Laser Ionisation Fluence

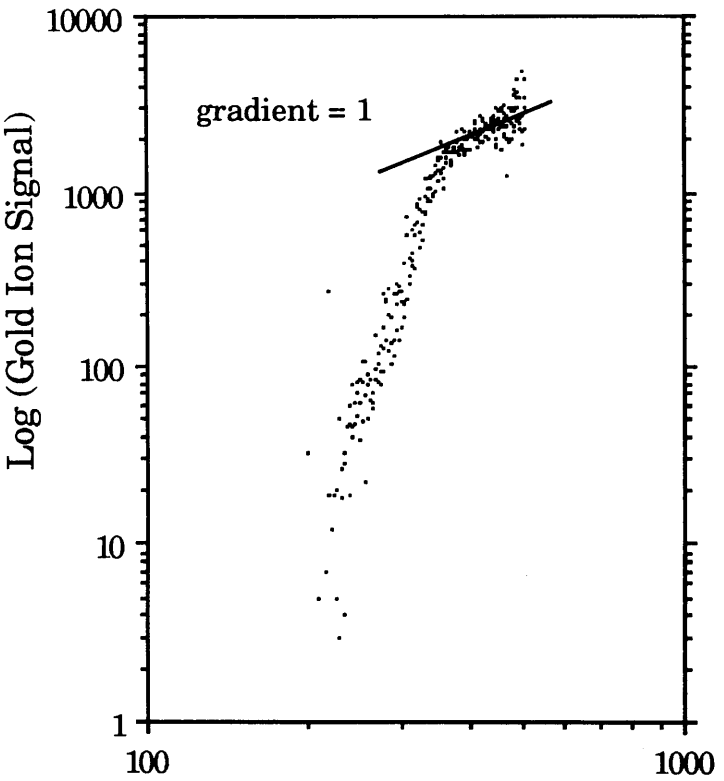

Fig 7.5: Log-Log Plot of Gold Ionisation Signal vs Laser Ionisation Fluence

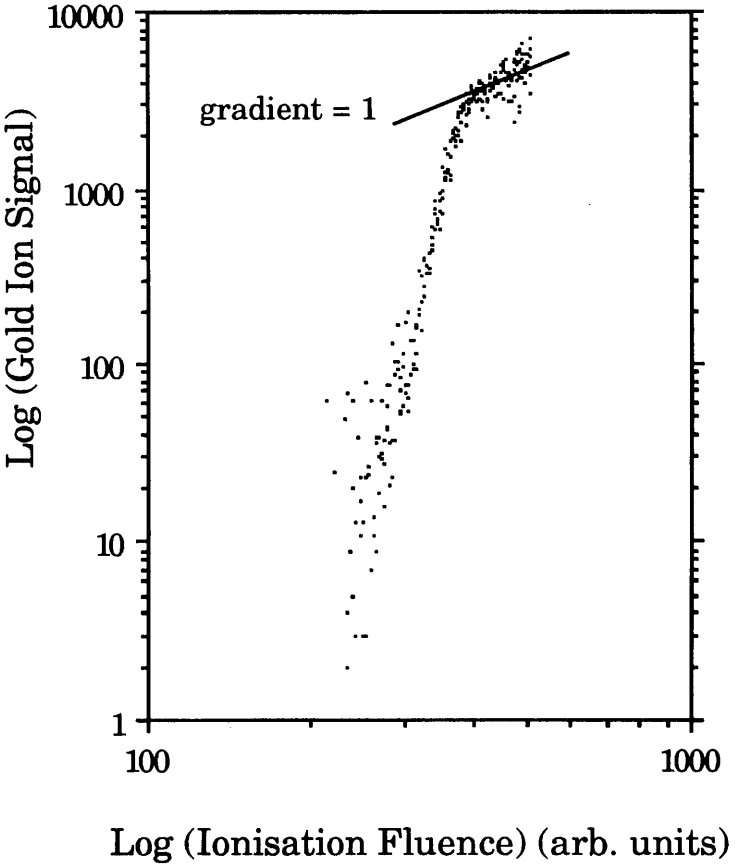

lasers were 6ns (for Krönert) and 10ns (at Glasgow). These differences are believed to account for the different fluences.

§5 Detection of Trace Gold in a Copper Matrix

There were five different samples supplied for the trace analysis. Each sample consisted of a copper matrix which was implanted with gold and silver in equal amounts (Hirvonen 1980, Preece 1980). The samples contained gold (and silver) in proportions of 1500ppm, 750ppm, 100ppm, 50ppm and 10ppm. [ppm in this case means parts per million atomic]. The samples were mounted using non-conducting epoxy on the centre of a stainless steel stub. Due to the nature of the affixing process the surfaces of some of the samples had epoxy residue adhering to them. This was removed inside the machine, with the sample in situ, by using the ablation laser at very high fluences. This was only required once for each sample. Before each insertion into the instrument the samples were cleaned with Analar grade methanol (May & Baker Ltd, Dagenham, England) to remove any greasy deposits, and rinsed with distilled water.

The ablation laser, after being stabilised as described in §2, was focussed loosely into the centre of the instrument to give a spot of ~1mm^2. After initial alignment the position of the ablation laser beam was held constant throughout the remainder of these experiments. The power was monitored by using a glass slide to deflect to about 4% of the beam into a Molectron joulemeter.

The original ablation laser power was a compromise between a high enough fluence to provide a good resonant ionisation signal and a low enough fluence to maintain LIMA ion leakage to a manageable level. As mentioned earlier (chapter 6) a large LIMA ion signal, in this case from the copper matrix, degrades the stability of the time of flight system. This will have the effect of making the gold RIMS peak temporally unstable. While this may not significantly affect the absolute number of gold ions being transmitted, it will have the effect of reducing the height of the peak above the background. This results in a loss of sensitivity and accuracy. This initialisation was performed on the 1500ppm sample. Earlier attempts using a pure gold foil sample resulted in

severe space charge effects from the resonant ions, before any effects from the ablation laser could be gauged. The ablation fluence used was $3mJmm^{-2}$.

The ablation laser was allowed into the chamber to clean the sample for a period of approximately half an hour before any analysis, to remove any contaminants from the sample surface.

The post-ionising laser, with both fundamental and doubled components present, was directed into the chamber 2mm from the sample. The energy of the post-ionising laser was 100μJ in all cases except the 10ppm case. Due to the ageing of the dye used the energy for the 10ppm case started at 100μJ but fell to ~80μJ after 2000-3000 shots. The area of the post-ionisation laser was $\sim 1mm^2$. The delay between the lasers was determined from fig 6.24, which shows the signal size vs delay between lasers for the 100ppm sample. The delay used was 2μs.

For each sample twenty consecutive 1000 shot runs were acquired in the normal manner for a multi spec analysis. During the analysis the laser ablation energy and the ionising laser energy were monitored. If the energies should vary excessively, or appear to drift, the run was aborted and restarted (with the exception of the 10 ppm sample as described above). The output from these runs is shown in fig 7.6 to 7.10.

As can be seen from these plots the stability of the signal for each 1000 shot analysis varies from being very good, in the case of the 100ppm sample, to being poor. There is no apparent correlation with gold concentration in each sample, which indicates that the variation in the signals is not caused counting statisitics. The cause of the variations in peak heights is thought to be caused by small fluctuations in the ablation laser fluence which leads to a relatively large variation in neutral flux.

From each run the average ionisation signal and the standard deviation can be calculated. A log-log plot of average ionisation signal against sample concentration is shown in fig 7.11. It can be seen that the points lie very close to a straight line of gradient ~1. The 10ppm point lies below the line, which is

Fig 7.6: Stability of Ion Signal from 1500ppm Sample

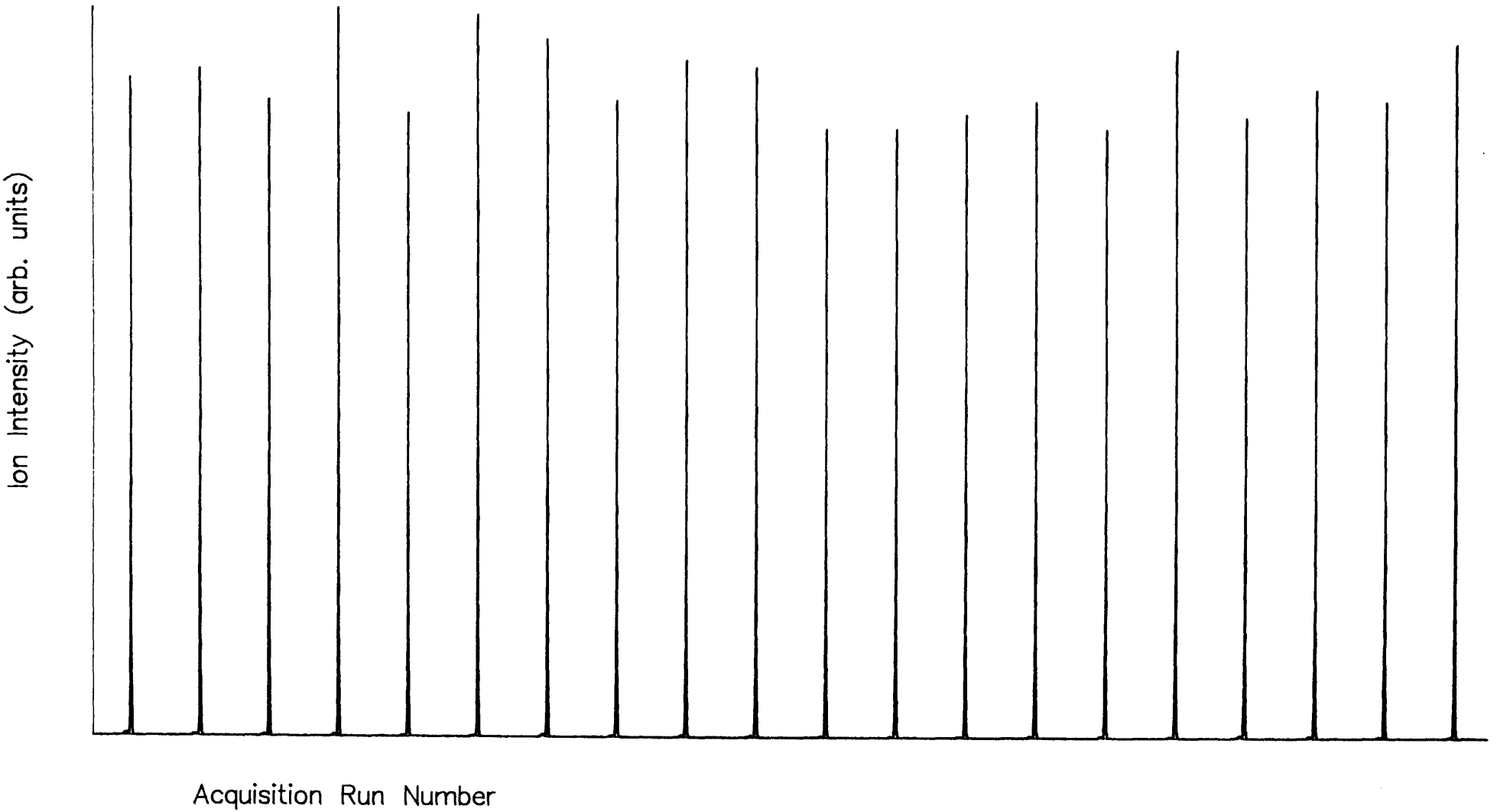

Fig 7.7: Stability of Ion Signal From 760ppm Sample

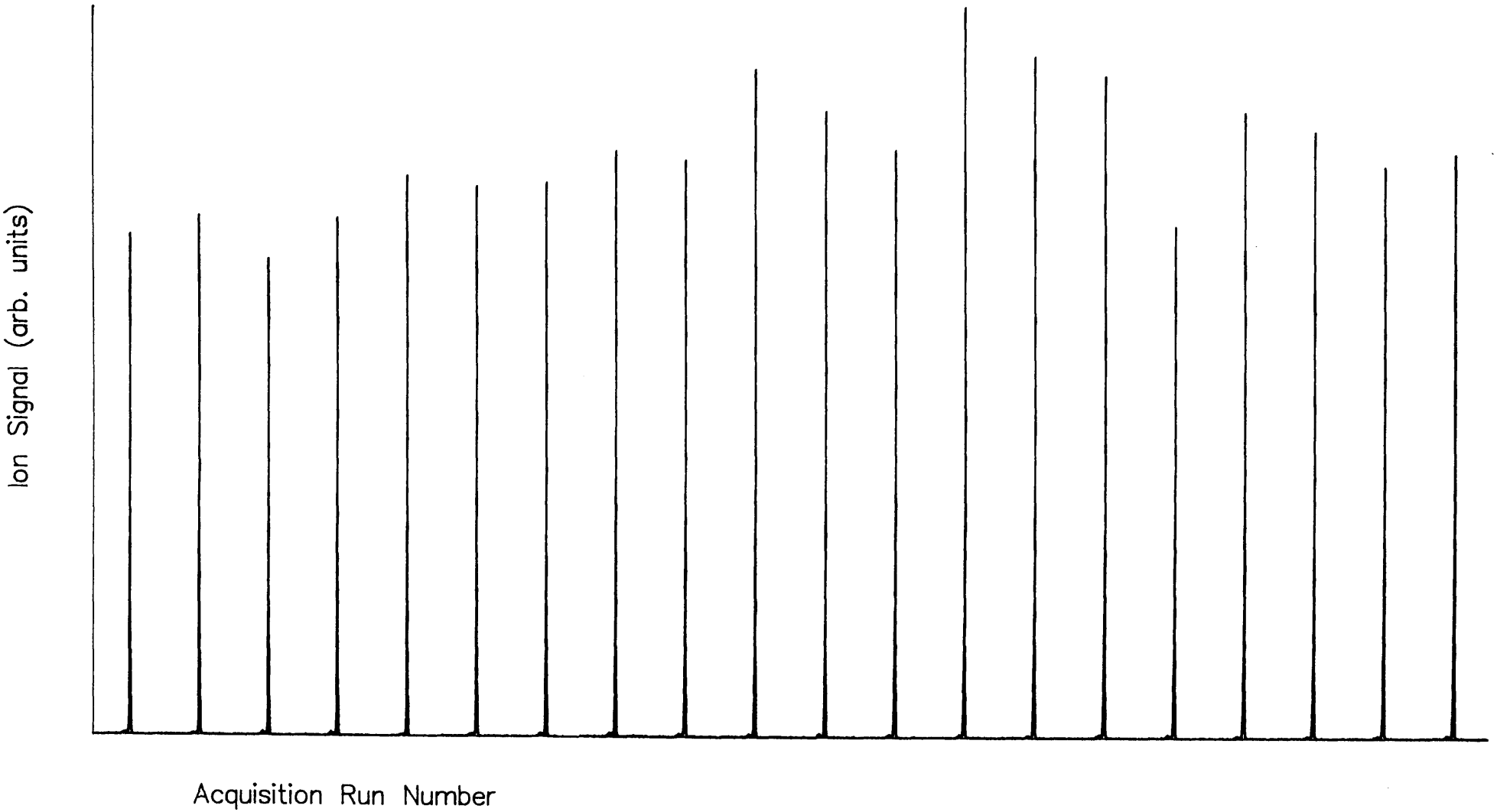

Fig 7.8: Stability of Ion Signal from 100ppm Sample

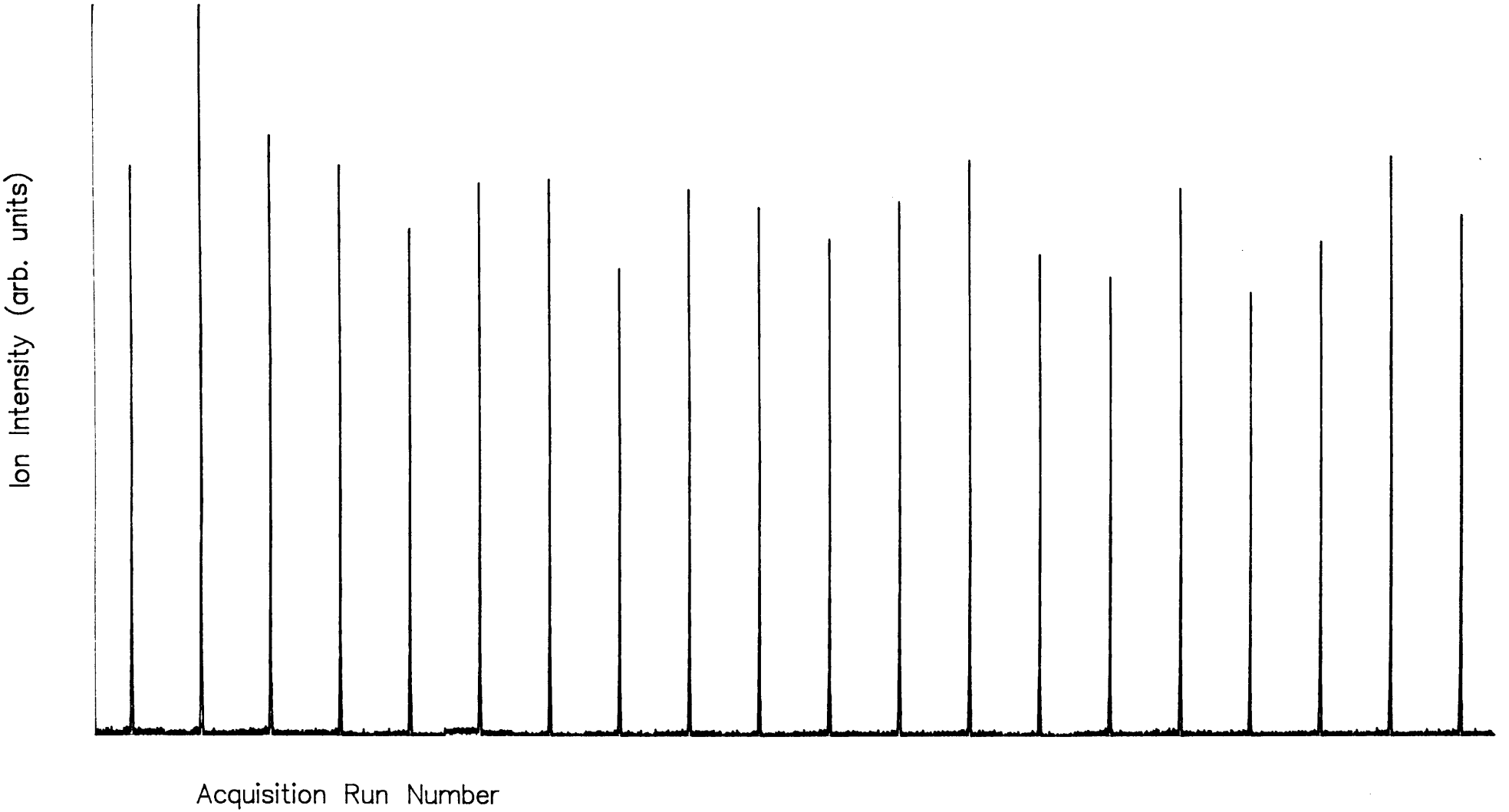

Fig 7.9: Stability of Ion Signal from 50ppm Sample

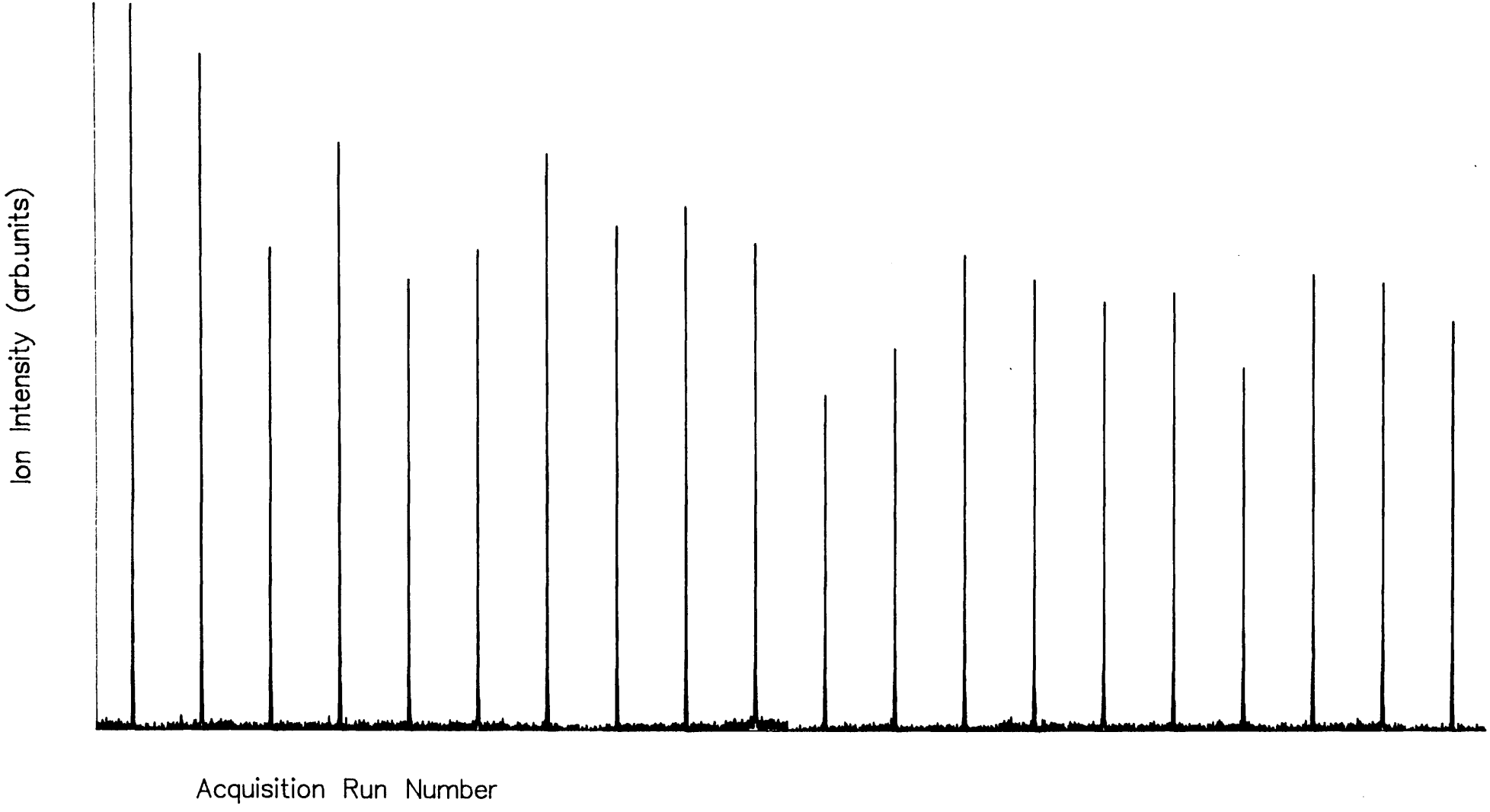

Fig 7.10: Stability of Ion Signal from 10ppm Sample

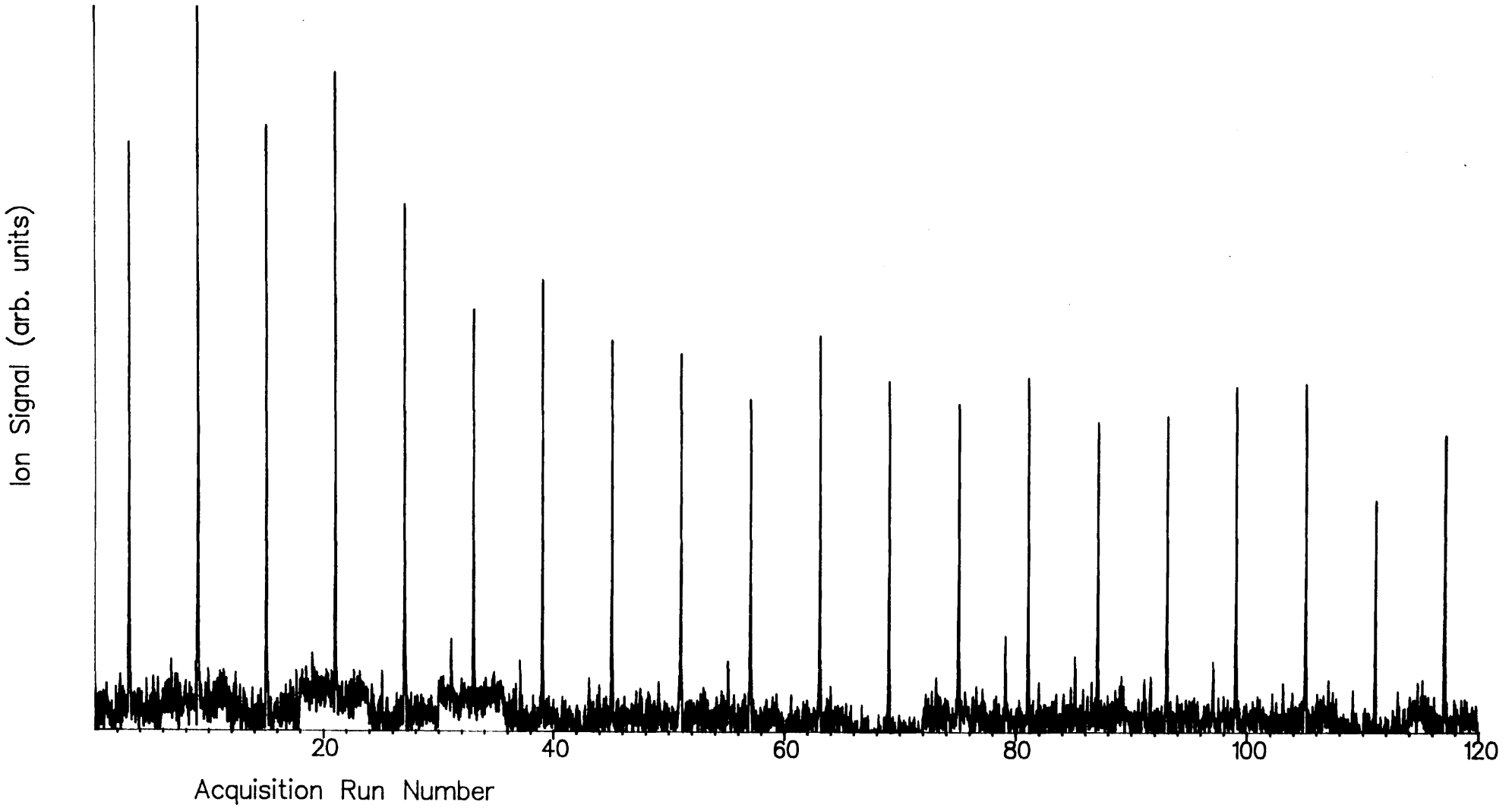

Fig 7.11: Gold Ion Signal versus Sample Concentration

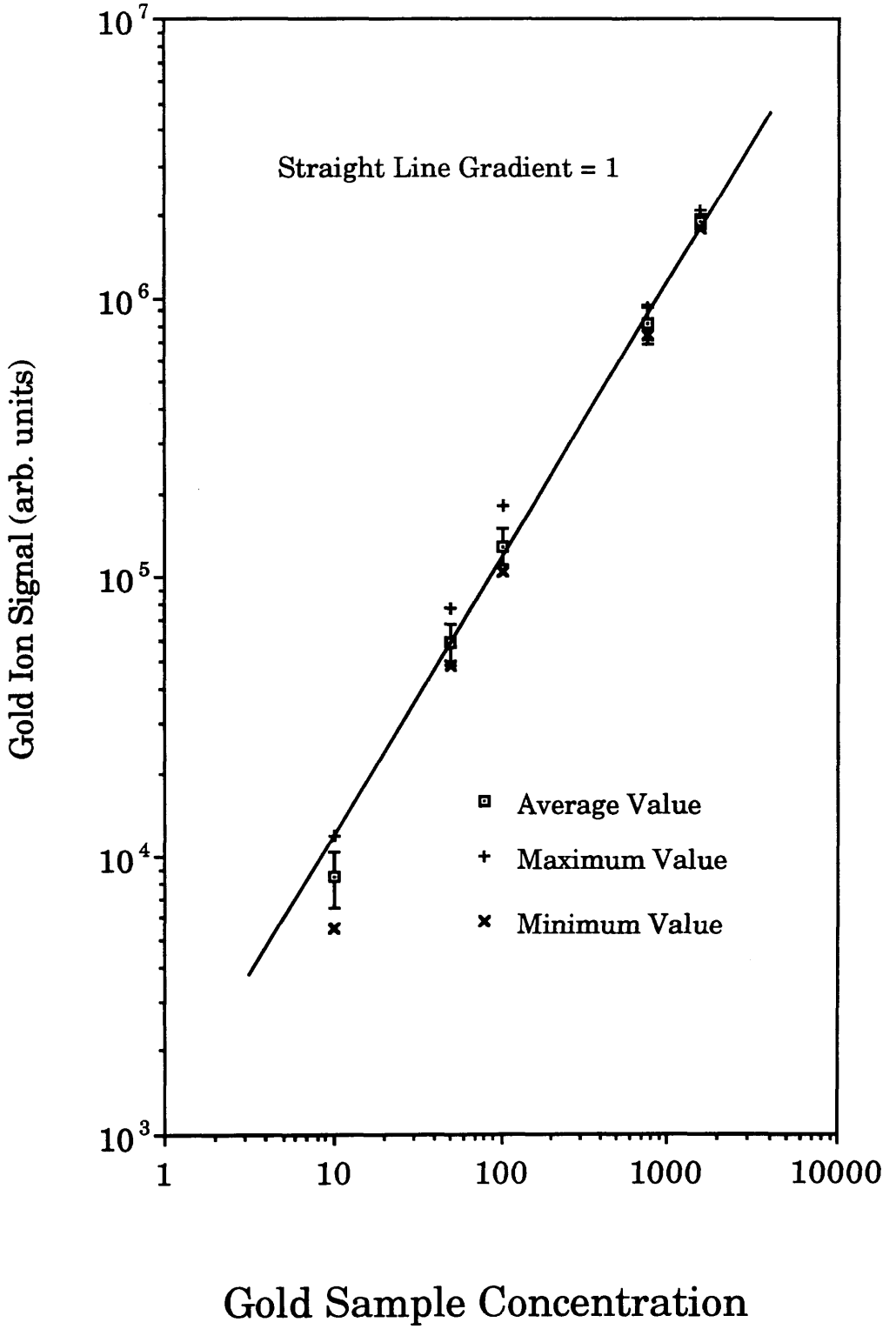

expected considering the decrease in laser power that occurred while this data was being acquired.

For the 10 ppm sample a 10000 shot run was acquired under the same conditions as the runs above. In this case the ionising laser energy was 80μJ. The spectrum obtained is shown in fig 7.12. From this the sensitivity of the instrument, for this particular arrangement, is estimated to be 200ppb.

§6 Other Methods of Detecting Trace Amounts of Gold

There are several other methods of detecting trace amounts of gold, but these all have disadvantages or violate one of the three conditions mentioned at the start of the chapter. Colorimitery (Merejkovsky 1933, Natelson 1951), Fluorimetry (Marienko 1954, White 1970) and Chromatography (Stolyarov 1973) are used for measurements of gold in organic and biological matrices. These can reach the required sensitivity but the samples need extensive preprocessing, and consequently violate the second condition. Emission spectroscopy (Gerlach 1931, Gaul 1933) and atomic absorption spectroscopy (Frajola 1967, Balazs 1972) are ruled out for similar reasons.

Neutron activation analysis (Koch 1960), while applicable to gold and capable of the required sensitivity, is ruled out in this instance as the analysis cannot be carried out *in situ*.

The two most important competing techniques are secondary ionisation mass spectrometry (SIMS) (Benninghoven *et al* 1987) and inductively coupled plasma mass spectrometry (ICPMS). SIMS is the method currently used in mineral analysis by Surface Science Western, and in the analysis of real samples has a sensitivity of no better than 2ppm (Chryssoulis 1990). ICPMS can be used in two modes: liquid samples can be injected into the plasma region or, in a method reported by Arrowsmith (1987), laser ablation may be incorporated to allow direct analysis of solid samples. The sample would require preprocessing before analysis by the liquid method, in violation of condition 1). The sensitivity of of the laser ablation initiated ICPMS is currently ~5ppm, which is lower than the required sensitivity.

Fig 7.12: Gold Spectrum from 10000 Shot Acquisition

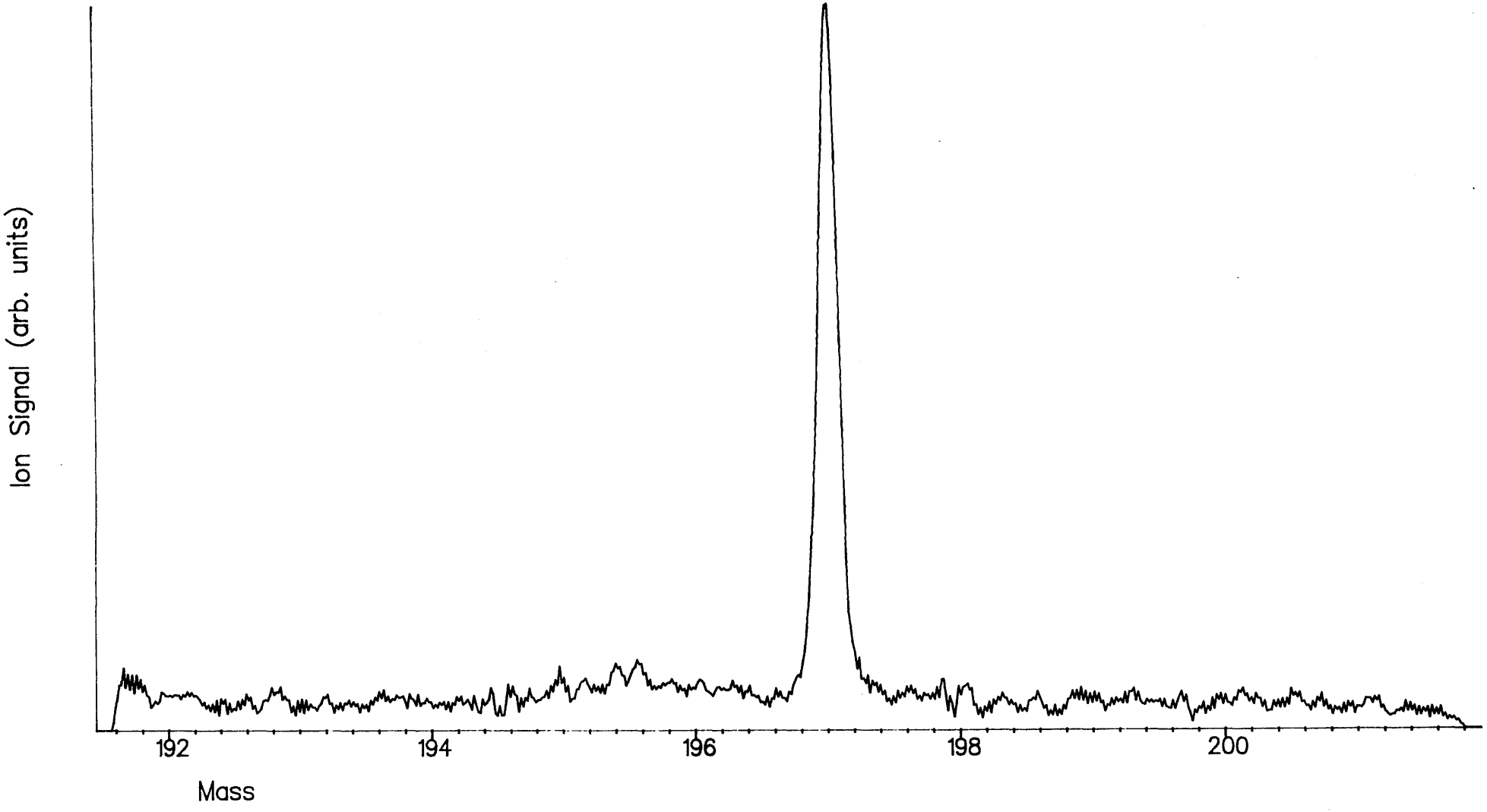

Chapter 8: Conclusions and Future Work

§1 Introduction

This chapter will examine the experimental work done and make suggestions for improving and extending this work. The impact of advances in technology in the field for RIMS, particularly the advent of tunable solid state lasers, will also be considered.

§2 Trace Analysis - Methods of Increasing Sensitivity

The sensitivity of the instrument for gold samples was estimated to be ~200ppb for an analysis time of 18mins, corresponding to a 10000 shot analysis. There are several methods of increasing sensitivity.

The first, and most obvious, of these is to saturate the ionisation process. Since the first step in the ionisation process is saturated it is only required to saturate the ionisation step. This can be achieved either by increasing laser power or by using a second, more powerful, laser to saturate the photo-ionisation step. The 266nm fourth harmonic of the Nd:YAG is ideally suited for the latter role, as one photon is only just sufficient to ionise the resonantly excited gold atom. Neither of these options were available with the experimental set up used. From Lee *et al* (1989) it was estimated that approximately <5% of the gold neutrals in the beam were being ionised. Saturation would therefore increase the sensitivity to ~10ppb.

Increasing the power of the laser that saturates the bound-bound transition leads to problems with power broadening (see chapter 2 §4), which is undesirable as it leads to a loss of selectivity. Another convenient method of resonantly ionising gold is to use a '2+1' scheme, using the transition to the $7s\ ^2S_{1/2}$ level using 367.0nm laser radiation. The fluence required to saturate the bound step of a '2+1' transition is similar to that

required to saturate the ionisation step. Consequently a '2+1' ionisation scheme may be preferable as saturation can be achieved by only one laser without loss of selectivity.

Secondly, the detector used had a reduced gain of ~10^5 as opposed to 10^7 when new. This would appear to increase the sensitivity to 100ppt but this only occurs if the noise in the detector is caused by dark current only. There is an additional source of noise in the detector (see below) so a hundredfold increase in gain would not give a commensurate increase in sensitivity. However the larger ion signals from the detector would reduce the effects of other sources of noise (eg. quantisation noise from the transient digital recorder) so an increase in sensitivity of at least ×5 is expected, to give a detection limit of 2ppb.

The source of the additional noise at the detector was investigated. The main cause is ions, produced by ions generated in the laser ablation process, arriving at the detector. These "secondary laser ions" are not directly caused by the laser ablation process itself but by collision between the laser ablation ions and the grids that are present in the instrument. These ions are produced as shown in fig 8.1. This problem was partially solved by placing a low energy ion filter in front of the detector, which removes any secondary laser ion contribution from the front two reflectron grids. Ions produced by the final reflectron grid are still problematical.

Primary laser ions (ie. those produced directly in the ablation process) could also reach the detector. This type of ion reaches the detector when a large number are formed in the ablation pulse, causing space charge effects and a consequent lowering of their energy. This was not a problem as the number of ions produced at the energies and fluences used were generally below that necessary for such an effect. At high fluences and energies (eg. 15mJmm^{-2} with a total energy of 15mJ being deposited in 10ns) leakage was almost continuous, resulting in severe degradation of the performance of the instrument.

There are two different possible approaches to the problem of stopping the primary and secondary laser ions. Firstly, the grids on the reflectron can be removed. This prevents the ions being created in the first place. Generally, removing grids from a reflectron will result in the reflectron being inoperative. However, by designing the reflectron correctly gridless operation is possible (Bruker, W. Germany)

The second solution is to stop the ions formed in the laser ablation process from being accepted through the ion optics. There are two methods that can achieve this: the first is to pulse the ion optics and the second is to arrange the (steady state) fields so that the ions formed in the ablation process are not accepted into the flight tube.

Pulsed ion optics have been used by many authors (Arlinghaus 1990) and have generally been found to be effective. The main drawback is that the requirements for successful pulsed operation are difficult to meet, requiring dedicated and expensive pulser units.

By arranging the electric fields of the ion optics appropriately ions produced at the surface of the sample (eg. SIMS ions or LIMA ions) can be rejected from the TOF drift tube, whereas those formed away from the surface (eg. RIMS ions) are accepted. Fig 8.2 shows one possible arrangement, allowing an accelerating voltage of >1kV to be used and a good geometric overlap to be obtained. A complete description of ion inversion optic modelling and implementation is given in appendix B. This includes results from an instrument at Glasgow using inversion optics. It suffices to say here that such designs have proved very effective at the suppression of unwanted laser ablation ions in a TOF mass spectrometer.

An important advantage of such ion optic designs is that they replace the need for high voltage pulses, which require very fast rise and fall times (~100's ns) (ie high temporal precision) with well defined steady state electric fields (achieved through high geometrical precision). Of the two methods, high geometrical

Fig 8.1: Production of Low Energy Ions in Reflectron

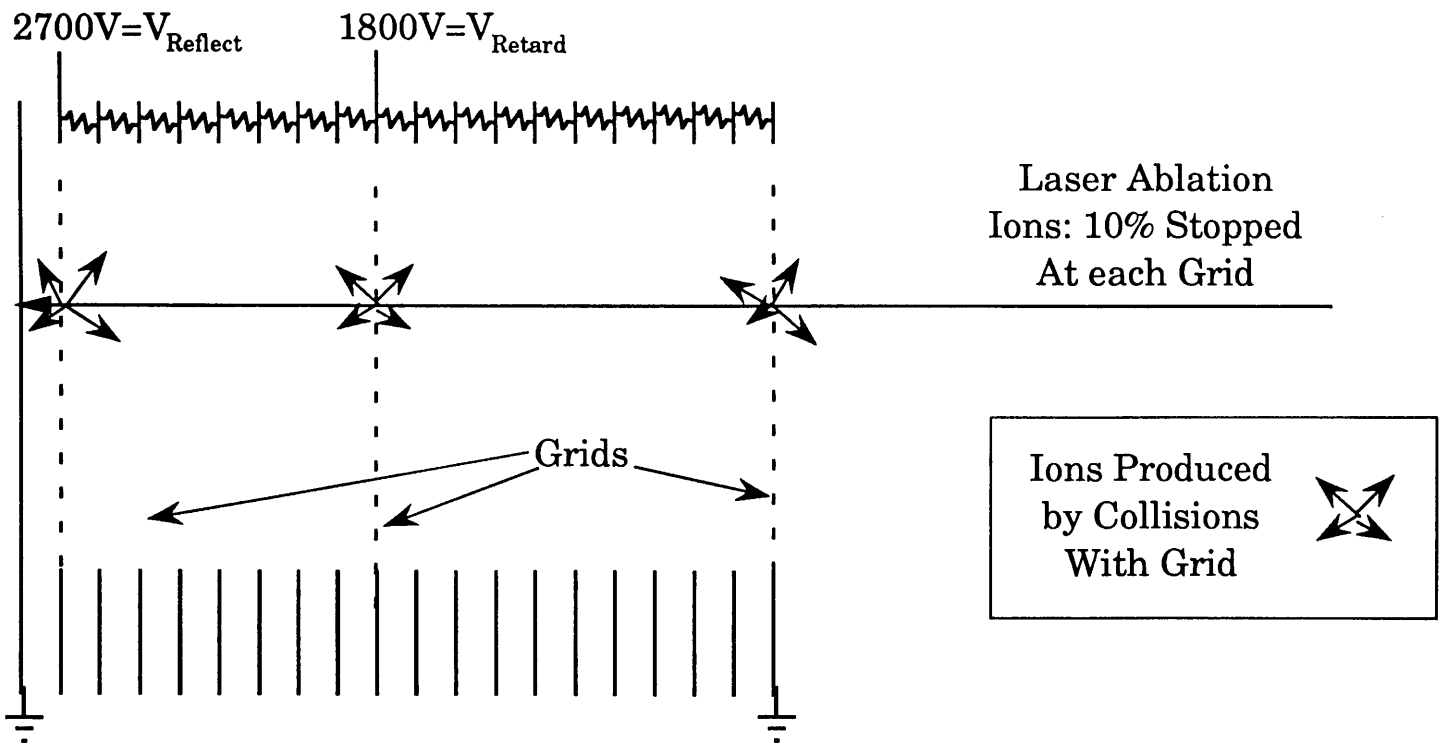

Fig 8.2: Ion Inversion Optics for the Kratos Machine

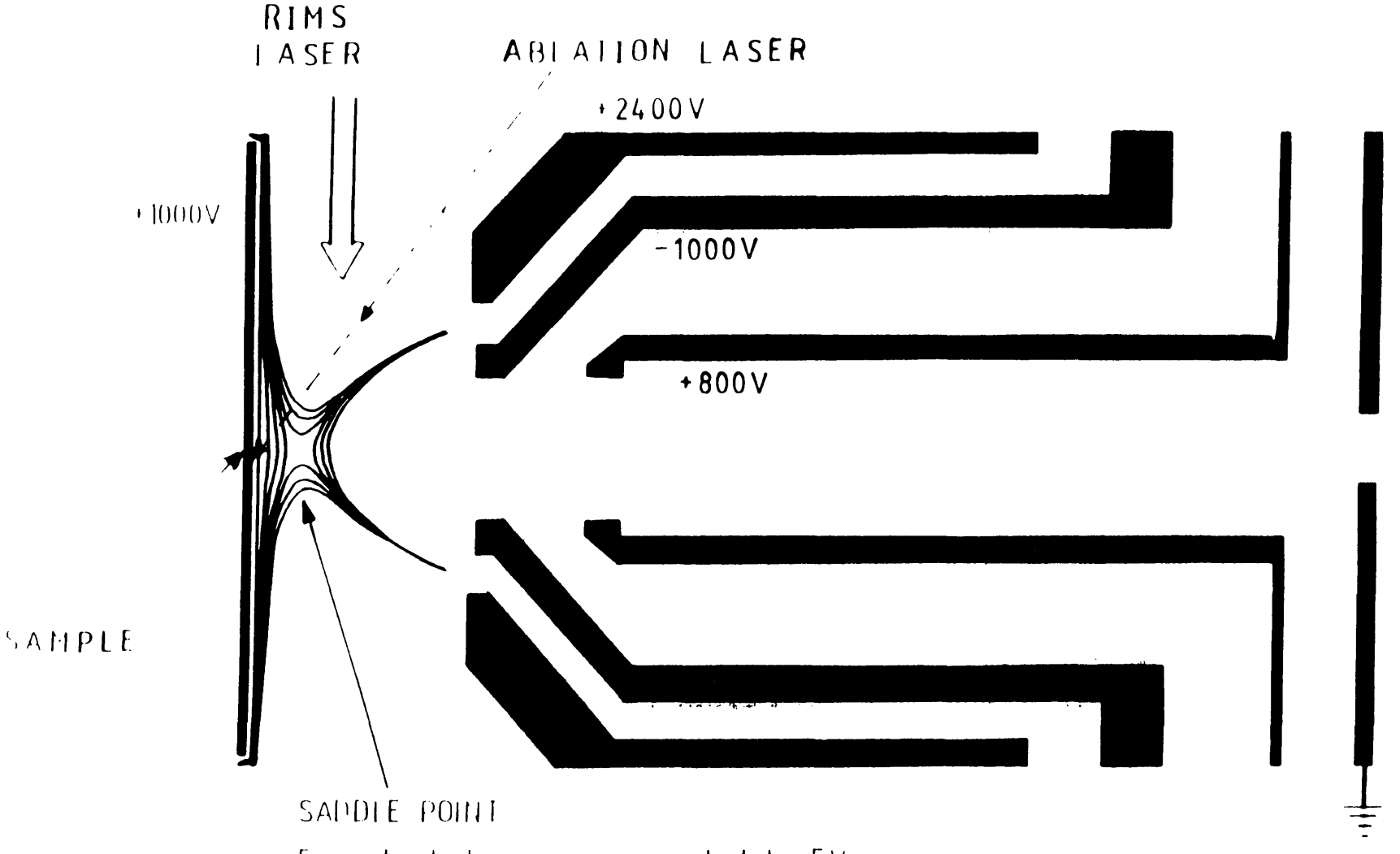

precision is less expensive and more robust. Inversion designs have the drawback of lower geometrical overlap with an ablation or sputter plume, since the post-ionising laser must intercept the beam a few mm (typically >2mm) away from the surface. For ion sputtering optimum geometric overlap is achieved by having the post-ionising laser very close to the surface. For laser ablation the geometric overlap is not reduced to the same extent due to the strongly forward peaked nature of the laser ablation process.

§3 Advances in Solid State Tunable Light Sources

One major disadvantage inhibiting commercial acceptance of RIMS is the lack of a robust tunable laser source. Dye lasers, while useful in a research environment, are not acceptable to industry due to the toxic nature of the dyes and their solvents. Recent developments in the field of tunable solid state lasers should help to alleviate this problem. An ideal commercial system would be a 'black box' where the user (possibly a computer) enters a desired wavelength, and the box outputs that wavelength with no other operations required.

Three of the most promising solid state devices are the titanium doped sapphire laser {Ti^{3+}: Al_2O_3} (Moulton 1982), the Optical Parametric Oscillator {OPO}(Giordmaine and Miller 1965) and the Alexandrite laser {$BeAl_2O_4$} (Walling *et al* 1979, Krasinski *et al* 1986, Pete *et al* 1986).

The absorbtion and emission spectra for Ti:Sapphire are shown in fig 8.3. As can be seen the emission spectrum is broad and continuous from 1100nm to 660nm. The energy level diagram for Ti:Sapphire, showing pumping and lasing transitions, is given in fig 8.4. The short lifetime of the upper state makes flashlamp pumping difficult although possible. The broad absorbtion band centered around 530nm, together with the short upper state lifetime, makes doubled Q-switched Nd:YAG pumping (532nm) ideal for this material. The Ti:Sapphire laser lases in the range of 1070nm to 670nm. Complete wavelength coverage from 1.07μm to 206nm can be obtained with a scheme similar to that in fig 8.5.

Fig 8.3: Absorption and Emission Ranges of Ti:Sapphire.

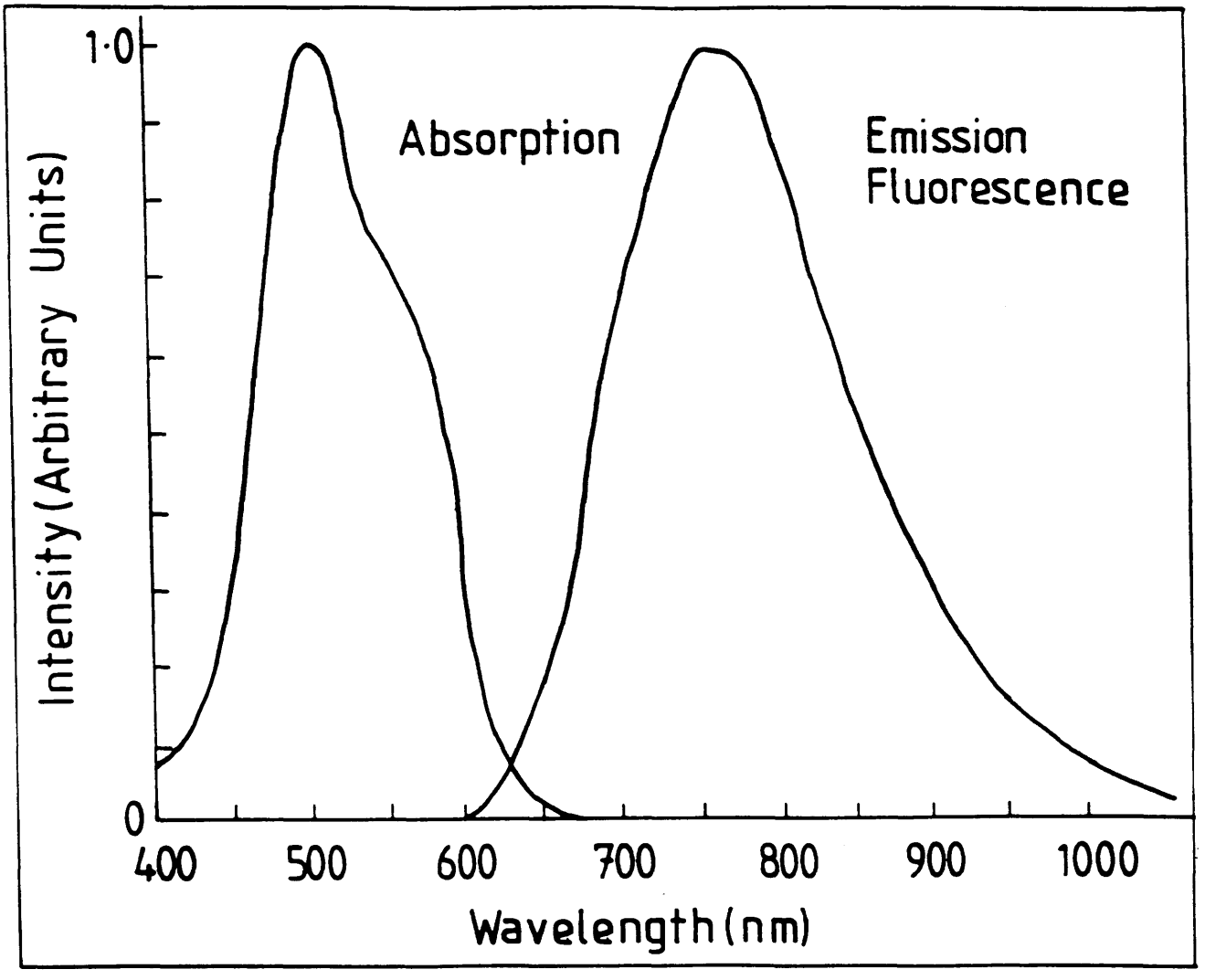

Fig 8.4: Ti:Sapphire Pumping and Laser Transitions

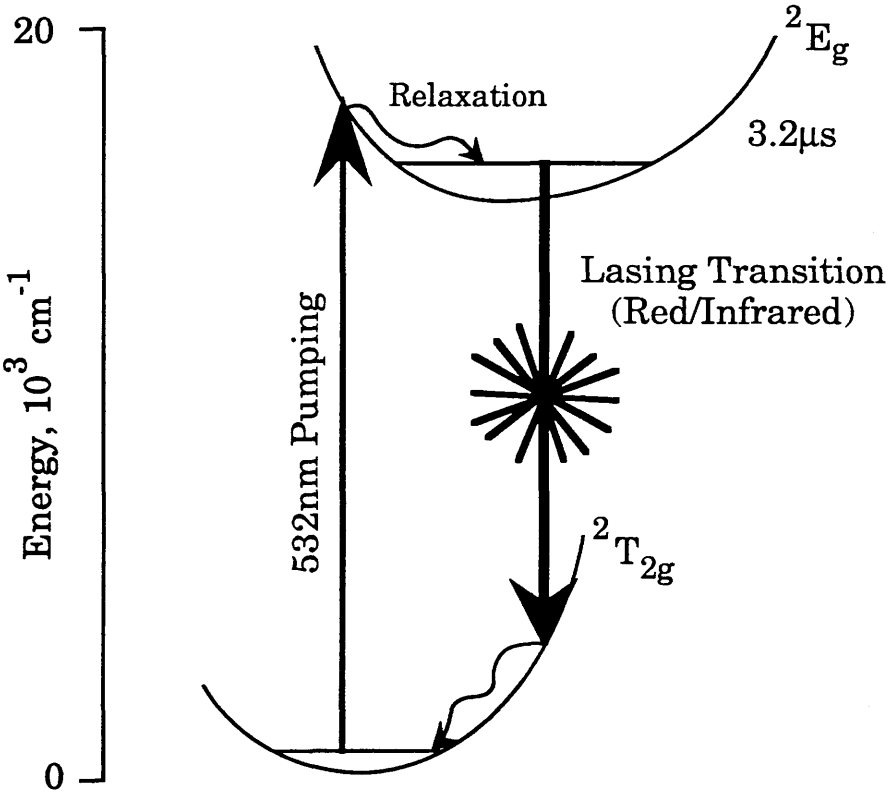

Fig 8.5: A Practical Ti:Sapphire Laser Scheme for Wavelength Coverage

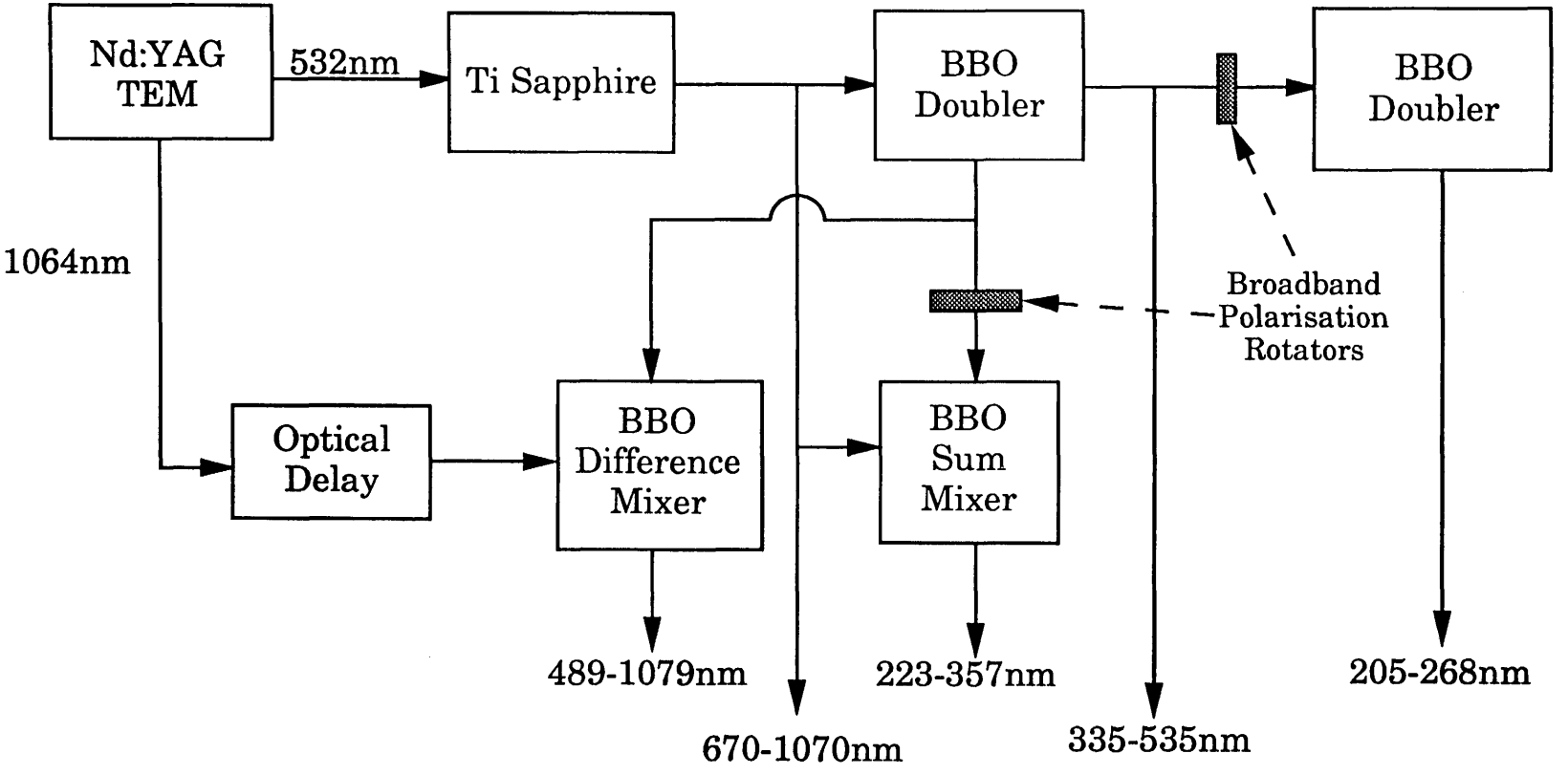

The Alexandrite laser is another tunable solid state laser. It has pumping transitions in the range 630nm to 380nm and is consequently suitable for flashlamp pumping. The tuning range is from 800nm to 720nm. This narrower range is partly compensated by the high pulse energies available from the alexandrite, which allows doubling, trebling and Raman shifting to provide complete wavelength coverage from 2μm to 200nm. A suitable scheme is shown in fig 8.6.

The final tunable solid state light source is not a laser but an optical parametric oscillator {OPO}. Although first demonstrated in 1965 the use of OPOs has been hindered due to the poor mechanical and optical properties of the non-linear crystals required. With the advent of βBBO these deficiencies have been rectified. Several papers have discussed βBBO OPOs in the past few years (Fan *et al* 1988, Cheng *et al* 1988, Bosenberg *et al* 1989, Burdulis *et al* 1990).

An OPO consists of a birefringent crystal within an optical cavity. When this crystal is irradiated by a suitable pump laser (eg 355nm tripled Nd:YAG) two beams of coherent light, called the signal and idler beams, are generated. The frequencies of these beams are related by $\omega_p = \omega_s + \omega_i$ (where ω_p, ω_s, ω_i refer to the pump, signal and idler beams respectively) from the conservation of energy. Maximum gain from a parametric oscillator is obtained when $k_p = k_s + k_i$ (conservation of momentum). To satisfy this latter condition the angle between the pump beam and the optic axis of the crystal is varied, thus resulting in an angle tuned device. Fig 8.7 shows the tuning curve from a βBBO OPO pumped by 266nm Nd:YAG (from Ebrahimzadeh *et al* 1990). A proposed OPO system suitable for RIMS is shown in fig 8.8.

Each of these systems has its own advantages and disadvantages. A Ti:Sapphire system, to obtain complete wavelength coverage, requires a pump laser, the Ti:Sapphire laser, and four harmonic generation and mixing crystals. This leads to an extremely complex system. One advantage is that the

Fig 8.6: Wavelength Coverage for Alexandrite Laser

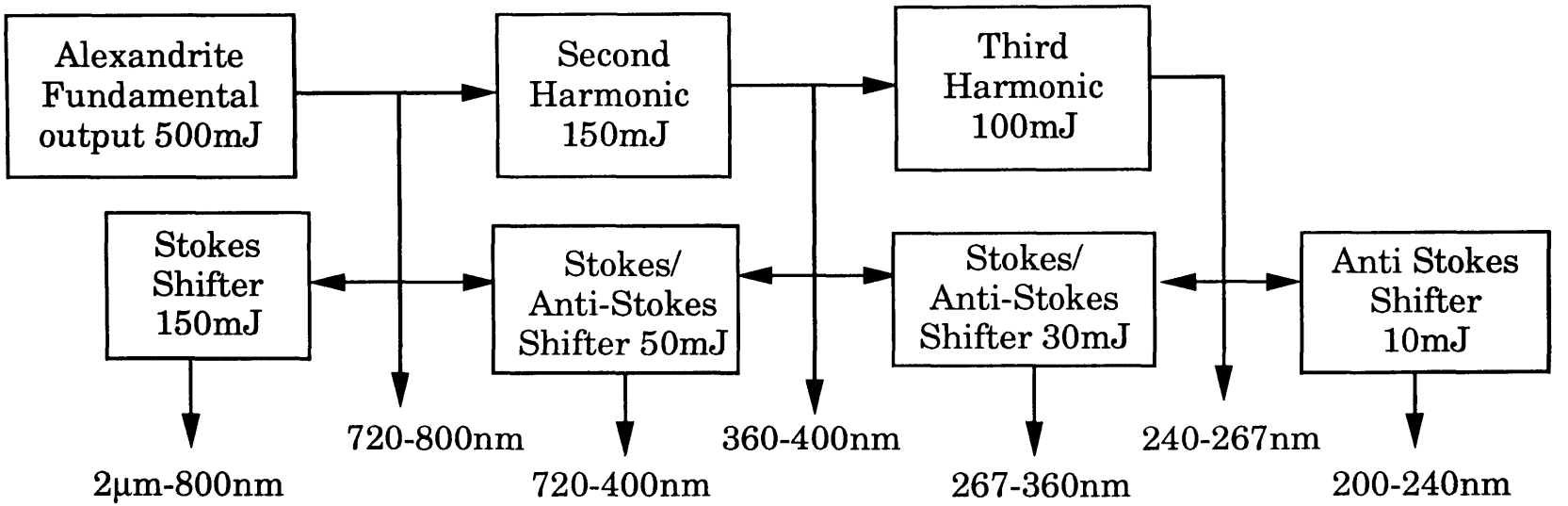

1. Full wavelength coverage requires the use of several different Raman shifting gases. Required in this case are: O_2, H_2 , D_2, CH_4 , and N_2 . (Light Age Inc 1990)

2. Efficiencies are from Light Age Inc (1990). They are : 2nd Harmonic 30%, 3rd Harmonic 25% First Stokes (conversion to the red) 30%, First Anti-Stokes (to the blue) 10%.

Fig 8.7: Tuning range of β-BBO

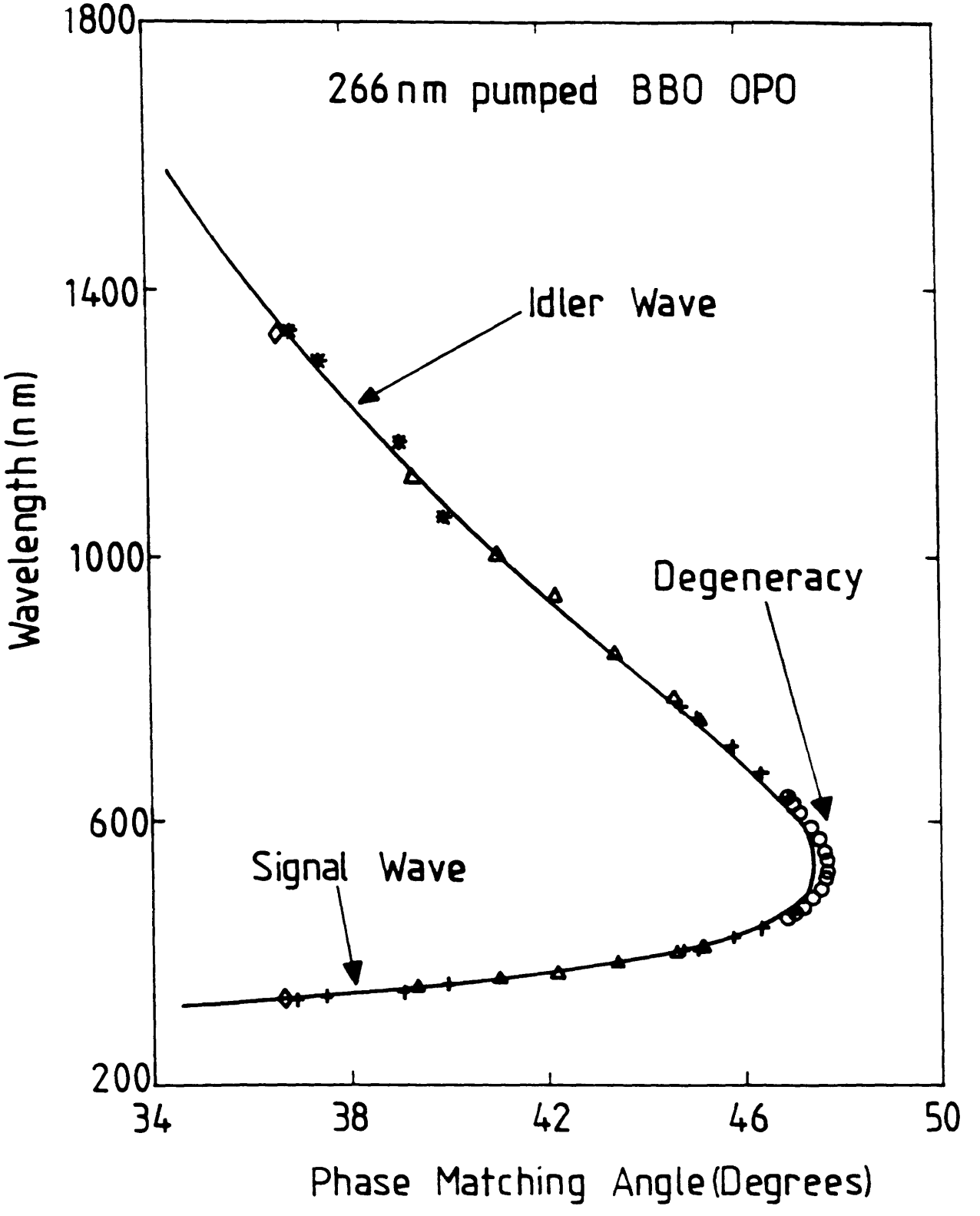

Fig 8.8: Optical Parametric Oscillator Tuning Scheme to Provide Wavelength Coverage

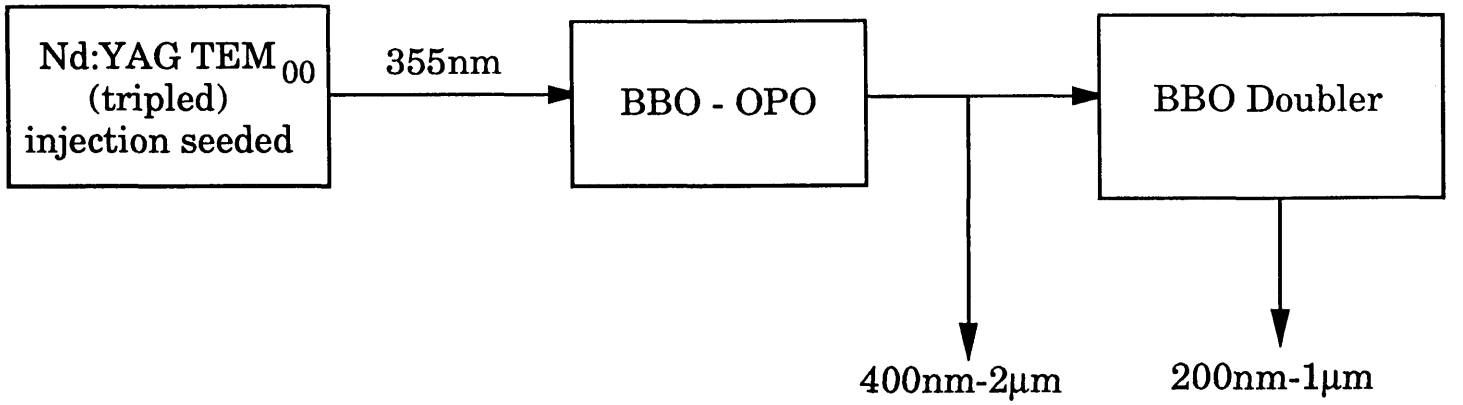

optical quality of the output beam is not strongly dependent on the quality of the pump laser.

Alexandrite lasers, with their narrower tuning range, have a complex tuning system which requires Raman shifting in several different gases. This last complication makes the Alexandrite lasers use in commercial RIMS applications less feasible, as it makes 'black box' operation far more complex.

OPO operation is the hardest to evaluate at the moment, due to their relatively recent introduction and consequent incomplete development. An OPO with no wavelength selective elements, has a very broadband output (~nms), especially near degeneracy (ie when $\omega_i \simeq \omega_s$). Recently Bosenberg *et al* (1989) and Burdulis *et al* (1990) have demonstrated linewidth narrowing by incorporating a diffraction grating in the cavity, giving linewidths of 0.03nm while still maintaining good pump conversion efficiency (9% as opposed to ~15%). The two biggest disadvantages of an OPO system are the requirement for a very high quality pump laser, since OPO output cannot be decoupled from the pump laser, and the need for multiple sets of mirrors for the optical cavity, leading to mechanical complications. This last requirement is due to the very wide range of wavelengths produced within the cavity.

There are other, pragmatic, considerations governing the choice of optical sources for RIS or RIMS. Patents exist covering the use of laser initiated RIS for trace analysis (Hurst *et al* 1984, Hurst *et al* 1976) and also covering the alexandrite laser system (US patents #3,866,142 and #4,272,733). Other manufacturers are understandably reluctant to embrace these technologies while these patents are in force. Ti:sapphire lasers and OPOs are public domain and consequently more liable to be developed by independent manufacturers. Another important consideration with OPOs is that the 1984 "*Sputter Initiated Resonance Ionisation Spectroscopy*" patent, the claims explicitly mention *laser* initiated resonant ionisation spectroscopy. Hence, RIS or RIMS utilising OPOs (which are *not* lasers) are not covered by this patent.

§4 Other RIMS methods

Pulsed laser are widely used in RIMS because they have sufficient power to ionise every atom interrogated whereas continuous wave (CW) lasers deliver insufficient fluence for saturation. However, Miller and Nogar (1983a, 1983b) have demonstrated that in some cases, using CW lasers, the increase in the number of atoms examined offsets the lower fluence used, resulting in greater ionisation yields.

One major difference between CW RIMS and pulsed RIMS is the much narrower bandwidth of CW lasers. This allows isotopic selective ionisation schemes to be used (Cannon *et al* 1985). However the narrow bandwidth may be a disadvantage as it may result in incorrect isotope ratios unless the laser is scanned across the range of isotope shifts present. This would eliminate any advantages accrued through greater ionisation efficiencies.

In a development of CW RIMS, a semiconductor diode laser has been used as the initial step in RIMS of Lanthanum (Shaw *et al* 1989). Semiconductor diode lasers provide low cost operation with tunability, simplicity and ruggedness. In the Lanthanum study the diode laser was operated at 753.93nm, in the near infra-red. In few elements (mainly the rare earths) are such long wavelengths useful as an initial step in a RIMS process. However, with the continuing development of diode lasers towards shorter wavelengths complete coverage of the visible spectrum seems feasible. With the advent of efficient frequency doubling techniques for use at these low powers (Dixon 1990), an all diode laser excitation scheme is possible.

A new method of RIMS analysis, known as Resonant Laser Ablation {RLA}, has been extensively investigated at Glasgow by Dr Chris. Mc Lean and Dr Wang Li. Instead of resonantly post-ionising neutrals produced from the surface (by ion sputtering or laser ablation) the resonant laser is used to ablate the surface. If the flux of the laser is chosen carefully then resonant enhancements (ie the ratio of the ion signal when the laser is on

resonance as compared to the signal off resonance) of 800 have been achieved at Glasgow. A full description of RLA and associated effects as performed at Glasgow may be found in McLean (1990), Wang *et al* (1990) and McLean *et al* (1990). RLA has not to date been used as a tool for trace analysis, and so not definite statement can be made regarding its effectiveness in this role. There are reasons to believe that the suspected RLA ionisation mechanism will limit its performance in this field (see below).

RLA was first observed by Verdun *et al* (1987). They reported resonant enhancements of ~5 for cadmium and copper in metal doped polymers, and for molybdenum in a standard steel alloy sample. For one experiment on copper an enhancement of ~50 was reported. The widths of the resonances in these cases were very broad (0.4 - 0.7nm). Resonant enhancements have also been observed in sodium and copper by Pang *et al* (1988).

The RLA work performed at Glasgow has some advantages and disadvantages in comparison with laser ablation initiated RIMS. The technique only requires one laser, as opposed to the two normally required. The nature of the ion production in the RLA process almost completely eliminates any non-resonant background, such as the unwanted ions produced under more usual laser ablation conditions. The wavelength required for the RLA process to occur is identical (to within the bandwidth of the laser used (see references above)) to the resonant wavelength of a gaseous sample. This shows that RLA transitions are equivalent to normal free atom transitions and no searching for undocumented transitions occuring in solid samples is required.

One important disadvantage of RLA is the limitation on fluence required to maintain selectivity. At low fluences the only ions produced are the resonant ions. As the fluence is increased non-resonant ions are produced, leading to loss of selectivity.

The ionisation process in RLA is unclear, although energy pooling (the collision of two identical excited atoms leading to one ion and one unexcited atom) has been proposed as a mechanism (Wang *et al* 1990). If energy pooling is responsible for the

ionisation then this has important implications for the use of RLA as a trace analysis tool. The sensitivity of the method will not drop linearly with sample concentration but quadratically. Another unwanted feature of energy pooling ionisation is the impossibility of saturating the ionisation process, even if all atoms are excited.

Because of these problems, the most promising role for RLA would appear to be as a fast and (comparatively) inexpensive method for surface analysis and also, due to the coincidence of RLA and RIS transitions, an easy way of tuning lasers to a resonant frequency for RIMS studies using conventional atomisation techniques.

§5 Conclusions

This thesis demonstrates laser ablation as a useful and versatile atomisation source. It is capable of achieving very high neutral fluxes (of up to 10^{14} neutrals produced from one laser pulse compared to 10^{9} from one 1μA ion beam pulse). These high fluxes are essential for the most sensitive analyses. If an element of interest is present at a level of 1 part in 10^{15} (1 ppqn (part per quintillion)) then laser ablation will produce ~10^{14} neutrals (or on average one neutral of the element of interest every 10 shots) whereas ion sputtering will produce 10^{9} neutrals per shot, resulting in one neutral of interest every 10^{6} shots. Provided 'noise' rejection (ie. spurious signals produced by the atomisation process) can be reduced to similar levels in both mechanisms, then the potential advantages of laser ablation are immediately apparent.

Several difficulties remain with laser ablation. The problem associated with semiconductor profiling (eg long range heating resulting in destruction of lattice structures: see chapter 6) is very unlikely to be overcome, so ion sputtering will remain the preferred atomisation source in this field. In other areas the main disadvantage of laser ablation is the lack of information about matrix effects. In ion sputtering there is a vast body of work about matrix effects and different sputtering rates for different materials. This material has been acquired from investigations into the use of SIMS. Thus, until a similar body of knowledge is

built up about laser ablation, laser ablation is unlikely to supplant ion sputtering as a neutral source.

One of the most interesting effects observed in the laser ablation experiments was the dependence of the isotope ratio measurements on the delay between the firing of the ablation laser and the firing of the post ionising laser. This provides a limitation in the accuracy with which isotope ratio measurements can be achieved using laser ablation as a neutral source.

Finally, the utility of RIMS as a commercial analytical method must be assessed. The Kratos machine was originally designed as a possible commercial prototype for RIMS analysis. The performance of the instrument currently preclude its use 'as is' in a commercial environment. The most prominent problem are the tunable lasers used. As discussed above the likelihood of high quality tunable solid state lasers becoming available which are suitable for use on a RIMS machine is very high, and the current unsuitability of tunable dye lasers should not be taken as precluding industrial use of RIMS.

Similarly, many of the problems encountered with laser ablation arise from design inadequacies in the original design of the machine (ie gridded reflectron, poor rejection of laser ablation ions) and could be easily corrected in a commercial machine.

Consequently, with the improvements mentioned above, a commercial RIMS instrument, with routine sensitivity for most metallic elements of sub ppb, is feasible.

Appendix A: Properties of Gold

Elemental Properties:

Name:	Gold
Symbol:	Au
Atomic Number:	79
Atomic Weight:	196.9675 g mol^{-1}
Crystal Structure:	Face Centered Cubic
Atomic Radius:	144pm
Principle Oxidation Numbers:	+1, +3
Ionic Radii:	137pm, 85pm
Ionisation Potential:	9.225eV
Density:	19300kgm^{-3}
Melting Point:	1336.1K (primary reference point)
Boiling Point (1 atm):	3239K
Nuclear Spin (Au^{197}):	3/2

Electronic Structure:

$1s^2 2s^2 2p^6 3s^2 3p^6 3d^{10} 4s^2 4p^6 4d^{10} 4f^{14} 5s^2 5p^6 5d^{10} 6s^1\ {}^2S_{1/2}$

Miscellany:

Gold (*aurum*; shining dawn) is generally found in nature either as free metal or as auric telluride (or *calaverite*). It is generally removed from its ores by either cyaniding, smelting or electrolysis. Gold occurs in seawater to an extent of ~0.2mg/tonne, although it cannot, as yet, be profitably extracted. Uses of gold include jewelry, dental work, microelectronics and as a standard for monetary systems.

Isotope Data:

Isotope	Half Life (>1hr)	Comments
191	3.2h	
192	4.1h	
193	16.h	
194	39.5h	
195	183d	
196	6.18d	
197	stable	100% abundance
198	2.693d	(used in neutron activiation analysis)
199	3.15d	

From: *Handbook of Chemistry and Pysics 53rd Edition, CRC Press.*
Science Data Book, B.M. Tennent, Oliver Edinburgh, 1971

Appendix B: Ion Inversion Optics and Primary Ion Suppression.

§1 Introduction

In the resonant ionisation arrangement used in this thesis, the sample is vaporised by laser ablation to form a neutral plume. This plume is subsequently resonantly ionised and the ions produced analysed in a mass spectrometer. Thus, there are two types of ions present. The first are those produced by the laser ablation pulse and the second are those produced in the resonant ionisation process. In order to achieve the highest possible sensitivity it is imperative that the two types of ions be discriminated.

The impetus behind the development of these optics stemmed from the need to discriminate between the secondary ions (produced by ion sputtering) and resonant ions detected in a linear time of flight mass spectrometer. This spectometerand its associated instrumentation are described extensively elsewhere (McLean 1990).

Detailed in this appendix is a novel and simple method for discriminating between the laser ablation ions and the resonant ions. Firstly the concept behind the operation of the optics will be explained. Next the results from computer modelling will be given. Finally the results from a linear TOF-MS will be given, which shows the effectiveness of this method.

§2 Principle of Operation

Normal ion optics function, for positive ions, by providing a negative potential gradient from the sample to the first optic. This has the effect of accelerating the ions produced at the sample surface into the mass spectrometer. Inversion optics function by providing a saddle field between the sample and the first optic (fig B.1). Any ions formed at the surface of the sample will, instead of the negative gradient electric field, experience an positive gradient. The ions will be held at, or returned to, the

Fig B.1: Saddle Point in Ion Optics

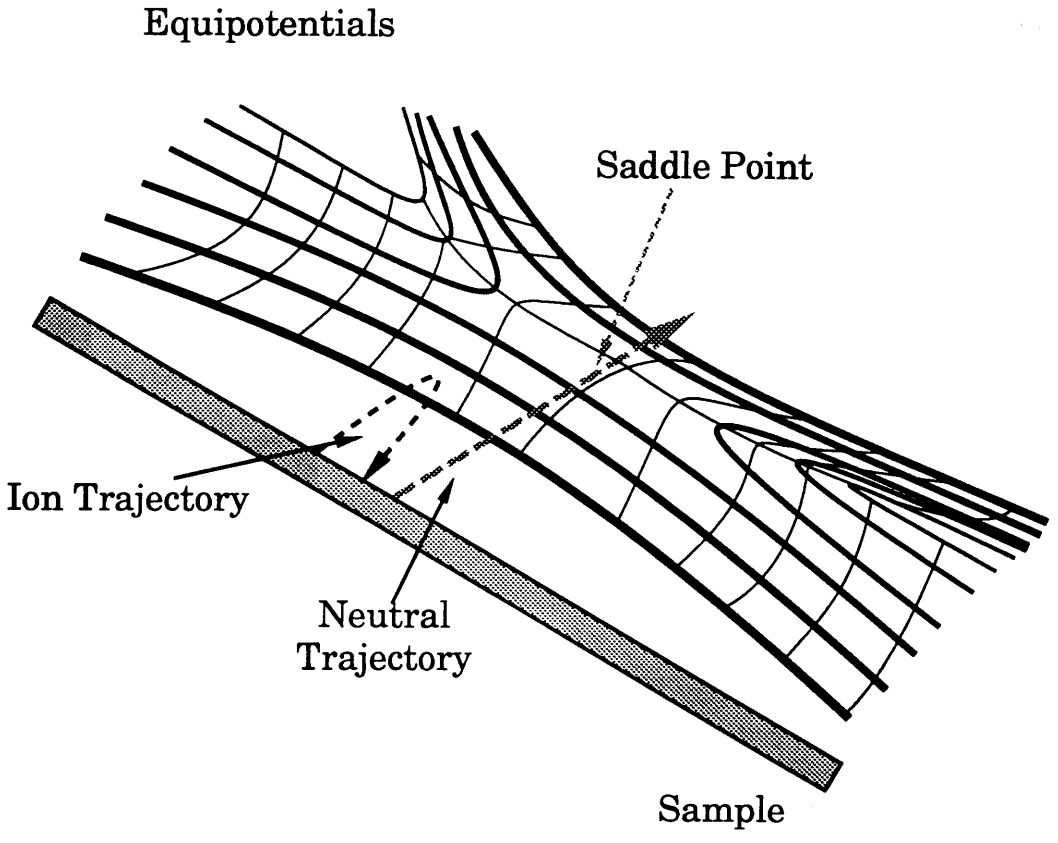

sample surface. The neutrals will be unaffected by this field and will travel through the saddle point unperturbed. Upon reaching the far side of the saddle point the neutral plume is interrogated by the resonant laser and ions are formed in the resonant ionisation process. These ions experience a normal acceleration field and are passed into the mass spectrometer in the usual fashion.

Other techniques exist to reject the unwanted ions. The use of a reflectron as a method for rejection has been described elsewhere in this thesis (chapter 3). Another method, described by Pellin *et al* (1986), used pulsed ion optics to reject secondary ions which are produced by ion sputtering. By pulsing the optics during the sputtering cycle the secondary ions produced can be made to remain at the surface.

§3 Computer Modelling of Ion Inversion Optics

The computer modelling of the ion optics was carried out using the program SIMION v3.11 (SIMulated ION)(Dahl 1987). This is a program written for use on a personal microcomputer and is specifically designed for modelling ion optics.

Two sets of optics have been modelled. The first set was designed for use in a linear time of flight system. Here the object of the design was an easily manufactured set of optics that displayed the desired properties. Fig B.2 shows the equipotential contours from the lens, with the saddle point indicated. Fig B.3 shows two sets of ion trajectories, one from each side of the saddle point. The ions have mass seventy and initial energy of 5eV. The main drawback of this design is the distance of the ionisation region from the sample.

Figs B.4 and B.5 show the equipotential contours and the ion trajectories for a second lens. This lens operates with a higher accelerating voltage and has the ionisation region closer to the sample. This allows greater overlap with the ablated plume.

§4 Implementation and Performance of Ion Optics

The first set of optics modelled above were implemented in a linear time of flight mass spectrometer. The pulses were krypton

Fig B.2: Linear TOF Inversion Optics Showing Equipotentials

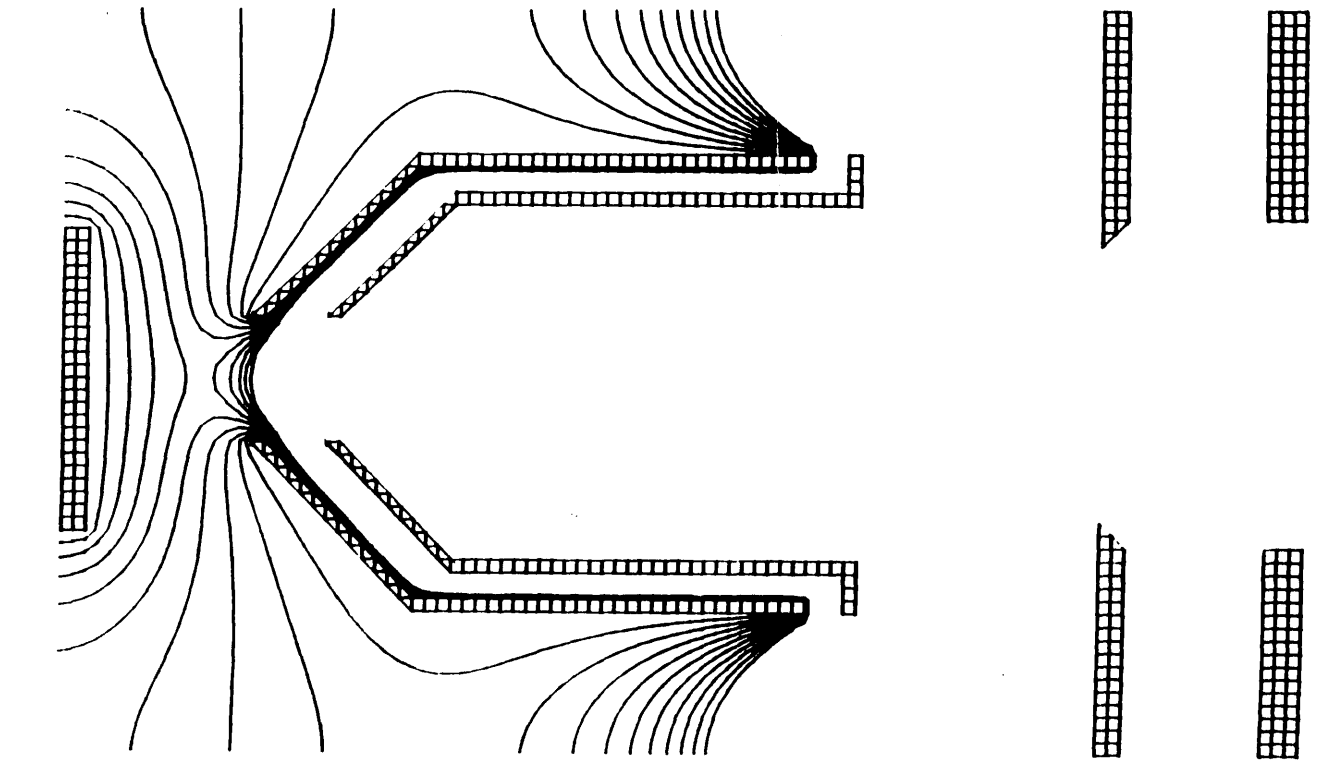

Fig B.3: Linear TOF Inversion Optics Showing Ion Trajectories

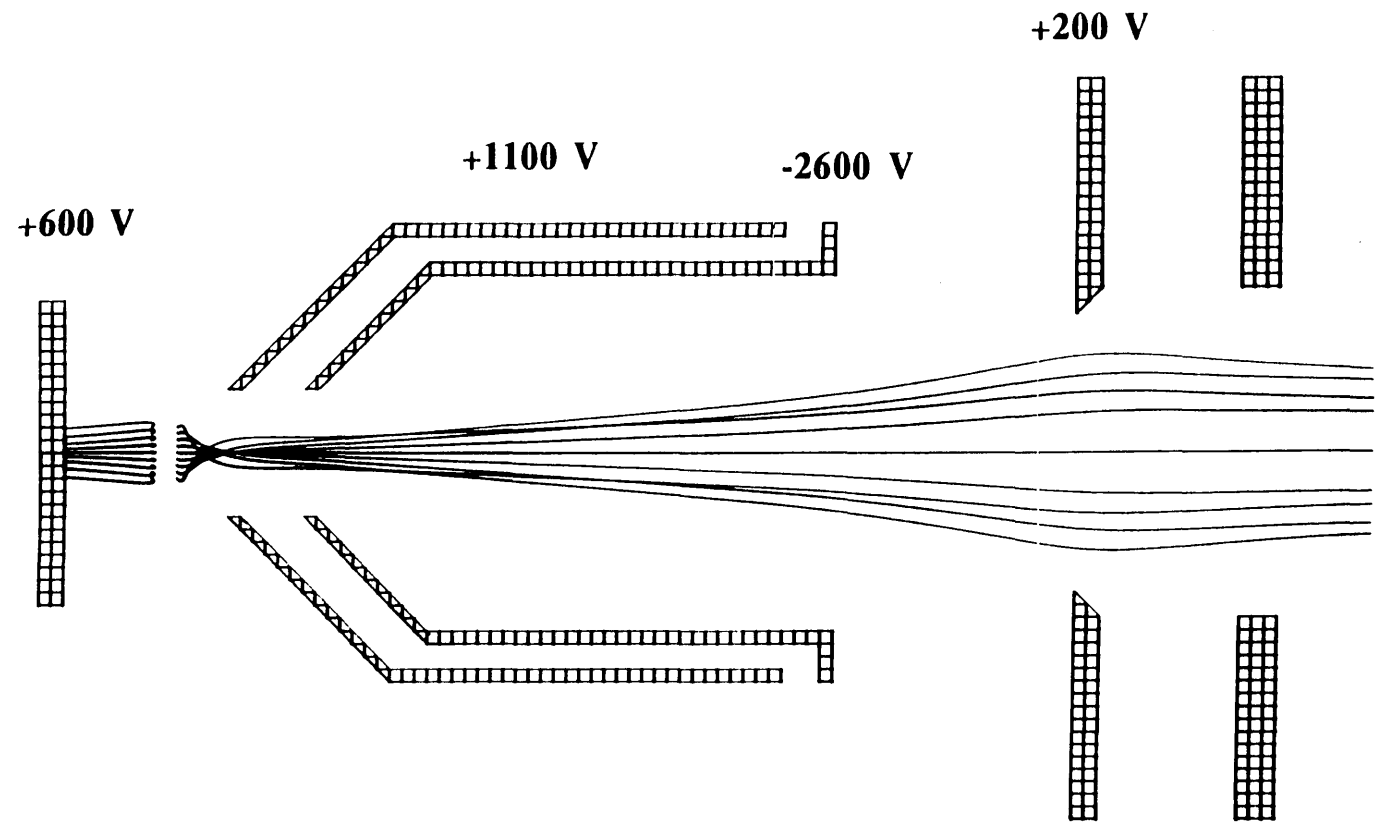

Fig B.4: High Voltage Inversion Optics Showing Ion Trajectories

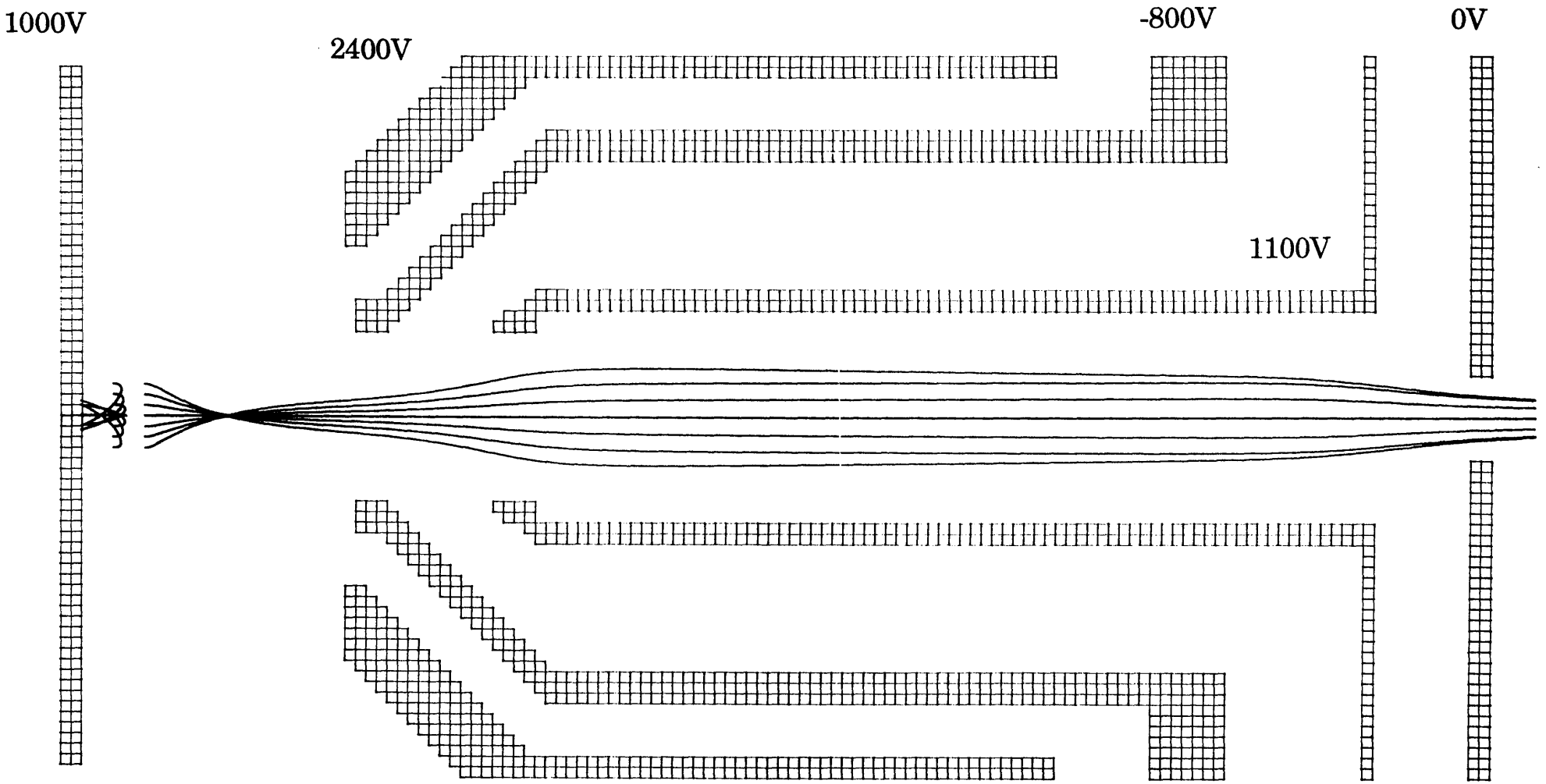

Fig B. 5: High Voltage Inversion Optics Showing Equipotentials

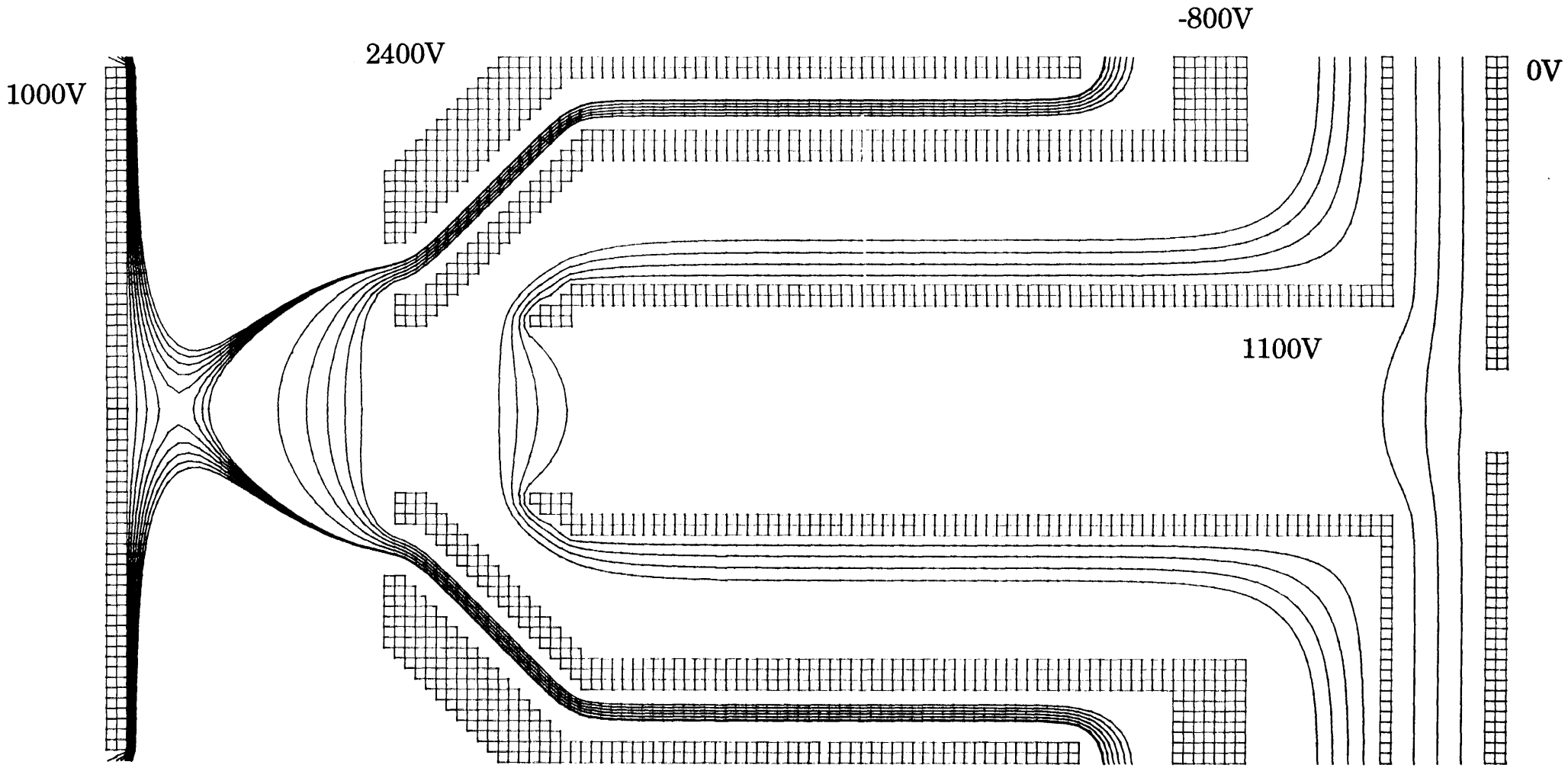

ions produced by a modified Kratos Macrobeam. Fig B.6 shows the performance of the instrument when the optics are operated in a non-saddle field mode. Due to the long primary ion pulse (3μs) it was not possible to seperate the ion components temporally. Clearly visible are the two RIMS peaks sitting on top of the very broad secondary ion peak. Although the RIMS peaks are visible, such operation is clearly undesirable. Fig B.7 shows the same arrangement with the ion optics operating in saddle field mode. The secondary ion peak in this case is substantially reduced.

§5 Conclusion

This appendix has demonstrated that rejection of ions produced in an ablation or sputtering process is feasible using only electrode geometry. The method is not restricted to pulsed vaporisation situations but, unlike pulsed optics, is applicable to continuous sputtering sources. Although demonstrated on a system using ion sputtering, it is expected that the same priciples will be as effective on a laser ablation initiated system. A laser ablation initiated system would be expected to have an advantage over an ion sputtering system due to the more forward peaked plumes produced by laser ablation. This would allow a larger geometric overlap of the plume by a post-ionising laser at the relatively large distances required for the operation of these optics. Thus a larger proportion of the neutral plume would be interrogated and greater sensitivity would ensue.

Fig B.6: Signal When Ion Optics are Operated in Non-inversion Mode

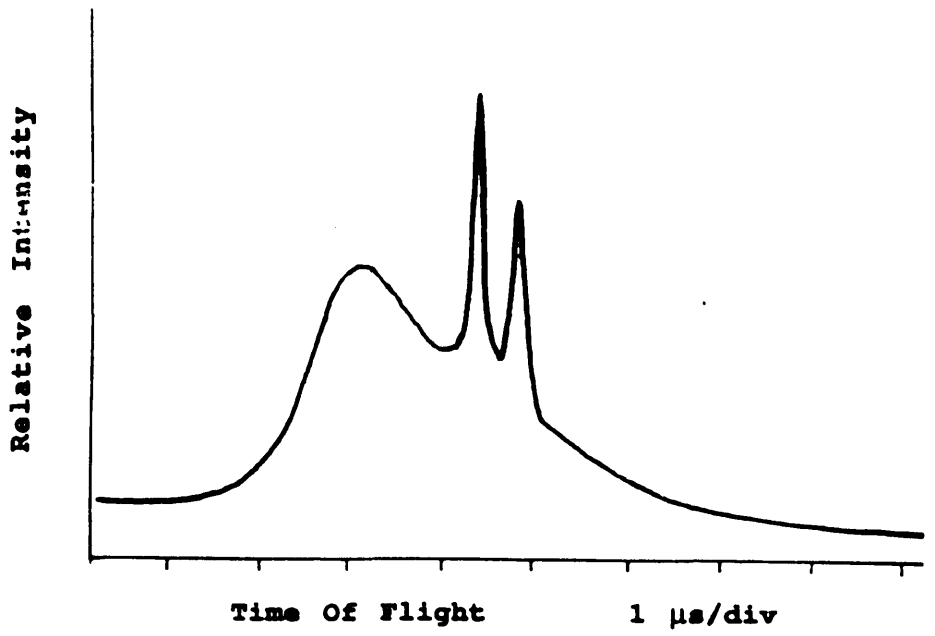

Fig B.7: Signal When Ion Optics are Operated in Inversion Mode

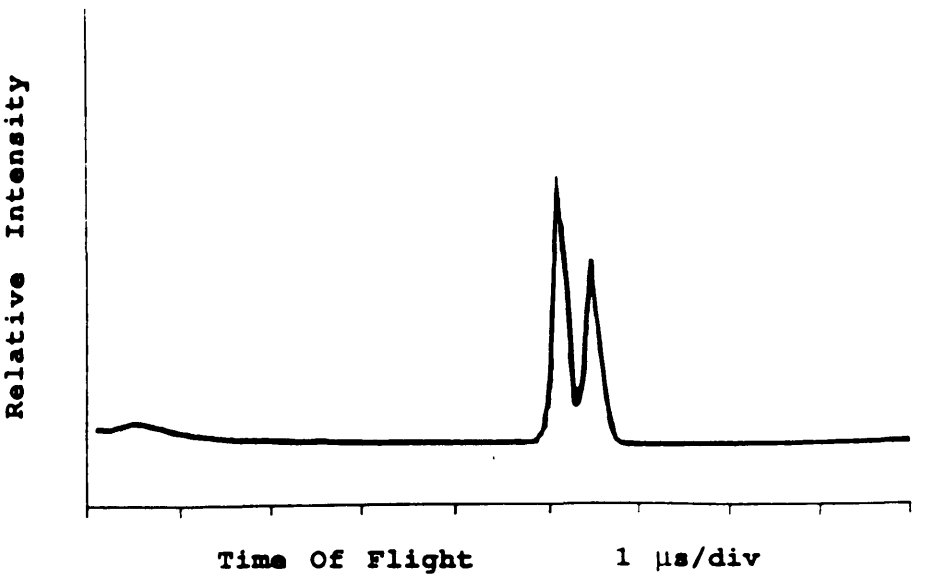

REFERENCES

Ambartsumyan R.V., Kalinin V.N. & Letokhov V.S., (1971), Sov. Phys. JETP Lett. **13** p217.

Ambartsumyan R.V. & Letokhov V.S., (1972), Applied Optics **11** p354

Ames F., Kluge H.-J., Suri B.M., Venugopalan A., Rimke H., Trautmann, N. & Kirchner R., (1990), "*RIS of Technetium in a Laser Ion Source for a Solar Neutrino Problem*", to be Published in 'RIS 90' by Institute of Physics Publishing.

Apel E.C., Anderson J.E., Estler R.C., Nogar N.S. & Miller C.M., (1987), "*Use of Two Photon Excitation In Resonant Ionisation Mass Spectrometry*", Appl Opt **26** pp1045

Apel E.C., Nogar N.S., Miller C.M. & Estler R.C., (1987b), "*RIMS disgnostics for laser desorption / laser ablation*", Resonance Ionisation Spectroscopy 1986, Inst. Phys. Conf. Ser. **84** (Ed Hurst G.S. and Grey Morgan C.) pp181-184.

Apel E.C., Anderson J.E., Estler R.C., Nogar N.S. & Miller C.M., (1987c), Appl. Opt. **26** pp1045.

Arlinghaus H.F., Spaar M.T. & Thonnard N., (1990),J. Vac. Sci. Technol., **A8** (3) pp2138.

Arlinghaus H.F., Thonnard N. & Schmitt H.W., (1989), "*Ultratrace Element Microcharacterisation of Surfaces and Solids with SIRIS*", in 'Microbeam Analysis - 1989' (Ed Russell P.E.), San Fransisco Press Inc.

Arlinghaus H.F., Thonnard N., Spaar M.T. & Jacobson K.B., (1990), "*Use of RIS to Significantly Increase the Speed of Sequencing of the Human Genome*", To be published in 'RIS 90' by Institute of Physics Publishing

Balazs N.D.H., Pole D.J. & Masarel J.R., (1972), Clin. Chem. Acta, **40** pp213.

Bebb H. B. & Gold A. (1966), Phys. Rev., **143** p1.

Beekman D.W., Callcott T.A., Kramer S.D., Arakawa E.T., Hurst G.S. & Nussbaum E., (1980), "*Resonance Ionisation Source for Mass Spectrometry*", Int. J. of Mass Spect. and Ion Phys. **34** pp89-97.

Beekman D.W. & Callcott T.A., (1985), "*Laser Ablation Studies using RIS*", Inst. Phys. Conf. Ser. **71** (Ed. Hurst G.S. and Payne M.G.) pp143-150.

Beekman D.W. & Thonnard N., (1989), "*Laser Ablation as an Atomization Source for Ultra Trace Element Ananlysis using Resonance Ionization Mass Spectrometry*", Inst. Phys. Conf. Ser. **94** (Ed. Lucatorto T.B. and Parks J.E.) p163.

Bekov G. I., Letekhov, V. S., Matveev O. I. & Mishin V. I., (1978), Optics Letters, **3** p159.

Bekov G.I. & Letokhov V.S., (1983), "*Laser Atomic Photo-ionisation Spectral Analysis of Trace Analysis*",Appl. Phys. B **30** pp161.

Bekov G.I., Letokhov V.S. & Radaev V.N., (1985) J. Opt. Soc. Am. B, **2** pp1554

Bekov G.I., Kudryavtsev Y.A., Auterinen I. & Likonen J., (1987), "*The Laser Ionisation Mass Spectrometer*", Inst. Phys. Conf. Ser. **84** (Ed Hurst G.S. and Grey Morgan C.) pp97.

Bekov G.I., Radaev V., Likonen J., Zilliacus R. & Auterinen I., Lakomaa E-L., (1987b), Anal. Chem **59** 2472.

Benninghoven A., Rüdenauer F.G. & Werner H.W., (1987), " *Secondary Ionisation Mass Spectrometry: Basic Concepts, Instrumental Aspects, Applications and Trends*", John Wiley & Sons, Chemical Analysis Series Vol 86.

Bingham R.A. & Salter P.L., (1976), "*Analysis of Solid Materials by Laser Microprobe Mass Spectrometry.*", Anal. Chem., **48** 12 pp1735-1740.

Boesl U., Neusser H.J. & Schlag E.W., (1980), J. Chem. Phys., **72** p4327.

Boesl U., Neusser H.J., Weinkauf R. & Schlag E.W., (1982), J. Chem. Phys., **86** p4857.

Boesl U., Grotemeyer J., Walter K. & Schlag E.W., (1987), Analytical Instrum. **16** (1) pp151.

Bosenberg W.R., Cheng L.K. & Tang C.L., (1989), Appl. Phys. Lett., **54** pp13.

Burdulis S., Grigonis R., Piskarskas A., Sinkevicius G., Siritaitis V., Fix A. Nolting J. & Wallenstein R., (1990), Optics Comm., **74** pp398.

Bushaw B.A. & Gerke G.K., (1989), "*Trace Isotopic Analysis by Double Resonance Ionization with CW Lasers and Graphite Furnace Atomization*", Inst. Phys. Conf. Ser **94** (Ed. Lucatorto T.B. and Parks J.E.) p277.

Cannon B.D., Bushaw B. A. & Whitaker T. J., (1985), "*Continuous Wave Double Resonance Ionisation Mass Spectrometry of Barium*", J. Opt. Soc. Am. B, **2** (9) p1542.

Cheng L.K., Bosenberg W.R. & Tang C.L., (1988), Appl. Phys. Lett., **53** pp175

Christie W.H. & Goeringer D.E., (1987), "*Small Sample Analysis Using Sputter Atomisation/Resonance Ionisation Mass Spectrometry*", Inst. Phys. Conf. Ser. **84** (Ed Hurst G.S. and Grey Morgan C.) p169

Corney A., (1977), "*Atomic and Laser Spectroscopy*", Claredon Press pp120.

Conzemius R.J. & Capellen J.M., (1980), "*A Review of the Applications to Solids of the Laser Ion Source in Mass Spectroscopy*", Int. J. Mass. Spec. Ion. Phy. **34** pp197.

Crane, J.K., Erbert G.V., Paisner, J.A., Chen H.L., Chiba Z., Beeler R.G., Combs R. & Mostek S.D., (1987), "*The Application of Atomic Vapour Laser Isotope Seperation to the Enrichment of Mercury*", Resonance Ionisation Spectroscopy 1986, Inst. Phys. Conf. Ser. **84** (Ed Hurst G.S. and Grey Morgan C.) pp 251-254.

Dahl D.A. & Delmore J.E., (1987), "*The SIMION PC/PS2 User's Manual Version 3.11*", Informal Report, Idaho National Engineering Laboratory, EGG-CS-7233 Rev. 2, November.

Dermtröder W., (1981), "*Laser Spectroscopy (2nd Ed)*", Springer Verlag.

Dingle T., (1987), Private Communication.

Dirac P.A.M., (1967), "*The Principles of Quantum Mechanics (4th Ed)*", Oxford Science Publications.

Dixon G.J., (1990), "*Frequency-dou bling Schemes Turn CW DPLs into Visible Sources*", Laser Focus World, Sept pp99.

Dovichi N. J., Moore D. S. & Keller R. A., "*Use of the Optogalvanic Effect and the Uranium Atlas for the Wavelength Calibration of Pulsed Lasers*", Applied Optics, **21** 8 pp1468-1473.

Donohue D.L., Young J.P. & Smith D.H., (1982), Int. J. Mass Spectrm. Ion Phys., **43** p293.

Donohue D.L., Smith D.H., Young J.P., Mc Kown H.S. & Pritcherd C.A., (1984), Anal. Chem., **56** p379.

Downey S. W., Amerson A.B. & Kopf R.F., (1990), "*Depth Profiling Resonant Ionisation Mass Spectrometry of Compound Semiconductors*", To be published in 'RIS 90' by Institute of Physics Publishing.

Eastham D. A., (1986), "*Atomic Physics of Lasers*", Taylor and Francis, pp164-169.

Ebrahimzadeh M., Henderson A.J. & Dunn M.H., (1990), IEEE J. Quantum Electron., **26**.

Estler R.C., Apel E.C. &, Nogar N.S., (1987), "*Laser Mass Spectrometric Studies of Optical Damage in CaF_2*", J. Opt. Soc Am. B, **4** 2 p281.

Estler R.C. & Nogar N.S.,(1990), "*Laser Mass Spectrometric Studies of High Temperature Superconductor Ablation*", SPIE proc. **1208**, Laser Photoionisation and Desorption Surface Analysis Techniques.

Fan Y.X., Eckhardt R.C., Byer R.L., Nolting J. & Wallenstein R., (1988), App. Phys. Lett., **53** pp2014.

Fassett J.D., Moore L.D., Shiedler R.W. & Travis J.C.,(1984), Anal. Chem. **56** pp203.

Fassett J.D. & Travis J.C., (1988), "*Analytical Applications of Resonance Ionisation Mass Spectroscopy*" Spectrochimica Acta, **43B** 1409.

Fassett J.D. & Paulsen P.J., (1989), Anal. Chem.**61** pp643A.

Feynman R.P., Vernon F.L. & Hellwarth R.W., (1957), J. Appl. Phys., **28** p49

Frajola W.T. & Mitchell P.B., (1967), Fed. Proc. (Abstracts), **26.**

Garrison B.J. & Winogard N., (1982), "*Ion Beam Spectroscopy of Solids and Surfaces*", Science **216** (4548) pp805.

Gaul, L.E. & Staud A.H., (1933), Arch. Dermat. Syph., **28** p790.

Gerke G.K., Bushaw B.A. & WHitaker, (1988), "*Low Levels of Radionuclide Analysis Using Resonantly Enhanced Collisional Ionisation*", Inst. Phys.Conf. Ser. **94** (Ed. Lucatorto T.B. and Parks J.E.) p311.

Gerlach W. & Gerlach W., (1931), Virchow's Arch. f. Path. Anat., **28** p209.

Giordmaine J.A. & Miller R.C., (1965), Phys Rev. Lett, **14** pp973.

Goeringer D.F., Christe W.H. & Valiga R.E., (1988), "*Investigation of Matrix Effects on the Neutral Fraction Ejected from Ion Bombarded, Uranium Containing Solids using Resonance Ionisation Mass Spectrometry*", Anal. Chem. **60** pp345.

Gold A. & Bebb H. B., (1965), Phys. Rev. Lett., **14** p60.

Gonl W., Kutsher R., Laue H.J. & Wolinik H., (1983), "*Time of FLight Mass Spectrometry for Ions of Large Energy Spread.*", Int. J. Mass Spect. Ion Proc., **48** pp411-414.

Goppart-Mayer M., (1931), Ann. Physik **9** p273.

Hahn J.H., Zenobi R. & Zare R.N., (1987), "*Subfemtomole Quantification of Molecular Adsorbates by Two Step Laser Mass Spectrometry.*", J. Am. Chem. Soc., **109** pp2842-2843.

Hecht E., (1987), "*Optics*", Addison Wesley Publishing Company, pp291.

Hirvoven J.K. (ed), (1980), "*Ion Implantation*", Academic Press, New York.

Houston C.M., Drysdale S.L.T., Jennings R., Land A.P., Ledingham K.W.D., Singhal R.P., Smyth M.H.C., Stewart D.T. & Towrie M., (1988), "*Two- and Three-photon ionisation transitions in Cs vapour.*", J. Phys. D.: Applied Physics **21** S59-S62.

Hutchinson J.M.R., Inn K.G.W., Parks J.E., Beekman D.W., Spaar M.T. & Fairbanks W.M., (1987), "*Investigation of Matrix Effect and Isotope Dilution in SIRIS Measurements of Uranium in Soils*", Nucl. Inst. Meth. B, pp578-584.

Hurst G. S., Payne M.G., Nayfeh M.H., Judish J.P. & Wagner E.B., (1975), Phys. Rev. Lett. **35** p82.

Hurst G. S., Payne M.G., Kramer S.D. & Young J.P., (1979), Rev. Mod. Phys. **51** 767-819.

Hurst G.S., Payne M.G. & Wagner E.B., (1976), United States Patent No. 3987302, , "*Resonant Ionisation for Analytical Spectroscopy*".

Hurst G.S., Parks J.E., Schmitt H.W., (1984), United States Patent No 4,442,354, "*Sputter Initiated Resonant Ionisation Spectroscopy*"

IEEE, (1975), Computer Automated Measurement And Control, IEEE standard 583-1975.

IEEE, (1978), General Purpose Interface Bus, IEEE standard 488-1978.

Jenkins F. A. & White H. E., (1981), "*Fundamentals of Optics (4th ed)*", Mc Graw-Hill International Student edition. pp532.

Kelly R. & Rothenburg J.E., (1988),*"Reconsidering the mchanisms of laser sputtering with Knudsen-layer Formation Taken into Account."*, Nucl. Instr. and Meth., **B32** pp341-348.

Kimock F.M, Baxter J.P. & Winogard N., (1983), Surface Sci. **76** pp343.

Kimock F.M., Baxter J. P., Pappas D. L., Kobrin P. H. & Winograd N.,(1984), Anal. Chem. **56** p2782.

Kock R.C., (1960), *"Activation Analysisi Handbook"*, Academic Press, New York.

Koppenaal D.W., (1988), *"Atomic Mass Spectroscopy"*, Anal. Chem., **60** 113R-131R.

Krasinski J., Papanestor P. & Heller D.F., (1986), SPIE Proc. **622** pp105.

Krätschmer W., Lamb L.D., Fostiropoulos K. & Huffman D.R., (1990), *"Solid C_{60}: A New Form of Carbon."*, Nature **347** pp354-358.

Kroll N.M. & Ganapathi V., (1985), *"Magnetic Monopole Interactions in Simple Atoms"*, Inst. Phys. Conf. Ser. **84** (Ed Hurst G.S. and Grey Morgan C.) p297

Krönert U., Bonn J., Kluge H.-J., Ruster W., Walleroth K., Peuser P. & Trautmann N., (1985),, Appl. Phys B. **38** pp65

Krönert U., Becker St., Hilberath Th., Kluge H.J. & Schulz C., (1987), *"Resonance Ionisation Mass Spectroscopy ith a Pulsed Thermal Atomic Beam"*, Appl. Phy. A **44** pp339-345.

Krönert U., Becker S., Bollen G., Gerber M., Hilberath T., Kluge J-H. & Passler G., (1989), *"Resonance Ionization Mass Spectroscopy of ^{184}Au ($T_{1/2}$ = 53s) and ^{183}Au ($T_{1/2}$ = 42s) in a Pulsed Atomic Beam"*, Inst. Phys. Conf Ser **94** (Ed. Lucatorto T.B. and Parks J.E.) pp155.

Kroto H.W., Heath J.R., O'Brien S.C., Curl R.F. & Smalley R.E., (1985), Nature **318** pp162-163.

Kudryavtsev Y.A. & Letekhov V.S., (1990), "*Detection of Very Rare Isotopes*", Physics World **3** 9 pp48-52.

Lambropolous P. & Zoller P., (1984), "*Multiphoton Ionisation Of Atoms*", Academic Press, Canada.

Land A. P., (1990), "Resonant Ionization Mass Spectrometry of Calcium", Thesis, University of Glasgow.

Laud B.B., (1985), "*Lasers and Non-linear Optics*", John Wiley and Sons.

Lee, J. K. P., Raut V., Savard G., Thekkadath G., Duong T. H. & Pinard J., "*Pulsed Ion Beam Produced Via RIMS*", Inst. Phys. Conf. Ser. **84** (Ed Hurst G.S. and Grey Morgan C.) p139.

Letokhov V., (1987), "*Laser Photoionisation Spectroscopy*". Academic Press.

Loudon R., (1973), "*The Quantum Theory of Light*",Claredon Press

Lui Y *et al* , (1986), Chem. Phys. Lett., **126** pp215-217.

Magnusson I., Axner O., Lindgren I. & Rubinstien-Dunlop H., (1986), Appl. Spect. **40**(7) pp968.

Marienko J. & May I., (1954), Anal Chem, **40** p1137.

Mayo S., Lucatorto T.B. & Luther G.G., Anal. Chem. **54** pp553(1982)

McLean C.J., Marsh J., Land A.P., Clark A., Jennings R., Ledingham K.W.D., McCombes P.T., Singhal R. & Towrie M., "*Resonant Laser Ablation*", Int. J. Mass Spect. Ion Proccess, **96** ppR1-R7.

McLean, (1990), "*The Application of Resonance Ionisation Spectroscopy to III-V Semi-conductor Surface and Depth Analysis.*", Thesis, Glasgow University.

Merejkovsky B.K. ,(1933), Bull Soc Chim Biol, **15** p1336

Meyerand Jr. R. G. & Haught A. F., (1963), Phys. Rev. Lett., **11** p401

Meyerand Jr. R. G. & Haught A. F., (1964), Phys. Rev. Lett., **13** p7.

Miller C.M., Nogar N.S. Gancarz A.J. & Shields W.R., (1982), Anal. Chem., **54** p2377.

Miller C.M. & Nogar N.S., (1983a), "*Continuous Wave Lasers for Resonance Ionisation Mass Spectrometry*", Anal Chem **55** pp 1606-1608.

Miller C.M. & Nogar N.S. (1983b), "*Calculation of Ion Yields in Atomic Multiphoton Ionisation Spectroscopy*", Anal. Chem., **55** pp481-488.

Miller C.M., Engleman R. & Keller R.A., (1985), J. Opt. Soc. Am. B **2** p1503.

Moore L.J., Fassett J.D. & Travis J.C., (1984), Anal. Chem. **56** pp2770.

Moulton P.F., (1982), Opt. News **8**(6) pp9.

Moulton P.F., (1987), "*Tunable Solid-state Lasers Targeted for a Variety of Applications*", Laser Focus/Electro-Optics August 1987 pp 56.

Natelson S. & Zuckerman J.L., (1951), Anal Chem, **23** p653.

Nestor J.R., (1982), "*Optogalvanic Spectra of Neon and Argon in Glow Discharge Tubes*", Appl. Opt. **21** (22) pp4154-4157.

Nogar N.S., Estler R.C. & Miller C.M., (1985), Anal.Chem. **57** pp2441.

Nogar N.S., Estler R.C., Fearey B.L., Miller C.M. & Downey S.W., (1990), "*Materials Analysis by Laser and Ion Beam Sputtering with Resonance Ionisation Mass Spectrometry*", Nuc. Instr. Meth. B **44** pp459.

Oechsner H., Schoof H. & Stumpe E., (1978), Surface Sci. **76** pp343.

Palmer B.A., Keller R.A. & Engleman R. Jr., (1980), "*An Atlas of Uranium Emission Intensities in a Hollow Cathode Discharge*", Los Alamos National Laboratory Report LA-8251-MS (Los Alamos National Laboratory, Los Alamos, N.M., July 1980).

Pang H. & Yeung E.S., (1988), "*Laser Enhanced Ionisation as a Diagnostic Tool in Laser Generated Plumes*", Anal. Chem. **61** pp2546.

Parks J.E., Schmitt H.W., Hurst G.S. & Fairbank Jr. W.M., (1983), "*Laser Based Ultrasensitive Spectroscopy and Detection*", Proc. SPIE **426** p32

Parks J.E., Beekman D.W., Schmitt H.W. & Spaar M.T., (1985), "*Ultrasensitive Elemental Analysis of Materials Using Resonant Ionisation Spectroscopy*", Talk Presented to the 1985 Spring Meeting of the Materials Research Society, at the Golden Gateway Holiday Inn, San Fransico, California, April 15-18.

Pedrotti, F.L. & Pedrotti L.S., (1987), "*Introduction to Optics*", Prentice Hall International Editions, p118-120.

Pellin M.J., Young C.E., Calaway W.F. & Gruen D.M., (1986), Nucl. Instr. Meth. in Phys. Research **B13** pp653.

Pete J.A. *et al*, (1986), SPIE Proc. **622** pp46.

Peuser P., Herrmann G., Rimke H., Sattelberger P., Trautmann N., Ruster W., Ames F., Bonn J., Kluge H. J. & Kronert U., (1985), Appl. Phys. B, **38** p249.

Preece C.M. & Horvonen J.K. (eds), (1980), "*Ion Implantation Metallurgy*", Metallurgical Society of AIME, Warrendale PA.

Quinn T.E., Murphy T.J., Moore L.J., Arlinghaus H.A., Spaar M.T., Taylor E.H. & Thonnard N., (1990), "*Boimedical Analyses Using Resonance Ionisation Mass Spectrometry*", to be Published in 'RIS 90' by The Institute of Physics Publishing

Rabi I.I., (1937), Phys. Rev., 51 p652.

Ralston J., Moretti A.L., Jain R.K. Chambers F.A., (1987), *"Intermixing of $Al_xGa_{1-x}As$ / GaAs Superlattices by Pulsed Laser Radiation."*, Appl. Phys. Lett., **50** 25 pp1817.

Ramandik G., Verlinden J. & Gijbels R., (1988), *"Spark Source Mass Spectrometry"* in Inoganic Mass Spectrometry Adams F., Van Grieken R. eds, Chem Anal Series No. **95**, Wiley, New York.

Ready F., (1971), *"The Effects of High Power Laser Radiaiton."*, New York Academic Press.

Rief J., Nielsen H.B., Petzoldt S., Matthias E., Westin E. & Rosén A., (1989), *"Probing Surface Electronic Structure of Ionic Crystals by Resonant Multiphoton Ionisation"*, IOP Conf. Ser. **94** (Ed. Lucatorto T.B. and Parks J.E.) pp189.

Robinson M.T., (1984), *"The Physics of Ion Sputtering"*, IOP Conf. Ser. **71** (Ed. Hurst G.S. and Payne M.G.) pp151.

Russell W.A., Papanastassiou D.A. & Tombrello T.A., (1977), Geochimica et Cosmochimica Acta, **42** pp1075.

ShenY.R., (1984), *"The Principles of Non-Linear Optics"*, Wiley Interscience.

Schäfer F.P., (1973), *"Dye Lasers"*, Springer Verlag.

Scheuler B. & Odom R.W., (1987), *"Non-resonant Multiphoton Ionization of the Neutrals Ablated in Laser Microprobe Mass Spectrmetry Analysis of GaAs and $Hg_{0.78}Cd_{0.22}Te$"*, J Appl. Phy., **61** (9) pp4652.

Schwarz S.A., (1987), J. Vac. Sci. Technol. A. **5**(3) pp308.

Shaw R.W., Young J.P. & Smith D.H., (1989), *"Diode Laser Initiated Resonance Ionisation Mass Spectrometry of Lanthanum"*, Anal. Chem. **61** pp695-697.

Snyder J.J., Lucatorto T.B., Debenham P.H. & Geltman S., (1985), *"Ultrasensitive Laser Isotope Analysis in an Ion Storage Ring."*, J. Opt. Soc. Am. B., **2** 9 pp1497-1501.

Spectron, (1986), *"Spectron Laser System type SL2Q + SL3A User and Maintanence manual"*.

Spengler B., Bahr U. & Hillenkamp F., (1989), "*Parameters of UV-laser Desorbed Molecules as Measured by Multiphoton Ionisation*", IOP Conf. Ser. **94** (Ed. Lucatorto T.B. and Parks J.E.) pp137.

Sorokin P. P. & Lankard J. R., IBM J. Res. Develop. **10** p162

Stanford Research Systems Inc, (1987), "*Digital Delay / Pulse Generator Operation and Service Manual*", Stanford Research Systems.

Stolyarov K.P., Grigoriev N.N. & Khomenok G.A., (1973), Chem. Abst., **78** 78233V.

Travis J.C., Fassett J.D. & Lucatorto T.B., (1986), "*Resonance Ionization Mass Spectrometry*" Inst. Phys. Conf. Ser. **84** (Ed Hurst G.S. and Grey Morgan C.) p91

Thomas P, (1990), "*Inorganic Nonlinear Materials*", Physics World, **3** 3.

Towrie M., (1989), Private Communication.

Ullman J.D.., (1985), " *Double Beta Decay*", Inst. Phys. Conf. Ser. **84** (Ed Hurst G.S. and Grey Morgan C.) p350.

Verdun F.R., Krier G. & Muller J.F., (1987), "*Increased Sensitivity in LAMMA by Using Two Photon Ionisation Processes*", Anal Chem., **59** pp1383.

Vertes A., Gijbels R. & Adams F., (1990), "*Diagnostics and Modelling of Plasma Processes in Ion Sources*", Mass Spectrometry Reviews **9**(7), pp71.

Voronov G. S. & Delone N. B., (1965), Sov Phys JETP lett., **1** p66.

Walker R.J. & Fasset J.D., (1986), Anal. Chem. **61** 643A.

Walling J.C. *et al*, (1979), Opt. Lett. **4** pp182.

Wallmeroth K., *et al*, (1987), "*Sudden Change in the Charge Distribution of Light Gold Isotopes*", Phys. Rev. Lett., **58** p1516.

Wang L., McLean C.J., Borthwick I., Jennings R., Ledingham K.W.D., McCombes P.T. & Singhal R., (1990), To be Published in "RIS '90", Inst. Phys. Publishing.

White C.E. & Argauer J., (1970), "*Flourescence Analysis: A Practical Approach.*", Marcel Dekker, New York.

White H.E., (1934), "*Introduction to Atomic Spectra*", McGraw-Hill Book Co. Inc., New York.

Whitten, W.B. & Ramsey J.M., (1990), "*Isotope Ratio Biases in Resonance Ionisation Mass Spectroscopy Due to Population Trapping.*", Applied Spectroscopy **44**(7) pp1188-1192.

Wiley W.C. & McLaren I.H., (1955), Rev. Sci. Instr., **26** 12 p1150.

Williams M.W. & Beekman D.W., Swan J.B., Arakawa E.T., (1984), Anal. Chem **56** pp1348.

Winograd N., Baxter J.P. & Kimock F.M., (1983), Chem. Phys. Lett. **88** p581.

Winogard N., (1989), "*Surface Studies using Ion Beams and MPI*" IOP Conf. Ser. **94** (Ed. Lucatorto T.B. and Parks J.E.) pp183.

Winograd N., (1990), SPIE Proceedings vol 1208.

Wiza J.L., (1979), "*Microchannel Plate Detectors*", Nucl. Inst. Meth. **162** pp587-601.

Young C.E., Pellin M.J., Calaway W.F., Jørgensen B., Schweitzer E.L. & Gruen D.M., (1987), "*Trace Surface Analysis via RIS/TOF Mass Spectrometry*", Inst. Phys. Conf. Ser. **84** (Ed Hurst G.S. and Grey Morgan C.) p163.

Young J.P., Shaw B.W. & Smith D.A., (1989), "*Resonance Ionisation Mass Spectrometry*", Anal. Chem. **61**(22) pp1271A.

Zakheim D.S. & Johnston P.M., (1980), Chem. Phys., **46** pp 272.

Zandee L., Bernstein R.B. & Lichin D.A., (1978), J. Chem. Phys, **69** p3427

Zandee L. & Bernstein R.B., (1978), J. Chem. Phys, **71** p1359.

Zilliacus R., Lakomaa E-L. & Likonen J., (1989), "*Matrix Effects in RIS analyses using thermal atomisation*", IOP Conf. Ser **94** (Ed. Lucatorto T.B. and Parks J.E.) pp159.

Zhang Q.L. *et al*, (1986), J.Chem. Phys. **90** pp525-528.

Antonov V.S. *et al*, (1978), Optics Letts. **3** pp37.

Chryssoulis S., (1990), private communication.

McCombes P.T. *et al*, (1990), SPIE Proceedings **1208**.

Winogard N. *et al*, (1982), Chem Phys. Letts, **88** pp581.